



**AN APPLICATION OF LONG-OFFSET TRANSIENT
ELECTROMAGNETIC (LOTEM) AROUND A
SALT DOME NEAR HOUSTON, TEXAS**

Mr. ANDRI YADI PAEMBONAN

**A THESIS FOR DEGREE OF MASTER OF SCIENCE
KHON KAEN UNIVERSITY**

2018

**AN APPLICATION OF LONG-OFFSET TRANSIENT
ELECTROMAGNETIC (LOTEM) AROUND A
SALT DOME NEAR HOUSTON, TEXAS**

Mr. ANDRI YADI PAEMBONAN

**A THESIS SUBMITTED IN PARTIAL FULFULLMENT OF THE
REQUIREMENTS FOR THE DEGREE OF MASTER OF SCIENCE
IN GEOTECHNOLOGY
GRADUATE SCHOOL KHON KAEN UNIVERSITY**

2018



**THESIS APPROVAL
KHON KAEN UNIVERSITY
FOR
MASTER OF SCIENCE
IN GEOTACHNOLOGY**

Thesis Title: An Application of Long-Offset Transient Electromagnetic (LOTEM)
around a Salt Dome near Houston, Texas

Author: Mr. Andri Yadi Paembonan

Thesis Examination Committee:

Dr. Kurt M. Strack	Chairperson
Dr. Weerachai Sarakorn	Member
Asst. Prof. Dr. Rungroj Arjwech	Member

Thesis Advisors:

..... Advisor
(Asst. Prof. Dr. Rungroj Arjwech)

.....
Prof. Dr. Surasakdi Wongratanacheewin	Assoc. Prof. Dr. Pornthap Thanonkeo
Dean, Graduate School	Dean, Faculty of Technology

Andri Yadi Paembonan, 2560 .การประยุกต์ใช้วิธีการสำรวจ Long-Offset Transient Electromagnetic)LOTEM (โดยรอบ

บริเวณโคมเกลือใต้เมืองสุแดน รัฐเท็กซัส .วิทยานิพนธ์ปริญญาวิทยาศาสตรมหาบัณฑิต สาขาวิชาเทคโนโลยีธรณี บัณฑิตวิทยาลัย มหาวิทยาลัยขอนแก่น.

อาจารย์ที่ปรึกษาวิทยานิพนธ์: ศศ.ดร. รุ่งโรจน์ อ่าวเวทย์

บทคัดย่อ

การศึกษารุ่นใต้เกลือและใต้ทะเลที่เกี่ยวกับความสัมพันธ์ของน้ำมันและก๊าซธรรมชาติ และการติดตามระหว่างการเพิ่มปริมาณการผลิตน้ำมัน (Enhanced Oil Recovery) (ซึ่งโดยทั่วไปจะใช้ความรู้ทางธรณีวิทยาและธรณีฟิสิกส์สำหรับแปลผลและรวบรวมข้อมูล โดยการศึกษารุ่นใต้เกลือ ข้อมูลถูกวิเคราะห์และแปลผลมาจากฮาร์ดแวร์ใหม่ วิธีการสำรวจคลื่นแม่เหล็กไฟฟ้า 2 วิธีคือ Long-Offset Transient Electromagnetic)LOTEM (และ Focused Source Electromagnetic)FSEM (ถูกใช้เหนือพื้นที่โคมเกลือบริเวณเมืองสุแดน รัฐเท็กซัส ข้อมูลถูกประมวลผลโดยใช้ซอฟต์แวร์ใหม่ในหลายขั้นตอนเพื่อให้ได้อัตราส่วนสัญญาณต่อสัญญาณรบกวนที่ดีที่สุด ซึ่งพบว่าแบบจำลองความต้านทานไฟฟ้า 1 มิติ สอดคล้องได้ดีกับลักษณะทางธรณีวิทยา โดยชั้นนำไฟฟ้าที่มีสภาพนำไฟฟ้าต่ำกว่า 1 โอห์ม-เมตร ประกอบด้วยชั้นตะกอนของชุด Lissie หรือ Wills มีความลึกประมาณ 50 เมตร ชั้นที่มีความต้านทานไฟฟ้าต่ำมาก ๆ บ่งบอกถึงผลกระทบการเปลี่ยนแปลงที่ควิน ชั้นต้านทานไฟฟ้ามีค่าสภาพนำไฟฟ้าสูงถึง 30 โอห์ม-เมตร มีความหนาไม่แน่นอนอาจจะมีถึง 30 เมตร และความลึก 30 เมตร โดยประมาณ ชั้นนี้อาจถูกผลกระทบจากเกลือปิด ชั้นที่สามมีความต้านทานไฟฟ้าต่ำ โดยต่ำกว่า 10 โอห์ม-เมตร ประกอบด้วยตะกอน ที่ความลึกระยะ 70 เมตร ชั้นที่สี่แสดงค่าความต้านทานไฟฟ้าเพิ่มขึ้น จนถึงความลึก 300 เมตร ซึ่งแสดงถึงฐานของเกลือ ข้อมูลเหล่านี้แสดงชั้นค่าความต้านทานไฟฟ้าที่สอดคล้องกับการแปลผลของ Direct Warren Log การแปลผล LOTEM ก่อให้เกิดการผกผัน และการวิเคราะห์ข้อมูลทางสถิติ ทำให้สามารถแยกข้อมูลทางธรณีวิทยาที่นำเชื่อถือออกจากที่ไม่น่าเชื่อถือ ข้อมูลเหล่านี้ทำให้เข้าใจถึงลักษณะของโคมเกลือ ค่อกาจากนั้นเป็นการเปรียบเทียบแบบจำลอง 3 มิติ ของ FSEM ในขณะที่แบบจำลอง 3 มิติ ไม่ได้ทำให้เห็นเกลือปิด แต่สามารถยืนยันข้อมูลทีวีเคราะห์มาแล้วได้ ความหลากหลายของแบบจำลอง 3 มิติ ใช้ยืนยันความถูกต้องภายใต้โคมเกลือ และแสดงการตอบสนองเป็นแบบจำลอง 3 มิติที่สมบูรณ์แบบ

Andri Yadi Paembonan, 2017. **An Application of Long-Offset Transient Electromagnetic (LOTEM) around A Salt Dome near Houston, Texas.**

Master of Science Thesis in Geotechnology, Graduate School, Khon Kaen University.

Thesis Advisor: Asst. Prof. Dr. Rungroj Arjwech

ABSTRACT

Studying sub-salt and sub-basalt associated with oil and natural gas accumulation and monitoring during enhanced oil recovery (EOR) operation commonly involve both geologic and geophysical knowledge for interpretation and integration. Using a sub-salt application as example, new processing and interpretation methodology was applied to the data from new hardware. Two electromagnetic methods, Long-Offset Transient Electromagnetic (LOTEM) and Focused Source Electromagnetic (FSEM) are applied over a salt dome near Houston, Texas. The data were processed using the new software in several defined stages to yield best signal-to-noise ratios. The best fit 1D resistivity models suggest the geological setting. The conductive layer, below 1 Ωm , consists of sediment from Lissie or Wills formation. It extends to a depth of approximately 50 m. Very low resistivity layer may imply the static shift effects in surface. The resistive layer, up to 30 Ωm , has a variable thickness of up to 30 m in approximately 30 m depth. This layer may be interrupted by salt overhang. A low resistivity characterizes the third layer below 10 Ωm consisting of sediment with a depth interval of 70 m. The forth layer shows the resistivity increase up to 300 m depth indicating a salt body. It represents a resistive layer and similar to Direct Warren log interpretation. LOTEM processing leads to inversion and the detailed statistical analysis allowing us to separate reliable from unreliable parts of the geologic model. This led to a clear understanding that the salt dome overhang is seen by the data. Subsequently, this is compared with the FSEM 3D modeling. While the 3D modeling does not have the tools to see the overhang on its own, it could confirm it once known from this analysis. Various 3D models verify the sensitivity under the salt dome and show that the 3D model is highly equivalent.

DEDICATION
TO MY BELOVED PARENT, MY BROTHERS AND SISTERS,
AND ALL OF MY RELATIVES AS WELL AS ENTIRE TEACING
STAFF DURING MY EDUCATION.

ACKNOWLEDGEMENTS

I would like to express my deepest gratitude to my advisor, Assistant Professor Dr. Rungroj Arjwech for his time, advice, guidance, and patience throughout my education period and even for thesis evaluation. He dedicated his freely of time to provide the strategic and knowledgeable support to complete this thesis.

I also give my sincere thanks to my lectures, staffs, special thanks for Mr. Sakorn Sangchompoo, Dr. Kritika Trakoolngam, Assoc. Prof. Ladda Wannakao, Asst. Prof. Patchrasu Wannakao, and geophysics students for their support and helps during my study in Khon Kaen University. Especially, I would like to thanks to Khon Kaen University giving me a chance and providing me the Scholarship to study and doing research.

My sincere thanks are also to my outsider co-advisor, Dr. Kurt M. Strack and his staff at KMS Technologies, especially to Dr. Sonya Davydycheva, Tilman Hanstein and Prof. Maxim Smirnov for their supports and helps to complete this research.

I am so grateful having the friendly and cheerful friends who have helped me in my daily life, special thanks to Nova, Nirma, Diah, Ipung, Dariono, Agi, Thwe, Daniel, and all Indonesian students in Khon Kaen University. Unforgettably, the acknowledgment is given to the Pathway family, specially to Pastor Shane and family who have brightened and taught me.

Notably, I am so grateful born and raised in my family. I do appreciate to my parent for providing valuable encouragement through my life, and also to my siblings and my beloved one who always give me the sincere affection and support during my education.

Andri Yadi Paembonan

TABLE OF CONTENTS

	Page
ABSTRACT (IN THAI)	I
ABSTRACT (IN ENGLISH)	II
DEDICATION	III
ACKNOWLEDGEMENTS	IV
TABLE OF CONTENTS	V
LIST OF TABLES	VII
LIST OF FIGURES	VIII
CHAPTER I INTRODUCTION	1
1.1 Background	1
1.2 Objective	3
1.3 Scopes of study	3
1.4 Expected outcome	4
1.5 Area of study and data base	4
CHAPTER II LITERATURE REVIEW	7
2.1 Basic Theory of Electromagnetics (EM)	8
2.2 Previous studies of EM applications	16
2.3 General geology of study area (Hockley)	20
2.4 Signal processing theory	27
2.5 Inversion theory	36
CHAPTER III METHODOLOGY	44
3.1 Signal processing	45
3.2 Inversion	55

TABLE OF CONTENTS (Cont.)

	Page
CHAPTER IV RESULTS AND DISCUSSION	61
4.1 Processing evaluation result	61
4.2 Hockley Results	63
4.3 Interpretation	76
CHAPTER V CONCLUSION AND RECOMMENDATION	79
5.1 Conclusion	79
5.2 Recommendation	81
REFERENCES	82
APPENDICES	90
APPENDIX A	91
APPENDIX B	96
APPENDIX C	115
APPENDIX D	131
APPENDIX E	134
APPENDIX F	196
RESEARCH PUBLICATION	203
CURRICULUM VITAE	204

LIST OF TABLES

	Page	
Table 1. 1	Transmitter electrode connection to KMS-5100.	6
Table 1. 2	The list of instruments for each station used in this field work.	6
Table 1. 3	Transmitter configuration for each station.	6
Table 2. 1	Stratigraphy of Cenozoic era, the Coastal Plain of Texas	22
Table 4. 1	Statistical analysis for electric field, Rx3Ex inline transmitter.	68
Table 4. 2	Statistical analysis for Rx1 electric field (Ex) broadside transmitter.	72

LIST OF FIGURES

	Page	
Figure 1. 1	Map of the study area.	5
Figure 2. 1	Direction of the induced current.	9
Figure 2. 2	Measures natural variation of EM field.	10
Figure 2. 3	Typical LOTEM transmitter and receiver setup.	12
Figure 2. 4	System of smoke rings for the grounded wire dipole in a two-layered earth model.	13
Figure 2. 5	The experimental setup with three-electrode quadrupole receive.	15
Figure 2. 6	FSEM diagram.	15
Figure 2. 7	An example of using MT for sub-salt interpretation.	16
Figure 2. 8	Interpretation derived from well-log report with the major lithological unit and LOTEM prediction.	17
Figure 2. 9	Interpretation of LOTEM resistivity section from individual 1D inversion.	18
Figure 2. 10	Simulated response of surface-to-borehole EM for a period of 2 years.	19
Figure 2. 11	The location of salt dome basin in the Gulf Coast.	23
Figure 2. 12	Salt domes around Houston, Texas, including Hockley salt dome.	24
Figure 2. 13	Section across Hockley salt dome, Southwest-Northeast.	24
Figure 2. 14	Section across Hockley salt dome, Southeast-Northwest.	25
Figure 2. 15	Geologic map of Harris County.	26
Figure 2. 16	The filtering transient data using the true amplitude notch filter.	29
Figure 2. 17	Filtering of transient data using lock-in filter.	30
Figure 2. 18	Amplitude response of n-th order Butterworth function.	31
Figure 2. 19	The symmetric rejection selective stack technique with a cut-off of 20% at both ends of the sorted amplitudes to stack the data.	34

LIST OF FIGURES (Cont.)

	Page
Figure 2. 20 Stacked data using the area-defined rejection selective stack technique.	35
Figure 2. 21 Smoothed data using recursive average filter.	36
Figure 2. 22 Inverse modeling functional diagram.	37
Figure 3. 1 The workflow diagram of the data processing.	44
Figure 3. 2 The data header.	46
Figure 3. 3 The example of signal display in KMS-820 tools.	46
Figure 3. 4 Flow diagram of data processing.	47
Figure 3. 5 An example of time alignment as part of synchronization of transmitter and receiver data.	48
Figure 3. 6 The merged data.	49
Figure 3. 7 Resampling frequency of transmitter data.	50
Figure 3. 8 Filtering the signal from noise.	52
Figure 3. 9 Signal after stacking showing the smoother signal.	53
Figure 3. 10 The smooth data of magnetic field and electric field.	54
Figure 3. 11 Cumulative conductance and transverse resistance analysis from the Occam's inversion to generate the starting model of Marquardt inversion.	57
Figure 3. 12 Data analysis using eigenvector and importance to resolve layer of both parameters (resistivity and thickness).	58
Figure 3. 13 3D visualization steps.	59
Figure 3. 14 Comparison between measured signal and the forward modeling calculation of Occam's model and layered model.	59
Figure 4. 1 The transmitter signal measured in the different area and with different transmitters.	62
Figure 4. 2 The time shift between transmitter and receiver decreasing from the day 1 to day 3.	63
Figure 4. 3 Distorted curve of magnetic field Rx1 roadside.	64

LIST OF FIGURES (Cont.)

	Page	
Figure 4. 4	1D Occam inversions results of E-field (Ex) inline transmitter.	65
Figure 4. 5	The Marquardt inversion generated of electric field (Ex) for receivers, Rx1 to Rx3.	66
Figure 4. 6	The best fit Marquardt model of electric field for receiver site 1 to 3.	67
Figure 4. 7	1D Occam inversions results of E-field (Ex) broadside transmitter.	70
Figure 4. 8	The best fit Marquardt model of electric field.	71
Figure 4. 9	Comparison between measured signal and forward calculation of Occam's model and layered model showing the similarity.	73
Figure 4. 10	3D visualization of Occam model.	74
Figure 4. 11	3D visualization of Marquardt inversion result.	75
Figure 4. 12	Cross section of 3D model of the salt dome.	76
Figure 4. 13	Direct Warren log and the location.	77
Figure 4. 14	Interpretation with the previous study.	78

CHAPTER I

INTRODUCTION

Here, the background contains addresses first the overall description of this research including the challenge in using geophysical method in oil and natural gas exploration and monitoring and the drawback of using seismic method to study the area covered by salt and the alternative method such us electromagnetic and gravity. Second, the objective of this research includes the processing as the main propose of this study, and to support this, time-lapse monitoring and a feasibility study. Third the scope of study described the processing and its verification objectives. Fourth, as expected outcome a verification with independent studies is considered. Fifth, the study area data base is provided.

1.1 Background

Studying sub-salt and sub-basalt that is associated with oil and natural gas accumulation and monitoring during enhanced oil recovery (EOR) operation are still the challenging tasks for geophysicists. Exploration and production commonly involve both geologic and geophysical knowledge for interpretation and integration. Geophysical methods, including data processing, and geologic approaches have to be integrated to improve and obtain a reasonable sub-salt or sub-basalt interpretation. Here, various geophysical methods are applied to image sub-salt and they are tested in a time-lapse application (monitoring) where higher accuracy is required.

Various methods have been employed for sub-salt exploration including gravity and magnetic investigation (Peterst & Dugan, 1945), gravity survey, refraction seismograph survey and test drilling (Nettleton, 1947), seismic 2D processing and 3D modelling and gravity 3D modelling (Starich et al., 1994), the single geophysical study using vertical seismic profiling (Deri & Sparlin, 1990; Whitmore & Lines, 1986), radar (Stewart & Unterberger, 1976), and borehole radar (Siever & Elsen, 2010), magnetotellurics (MT) (Zerilli et al. 2002), 3D inversion and synthetic MT study

(Avdeeva et al., 2012), as well as geological investigation (Jackson & Seni, 1984). For sub-basalt exploration MT (Beamish & Travassos, 1992) and controlled source electromagnetic (CSEM) (Morrison et al., 1996; MacGregor & Sinha, 2000; Strack & Pandey, 2007), integrated seismic and electromagnetics (Colombo et al. 2012), and MT and gravity (Jegen et al., 2009) are used.

The seismic technique is widely used to image the subsurface both salt dome, (Beckman & Williamson, 1990: an example in the Gulf Coastal Plain), and the sub-basalt formation (Petersen et al., 2006; Shah, 2009). Extensive improvements also have been made in seismic data processing to determine the sub-salt with good accuracy of data analysis and developed interpretation, such as new seismic attribute: saliency-based at-tribute (Shafiq et al., 2016) and codebook-based learning model (Amin & Deriche, 2016). However, in several areas covered by salt or basalt, the seismic method did not give the stratified result due to imaging difficulties associated with high-velocity layers (MacGregor & Sinha, 2000). The seismic energy is often hampered by extensive salt canopies, sheets and other salt bodies which absorb or redirect the seismic waves, resulting in poor seismic imaging (Coburn, 2002). Therefore, other methods such as electromagnetic technique including Control Source Electromagnetic (CSEM) (Hussain et al., 2012), Magnetotellurics (MT) (Zerilli et al., 2002; Avdeeva et al., 2012; Strack pers. communication) can be a possible alternative and/or complementary method.

For frequency and time domain electromagnetics, salt is almost transparent because salt is high resistive and electrically isotropic, and the salt-to-host rock boundaries are a perfect target due to their high resistivity contrast. This also the advantages of using EM for monitoring fluid injection during enhanced oil recovery (EOR) operation using time-lapse methods where the resistivity changes between brine and hydrocarbon are determined. Ceia et al (2007) used 1D modeling of LOTEM integrated with other EM method, and with the geological information to interpret the resistivity changes.

The LOTEM method has been used in many oil and gas industries because of the unique way of defining the resistivity at depth from the surface. The method aids geological interpretation as the resistivity is correlated to different pore fluids and

Deleted: -

Deleted: -

porosity. In general, LOTEM has less ambiguity among of non-seismic methods, but it is more difficult to interpret than other geophysical techniques (Strack, 1992).

The main focus in this research is the processing of LOTEM data from the area around Hockley salt dome at the West of Houston, Texas, where several techniques have been applied earlier (not part of this study) measured with brand new hardware using novel software workflows to reduce the noise and to produce the best data sets. The data utilize KMS software for the signal processing, and data inversion software (EMUPLUS) from University of Cologne. LOTEM Suite, IX1D from Interpex is used for feasibility study and analyses. Additional, 3D modeling/integration requires more research outside the scope of this thesis.

1.2 Objective

The main purpose of this study is to process and interpret the Long Offset Transient Electromagnetic (LOTEM) data using new hardware and processing methods from the survey around a Salt Dome near Houston, Texas. The data were acquired by KMS Technologies. Further, the processing of an example of time lapse study and the feasibility study from the real oil reservoir is extended in this study.

1.3 Scopes of study

1.3.1. This study uses data from the Hockley salt dome, processed using KMSPro prototype software, and then inverting the data and comparing with the 3D EM modeling performed by S. Davydycheva, KMS Technologies (pers. communications);

1.3.2 The individual data sets were quality controlled and processed with detailed evaluation of each step. The interpretations are carried out by analyzing 1D inversions and then integrated with previous 3D EM modeling studies and available geologic information;

1.3.3 During the processing, several details in the data (including DC levels, stacking and synchronization) were checked, as described in Appendix B. Many software corrections and improvements were suggested that allowed us to get more reliable data processing;

1.3.4 For readability of this work, the details are reported in separate appendices with key results discussed in the main body.

1.4 Expected outcome

1.4.1 The data processing reduces the cultural noise. The details are verified in Appendix C.

1.4.2 The result of this study is 1D interpretation of salt dome area and revealing 3D effects which limited the 1D interpretation.

1.4.3 The advantages of using this method is the ability to figure out the structure of the salt body much better than the lower-resolution magnetotellurics allows.

1.4.4 The method will be used to evaluate and corroborate interpretation of other method.

1.4.5 The depth of investigation of the LOTEM method can reach up to several kilometers below the Earth surface (Strack, 1992).

1.4.6 The forward calculation study allows us to understand how the data acquisition is performed.

1.4.7 An example of the time lapse study and the feasibility study from the oil reservoir confirms reliability of the processing.

1.5 Area of study and data base

The area of the Hockey salt dome is located at 13227 Sunrise Bluff Dr. on Jack Rd and Katy Hockley Rd (Figure 1.1). The area, in general, is covered by the grass field, marsh and swampy area where the transmitter dipoles were located at the upper part and the receivers were in the lower part.

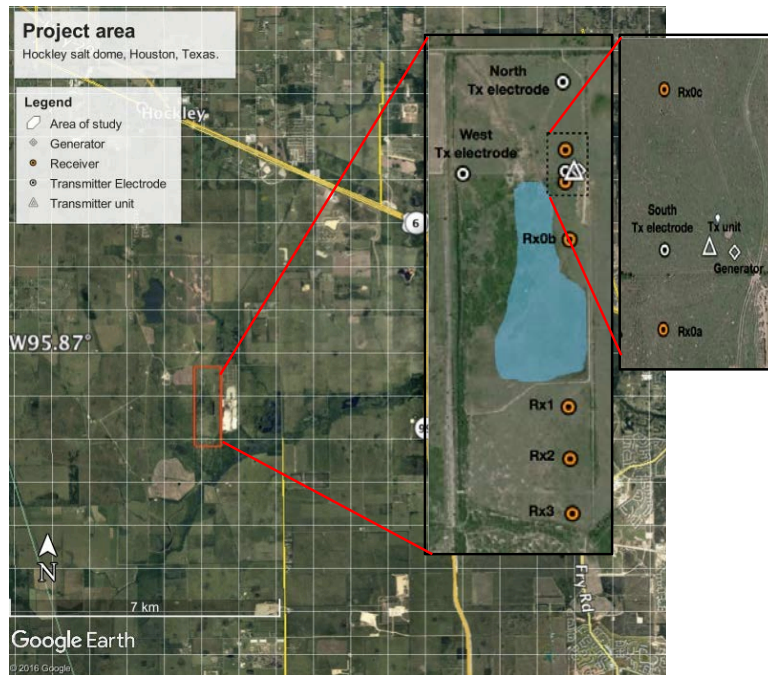


Figure 1.1 Map of the study area. Showing the ‘wet’ area (light blue shaded). On the Eastern edge of the survey map is an operating salt mine.

The transmitter is designed for 400 m in E-W and 350 m N-S directions. In practical, the first receiver (Rx1) is at 900-m offset instead and follow by second receiver (Rx2) and third receiver (Rx3) with offset 110 m and 130 m respectively. The transmitter electrode and receiver locations were obtained from GPS. The location of Rx0b, Rx1, Rx2 and Rx3 were obtained from KMS-820’s GPS information, while the other from an independent GPS device.

Following is a summary of the measurements and data to be processing and investigated. In this study, the transmitter is operated in two directions and connection between electrodes and terminal plug as shown in Table 2:

- 1.) N-S direction: Inline transmitter
- 2.) E-W direction: Broadside transmitter.

Table 1.1 Transmitter electrode connection to KMS-5100.

Direction	Configuration	Terminal plug on KMS-5100	
		Positive (red)	Negative (black)
N-S	Inline	North transmitter electrode	South transmitter electrode
E-W	Broadside	West transmitter electrode	South transmitter electrode

During the data acquisition, the following sensors were used at the measurement stations: the electric field sensors, LEMI-701 grounding electrodes, and magnetic field KMS-029 fluxgate sensors, LEMI 120 coils, and air loops, as well as geophones for micro seismic measurement (description of the hardware can be found in www.KMSTechnologies.com). The acquisition units might be changed from test to test. At the receiver locations Rx1, Rx2 and Rx3 (shown in Figure 1.1), there were two geophones, one connected to KMS-820 and the other one connected to KMS-831. The details are given in Table 1.2 and 1.3.

Table 1.2 The list of instruments for each station used in this field work.

Ch.	Signal	Sensor	Receivers station					
			Rx0a	Rx0b	Rx0c	Rx1	Rx2	Rx3
1	Ex (N-S Electric field)	Electrode	√	√	√	√	√	√
2	Ey (W-E Electric field)	Electrode	√	√	√	√	√	√
3	Hz (Magnetic field)	Air-loop				√	√	√
4	Hz (Magnetic field)	LEMI-120				√		
4-6	Seismic	3C Geophone				√	√	√
7-9	Hx, Hy, (Horizontal magnetic field) Hz (vertical magnetic field)	KMS-029 fluxgate sensor				√	√	√

Table 1.3 Transmitter configuration for each station.

Transmitter direction	Receivers station					
	Rx0a	Rx0b	Rx0c	Rx1	Rx2	Rx3
Inline	1 st & 3 rd May	2 nd & 3 rd May	1 st May	7 th & 8 th May	7 th & 8 th May	7 th & 8 th May
Broadside				5 th May	5 th May	5 th May

CHAPTER II

LITERATURE REVIEW

This chapter consists of five sections:

2.1 Basic theory of Electromagnetic methods including Magnetotelluric (MT), Long-offset Transient Electromagnetics (LOTEM) and Focused Source Electromagnetics (FSEM).

2.2 Previous literature of using LOTEM,

2.3 General geology of study area, specifically the Hockley salt dome in Gulf Coastal Plain, Texas.

2.4 Data processing theories where the key processing elements used herein is reviewed.

2.5 Inversion theories to discuss the parts of the inversion that are used within this thesis.

The geophysical methods are divided into natural source (passive) and man-made source (active or controlled source) methods. Passive methods include Magnetotelluric (MT), Audio Frequency Magnetotelluric (AFMAG) and self-potential techniques (Vozoff, 1972 & 1990). The active methods include frequency and time domain-controlled source EM. Among the latter, LOTEM and FSEM, are used for hydrocarbon and geothermal for depths up to 4 km below the earth surface. their differences and their concepts are described.

In this research, the data processing includes pre-stack, stacking, and post-stack data processing followed by the data inversion. The acquisition of the data was done before this thesis was started.

The geology of Gulf Coastal Plain defines the framework and give us the idea to image geophysical results. The Hockley salt dome includes regional aquifers, permeable zones, and confining units and facilitates in interpreting the result. This is compared to the results of the data inversion to avoid geophysical misinterpretation.

Deleted: ; Vozoff,

2.1 Basic Theory of Electromagnetics (EM)

The basic theory of electromagnetics can be expressed in mathematical formulation by Maxwell's equations as follow (Fleisch, 2008):

Gauss's Law for electric fields:

$$\nabla \cdot \mathbf{E} = \frac{\rho}{\epsilon_0} \text{ (Differential form)} \quad (2.1)$$

$$\oint_S \mathbf{E} \cdot \mathbf{n} \, da = \frac{q_{enc}}{\epsilon_0} \text{ (Integral form)} \quad (2.2)$$

Gauss's Law for magnetic field:

$$\nabla \cdot \mathbf{B} = 0 \text{ (Differential form)} \quad (2.3)$$

$$\oint_S \mathbf{B} \cdot \mathbf{n} \, da = 0 \text{ (Integral form)} \quad (2.4)$$

Faraday's Law of induction:

$$\nabla \times \mathbf{E} = -\frac{\partial \mathbf{B}}{\partial t} \text{ (Differential form)} \quad (2.5)$$

$$\oint_C \mathbf{E} \cdot d\mathbf{l} = -\frac{d}{dt} \oint_S \mathbf{B} \cdot \mathbf{n} \, da \text{ (Integral form)} \quad (2.6)$$

Ampere-Maxwell's Law:

$$\nabla \times \mathbf{B} = \mu_0 \left(\mathbf{J} + \epsilon_0 \frac{\partial \mathbf{E}}{\partial t} \right) \text{ (Differential form)} \quad (2.7)$$

$$\oint_C \mathbf{B} \cdot d\mathbf{l} = \mu_0 \left(I_{enc} + \epsilon_0 \frac{d}{dt} \oint_S \mathbf{E} \cdot \mathbf{n} \, da \right) \text{ (Integral form)} \quad (2.8)$$

where ∇ is differential operator, electric field (E) in N/C or V/m, magnetic field (B) in Testla, charge density (ρ) in C/m³, amount of charge (q) in C, the electric permittivity of the free space (ϵ_0), the magnetic permeability of free space (μ_0), electrical current (I) (A), electrical current density (J) in A/m², increment of surface (da) (m²), incremental segment of part of C (dl), unit normal vector (n), surface integral (S), line integral (C).

The electric field is induced by the quasi-static magnetic field following Faraday's law (Figure 2.1):

$$\nabla \times \mathbf{E} = -\frac{\partial \mathbf{B}}{\partial t} \text{ or } \text{Emf} = -N \frac{\Delta \Phi}{\Delta t} \text{ (Flux rule)} \quad (2.9)$$

where, N is the number of returns, $\Phi = BA$, B is the external magnetic field, and A is the area of coil. The induced electric field excites currents in conductors that obey Lenz's law (-): so that "The direction of induced currents tends to oppose changes in magnetic flux".

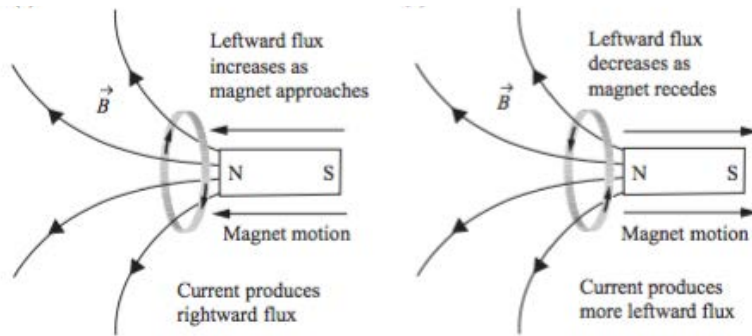


Figure 2.1 Direction of the induced current showing the electric fields induced by quasi-static magnetic fields (Fleisch, 2008).

The geophysical techniques utilize both active and passive EM methods. Passive EM methods use natural sources in the Ionosphere and are mostly covered by magnetotelluric (MT) method. Active methods are the man-made sources or transmitter such as Control Source Electromagnetic (CSEM). They are separated into Frequency-domain Electromagnetic (FDEM) and Transient or Time-domain Electromagnetic (TDEM), the later including LOTEM as specific technique. The following is only the brief explanation, and the more explanation can be found in many references.

2.1.1 Magnetotellurics (MT) as passive method

This technique uses natural sources known as the primary electromagnetic field from the sun and from other natural sources such as thunderstorms, that reaches the Earth's surface and then induces EM field in the subsurface, being passive method. The part of electromagnetic field is reflected back from the subsurface structures and the remaining part penetrates in to the Earth. Furthermore, the induced electric current, known as telluric current, produces a secondary magnetic field since the Earth acts as a relatively good conductor.

The time variation of both magnetic field $B(t)$ and the induce electric field $E(t)$ is measured simultaneously to determine the electrical properties (e.g. electrical conductivity) of the subsurface by relationship between the transfer functional of both components, horizontal electric (E_x and E_y), horizontal magnetic (B_x and b_y) and vertical magnetic (B_z) components as showing in Figure 2.2. In

addition, the depth of penetration is determined by developing theory of electromagnetic field frequency.

There are two sources generating the MT signal as following:

- The lower frequency signal ($< 1\text{Hz}$), more than 1 cycle per second, is originated from the interaction of the solar wind with the earth's magnetic field.
- The high frequency signal ($> 1\text{Hz}$), less than 1 cycle per second, is created by world-wide thunderstorm activity, usually near the equator. (mostly Audio-magnetotellurics range)

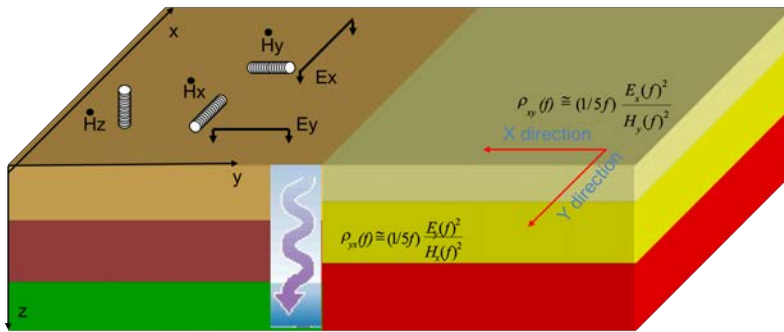


Figure 2.2 Measures natural variation of EM field, source from ionosphere & worldwide thunderstorm activity; Source field can be handled as vertical plane wave, influenced by ground conductivity (KMS Technologies, 2016).

Apart from the Maxwell's equations, above, Faraday's law, Ampere's law and Gauss's law for both electric and magnetic field are connected by the following constitutive relationship:

$$J = \sigma E \quad (2.10)$$

$$D = \epsilon E \quad (2.11)$$

$$B = \mu H \quad (2.12)$$

where E (V/m) and H (A/m) are the electric and magnetic fields, respectively, and B is the magnetic induction. D (C/m²) is the displacement current and ρ (C/m³) is the electric charge density owing to free charges. J and $\partial D/\partial t$ (A/m²) are the current density and the varying displacement current respectively. σ (S/m) is the electrical conductivity

(its reciprocal being the electrical resistivity $\rho = 1/\sigma$ (Ωm), ε (F/m) is the dielectric permittivity, and μ (H/m) the magnetic permeability. They describe intrinsic properties of the materials through which the electromagnetic fields propagate.

Furthermore, in the medium interface causing the EM property discontinuities between two different material, 1 and 2, the following boundary condition for two electromagnetic fields and currents:

$$\mathbf{n} \times (\mathbf{E}_2 - \mathbf{E}_1) = 0, \quad (2.13)$$

$$\mathbf{n} \times (\mathbf{H}_2 - \mathbf{H}_1) = \mathbf{J}_s, \quad (2.14)$$

$$\mathbf{n} \times (\mathbf{D}_2 - \mathbf{D}_1) = \rho_s, \quad (2.15)$$

$$\mathbf{n} \times (\mathbf{J}_2 - \mathbf{J}_1) = 0. \quad (2.16)$$

The most important measured data in MT is the magnetotelluric impedance (Z) introduced by Tikhonov (1950) and Cagniard (1953) related to the processes in the ionosphere and magnetosphere, and defined as follow:

$$Z_{xy} = \frac{E_x}{H_y} = \frac{i\omega\mu}{k} \quad (2.17)$$

and

$$Z_{yx} = -\frac{E_y}{H_x} \quad (2.18)$$

It possible to prove that true resistivity in the homogeneous half-space is connected to the MT impedance as follows:

$$\rho = \frac{1}{\sigma} = \frac{|Z|^2}{\mu\omega} \quad (2.19)$$

$$\rho = \frac{T}{2\pi\mu} |Z|^2 \quad (2.20)$$

which lead to the following equation:

$$\rho = 0.2 T \frac{|E_x|^2}{|H_y|^2} \quad (2.21)$$

$$\rho = \frac{1}{5 f} \frac{|E_x|^2}{|H_y|^2} \quad (2.22)$$

where ρ is resistivity in $\Omega\text{-m}$, E is the horizontal electric field in mv/km , H is the orthogonal horizontal magnetic field in γ , T is the period in seconds, f is the EM frequency, the propagation constant (Vozoff, 1972 & 1990; & Naidu, 2012).

2.1.2 Long Offset Transient (Time-domain) Electromagnetic (LOTEM)

In the LOTEM exploration, the distance between the transmitter and the receiver is typically chosen to be approximately equal to or greater than the desired exploration depth (Sheriff, 2002). These measurements require a tradeoff between constraints of the practical field aspects such as powerline noise, which restricts the method to minimum offset in order to obtain signal frequencies undistorted by power line noise or analog filter used in the system, and the theory, which requires the receiver to be as close as possible to the transmitter to avoid uncertainties due to lateral inhomogeneity. A detailed theory of LOTEM method and its applications is given by Strack (1992).

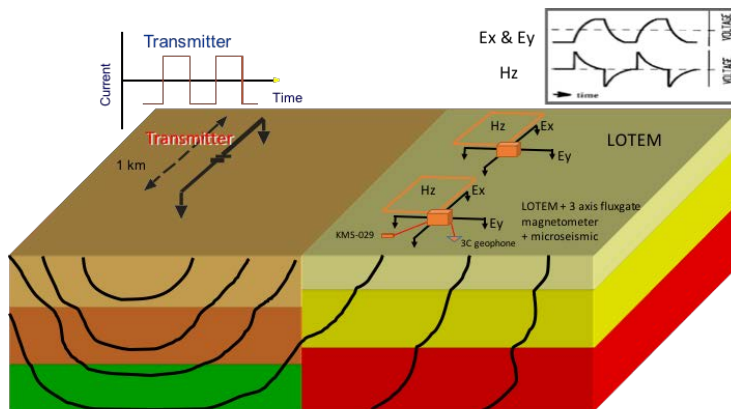


Figure 2.3 Typical LOTEM transmitter and receiver setup (modified from KMS Technologies, 2016).

The data measurement system for the land application where a square wave current is injected directly into the ground through the electrodes of transmitter dipole as shown in Figure 2.3. Figure 2.4 shows a system of so-called smoke rings illustrating the energy distribution in the subsurface. Then the current switching induces electromagnetic induction current in the subsurface. The induction currents flow perpendicularly to the plane. The Earth response is measured by two electric field sensors and by two to three magnetic field sensors or loops/coils, which record the time-derivative of the vertical magnetic field as voltages induced in the loop.

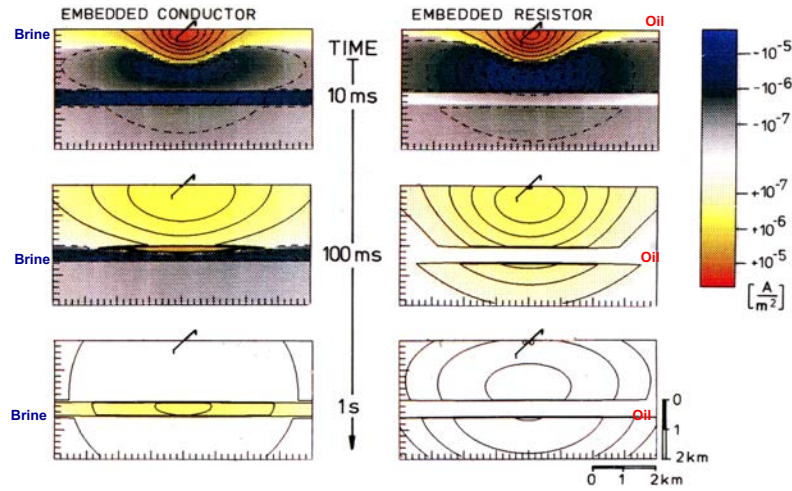


Figure 2.4 System of smoke rings for the grounded wire dipole in a two-layered earth model. The contours represent line of equal electric field strength and the dashed line mark the field of the opposite polarity (after Strack, 1992).

The equations governing the voltages measured by induction loop magnetometers, U , or electric field sensor, E_x and E_y , are following:

$$U_z(r, t) = \frac{-1}{2\pi} \int_{-\infty}^{\infty} \mu_0 A e^{i\omega t} \frac{D_0 \cos \phi}{4\pi} \int_0^{\infty} \frac{B_E(k, \omega) - k}{B_E(k, \omega) + k} k J_1(k, r) dk d\omega \quad (2.23)$$

$$E_x(r, t) = \frac{-1}{2\pi i} \int_{-\infty}^{\infty} \frac{e^{i\omega t}}{\omega} \frac{-i\omega \mu_0 D_0}{4\pi} \int_0^{\infty} \left\{ \left(\frac{2 B_M(k, \omega) - B_M(k, 0) - k}{k_1^2} - \frac{2}{B_E(k, \omega) + k} \right) \left(k J_{01}(k, r) - \frac{2}{r} J_1(k, r) \right) \cos^2 \phi + \frac{1}{r} J_1(k, r) \frac{B_E(k, \omega) - k}{B_E(k, \omega) + k} k J_0(k, r) \right\} dK d\omega + \frac{\rho_1 D_0}{2\pi r^3} (2 - 3 \sin^3 \phi) \quad (2.24)$$

$$E_y(r, t) = \frac{-2}{2\pi i} \int_{-\infty}^{\infty} \frac{e^{i\omega t}}{\omega} \frac{-i\omega \mu_0 D_0 \cos \phi \sin \phi}{4\pi} \int_0^{\infty} \left\{ \left(\frac{2 B_M(k, \omega) - B_M(k, 0) - k}{k_1^2} - \frac{2}{B_E(k, \omega) + k} \right) \frac{B_E(k, \omega) - k}{B_E(k, \omega) + k} k J_0(k, r) \right\} dK d\omega + \frac{3 \rho_1 D_0 \cos \phi \sin \phi}{4\pi r^3} \quad (2.25)$$

where U_z is the voltage induced in the induction coil with the area of A , ϕ is the angel between the x -coordinate (parallel to the transmitter dipole), and the offset vector r , y is the coordinate perpendicular to the transmitting dipole, ω is the angular frequency, k

is the wave number, J_0 and J_1 are Bessel function, E_x and E_y are the voltages measured with electric field sensor of length, and D_0 is the transmitter dipole moment. BE_1 and BH_1 are reciprocal modified impedances at the surface.

For different electromagnetic field component, all time apparent resistivity can be derived as following formulae:

The time derivative of vertical magnetic field (U_z):

$$\rho_{a,z}^{ET}(t) = \frac{2\pi r^5}{3AD_0Y} U_z(t) \quad (2.26)$$

$$\rho_{a,z}^{LT}(t) = \left(\frac{AD_0Y}{40\pi\sqrt{\pi}U_z(t)} \right)^{\frac{2}{3}} \left(\frac{\mu_0}{t} \right)^{\frac{5}{3}} \quad (1.27)$$

or, as a function of the electric field (E_x):

$$\rho_a^{ET}(t) = \frac{4\pi r^3 E_x}{3D_0 \sin^2 \phi} \quad (2.28)$$

$$\rho_{a,z}^{LT}(t) = \frac{-2\pi r^3 E_x}{D_0(1-\frac{2}{3}\sin^2 \phi)} \quad (2.29)$$

or the electric field (E_y):

$$\rho_a^{ET}(t) = \frac{-4\pi r^3 E_y}{3D_0 \cos \phi \sin \phi} \quad (2.30)$$

$$\rho_a^{ET}(t) = \frac{-4\pi r^3 E_y}{3D_0 \cos \phi \sin \phi} \quad (2.31)$$

where ρ_a^{ET} is early time apparent resistivity ($t \rightarrow 0$), and ρ_a^{ET} is the late time apparent resistivity ($t \rightarrow \infty$) (Strack, 1992).

2.1.2 Focused-Source Electromagnetic (FSEM)

The new FSEM method, introduced by geophysicist from Russia (Davydycheva et al., 2006), utilizes the concepts of obtaining deep resistivity data by focusing the EM field in the vertical direction, eliminating the horizontal component of electric current density. It is an improvement of the conventional CSEM method, which has significantly higher spatial resolution and provides deeper resistivity data.

FSEM technique uses the vertical focusing of the EM field, its idea was inspired by the resistivity well logging such as focused laterolog. It was applied to hydrocarbon exploration to provide meaningful interpretation, with the spatial resolution higher and the depth of investigation greater, than the conventional CSEM (Davydycheva et al., 2006; Davydycheva & Rykhlinski, 2009).

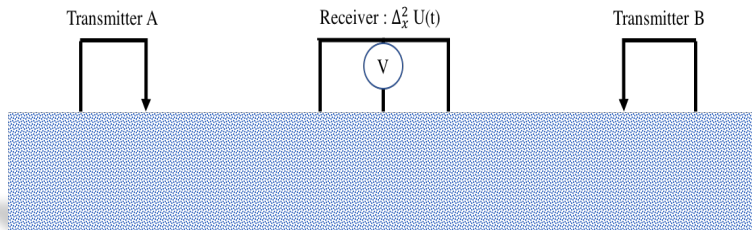


Figure 2.5 The experimental setup with three-electrode quadrupole receiver (modified sketch from Davydycheva et al., 2006).

The quadrupole current receiver is located between two grounded dipoles current transmitter (Figure 2.5), and the offset between transmitter and receiver can vary in the range of several kilometers. Figure 2.6 shows the current flow of using the FSEM method.

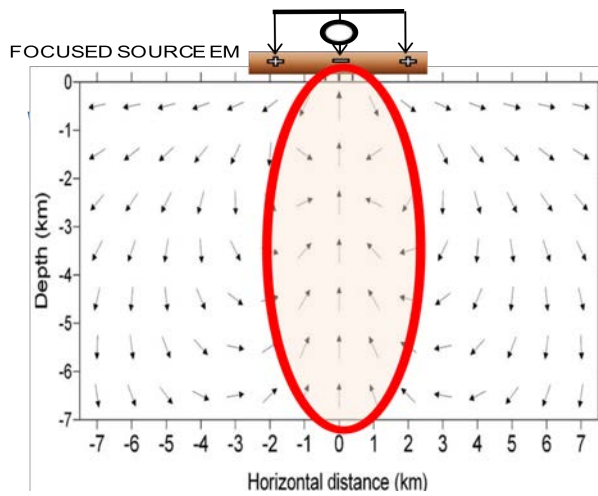


Figure 2.6 FSEM diagram showing how the current flows below the three-electrode receiver. The current is more concentrated or focused in the vertical direction, which gives the name Focused-source Electromagnetic to the method (Davydycheva et al., 2006).

2.2 Previous studies of EM applications

Recently, EM methods have been widely used in hydrocarbon exploration because of their ability to reveal high-resistive layers. They have been applied even in the difficult exploration environments such as sub-salt or sub-basalt, (typically blocking DC current flow) and can complement other geophysical methods. Several studies have been published to increase the accuracy of the results. The following is the overview of some previous studies of using EM, mostly LOTEM application for hydrocarbon exploration and monitoring.

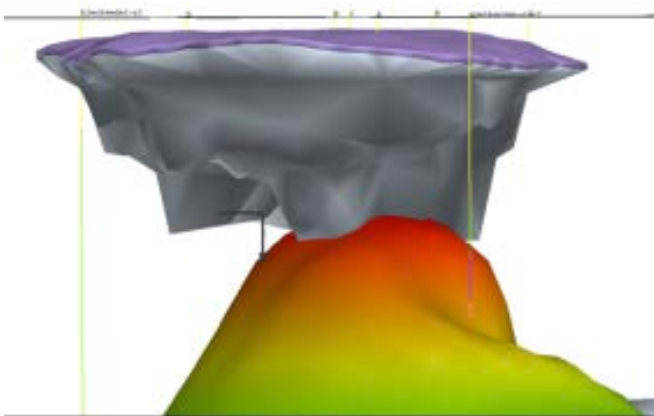


Figure 2.7 An example of using MT for sub-salt interpretation, showing the upper part of the salt dome (Buehmann et al., 2002).

For sub-salt application, several electromagnetic (EM) studies have been employed including magnetotelluric and CSEM which yielded interpretation of a salt dome overhang. A 3D inversion was applied to reveal the overhang in the shallow salt structure even though only the profiling data were available (Avdeeva et al., 2012). Marine CSEM has also been applied to the salt dome and stratigraphic trap reservoir using 2D forward modeling to discriminate between the hydrocarbons and the brine saturated rocks. CSEM data inversion is the tool of choice to go from measurements to interpreted model (Hussain et al., 2012). The high-resolution gravity and magnetotelluric significantly improve the seismic interpretation of the salt dome geometry (Figure 2.7). The integration leads to a new and more reliable model (Buehmann et al., 2002).

Strack et al (1990), and Strack and Pandey (2007), have applied LOTEM to a sub-basalt study using 1D inversion and 3D forward modeling. The amount of conductive sediments is estimated below the basalt trap. The result indicates the sediment thickening below the basalt showed in the conductance map. Moreover, the result is integrated with gravity, deep seismic, deep electrical and the logging data from a drilled well. The interpretation shows that the agreement between the LOTEM predicted model and the lithological unit is about 90-95 % (Figure 2.8).

Actual well result					Pre-drill prediction		
Age	Formation	Depth (m)	Litho log	Lithological description	Tectonics	Prediction	
Upper Cretaceous to Paleocene	Deccan trap	-1000	[Patterned]	Basalt/ weathered basalt with amygdalites at places traversed by calcite	Late drift phase	Trap Basalt	
		-1200					
Upper Jurassic to Lower Cretaceous	Wadhwan	-1400	[Patterned]	Dominantly sandstone with clay intercalations. Sand stone is light grey to brow, fine to coarse grained, feebly cacl. Claystone is brick red hard and compact		Traditional early drift phase	Sediments
		-1600					
	Dhrangadhra	Upper	-1800	[Patterned]	Dominantly claystone with intercalations of sand Sandstone brownish grey medium grained hard and compact	Rift sequence	
			-2000				
		Lower	-2200	[Patterned]	Dominantly claystone, dark grey to brown with sandstone intercalation Sandstone white to light grey mod. Hard and compact non-calc.		
			-2400				
Jurassic?	Lodhika	Upper	[Patterned]	Dominantly claystone Tuff Conglomerate (polymictic) Sandstone light brown to colorless Medium to very coarse grained Claystone brick red to maroon in color Sandstone brown, fine to coarse grained with alteration of siltstone and clays stone	Rift sequence	Basalt	
							Lower
		-2800	[Patterned]	Basalt/dolerite Amygdaloidal basalt with red/maroon colored claystone			
		-3000					
-3200	[Patterned]	Basalt. Fine grained fractured tuff. Light green to dark green with chocolate brown clasts = hard and compact Tuff					
-3400							

Figure 2.8 Interpretation derived from well-log report with the major lithological unit (left) and LOTEM prediction (right). The agreement is 90-95% (modified from Strack & Pandey, 2007).

The other application of LOTEM was conducted in covered thick basalt, several tens of meters to one kilometer, where seismic exploration is prohibited (Strack et al., 1990). The interpretation shows the consistence along the profile indicating to a clearly expressed basalt layer. The area below basalt shows the conductive layers which represent the sediment followed by the resistive basement (Figure 2.9).

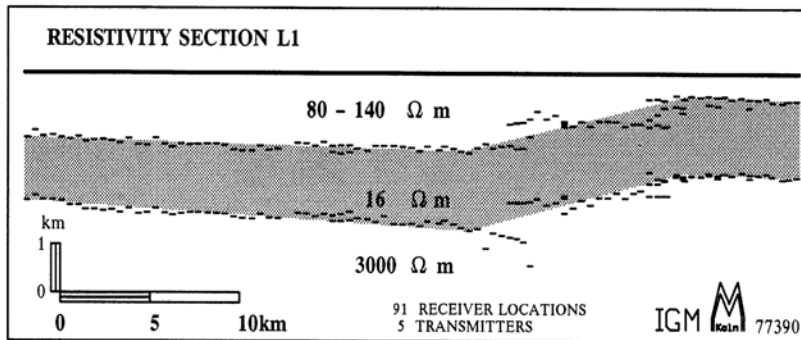


Figure 2. 9 Interpretation of LOTEM resistivity section from individual 1D inversion. The basalt varies in thickness from few hundred meters up to one kilometer, and hydrocarbon prospective sediment is suspected below the basalt. (Strack et al., 1990).

Another example from a thick carbonate formation, of the depth of two kilometers below the strata including thin volcanic section was revealed by the seismic exploration. The 1D inversion results compared with the seismic data and available well logging data displays the correspondence between the resistivity image or the depth profile with the seismic reflector data (Strack et al., 1990). Encouraging results was also achieved in a rugged area of sediments covered by limestone, while the seismic method was not satisfactory because of the high-velocity surface layer and the great velocity variations in the subsurface (Yan et al., 1997).

The electromagnetic (EM) applications to the reservoir monitoring have been suggested in several publications, for example Constable (2010), Ceia et al. (2007), and Wilson et al. (2015). Wilson et al. describe the time-lapse EM monitoring system including a processing unit in communication with at least one EM field sensor to determine an attribute change in an Earth resistivity model.

The LOTEM application including 1D interpretation was employed for a monitoring of fluid injection for enhanced oil recovery (EOR). It was combined with another EM method, inductive multi-frequency, and with the available geological information. The results show that LOTEM makes it possible to observe the oil and the injected water contact (Ceia et al., 2007).

Colombo et al. (2010) shows a feasibility study of CSEM surface-to-borehole measurement in Ghawar field, Saudi Arabia reflecting oil-water fluid substitution. The feasibility study is conducted for a three-year flood front monitoring program, with repeated time interval of six months for each monitoring survey. The result shows the sensitivity to the fluid saturation changes in the reservoir (Figure 2.10).

Strack and Aziz (2012) explained the advantages of the full field array electromagnetic, while receiving EM sensors are included in seismic spreads, with fluxgate sensors used for the low frequency MT, and induction coils for the high frequency components. They suggested that the surface-to-borehole measurement are the required since the surface CSEM data will inherently still have rather low spatial resolution.

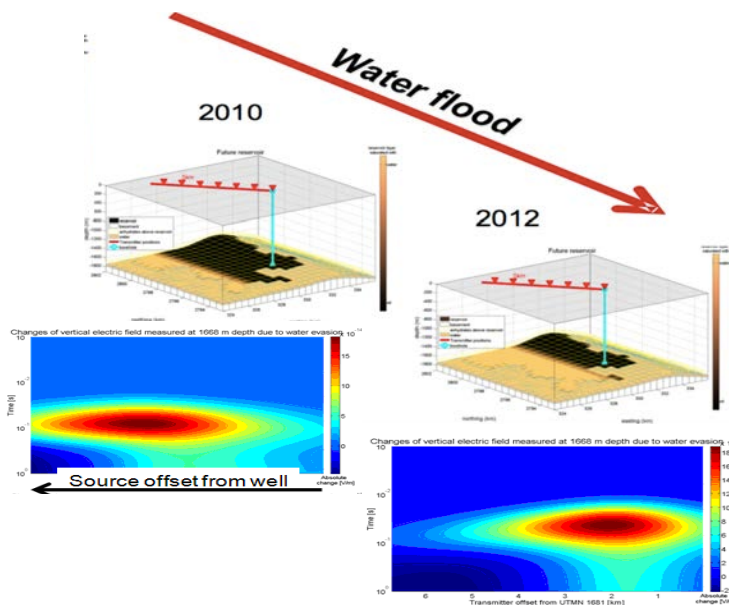


Figure 2.10 Simulated response of surface-to-borehole EM for a period of 2 years. The differences relative related to resistivity change are clearly shown in the derived model (after Colombo et al, 2010).

Yan et al. (2017) studied the monitoring survey for shale gas hydro-fracturing using TDEM with high power transmitter and many acquisition channels in the area of Fulin shale gas exploitation zone in southern China. The residual dynamic 3D image produced by capturing voltages change after the data processing and the resistivity residual imaging with the calibration of seismic and horizontal logging data, identified the shape of fractured volume. The results show the promising application for monitoring of shale gas fracturing.

The above-mentioned applications show that the LOTEM technique can be effectively employed even in difficult exploration environments. It has been employed in the presences of very strong cultural noise as well as in the rugged area. The interpretation shows the excellent agreement with another geophysical and geological interpretation. it can also complement another geophysical method such as gravity to obtain the satisfactory result.

2.3 General geology of study area (Hockley)

The U.S. Geological Survey was begun in 1978 to investigate regional ground-water systems, encompassing all major aquifer systems in Cenozoic deposits to late Cretaceous units locally in the Gulf Coastal Plain. The area is about 290,000 square miles and includes Alabama, Arkansas, Florida, Illinois, Kentucky, Louisiana, Mississippi, Missouri, Tennessee, and Texas, also including about 60,000 square miles in the total of offshore area in the Gulf of Mexico (Hosman, 1996).

The major tectonic events and structural features affect the Cenozoic sedimentation. Cyclic Tertiary environments which produced alternating marine and continental sequences relate to trends and patterns of depositional. Hosman and Weiss (1991) and Weiss (1992), described the subdivision of Cenozoic deposits into aquifers and confining units for analysis of regional ground stratigraphic units. The heterogeneity of the sediments and geologic correlation problems influence the delineation of the geohydrology units.

2.3.1 Geologic History

Catastrophic geological events were largely controlled by Cenozoic deposition in the Gulf Coast geosyncline and the Mississippi embayment taking place at the end of the Paleozoic Era. The basic configuration was begun with deformation of the Paleozoic surface prior to Mesozoic deposition. Mesozoic deposition produced vast accumulations of sediment in the Gulf Coast geosyncline and in the lesser extent in the Mississippi embayment (nonetheless substantial amounts). Triassic and Jurassic deposits of unknown thickness filled and deepened the geosyncline. The next movement of Cretaceous seas left mostly marine deposits along of the northernmost limit of the Mississippi embayment and put the floor for Cenozoic sediments which were to follow (Hosman, 1996; Hosman & Weiss, 1991).

2.3.2 Stratigraphy

Since 1903, stratigraphy of the Texas Gulf Coast has been proposed at least seven stratigraphic classifications because of the correlation difficulties of the lithologic units often caused by sediments appreciable heterogeneity, discontinue beds, a general absence of index fossils and diagnostic electric log signatures in the subsurface. The sequence of stratigraphic units below from the oldest to the youngest one includes Trinity and Quaternary era. Trinity era includes Midway Group of Oligocene series, and Wilcox Group of Oligocene or Eocene Series. The next stratigraphic unit is shown in Table 2.1 as follows:

Table 2.1 Stratigraphy of Cenozoic era, the Coastal Plain of Texas (modified from Baker, 1995).

Era	System	Series	Stratigraphic units			
CENOZOIC	Quaternary	Holocene	Alluvium			
		Pleistocene	Beaumont clay			
	Lissie formation					
	Willis sand					
	Tertiary	Pliocene	Gollad sand			
		Miocene	Fleming Formation / Lagarto clay			
			Oakville sandstone			
			Surface	Subsurface		
			Catahoula tuff or sandstone	Upper part of Catahoula tuff or sandstone	Anauac Formation	“Frio” Formation
		Oligocene	Surface Frio clay		Subsurface Vicksburg Group equivalent	
			Jackson Group	Whitsett Formation	Fashing Clay Member	
					Calliham sandstone Member or Todilla Sandstone Member	
					Dubose Member	
					Deweeseville Sandstone Member	
					Conquista Clay Member	
					Dilworth Sandstone Member	
					Manning Clay	
					Wellborn Sandstone	
					Caddell Formation	
	Eocene	Claiborne Group			Yegua Formation	
			Cook Mountain Formation			
			Sparta Sand			
			Weches Formation			
			Queen City Sand			
			Reklaw Formation			
			Carrizo Sand			
			Wilcox Group			
	Paleocene	Midway Group				

2.3.3 Salt dome

Salt domes in the south-central United States located in five distinct regions, known as salt basins, probably reflect thick accumulations of sedimentary salt. Later sedimentary deposits formed overburden reassures and its density differences then caused the salt to flow into salt structures. Figure 2.11 show the salt basins: South Texas, East Texas, North Louisiana, Mississippi, and Gulf Coast. From the map show that the largest salt basin is the Gulf Coast salt basin, underlies southeastern Texas, southern Louisiana, and the adjacent Continental Shelf (Beckman & Williamson, 1990).

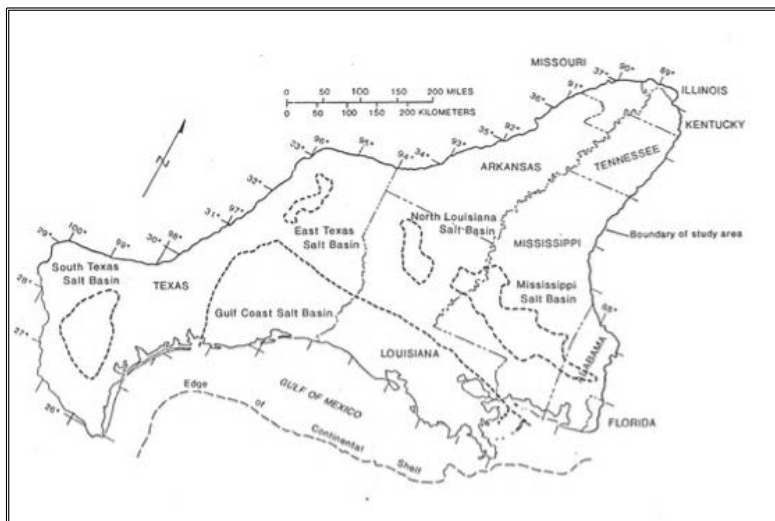


Figure 2.11 The location of salt dome basin in the Gulf Coast (Beckman & Williamson, 1990).

Hockley salt dome (Figure 2.12) is among the largest of the discovered salt domes of the Gulf Coast region. It was discovered by Spindletop in 1902 and drilled by Lee, Napier and Spears (Canada, 1953). Since it was discovered, the twenty-two years, which have elapsed, approximately fifty wells have been drilled around it to depths ranging from 200 to 4,600 feet or 60 to 1402 m, and oil, gas, and sulfur were obtained from the exploration (Anderson, Eargle, & Davis, 1973).

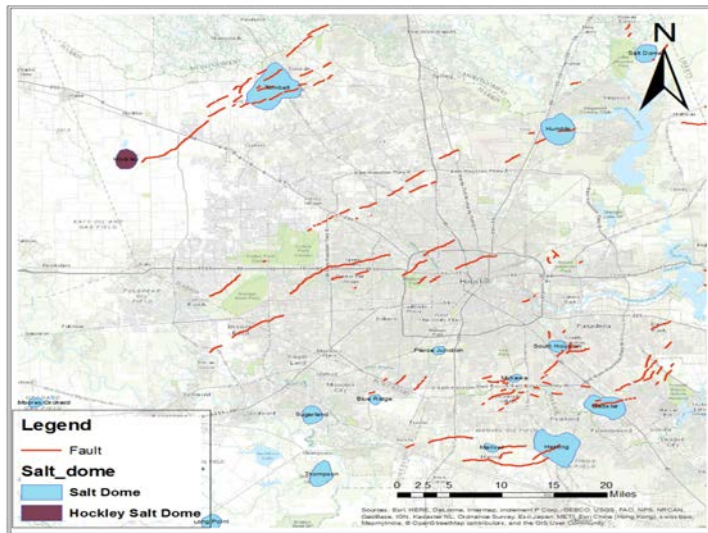


Figure 2.12 Salt domes around Houston, Texas, including Hockley salt dome.

Around Hockley salt dome, various studies have been carried out using geological approach and geophysical method such as gravity (Allen, Caillouet, & Stanley, 1955) and seismic diffraction (Linville & Dablain, 1985), geologic interpretation (Deussen & Lane, 1925) as shown in Figure 2.13 and Figure 2.14.

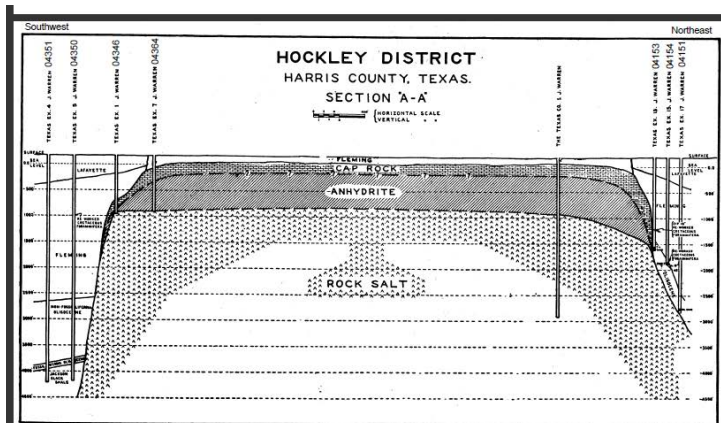


Figure 2.13 Section across Hockley salt dome, Southwest-Northeast (Deussen & Lane, 1925).

In 1945, 17 wells for sulfur, 41 well for oil or gas before firs production, and 69 additional wells was drilled before the oil field was brought. From porous anhydrite sheaths and from sediment in the undercut beneath the overhang of the salt dome, some wells also were drilled to produce (Anderson et al., 1973)

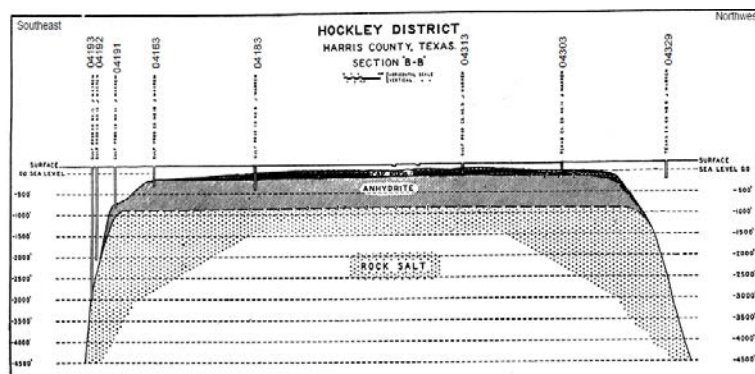


Figure 2. 14 Section across Hockley salt dome, Southeast-Northwest (Deussen & Lane, 1925).

The depth of the cap rock in this area is around 23 to 30 m (Canada, 1953; Hawkins & Jirik, 1966), and 76 feet (23 m) at the mine shaft, with the thickness in the northeast of 995 feet (303 m) and 934 feet (285 m) thick at the mineshaft. Anhydrite has many slicken-sided fractures including vuggy (a small cavity in a rock or vein) gypsum layer containing gypsum crystals and water and cavernous calcite layer (Anderson et al., 1973).

Deleted: 1996

2.3.4 Geologic setting of the study area

Base on geologic map, two main formations, Lissie and Willis formation, cover the study area (Hockley salt dome) as describe in following explanation of those formation.

2.3.4.1 Lissie formation

The Lissie Formation is part of the Houston Group (McClintock et al., 1972) with the thickness approximately 60 m. Both the upper and the lower part of Lissie Formation consist of clay, silt, sand and the minor amounts of gravel. In the lower part, gravel is slightly coarser than in the upper part, and also iron

oxide concretion is more abundant than in the upper part (Darton, Stephenson, & Gardner, 1937).

2.3.4.2 Willis formation

The coarsest of the Pleistocene Formations is Willis Formation, which comprises clay, silt, sand, and minor siliceous gravel of granule to pebble size including some petrified wood; sand coarser than in younger units. Deeply weathered and lateritic units were indurated by clay and cemented by iron oxide locally, and the maximum thickness of approximately 23 m (Darton et al., 1937; McClintock et al., 1972).

2.3.4.3 Fault system

Extending from the Hockley salt dome, there is a fault zone named Hockley fault that is more than five miles long from Northeast to Southwest of Hockley and across Highway 290 to its terminus in Fairfield Village (Figure 2.15).

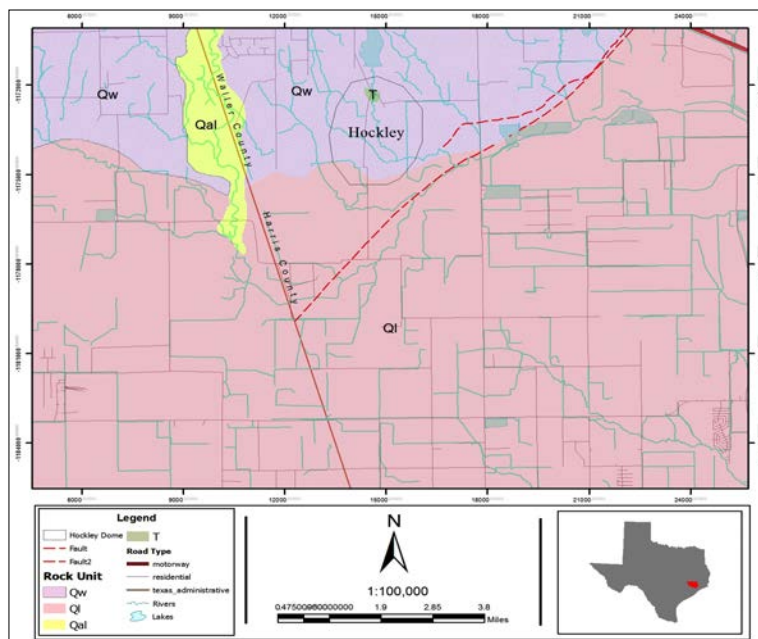


Figure 2.15 Geologic map of Harris County showing the three major formations: The Willis, the Lissie, and the Beaumont including Hockley fault.

There were several geophysical investigations in this area to detect fault zone. Khan et al., (2013) used airborne LiDAR supported by GPS data and undertook geophysical survey, GPR, seismic reflection, and gravity, to identify several new faults, and furthermore it was used to update the map of the Huston and the surrounding. Another method, several resistivity surveys, has also been carried out to investigate fault in this area (Saribudak, 2011).

Deleted: , 2012

2.4 Signal processing theory

During data measurement, the input signal combine with the effect of data generation process to produce output signal. To visualize this, the *Black Box* concept is described (Strack, 1992). The *true signal* and the earth response enter into *Black Box*, modified to produce output which is measured signal. For the field data acquisition, a combination of distortion in the data acquisition and transmitter system reflect the *Black Box*. The distortions are introduced both transmitter (Imperfection in wave form and induced polarization or coupling effect) and receiver (Amplitude response temperature drifts, etc.).

The black box concept can be explained as a *convolution* mathematically:

$$\text{Output (t)} = \text{Input (t)} * \text{Black Box (t)} \quad (2.32)$$

or

$$y(t) = x(t) * s(t), \text{ where } * \text{ is called } \textit{convolution}. \quad (2.33)$$

Furthermore, to remove the effect of the systematic distortions of the signal from earth response, the inverse of *convolution* (*), so called *deconvolution* can be performed.

Most of the EM measured signals are often superimposed by noise, periodic and sporadic noise, and it has direct effect to the poor signal to noise ratio (SNR). The periodic noise usually come from the local power network (50 or 60 Hz and harmonics) and the railway. The sporadic noise is often measured with time series which appears spikes, steps or drifts. The way to reduce those noise in order to obtain “true” signal from the measure data is described as follow.

2.4.1 Filtering

The measured signal polluted by the periodic noise is usually handled by the filtering. This approach based on the assumption, that the known periodic signal can be reproduced using Fourier series. The filters include notch filter, lock-in filter, and Butterworth low-pass filter, as well as the thresholding as the additional. The following are some explanations of the filters with their weaknesses and respective advantages.

2.4.1.1 Notch filter

The notch filter is used to reject a narrow frequency bands while leaving the remaining spectrum unchanged. The most common example is to reject the 60 Hz noise from power lines. The pole and zero have equal (logarithmic) relative distances from the unit circle. The zero is put closer to the circle, and then the frequency at located zero is exactly canceled from the spectrum of input data (Claerbout, 1985).

Standard recursive filters were modified for LOTEM to avoid signal amplitude attenuation (Strack et al., 1989). The digital filter should not only suppress the noise but also maintain the amplitude, which mostly contains the resistivity information is mostly contained. The amplitude attenuation is eliminated when the position of the poles and zero is chosen such that

$$\frac{|z_n-1|^2}{|z_n+1|^2} = \frac{|z_p-1|^2}{|z_p+1|^2} \text{ or } \frac{(1-\alpha)^2+\beta^2}{(1+\alpha)^2+\beta^2} = \frac{(1-x)^2+y^2}{(1+x)^2+y^2} \quad (2.34)$$

This yield a recursive formula in the z-plane

$$H(z) = \frac{Y(z)}{X(z)} = \frac{(z-z_n)(z-z_n^*)}{(z-z_p)(z-z_p^*)} = \eta \frac{z^2-2\alpha z+1}{z^2-2\alpha\eta z+2\eta-1} \quad (2.35)$$

$$\text{with the normalization for gain 1, } \eta = \frac{z_p-1}{z_n-1} \quad (2.36)$$

$$\text{We define } x = \eta\alpha, \text{ and obtained } y^2 = \frac{2x}{\alpha} - (1-x^2) \quad (2.37)$$

where $H(z)$ is the filter function given by the ration of the output function $Y(z)$ and input function $X(z)$. z_n and z_p is the positions of the zero and poles, respectively. η is the proportionally factor, also called the bandwidth, combining the real part of the pole, x , with the real part of the zero, α , and y in the imaginary.

With multiplication with z meaning a shift by one step in time domain, the simple reformulation can be obtained from the above equation:

$$Y_0 = \frac{1}{2^{n-1}} [\eta X_{n-2} \alpha \eta X_{n-1} + \eta X_{n-2} + 2\alpha \eta Y_{n-1} - Y_{n-2}] \quad (2.38)$$

$Y_{-1} = Y_{-2} = X_0$ as the starting values (Strack [et al.](#), 1989; Strack, 1992) Figure 2.16 show the example of this filter application.

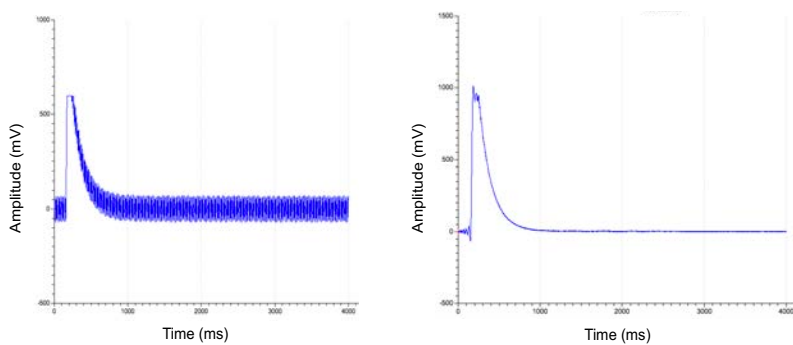


Figure 2.16 The filtering transient data using the true amplitude notch filter, a) Original field data, b) filtered data.

2.4.1.2 Lock-in filter

In some cases, the transient cannot be recovered from the signal by digital recursive, notch filter for example when the transient rises sharply between the sample point. The different filter is needed to solve this issue. The lock-in filter calculates the data before the start of the transient to the optimum noise, locks to the phase of the noise, and subtracts from the single record pre-stack. It also concise a series of cosine and sine function matching with the periodic component of the noise in a least square sense (Strack, 1992). The example shows in Figure 2.17.

Deleted: el

Deleted: ;

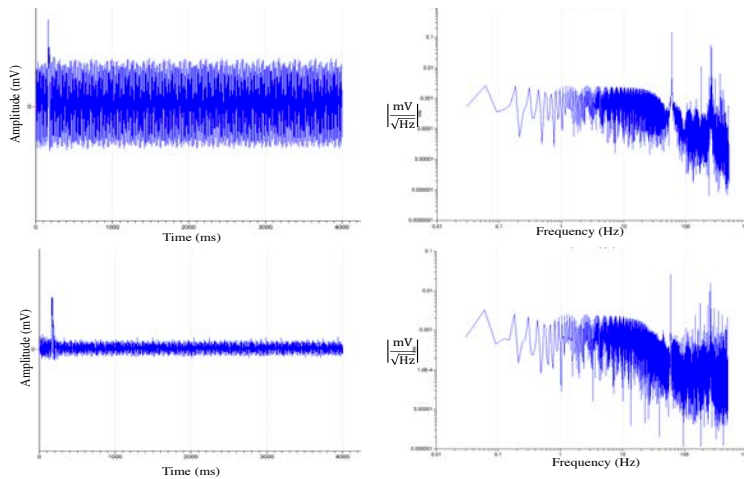


Figure 2.17 Filtering of transient data using lock-in filter. In the left show the raw data (above) and filtered data (below), and the right show the spectra of the raw data (above) and after filtering (below).

2.4.1.3 Butterworth low-pass filter

The characteristic of an ideal low-pass filter is its ability to perfectly pass signals below the cutoff frequency and eliminate signals above the cutoff frequency. Various trade-offs can increase optimum performance for a given application in real filters (Karki, 2000).

$$|H(j\omega)|^2 = \frac{1}{1+(\omega)^{2n}} \quad (2.39)$$

where, H is transfer function, and n represents both the transfer function order and the realized filter. Figure 2.18 shows the comparison of Butterworth approximation for n {2, 3, 5, 10}, observed that $|H(0)|=1$ and $|H(j1)|=0$. Butterworth approximation approaches to the ideal low-pass characteristic for $n \rightarrow \infty$. For all n values in terms of the decibel scale, the Butterworth magnitude response starts from 0 dB at DC and drops down by 3 dB at $\omega c=1$ rad/s (Ayten, Vural, & Yildirim, 2011).

Deleted: et al.

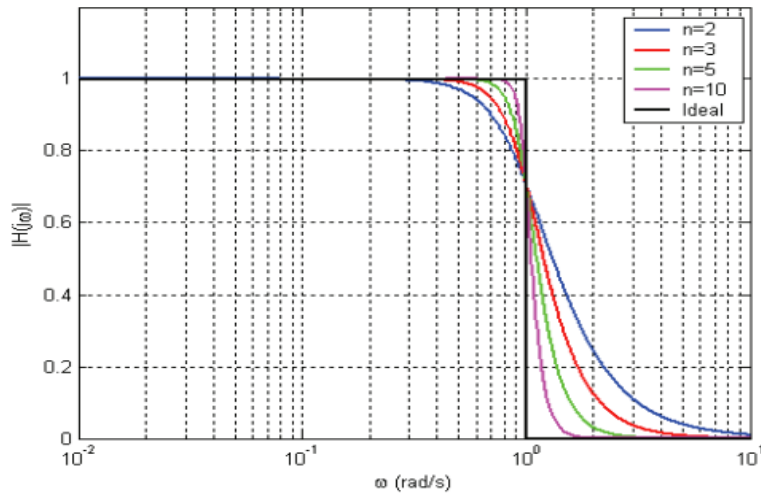


Figure 2.18 Amplitude response of n -th order Butterworth function (Ayten et al., 2011).

Maximally-flat-magnitude-response filters, Butterworth filters, are optimized for gain flatness in the pass-band. The attenuation is -3 dB at the cutoff frequency and -20 dB/decade/order above the cutoff frequency. The transient response of the Butterworth filter to the pulse input indicates moderate overshoot and ringing (Karki, 2000).

The order of the Butterworth filter is dependent on the specifications which include the edge frequencies and gains. The standard formula for the Butterworth order calculation is given by

$$n_B = \frac{\log[(10^{-0.1 a_{\text{stop}}}-1)/(10^{0.1 a_{\text{pass}}}-1)]}{2 \log(\omega_{\text{stop}}/\omega_{\text{pass}})} \quad (2.40)$$

In this formulation, the ratio of the stopband and passband frequencies is important, not either one of these independently. The value of n calculated using this equation must always be rounded to the next highest integer to guarantee that the specifications will be met by the integer order of the filter designed (Thede, 2004).

2.4.1.4 Thresholding (Automatic detection)

Thresholding is the processing tools used in wavelet signal processing to reduce the noise in signal, image compression and signal recognition. It aims to repress the additive noise $w(k)$ from the signal $x(k)$ where

$$x(k) = u(k) + w(k) \quad (2.41)$$

The thresholding for noise suppression is carried out from the signal $x(k)$ decomposed into L-level of wavelet transform yielded wavelet coefficients (Hawwar & Turney, 2000).

Using the wavelet transform, the signal energy can be concentrated on some large wavelet coefficients and distribute the noise energy throughout the whole wavelet domain with the result that large amplitude wavelet coefficients may be produced by the useful signal, and the small amplitude is likely to represent the noise (He et al., 2014). Donoho and Johnstone (1994) divided wavelet threshold method into three steps:

- 1) Choosing the appropriate wavelets basis and decomposition scale and computing the corresponding wavelet coefficients,
- 2) Selecting the proper threshold and thresholding function and obtaining the estimated values of the wavelet coefficients,
- 3) Reconstructing the signal based on the estimated values of wavelet coefficients by inverse wavelet transform.

Universal thresholding is used in some noise removal applications in which the noise statistics is known. The threshold value is set based on the noise statistics. The threshold value is set to be:

$$\sigma = v \sqrt{\frac{2 \log(l)}{l}} \quad (2.42)$$

where σ is the threshold (gate) value, v is the standard deviation of the noise and l is the cardinality of the data set. This threshold value can be used in either hard or soft thresholding. There are two thresholding functions widely used, called hard thresholding function and soft thresholding function. Hard thresholding, sometimes is called gating. If a signal (a coefficient) value is below a preset value, it is set to zero (Mishra & Verma, 2013).

$$y = x \text{ for } x \geq \sigma \quad (2.43)$$

Deleted: et al

Deleted: .

Deleted: 2006

Deleted: choosing

Deleted: selecting

Deleted: reconstructing

Deleted: (He et al., 2014)

Deleted: ?

$$y = 0 \text{ for } x < \sigma \quad (2.44)$$

Soft thresholding is defined as

$$y = f(x - \sigma) \text{ for } x \geq \sigma \quad (2.45)$$

$$y = 0 \text{ for } x < \sigma \quad (2.46)$$

2.4.2 Selective statistic application (stack)

The sporadic noise which may cause by natural sources, is not recognized and cannot be removed by using filter. This kind of noise can be eliminated using stacking method. The following, several stacking methods are elaborated.

2.4.2.1 Mean

Mean stacking is the simplest method (Mayne, 1962). This method is a special, simple case of more common stacking methods like the Super stack. Nevertheless, many higher-level considerations are based on it (Mayne, 1967). The Straight Stack sums up the sample amplitude values at the isochrones locations and divides by the number of values, for all channels to be processed:

$$a_t^{\text{Straight Stack}} = \frac{1}{N} \sum_{i=1}^N S_i \quad (2.47)$$

N is the number of isochrones values, S_i the amplitude at a sample location, and a Straight Stack t is the amplitude of the stacked trace at a respective time (Ruckemann, 2012).

2.4.2.2 Median

The median amplitude values from traces to be stacked are picked. The stacked trace contains the median value for every sample at the same time with the amplitudes along the CPM gather. Thus, the median stack does not result from summed up values which can appear like adding high-frequency noise. This is reduced by summing up more than one amplitude, which after resorting the input values follow in rising sequence around the central position to exclude extreme amplitude value groups from the stack. This can be done by alpha-trimmed mean stack (Ruckemann, 2012).

2.4.2.3 Trimmed mean

The concept of trimmed filters is to reject the most probable outliers, some of the very small and the very large values (Poularikas, 1999). The trimmed mean stacked (TMS) can be described by the following algorithm:

$$a^{\text{TMS}} = \frac{1}{N-K} \sum_{i=\frac{K}{2}+1}^{N-\frac{K}{2}} S_i \quad (2.48)$$

with number N of samples, overall number K of excluded sample values, the amplitude S_i at the respective sample, and the amplitude a^{TMS} of the stacked trace at the respective time. The TMS is a generalization of the Straight Stack. The amplitudes of a gather are sorted by value, numbered, and summed up at a time using the values up to a defined amplitude number. The summation for non-symmetrical elimination of extreme amplitudes can be performed (Ruckemann, 2012)

2.4.2.4 Selective stacking

The selective stacking technique, either symmetric or area-defined rejection technique which use different rejection criteria, was applied to handle sporadic noise. The symmetric (known as alpha-trimmed mean) selective technique is rarely used due to computational expense. Both selective stacking techniques sort the data amplitudes in ascending order for at each time sample for all transients.

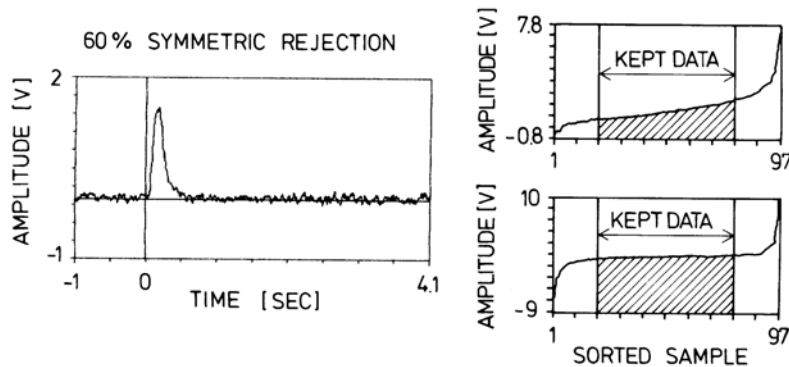


Figure 2.19 The symmetric rejection selective stack technique with a cut-off of 20% at both ends of the sorted amplitudes to stack the data. Showing the kept data in the middle while all others are rejected (after Strack et al., 1989).

For the symmetric rejection, as shown in Figure 2.19, the predetermined total number percentage of transients is symmetrically rejected from both ends of the sorted amplitudes, and a preliminary average and standard deviation are calculated for the remaining of the data. For the area-defined rejection (Figure 2.20), calculations of amplitude frequency distributions are generated from sliding overlapping windows over the sorted amplitude curves for each time sample of all transients. All the data within the area under distribution symmetric curve are kept and a percentage of that area about maximum is calculated (Strack et al., 1989).

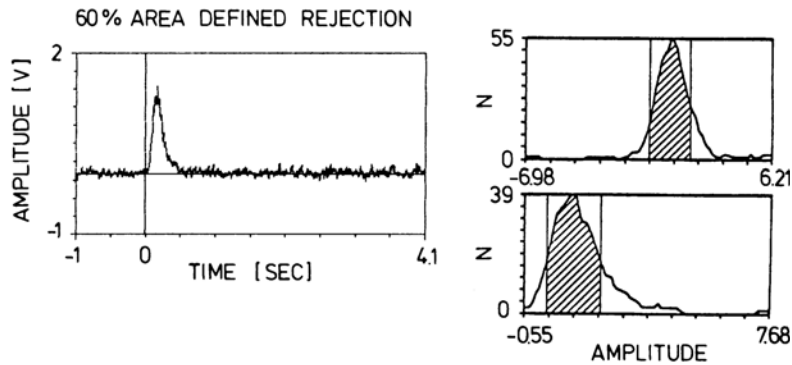


Figure 2.20 Stacked data using the area-defined rejection selective stack technique. The shaded area is defined to keep 60% (after Stack et al., 1989).

2.4.3 Smoothing (post-stack)

To obtain the data as smooth as possible a recursive average filter, also known as moving average, is introduced in the last step. The moving average filter is commonly used in DSP for optimal reducing random noise while retaining a sharp step response. This makes it the premier filter for time domain encoded signals (Smith, 1997). The smoothed result is expected, after this filter is applied as shown in Figure 2.21.

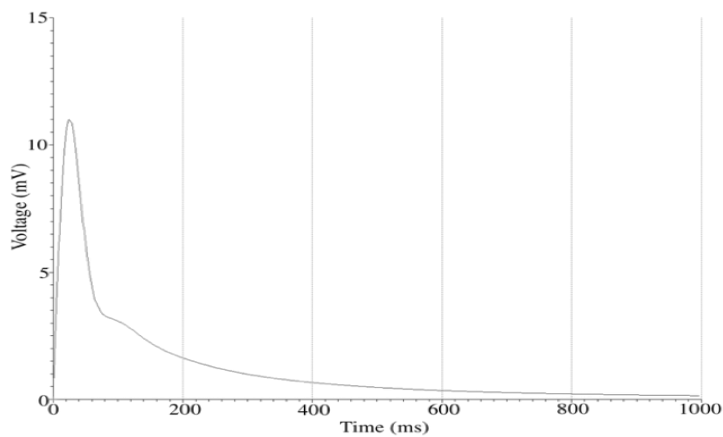


Figure 2.21 Smoothed data using recursive average filter (Paembonan et al., 2017).

2.5 Inversion theory

To interpret geophysical data, the data inversion is usually used as the method to further process the filtered and smoothed data. The main goal of inversion is to find the optimum earth model with the resistivities and layer thickness that fits the measured data. Lines and Treitel (1984) and Jupp and Vozoff (1975 & 1977) had reviewed the performance of inversion method which is suitable for LOTEM data. Furthermore, the new application of inversion such as Occam's inversion is explained in this chapter. Figure 2.22 shows the functional diagram for data inversion.

2.5.1 General term of 1D inversion

Inversion processing is typically done in logarithmic scale and for logarithmic parameter, since all the parameter are physical and cannot become negative. In logarithmic scale, the data is also more reasonable to see the physical point, since the EM waves are damped exponentially in the subsurface (skin effect), that allows the large dynamic range in the signal and stability of the inversion processes.

The simplest model is usually described by a few parameters such as resistivities and the thickness in one-dimensional (1D) space. The output parameter of the electromagnetic methods is the resistivities, ρ_i , and the thicknesses, h_i , of the layers (Figure 2.22).

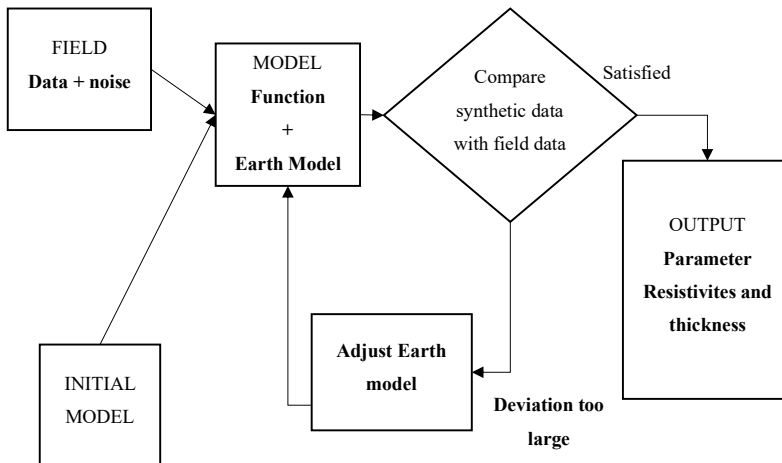


Figure 2.22 Inverse modeling functional diagram (Strack et al., 1989).

An interpretation of the LOTEM is based on two main goals of inversion technique. First, the data inversion is used to minimize the difference between the observed data and modeled data. Second, it is used to estimate the reliability of the model by calculating confidence bounds. In the linear problem, the Gauss-Newton method always works, but for non-linear problems, the problem must be linearized by expanding it into a Taylor series. The measured LOTEM data at time points t_1, \dots, t_N , are represented by the vector:

$$\mathbf{d} = (d_1, \dots, d_N)^T \text{ with } \mathbf{d} \in [N \times 1] \quad (2.49)$$

The vector of model parameter \mathbf{m} represents an appropriate parameterization of the earth which consists of the layer resistivities and the layer thicknesses. In the one-dimension model, the subsurface is generally divided in horizontal layers and all electrical parameters (resistivities) remain constant within these layers. If K is number of layers, which, in this case, the vector \mathbf{m} has $M = 2K - 1$ entries. The $K - 1$ -layer thicknesses h_k and K layer resistivities ρ_k are represented in a model parameter vector \mathbf{m} .

$$\mathbf{m} = (h_1, \dots, h_{K-1}, \rho_1, \dots, \rho_K)^T \quad (2.50)$$

In the LOTEM data inversion, another model parameter called calibration factor (CF) is often used. Another thing needed for the inversion is a forward

modeling calculation. This can compute the synthetic data corresponding to the assumed model parameter the real subsurface. Model vector m used for the forward calculation in ideal case would equal to the measured data \mathbf{d} . The relationship between the data vector and the model parameter vector is given by the forward modeling operator f .

$$f(m) = (f_1(m), \dots, f_N(m))^T \quad (2.51)$$

However, in the practical case no model will reproduce the real noisy measured data. Hence, we need to define a measure for the misfit. In uncorrelated case, the distributed noise normally leads to a least-squares approach. Next, we introduce a residual vector q as the recursive calculation determining the model discrepancy:

$$q = (d - f(m))^T (d - f(m)) \quad (2.52)$$

In general, for physical reasons, the relative difference between d and $f(m)$ is considered instead of the absolute difference (Jupp & Vozoff, 1975). Therefore, weighting observed and calculated data with a weighting matrix is introduced as follows

$$W = \text{diag}(1/d_1, \dots, 1/d_N) \quad (2.53)$$

The equation 5.20 becomes

$$q = (Wd - Wf(m))^T (Wd - Wf(m)) = (d - f(m))^T W^2 (d - f(m)) \quad (2.54)$$

where $W^2 = W^T W$.

The non-linear problem including the operator f is still a function of m . Thus, a first order Taylor expansion is used for linearization of $f(m)$. In non-linear inversion problems, the conventional approach suggests starting with some reasonable initial guess (starting model) m_0 . For small model perturbation δm , where $\delta m = m - m_0$, $f(m) = f(m_0 + \delta m)$ the operator f can be approximated as follows:

$$f(m)|_{m=m_0} = f(m_0) + J|_{m=m_0} \delta m \quad (2.55)$$

where J is the Jacobian matrix with the form

$$J_{ij} = \left. \frac{\partial f_i(m)}{\partial m_j} \right|_{m=m_0} \quad (2.56)$$

$$J = \begin{bmatrix} \frac{\partial f_1}{\partial p_1} & \dots & \frac{\partial f_1}{\partial p_M} \\ \vdots & \ddots & \vdots \\ \frac{\partial f_N}{\partial p_1} & \dots & \frac{\partial f_N}{\partial p_M} \end{bmatrix} \text{ for } i=1, \dots, N \text{ and } j, \dots, M \quad (2.57)$$

The change in the model parameter m_j results in the change of f_i .

Therefore, the data misfit or residual q becomes:

$$q = (d - f(m_0 + J \delta m))^T W^2 (d - f(m_0 + J \delta m)) \quad (2.58)$$

substituting $\delta d = d - f(m_0)$ gives

$$q = (\delta d - J \delta m)^T W^2 (\delta d - J \delta m) \quad (2.59)$$

The classical mathematical approach to an optimization problem would now be to find the external values of $q(m)$ by searching for a vector m for which

$$\frac{\partial q(m)}{\partial (m)} = 0 \quad (2.60)$$

So that $\frac{\partial}{\partial (\delta m)} (\delta d - J \delta m)^T W^2 (\delta d - J \delta m) = 0$

$$\frac{\partial}{\partial (\delta m)} W^2 (\delta d^T \delta d - J^T \delta m^T \delta d - \delta d^T J \delta m + J^T \delta m^T J \delta m) = 0$$

$$2W^2 (-J^T \delta d + J^T J \delta m) = 0$$

$$-2W^2 J^T \delta d + 2W^2 J^T J \delta m = 0$$

$$W^2 J^T J \delta m = W^2 J^T \delta d \quad (2.61)$$

Rearranging the result of equation (2.57) for δm results in the following equation:

$$\delta m = (J^T W^2 J)^{-1} J^T W^2 \delta d \quad (2.62)$$

The solution provides an improvement of the starting model m_0 . It is generally referred to as the Gauss-Newton or unconstrained least-squares solution. However, because f was linearized using the first order Taylor expansion by dropping higher order terms, $q(m_0 + \delta m)$ will generally not reach the minimum. Therefore $m_1 = m_0 + \delta m$ is used as a new initial guess for the next iteration step and a new model update is calculated. The model update for the n^{th} iteration step is calculated according to following expression:

$$\delta m_n = (J_{n-1}^T W_{n-1}^2 J_{n-1})^{-1} J_{n-1}^T W_{n-1}^2 \delta d_{n-1} \quad (2.63)$$

where $J_{n-1} = J|_{m=m_{n-1}}$ and $\delta d_{n-1} = d - f(m_{n-1})$. This process is repeated until $q(m_n)$ is sufficiently small, or until some any other stopping criteria are met. To keep all model parameters positive, the model vector is often transformed logarithmically, e.g. $m = (\rho_1, \rho_2, h) \rightarrow \delta m = (\ln \rho_1, \ln \rho_2, \ln h)$. Then, all inversion steps are performed using the δm (Jupp & Vozoff, 1975).

2.5.2 Marquardt Inversion

The Marquardt-Levenberg method, also called damped least squares inversion is based on the concept of Levenberg (1944). This inversion scheme became very popular after a publication of Marquardt (1963). The algorithm is applied to inversion problems with a distinct number of layers, where both layer resistivities and thicknesses are accounted for in the inversion. Compared to the Gauss-Newton method, an additional constraint is introduced that limits the variation of δm . The constraint increases the numerical stability of the inversion and reduces the influence of unimportant or irrelevant model parameters. Following Strack (1992), the normal Equation (2.59) is modified to

$$\delta m_n = (J_{n-1}^T W_{n-1}^2 J_{n-1} + K^2 I)^{-1} J_{n-1}^T W_{n-1}^2 \delta d_{n-1} \quad (2.64)$$

$$\delta m_n = (J_{n-1}^T W_{n-1}^2 J_{n-1} + K^2 I) = J_{n-1}^T W_{n-1}^2 \delta d_{n-1} \quad (2.65)$$

where I is the identity matrix and K^2 is the damping factor. The additional term limits the length of the model update vector depending on the value of K^2 . The solution is constructed using mainly eigenvectors of $J^T W^2 J$ with high eigenvalues. For these eigenvectors, it is more likely that the Taylor- expansion is valid (Jupp & Vozoff, 1975). The inverse of equation (2.60) is often calculated using the Singular Value Decomposition (SVD) (Lanczos, 1964). This algorithm is very precise and also makes statements about the inversion statistics. It stated that any $N \times M$ -matrix J can be split up using SVD as

$$J = USV^T, \quad (2.66)$$

including the following matrices:

- a. The orthogonal matrix $U \in N \times N$ consists of eigenvectors N that span the data space. the columns of U contain the individual eigenvectors of JJ^T .

$$JJ^T U = S^2 U \quad (2.67)$$

- b. Similarly, $V \in R^{M \times M}$ spans the model space and contains the M eigenvectors of $J^T J$ space.

$$J^T J V = S^2 V \quad (2.68)$$

- c. The matrix $S \in N \times M$ is a diagonal eigenvalue matrix whose diagonal elements λ_i are non-negative and called singular values which are usually arranged in order of decreasing size (Menke, 1984), meaning $S_1 \geq S_2 \geq \dots \geq S_M \geq 0$.

The matrices U and V containing the orthonormal column vector satisfy the following relationship:

$$U^T U = V^T V = V V^T = I \quad (2.69)$$

Two diagonal matrices S^* and T is defined such that]

$$S^* = \begin{cases} \frac{1}{S_{ij}} & \text{for } S_{ij} > 0 \\ 0 & \end{cases} \quad (2.70)$$

T^* as the damping factors of the transformed parameter

$$T_{ij} = \frac{S_{ii}^2}{S_{ii}^2 + K^2} \quad (2.71)$$

so that, the solution of equation 2.60 (without weighting matrix) is

$$\delta m = V T S^* U^T \delta d \quad (2.72)$$

and substitute to equation 3.30 become

$$\begin{aligned} (J^T J + K^2 I) V T S^* U^T \delta d &= (V S^T U^T U S V^T + K^2 I) V T S^* U^T \delta d \\ &= (V S^2 V^T V T S^* U^T + V K^2 I T S^* U^T) \delta d, \quad (U^T U \cdot U^T = U^T \text{ and } V \cdot V^T V =, V) \\ &= (V (S^2 T S^* + K^2 I T S^*) U^T) \delta d \\ &= (V (S^2 + K^2 I) T S^* U^T) \delta d \\ &= V S U^T \delta d = I \delta d \end{aligned} \quad (2.73)$$

The inversion statistics results in the SVD as additional product that is another advantage of this method (Strack et al., 1989).

2.5.3 Occam's inversion

Occam's inversion concept in application for electromagnetic method, also called "smooth model", especially for the sounding, is based on assumption that the resistivity-depth structure should be as smoothest as possibly. It means the model fits the data within a reasonable tolerance. This inversion algorithm was introduced by Constable, Parker, & Constable (1987).

Typically, the subsurface is divided into a specific number of layers (± 40) with fixed thickness. The model vector p^* is therefore only dependent on the resistivity values of the individual layers ($p^* = (\rho_1, \dots, \rho_K)^T$), where K represents the number of the layer. The first one defines roughness as the summed-up differences adjacent layer of a K -layer case,

Deleted: at al.

$$R_1 = \int \left(\frac{\partial m^*}{\partial z} \right)^2 dz \quad (2.74)$$

$$R_2 = \int \left(\frac{\partial^2 p m^*}{\partial z^2} \right)^2 dz \quad (2.75)$$

or in the discrete representation

$$R_1 = \sum_{i=2}^K (\rho_i - \rho_{i-1})^2 \quad (2.76)$$

$$R_2 = \sum_{i=2}^{K-1} (\rho_{i+1} - 2\rho_i + \rho_{i-1})^2 \quad (2.77)$$

as the total change in differences with depth.

The $K \times K$ matrix R given by

$$R = \begin{bmatrix} 0 & 0 & 0 & \dots & 0 & 0 \\ -1 & 1 & 0 & \dots & 0 & 0 \\ 0 & -1 & 1 & \dots & 0 & 0 \\ \vdots & & & \ddots & & \vdots \\ 0 & 0 & 0 & \dots & -1 & 1 \end{bmatrix} \quad (2.78)$$

All the K resistivities of the model are given by m^* , and this can also be expressed as

$$R_1 = m^{*T} R^T R p^* \quad (2.79)$$

and

$$R_2 = m^{*T} (R^2)^T R^2 m^* \quad (2.80)$$

Applying roughness R_1 yield very smooth model with the small resistivity contrast between neighboring layers. For roughness R_2 , the resistivity contrast will be uniform meaning that the curvature will be held small. Additionally, the constraint will suppress layers that have a large resistivity contrast, but a small thickness compared to the surrounding layers (Haroon, 2012).

The minimizing problem is formulated as finding m^* for which both the misfit and the roughness are small. The model update δm_n^* can then be expressed as,

$$\delta m_n = (J_{n-1}^T W_{n-1}^2 J_{n-1} + \lambda K^2 K)^{-1} (J_{n-1}^T W_{n-1}^2 \delta d_{n-1} - \lambda K^2 K m_{n-1}^*) \quad (2.81)$$

2.5.4 Calibration factor

The shallow geological structures underneath the receivers may distort the measured LOTEM signal (Hoerd & Scholl, 2004). These shallow structures result in a shift of the whole transient to a higher or lower voltage. Additionally, this effect may be also produced by the receiver misalignment, improper definition of gain,

receiver area, current, offsets, etc. (Strack, 1992). This shift is considered within the inversion through an additional model parameter called the calibration factor (CF).

This factor is a scalar value with which the synthetic data is multiplied. Hence, the form of the transient doesn't change in the double-logarithmic representation. Newman (1989) concludes that this scaling allows for acceptable fits to the measured data and an accurate interpretation of the deeper geological sections. However, the near surface layering will be interpreted incorrectly. Therefore, it is desirable to fit the data with a calibration factor close to 1, so that the data is solely explained by the model parameters layer resistivity and layer thickness.

2.5.5 RMS (Root Mean Square) and χ -error for data fitting

The software EMUPLUS offers two separate means of judging the quality of data fitting. For both means, the inversion process stays consistent with the algorithm described above. Solely the entries of the weighting matrix change. If the Root Mean Square (RMS) error is chosen, the entries of the weighting matrix consist of the reciprocal data values times an estimated data error (RSE) used solely for weighting. The root-mean-square or RMS defined by

$$RMS = \sqrt{\frac{1}{N} \sum_{i=1}^N \left(\frac{d_i - f(m)_i}{d_i} \right)^2} \times 100 \% \quad (2.82)$$

This is an often-used measure of the misfit. If the data are weighted to their errors, the result is a different measure of misfit:

$$\chi = \sqrt{\frac{1}{N} \sum_{i=1}^N \left(\frac{d_i - f(m)_i}{d_i} \right)^2} \quad (2.83)$$

If the difference between the measured and the calculated data equals the data-error, $\chi=1$ corresponds to an optimal fit within the data-error. Values less than one correspond to over-fitted data, whereas $\chi>1$ is not sufficiently fitted (Haroon et al., 2015).

CHAPTER III METHODOLOGY

In this chapter, the data processing steps including the signal processing, data inversion and time-lapse calculation is described. The workflow diagram (Figure 3.1) shows general procedure of the data processing and interpretation including the data inversion and time-lapse calculation. The details of the procedure are described in Appendix B.

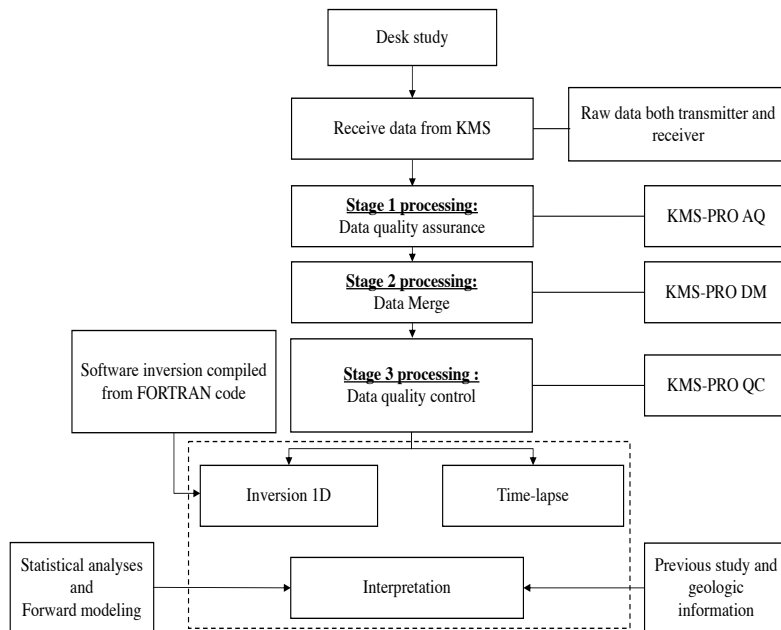


Figure 3. 1 The workflow diagram of the data processing, including data quality assurance, data merge and data quality control, and interpretation consisting of 1D inversion, time-lapse monitoring, statistical analysis, and the forward modeling.

3.1 Signal processing

The signal processing is divided into four stages:

3.1.1 Data quality assurance (using KMSProQA); at this stage, the assurance is provided to prevent the problem in signal processing. Field data acquisition error can be corrected here.

3.1.2 Data merge (using KMSProDM): at this stage, the electromagnetic from seismic data and merge the transmitter and receiver data are separated. This includes synchronizing receiver and transmitter. This step also includes alignment, time shift, and flip polarity, and resampling frequency,

3.1.3 Data quality control (KMSProQC): This processing stage aims to increase signal to noise ratio. The quality control which includes pre-stack processing (de-noising) staking, and post-stack processing (smoothing) is performed.

3.1.4 Processing evaluation including system response and time synchronization verification.

3.1.1 Quality assurance

All raw data recorded in the field, both transmitter and receiver data (EM and microseismic), have to be checked using the KMSProAQ for assurance. The aim to prevent or avoid the problems in quality control processing. The amplitude of the signal recorded in the receiver sometimes has incorrect arrangements and definitions of receiver coordinate and current. Meanwhile, the header contains all the information of parameter measurement parameters such as sensor type, position, sampling frequency, file name, etc. as shown in Figure 3.2. This needs to be checked to ensure that all information is correct. False header information can influence to the data processing and the interpretation. For example, if the GPS information is wrong, the station will be misunderstood, and the data misinterpreted.

```

Header
packet_starting_flag: KMSH
packet_length: 1000
host_Wi_network_address: 65329
KMS820_SN: KMS-820-16-0121
KMS820_network_address 4660
KMS820_network_address_mask 65535
send_packet_ID :6870
send_header_packet_ID :514
save_packet_ID :55
network_mode :
firmware_version : 9
unused_char3 :
fpga_version : 75
GPS_pos_info : 3025.478855,N,11243.461035,E,1
GPS_time_info : DA,070708.007,28,10,2016
GPS_syn_clk : 8.192000
sampling_frequency :1000
first_sample_acq_time :2
sampling_time_read_frame_interval :128
AD_main_temperature :219
AD_SYS_I :176
AD_N11V :398
AD_P11V :270
AD_SYS_V :378

```

Figure 3.2 The data header showing detailed information, such as equipment, acquisition features and GPS information.

The time is very important parameter in the data. Therefore, the time of all recorded data points also should be checked. As shown in Figure 3.3, the start time, when the transmitter switches on, should be processed. Hence, the data times must be edited, with subtraction of the start time, to avoid the problem with the data stacking, especially with low signals after the transmitter turn-off.

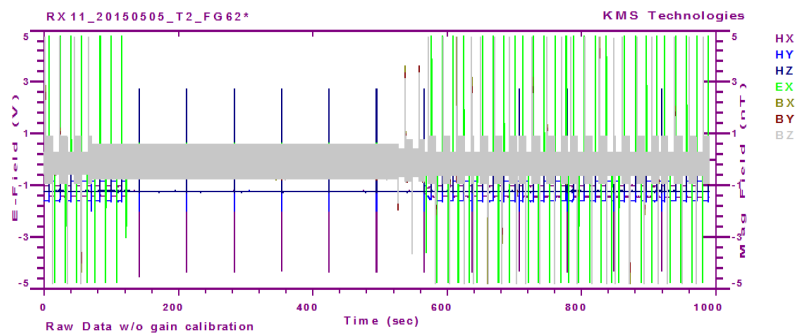


Figure 3.3 The example of signal display in KMS-820 tools, showing the signal of magnetic field (Hx, Hy, and Hz), electric field (Ex and Ey), and fluxgate magnetometer data (Bx, By, and Bz).

3.1.2 Data merge

The data merge comprises the data binning, defining seismic channels, exporting the seismic data to SEG-Y format, merging EM receiver and transmitter, and the header editing (Figure 3.4). The purpose of the merging transmitter and receiver data is their synchronization in time and the normalization of the transmitter current. Since the data sets include microseismic measurements recorded simultaneously with the EM data, they must be separated before the quality control processing.

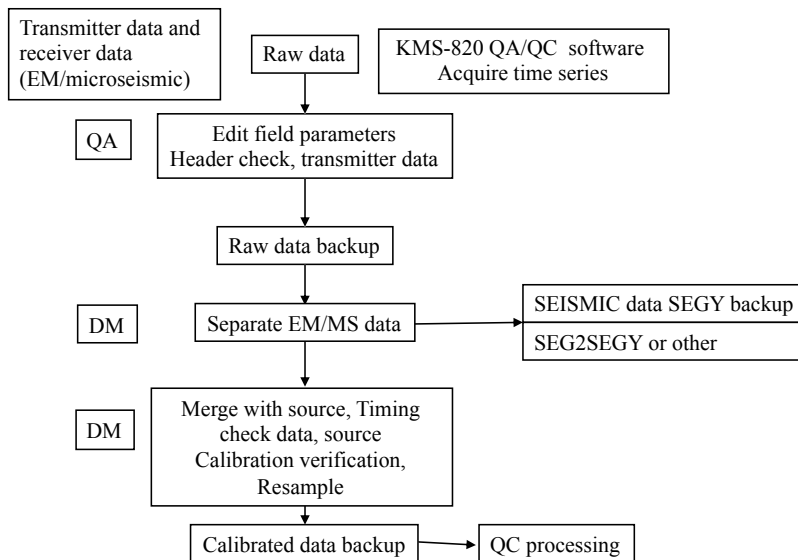


Figure 3.4 Flow diagram of data processing including Quality Assurance (QA) and Data Merge (DM) (modified from KMS Technology, 2016).

The following is additional steps in order to synchronize the transmitter and receiver data under Data Merge:

3.1.2.1 Align

Time synchronization of the transmitter and receiver data generally means that the data from these two devices (the receiver and the transmitter) have the same start time, the less the time error, the higher the synchronization precision. The GPS information is used expecting the transmitter and receiver signal in the same start time. The aligned transmitter and receiver data are shown in Figure 3.5.

Usually, when all GPS receivers work is designed, this is not necessary, but under field condition, often one GPS receiver drops out (for operational reasons) causing issues with this. Here is the verification that resulting delays are controllable.

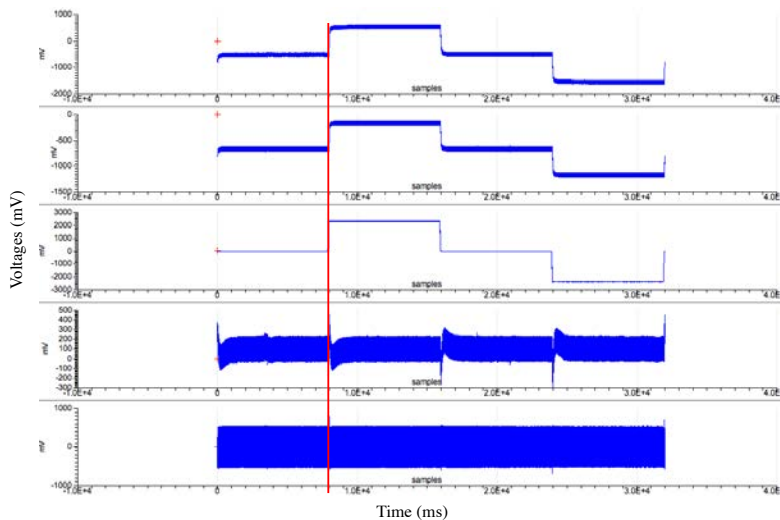


Figure 3.5 An example of time alignment as part of synchronization of transmitter and receiver data. Showing all the channel at the same start time.

3.1.2.2 Time Shift

The synchronization while doing the data merge should provide the same start time when the GPS work properly. Considering the operation environment of electromagnetic transmitter and receiver under the condition that the GPS signal failed, it is also a necessary to solve the issue of data synchronization. When synchronization of the data from the transmitter and the receiver is failed, in the later stage the data inversion can be wrong.

Due to the different recorded time in GPS, the different time between receiver and transmitter signal may be occurred, and it need to be shifted accordingly. The different time between the transmitter and receiver data and adjust them to the same onset is determined. First, the same start time of transmitter and receiver data is set up under the KMS-820 tools (QC/merge/crop binary file), and then followed by time alignment. Furthermore, the is checked whether is fit or not. If the

onset could not be determined, the next processing is to determine the onset and calculate the time different. Finally, the data with the same starts time are saved for the next processing while data with different starts time is shifted and also saved for processing.

3.1.2.3 Flip polarity

Different polarity of the signal, either receiver or transmitter, is influenced by several factors such as the direction of the transmitter and the receiver, inline or broadside, and the electrode connections. The direction of the electric field component E_x always should be perpendicular to the direction of E_y , and either E_y or E_x should be perpendicular or parallel to the transmitter direction. As shown in Figure 3.6, the polarity between the receiver E_x and the transmitter may be different. Therefore, below is the data to have the same polarity.

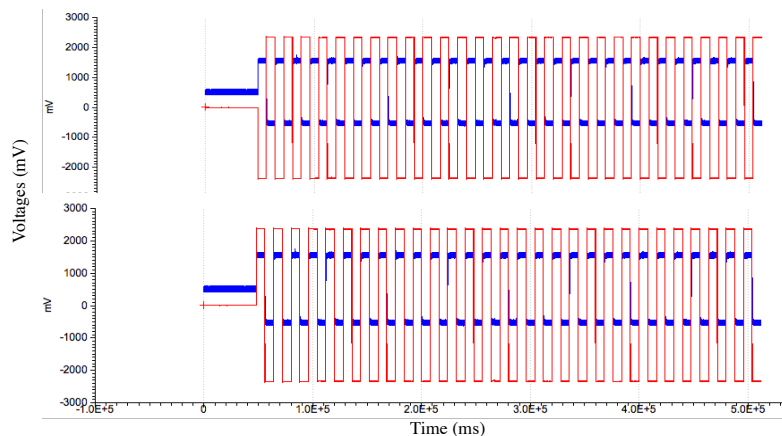


Figure 3.6 The merged data showing the different direction of transmitter and receiver signal polarity (above), and the matching curve (same direction) between transmitter and receiver signal after flipping polarity (below).

3.1.2.4 Resample

In some measurements, receiver data are acquired with different sampling frequencies to see which sampling frequency provides less noisy data. Meanwhile, before the data merge, the sampling frequency of the data set is calculated by the factor difference between the sampling frequency of the transmitter and of the receiver signals. To avoid the distortions from resampling frequency, anti-aliasing filter has to be applied.

An example of resampling is shown in Figure 3.7, where the sampling frequency of the receiver is 250 Hz and the sampling frequency of the transmitter is 40,000 Hz. The factor is calculated by dividing the sampling frequency of transmitter by the sampling frequency of the receiver. Therefore, the factor is 160 which is used for the resampling of the transmitter frequency.

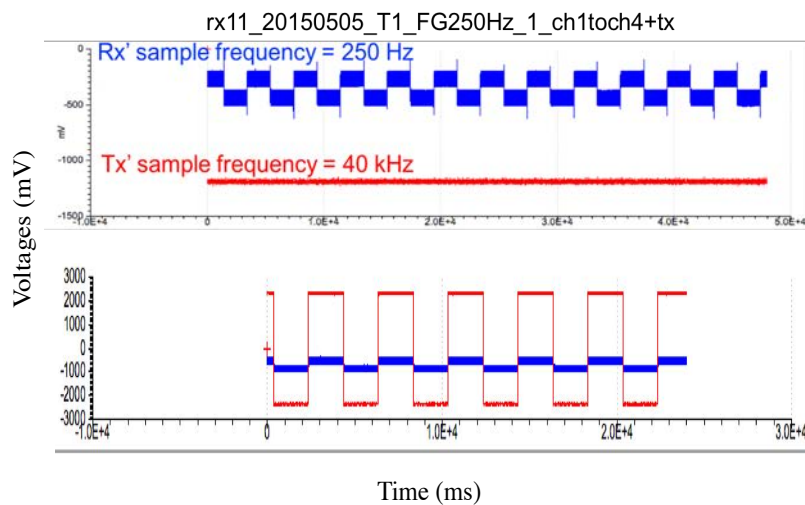


Figure 3.7 Resampling frequency of transmitter data; Before resampling (top), sample frequency of the transmitter is 40 kHz; after resampling, sample frequency of the transmitter and receiver is 250 Hz (Bottom).

3.1.3 Data quality control

The processing steps including pre-stacking, stacking, and post-stacking, were done using KMSProQC software. Most of the time the electromagnetic noise is much bigger than the signals, so that the recorded time series must be processed before interpretation. This processing includes certain steps:

First, the data are merged and converted to the binary KMS format using KMSProDM. The result contains all recorded time series of both electric and magnetic components at one receiver (Rx),

1. First, the data are merged and converted to the binary KMS format using KMSProDM. The result contains all recorded time series of both electric and magnetic components at the receiver (Rx),
2. Second, filtering each time series separately to reduce the periodic cultural noise, mostly from power lines,
3. Third, stacking all-time series selectively to reduce aperiodic noise,
4. Fourth, smoothing the stacked data using recursive average filter, while the DC level is corrected.
5. Finally, normalizing both the electric and the magnetic fields by the transmitter and receiver dipole moments, or converted to the apparent resistivities for further inversion.

3.1.3.1 Periodic Noise Filtering (pre-stack)

When the distortion caused by periodic noise cannot be completely filtered using instrument filter, digital filters, called true amplitude recursive filters, are used to significantly reduce such distortion significantly, (Strack et al, 1988). In general terms, the linear digital filter can be divided in two categories, that is a non-recursive filter, used to get output from the input only, and a recursive filter, used to evaluate the output from the previously output and has also the small number of the coefficients and thus speed in computation that is the its advantages (Strack,1992).

The low-pass filter was selected in this processing step to reduce influence of the harmonic noise (Figure 3.8 a and Figure 3.8 c), mainly from power line, for each data set. The characteristic of an ideal low-pass filter would

perfectly pass signals below the cutoff frequency and completely eliminate signals above the cutoff frequency. The main frequency of the noises in United States is 60 Hz, with and its several center harmonics (60, 80, 120, 180, 300, etc.). They were filtered out using automatic harmonics detection with threshold levels 3.00, with width 10 for each center. The filtered curve (Figure 3.8 b and Figure 3.8 d) shows that the minimal ringing effect appears due to the impulse respond of a perfect low-pass filter. The filtered transient is almost perfectly cleaned out from the harmonic noise and amplitude distortion.

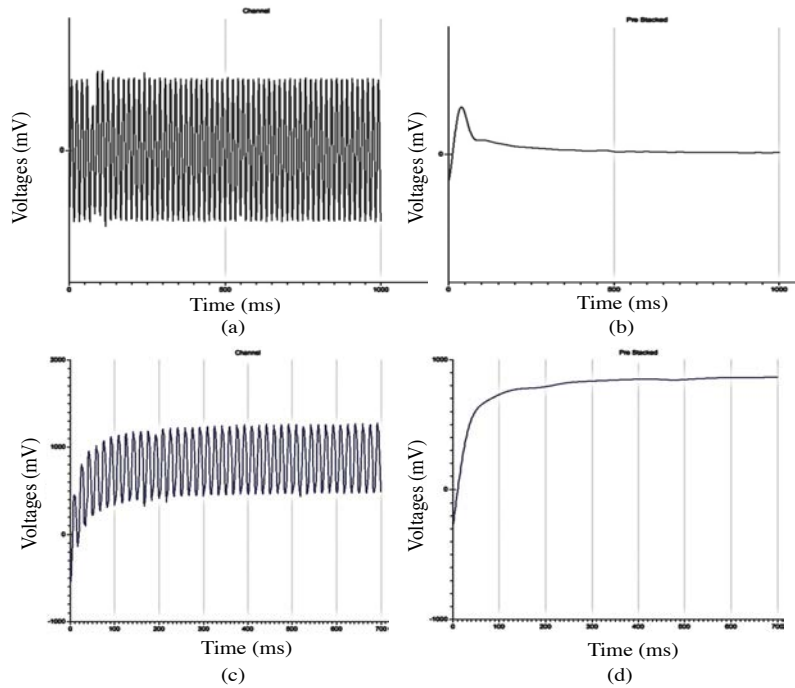


Figure 3.8 Filtering the signal from noise, mostly from power-line with 50 Hz frequency; (a) raw data of magnetic field and, (c) electric field, (b) the filtered data of magnetic field and (d) electric field.

3.1.3.2 Stacking (Gathering)

To compensate the unrecognized sporadic noise that could not be eliminated by pre-stack processing, and in the case if a strong distortion still exists, the selective stacking algorithm with adding $T/2$ additional stacking (mostly for 50% bipolar pulses) was performed (Figure 3.9). In other words, the spike would appear when the pulse is not exactly corresponding to switching time. The pulse should be processed in the half of period for the bipolar signal of 100% duty cycle and in a quarter of a period for 50% bipolar pulses. Other gathers are possible but not considered here. this is a new system and software, and it must be ensured the highest quality.

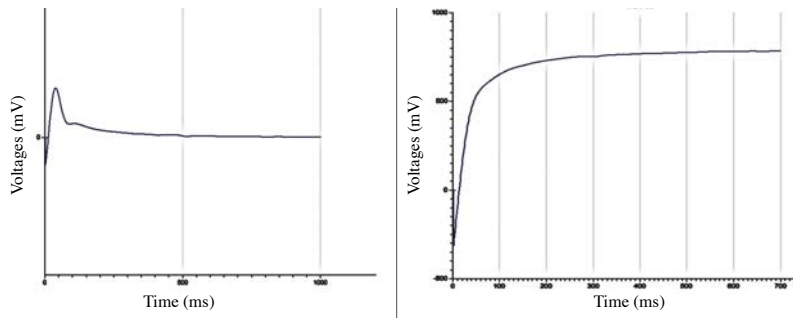


Figure 3.9 Signal after stacking showing the smoother signal; magnetic field (left), electric field (right).

3.1.3.3 Smoothing (Post-stack) and DC leveling

Under post-stacking, the recursive average was mainly applied to smooth the data, which can reduce the ringing due to Gibb's phenomenon (Figure 3.10). KMSProQC also provides the DC level correction. This allow us to set up the start time correctly.

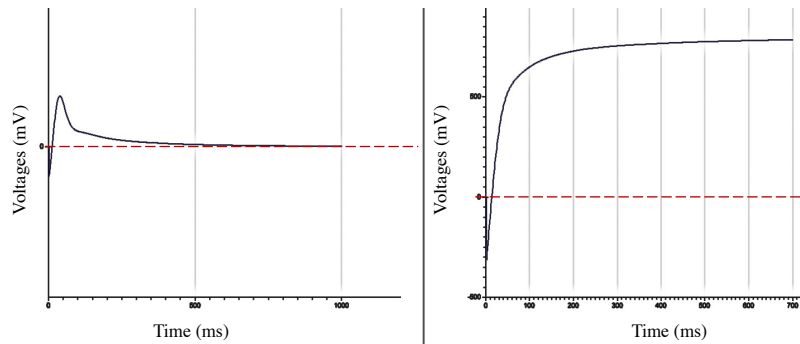


Figure 3.10 The smooth data of magnetic field (left) and electric field (right) after applying recursive average filter. The red dashed line showing the zero DC level.

3.1.4 Processing evaluation

As the data were acquired with the new-generation hardware (new generation), the response needs to be checked before the further data processing. System response measurement can be done in the laboratory or in the field. This aim to remove distortion due to the system itself. The data from multiple field tests in the USA (Hockley) and China using different transmitter are used to evaluate the system respond.

In this research, the system response was measured during the field survey in Hockley field test site in 2015, the system response for the electric fields depends on the contact resistivity of the receiver's grounding electrodes. The system response was measured in Rx0 place nearby transmitter. Other evaluation is the data synchronization that is explained in the data merge section.

As the data were processed with the new software, the study is extended to process the time-lapse and perform the feasibility study as described in Appendix F., to prove the appropriateness of the processing.

3.2 Inversion

For the interpretation of the salt dome, the last procedure is interpretation of the results of the data inversion. The interpretation is done by comparing the result from the inverted data with 3D forward modeling, 3D FSEM modeling, previous studies and geological a priori information as well as the statistical analysis of the inversion results.

3.2.1 1-D inversion

The 1D data inversion is processed in EMUPLUS software developed at the IGM Cologne that serves as the common 1D inversion tool to interpret the processed transients. The 1-D program EMUPLUS allows the inversion of data sets from different electric and magnetic fields LOTEM data (Ex, Ey, and Hz). It implements both Marquardt and Occam's Inversion. The basic theory and explanation of inversion is explained in the Chapter II. Additionally, EMUPLUS is possible to invert the frequency domain MT and MT data sets. Further it is possible to do joint-inversions (Vozoff & Jupp, 1975) up to 30 different data sets (Hoerdt, 1989; Commer, 1999).

The inversion is performed using by the following steps:

1. Converting the data to ASCII file format (*.kms) times and voltages.
2. The data normalization: the processed E-Field data are normalized by the transmitter dipole moment (transmitter length multiplied by the current) and the receiver dipole moment (the receiver length (V/m)), or converted to the apparent resistivities (early and late time); for the processed H-field data (Induced Voltage, Uz) are also normalized by the transmitter dipole moment (transmitter length and current) and the receiver dipole moment (the receiver area (V/m²));
3. Picking up some data point the most representative of the data set and saving them in EMUPLUS data input format (*.rek);
4. Input some requirement parameters in to the header for inversion such as offset, current, coordinate, etc.,
5. Running the program EMUPLUS, loading the data and setting the parameters before inversion. More detail of EMUPLUS can be found in Manual as written by Haroon et al. (2015).

Deleted: and

Deleted: with

6. Choosing the inversion method: either Occam's inversion (Smooth model) or Marquardt Inversion (Layered model).
7. The inverted data are displayed as a function of the depth and the resistivities, and also the thicknesses and the resistivities are included in the table. The result can be saved into the image files including inversion statistics and other output files.

3.2.2 Cumulative conductance and transverse resistance analysis

The cumulative conductance and transverse resistance are analyzed in order to generate the layer model from Occam model. The conductance (S) for every layer (n) is calculated by the thickness (h) divided by the resistivity (ρ). Therefore, the cumulative conductance is the successive additions from layer 1 to layer n.

$$S_n = \frac{h_n}{\rho_n} \quad (3.1)$$

The transverse resistance (T) for every layer (n) is multiplication of the thickness (h) and the resistivity (ρ). Therefore, the cumulative transverse resistance is the successive additions from layer 1 to layer n.

$$T_n = \rho_n h_n \quad (3.2)$$

Furthermore, the result is plotted in the curve to be analyzed as shown in Figure 3.11. Every curve changing is a representative to the resistivity changing. Hence, the resistivities are pick up from the point where the curve change and added the resistivity of the layer 1 and the last layer. Meanwhile, the thicknesses are calculated from the depth. In this research, the cumulative conductance and transverse resistance analysis is used to generate a layered 1-D model including the bed resistivities and thicknesses from an available resistivity well log data using the IX1D software (Appendix F).

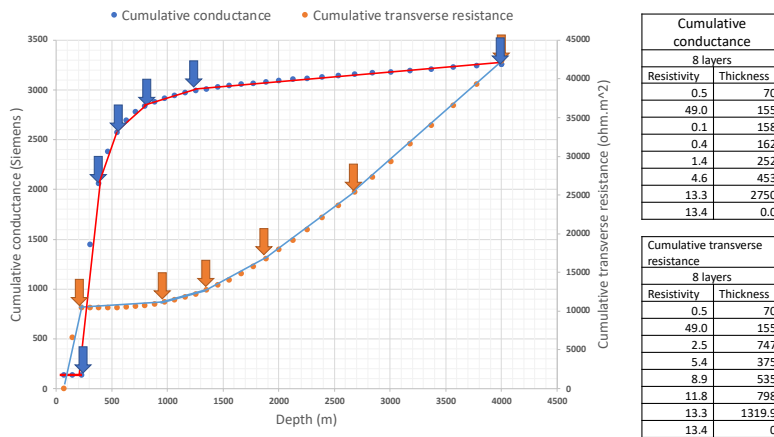


Figure 3.11 Cumulative conductance and transverse resistance analysis from the Occam's inversion to generate the starting model of Marquardt inversion.

3.2.3 Statistical (Eigenvalues and importance) analysis of layered model

The inversion results need to be analyzed in order to interpret the model. Especially for the layered model, it includes the inversion statistic. This allow us to analyze whether the output parameter, resistivities and the thicknesses can be resolve. It also includes the damping factor as well as the importance of each parameter.

Here, the V-matrix which contains the eigenparameter (Figure 3.12) is analyzed. The use of an analysis of original parameter combinations is to resolve the inversion result. Each Eigenparameter gives insight to an original model parameter whether it is resolved or not. The convention is often used to interpret the resolution characteristics of measured or calculated data. The entries of the V-matrix consist positive and negative value (Raiche et al., 1985).

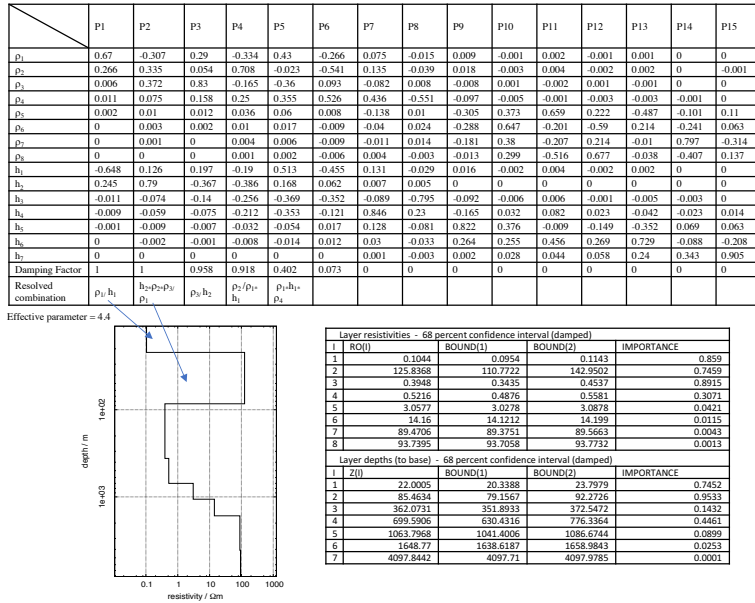


Figure 3. 12 Data analysis using eigenvector and importance to resolve layer of both parameters (resistivity and thickness). The V matrix and damping factor shown on table (above), and the table showing the importance of each layer resistivity and thickness (below).

3.2.4 3D visualization

To compare the result (model) and to better understand the geology, the 1D model is visualized using 3D visualization technique including the model interpolation. The model from both Occam' inversion and Marquardt inversion are plotted in the 3D visualization. Using the advanced Voxler 3D visualization from Golden Software, the inversion results can have interpolated and converted into a 2D cross section (Figure 3.13). Finally, all the models and 3D visualization are interpreted and compared with the previous study and with the geological information.

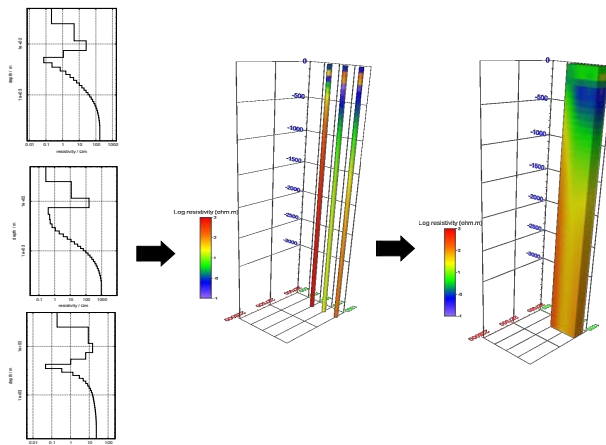


Figure 3.13 3D visualization steps, starting from 1D model plotted to the log model and interpolated together to produce 2D cross section.

3.2.5 Forward model

Here, the forward model can be used for two proposes:

1. To verify the reliability of results of Occam's model and layered model (Figure 3.14)
2. To generate the synthetic data from an available resistivity well log data by analyzing the cumulative conductance (also we can use the cumulative transverse resistance) which can produce a layered 1-D model including the bed resistivities and thicknesses.

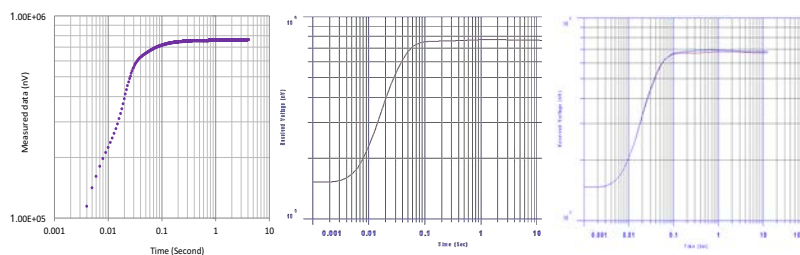


Figure 3.14 Comparison between measured signal and the forward modeling calculation of Occam's model and layered model show good agreement.

LOTEM suite software can handle the forward calculation of both vertical magnetic (Hz) and electric field (Ex, Ey). The resistivity and thickness of each layer model is the main input, and other parameters such as transmitter and receiver dipole moment, and offset is set up. The forward model allows plotting the result in the different curves of electric field (Measured data and normalized receiver data) and of the magnetic field in the measured data format, or early and/or late time apparent resistivity. To prove the reliable of the forward calculation result, this research is extended to estimate the synthetic data of E-fields and H-Field from the well log using an Petrophysics approach (Result in the Appendix F). This can demonstrate how geology gets converted to a realistic model and is properly scaled. In the inversion this approach is used in a reversed way.

CHAPTER IV

RESULTS AND DISCUSSION

4.1 Processing evaluation result

As the main objectives of this research, the processing is very important as high accuracy data is required for automation of the process., Independent cross check is carried out to ensure all steps and used parameters. The result of the forward calculation both result from Occam's inversion and layered model (Marquardt inversion) using different software is described in section 4.2.3.

The considerations related to the processing are the system response and data synchronization. As using the new hardware, it is needed to assure that the behaves is reliable. They are described in the following explanation, including the times shift related to the system response, and time synchronization result.

4.1.1 System response

The results from multiple field tests in the study area (USA), and China using different transmitter are consistent for both tests. In the result from different location, the ramp function, which is direct related to the system response, is about 2 ms (Figure 4.1). Since the signals are longer than 1 second (> 100 ms for the magnetic field) it means that the response effect of the polarity reversing transmitter would not influence at the receiver. Hence, the inversion does not need to use the system response.

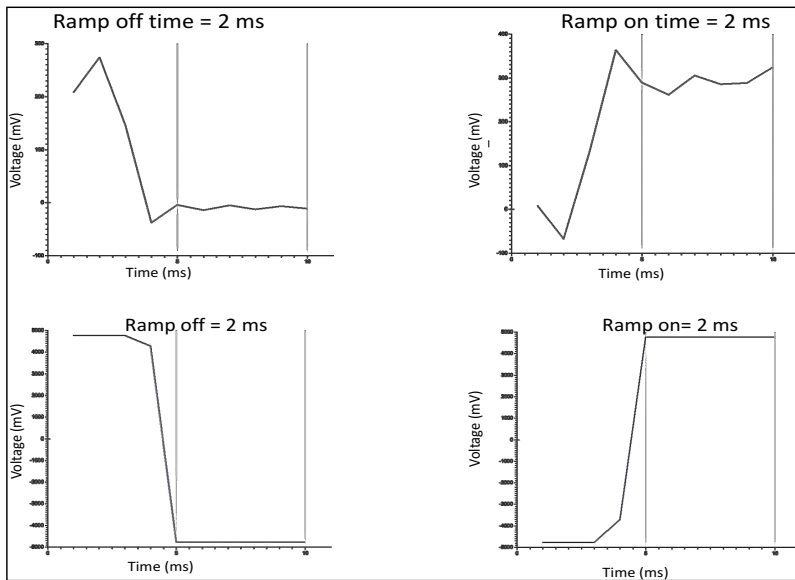


Figure 4.1 The transmitter signal measured in the different area and with different transmitters, the measurement in China (above) and below measurement in Hockley showing the same rum on and off.

4.1.2 Synchronization

The transmitter data is used to verify the time sift how much the different with the receiver data. The results show that the time synchronization decrease for all station (Figure 4.2). Station Rx1 decrease from 15 on 5th May 2015 to 1 on 8th May, 2015 while station Rx2 diminish from 4 to 0 while station Rx3 that the first is 44 on 5th May 2015 reach to 0 on 8th May 2015. This indicate that the system synchronization is more accurate.

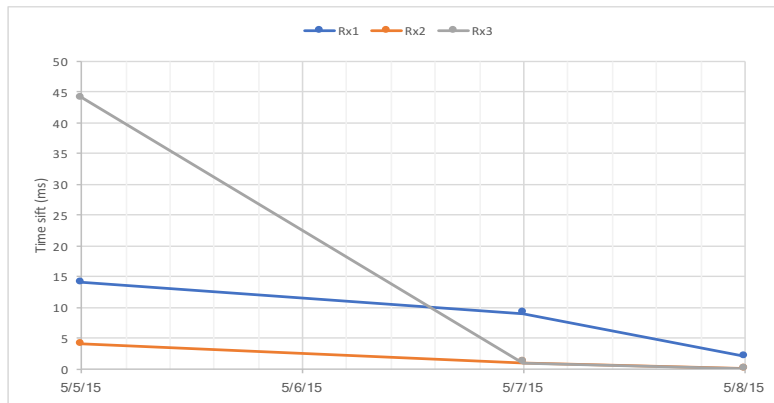


Figure 4. 2 The time shift between transmitter and receiver decreasing from the day 1 to day 3.

4.2 Hockley Results

Hockley survey used two different transmitter configurations, inline and broadside, explained separately in the following section. The inline transmitter shows the stronger signal than the broadside transmitter configuration, nevertheless it shows the higher calibration factor. This may be an effect of gain issue.

When examining the measured data with electric field E_x and magnetic field H_z , it is noticeable that most of the time series are superimposed by strong voltage drifts. A transient could be produced by low-pass filter, selectively stacking, and smoothed by recursive average filter. Further distortions of the transient are the likely consequence. This is the presumable cause leading to the deviant resistivity model. This is endorsed by the results of the receivers Rx1 to Rx3 which either lead to comparable inversion models. These stations were all measured on the same survey day. Common cause for this is static shift which is compensated by the calibrations factor and proven by Newman (1989).

Moreover, the great distorted transients are conspicuous in the magnetic field signal for all stations. A distorted signal can be identified by the form of a transient which change polarity during transient duration (Figure 4. 3). Theoretically, such signals are not possible to use 1D inversion method because they are identical to 3D structure or strong cultural noise (Strack, 1992).

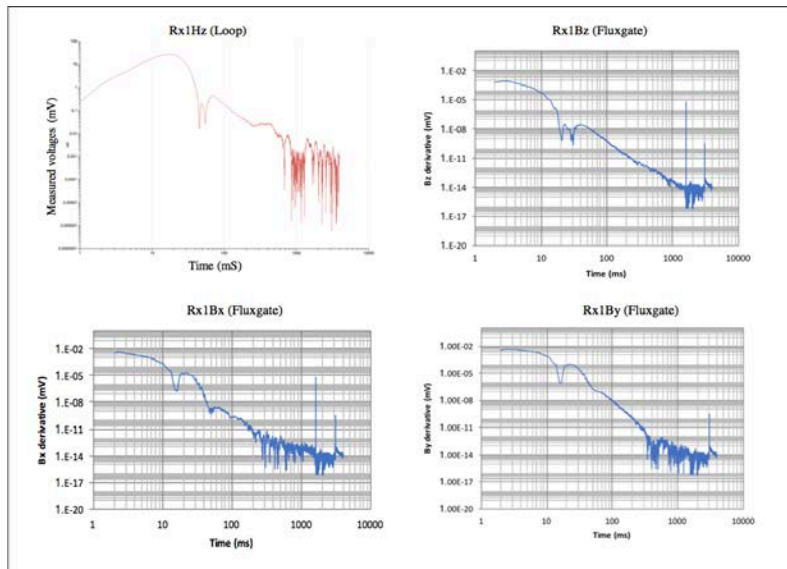


Figure 4.3 Distorted curve of magnetic field Rx1 broadside, vertical magnetic field (above), and horizontal magnetic field (below).

The inversion models of station Rx0a, Rx0b, and Rx0c are only conditionally reliable. All inversion results do not fit to the data, and the model show only a half-space. Hence, they are only used to verify the system response due to the station is very closed to the transmitter (Appendix E).

4.2.1 1D inversion using inline transmitter

The Occam's inversion models and corresponding data point and model of using inline transmitter with χ -errors (Haroon et al., 2015) are presented in Figure 4.4. In general, the Occam's inversion models have the poor data fitting for early times. This prove artifacts of the inversion which the prominent features are the oscillations for the roughnesses within the shallow depth range. In the result, the Occam's roughness constraint with the first derivative yield the model which is very smooth. Thus, the resistivity contrast between the neighboring layers is small. The χ -error is more than 1 ($\chi > 1$) due to the early time is not fitted enough, but it still shows a good result.

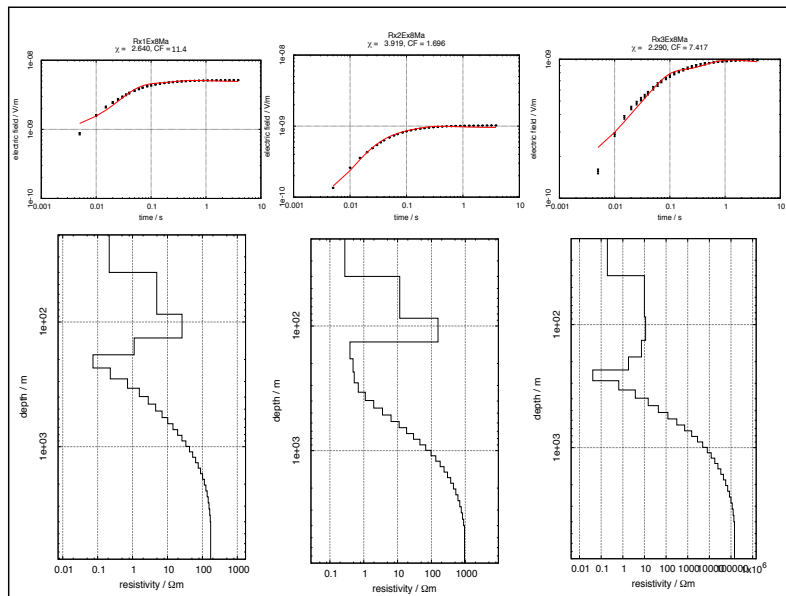


Figure 4.4 1D Occam inversions results of E-field (E_x) inline transmitter. The data fits corresponding to the inversion models (above) and the Occam's inversion conducted with a thirty-starting model for all stations (below).

From the result, Occam's inversion gives a minimum fit especially in the early time., so that its result is analyzed to derive the starting model for the Marquardt inversion to get the optimum fit between model and data. Furthermore, the starting model of Marquardt inversion is generated using cumulative conductance and transverse resistance analysis (Appendix D) from the Occam's inversion.

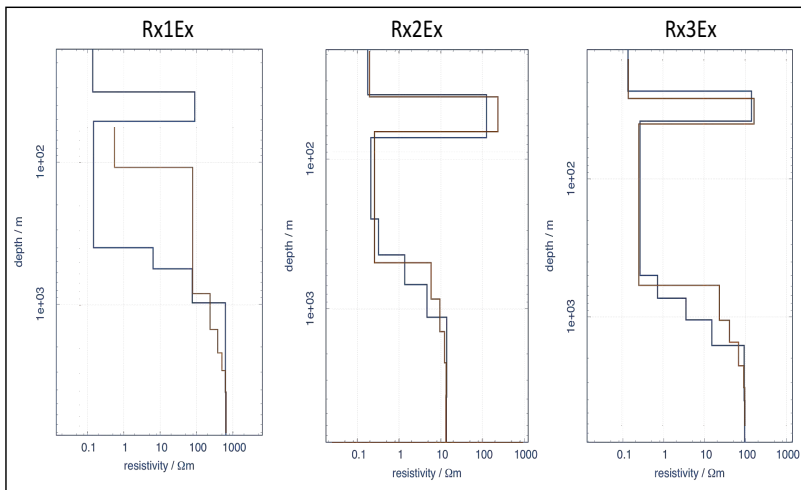


Figure 4.5 The Marquardt inversion generated of electric field (E_x) for receivers, Rx1 to Rx3. Starting model generated cumulative conductance (blue) and cumulative transverse resistance (orange) analysis.

All inversion models imply that the general stratification of the subsurface is consistent throughout the profile. The consistency of E_x and E_y model are well presented by resistivity model (Figure 4.6). The parameters show strong variations between the individual best-fit Marquardt models. Furthermore, those inversion results are analyzed using V-Matrix which include the original parameter and transform parameters, and the importance of each bound parameter to resolve the parameters of each layer.

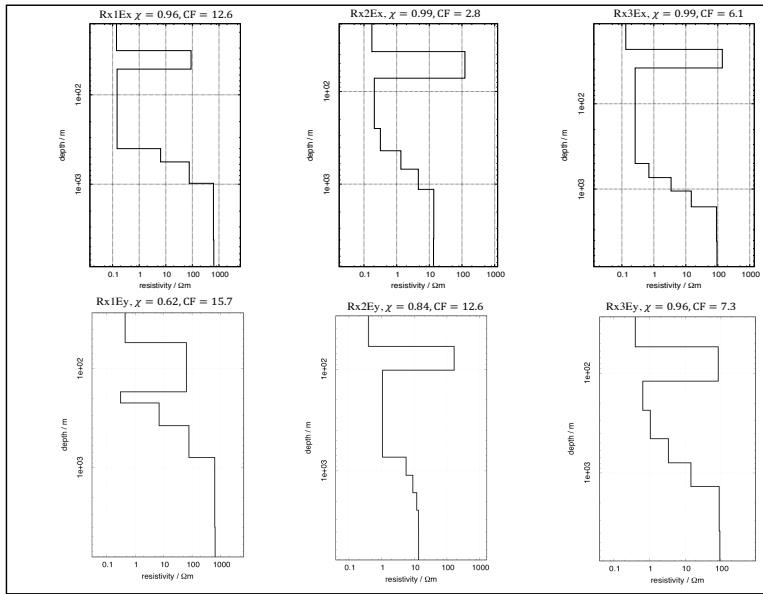


Figure 4.6 The best fit Marquardt model of electric field E_x (above) and E_y (below). The model is generated from a seven-layer model for Rx1 and an eight-layer model for Rx2 and Rx3.

The V -matrix of the LOTEM-inversion imply the relation between the transformed parameters P and the original parameters of the model which correspond for resolving layer. The transformed parameter corresponds to the column of V -matrix, and the original parameter corresponds to the row of V -matrix. In Table 4.1 for the first transformed parameter (P_2), it is obtained by:

$$\begin{aligned}
 P_1 = & -0.8 \log \rho_1 + 0.1 \log \rho_2 + 0.3 \log \rho_3 + 0 \log \rho_4 + 0 \log \rho_6 + \\
 & 0 \log 0 \log \rho_7 + 0 \log \rho_8 + 0.5 \log h_1 + 0.3 \log h_2 - 0.1 \log h_3 - \\
 & 0.1 \log h_4 + 0 \log h_5 + 0 \log 0 \log h_6 + 0 \log h_7
 \end{aligned} \quad (4.1)$$

This mean that parameter combination above $\frac{\rho_2^{0.1} \rho_3^{0.3} h_1^{0.5} h_2^{0.3}}{\rho_1^{0.8} h_3^{0.1} h_4^{0.1}}$ is resolved.

Table 4.1 Statistical analysis for electric field, Rx3Ex inline transmitter. Left table showing V-Matrix of a seven-layer model. The model was generated from Occam's inversion by analyzing cumulative conductance.

Transform Original par.	P1	P2	P3	P4	P5	P6	P7
ρ_1	0.1	-0.8	0.3	-0.2	0.1	-0.3	0.3
ρ_2	0.3	0.1	0.0	0.1	-0.2	0.6	0.5
ρ_3	0.1	0.3	0.3	-0.8	-0.4	-0.1	-0.1
ρ_4	0.0	0.0	0.1	0.1	-0.1	-0.1	0.0
ρ_5	0.0	0.0	0.0	0.0	0.0	0.0	-0.1
ρ_6	0.0	0.0	0.0	0.0	0.0	0.0	0.0
ρ_7	0.0	0.0	0.0	0.0	0.0	0.0	0.0
ρ_8	0.0	0.0	0.0	0.0	0.0	0.0	0.0
h_1	-0.5	0.5	0.2	0.0	0.4	-0.2	0.4
h_2	0.7	0.3	-0.4	-0.1	0.2	-0.5	0.1
h_3	0.0	-0.1	-0.3	-0.4	0.6	0.4	-0.4
h_4	0.0	-0.1	-0.2	-0.3	0.3	0.1	0.6
h_5	0.0	0.0	0.0	-0.1	0.0	0.0	0.2
h_6	0.0	0.0	0.0	0.0	0.0	0.0	0.1
h_7	0.0	0.0	0.0	0.0	0.0	0.0	0.0
Damping Factor	1.0	1.0	1.0	0.7	0.2	0.0	0.0
Resolved combination	$\frac{\rho_2 h_2}{h_1}$	$\frac{h_1 h_2 \rho_3}{\rho_1}$	$\frac{\rho_1 \rho_3}{h_2 h_3}$	$\frac{1}{\rho_3 h_3 h_4}$			

Effective parameters: 4.0

Layer resistivities - 68 percent confidence interval (damped)				
I	RO(I)	BOUND(1)	BOUND(2)	IMPORTANCE
1	0.13	0.13	0.14	0.8
2	138.91	136.68	141.18	0.2
3	0.26	0.24	0.29	0.7
4	0.70	0.69	0.71	0.1
5	3.46	3.45	3.48	0.0
6	14.87	14.85	14.89	0.0
7	91.53	91.49	91.58	0.0
8	94.5282	94.514	94.5425	0.00
Layer depths (to base) - 68 percent confidence interval (damped)				
I	Z(I)	BOUND(1)	BOUND(2)	IMPORTANCE
1	23.05	22.43	23.68	0.7
2	38.06	36.90	39.25	0.8
3	501.42	473.52	530.96	0.4
4	733.47	704.99	763.11	0.2
5	1053.85	1043.44	1064.36	0.0
6	1615.14	1610.29	1620.01	0.0
7	4063.2078	4063.1738	4063.2417	0.000

From the Table 4.1 V-Matrix of a seven-layer model of Rx1Ex, and the importance of each layer parameter are explained. The value is chosen from 0.3 to 1 for layer resolving analysis. P1 is the combination of resistivity-thickness ($\rho_2 h_2$) and h_1 , and P2 is equivalent to the conductivity-thickness of the first layer (h_1/ρ_1), h_2 , and ρ_3 . P3 is equivalent to 1 (one) per conductivity-thickness of the third layer ((ρ_3/h_3) , ρ_1 and h_2 , and P4 is combination of ρ_3 , h_3 , and h_4 . P5 would be required to solve other layers, unfortunately, the corresponding damping factor is too small (0.2). P6 and P7 are irrelevant due to the corresponding damping factor is equal to 0. The V matrix may also be used to assess how important a given layer parameter is. From the importance of each layer parameter, the resistivity of the layer 1 and 3 are important with the value above 5. The depth of layer 1, 2 and 3 show the great importance value which is closed to 1. Never less, the resistivity of layer 2 is considered.

Generalizing the results of the best-fit Marquardt inversion models suggests a resistive layer of ranging 20 Ωm to 300 Ωm with a thickness up to 30 m. This layer is interbedded by two conductive layers with the resistivity below 10 Ωm . The depth of this layer from the surface is 50 m approximately. The thickness of first conductor layer is about 30 m, and the thickness of second conductor layer is up to 180 m. The second conductive layer is underlined with a resistivity increase for all inversion models.

Indeed, the resistivity increase indicates the presence of the salt body, but the variations of the equivalent models imply that this layer is presumably not well resolved. This assumption is supported by the importance and eigenvalue of the model parameters and χ -errors is greater than 1 which means the data and model is not sufficiently fitted.

4.2.2 1D inversion using broadside transmitter

The inversion models of broadside transmitter are processed with similar thirty-layer resistivity structure of the Occam' inversion. Conspicuous is the lacking second resistive layer, presented in the inversion models of stations Rx1 to Rx3 in the previous section using inline transmitter.

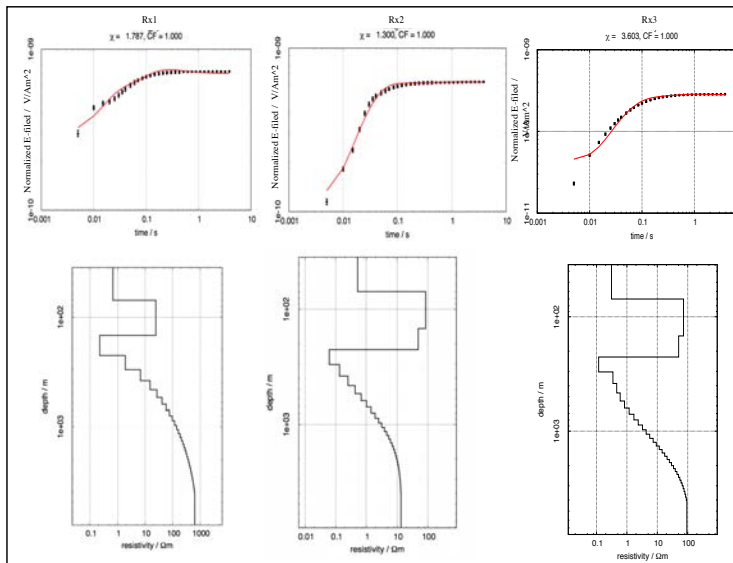


Figure 4.7 1D Occam inversions results of E-field (Ex) broadside transmitter arranged according to their positions along the profile. Starting from left to right, Rx1Ex to Rx3Ex.

Similar to inline transmitter, Occam's models of broadside transmitter have the poor data fitting for early times (Figure 4.7). Therefore, they are further translated to a seven-layer starting model for Rx1 and eight-layer resistivity starting model for Rx2 and Rx3 applied to Marquardt inversion. All inversion models imply that the general stratification of the subsurface is consistent as shown in Ex and Ey resistivity model (Figure 4.8).

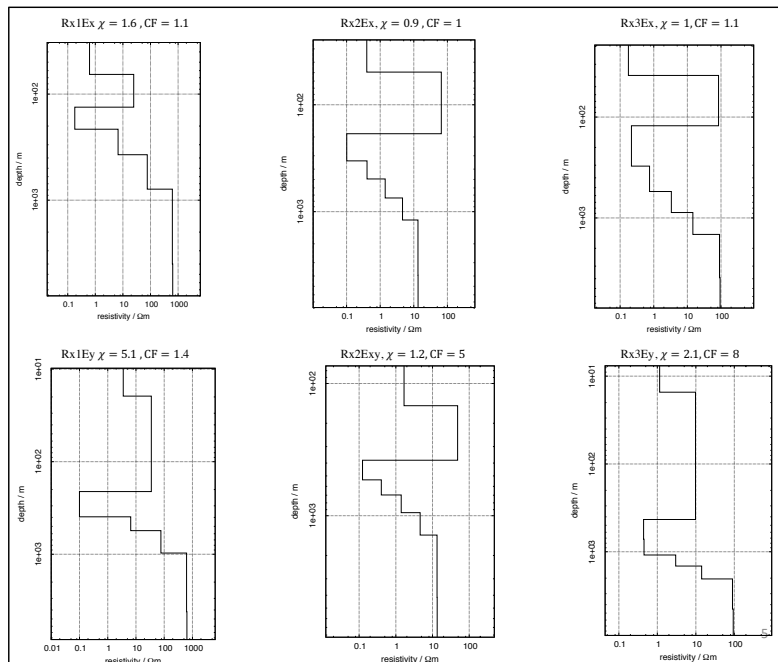


Figure 4.8 The best fit Marquardt model of electric field E_x (above) and the E_y (below). The model is generated from a seven-layer model for Rx1 and an eight-layer model for Rx2 and Rx3.

Based on the best fit Marquardt model with the calibration factor closed to 1, the inversion results of three stations show the similarity to models to the inline transmitter result. Two conductive layers with resistivity below $10 \Omega\text{m}$ flank a resistive layer up to $30 \Omega\text{m}$ with thicknesses varying from 80 to 160 m approximately. An increase in resistivity is again noticeable, implying the resistive target layer at a depth of 800 m to 4000 m. To verify those models, the importance and Eigenparameter are analyzed.

The resistivity value of the third layer possesses an intermediate to small importance denoting a moderate to low resolution of this model parameter. Indeed, the importance of the depths are slightly increased compared to the models of using inline transmitter and the second layer is resolved (Table 4.2).

Table 4.2 Statistical analysis for Rx1 electric field (Ex) broadside transmitter. V-Matrix (right) for individual inversion. The resolved combination shows that the depth and resistivity are fixed. The importance of resistivity and thickness for each layer (right-below).

Transform par. Original par.	P1	P2	P3	P4	P5	P6	P7	Layer resistivities - 68 percent confidence interval (damped)				
								I	RO(I)	BOUND(1)	BOUND(2)	IMPORTANCE
ρ_1	0.3	-0.8	0.3	-0.3	0.3	0.0	0.1	1	0.6108	0.5674	0.6576	0.9204
ρ_2	0.6	0.2	-0.3	0.4	0.5	0.1	0.4	2	32.755	29.1352	36.8245	0.5371
ρ_3	0.3	0.3	0.5	-0.3	-0.4	0.3	0.5	3	0.1678	0.1576	0.1787	0.3797
ρ_4	0.0	0.0	0.0	0.0	0.1	0.5	-0.3	4	7.0767	7.0623	7.091	0.0246
ρ_5	0.0	0.0	0.0	0.0	0.0	0.1	-0.1	5	77.1895	77.1704	77.2086	0.0025
ρ_6	0.0	0.0	0.0	0.0	0.0	0.0	0.0	6	620.1487	619.9661	620.3313	0.0011
ρ_7	0.0	0.0	0.0	0.0	0.0	0.0	0.0	7	638.4388	638.3203	638.5574	0.0006
h_1	-0.3	0.3	-0.2	-0.7	0.6	0.0	0.1	Layer depths (to base) - 68 percent confidence interval (damped)				
h_2	0.6	0.1	-0.4	-0.4	-0.3	-0.1	-0.3	I	Z(I)	BOUND(1)	BOUND(2)	IMPORTANCE
h_3	-0.2	-0.3	-0.6	-0.1	-0.3	0.4	0.5	1	53.7853	48.8847	59.1772	0.6708
h_4	0.0	0.0	0.0	0.0	-0.1	-0.7	0.4	2	109.524	98.3298	121.9926	0.8919
h_5	0.0	0.0	0.0	0.0	0.0	-0.1	0.0	3	179.823	164.155	196.9864	0.9333
h_6	0.0	0.0	0.0	0.0	0.0	0.0	0.0	4	434.0316	432.3493	435.7203	0.0339
Damping factor	1.0	1.0	1.0	1.0	0.2	0.0	0.0	5	847.0286	846.6716	847.3857	0.0039
Resolved combination	$\rho_2 h_2$	$\frac{h_1 \rho_3}{\rho_1 h_3}$	$\frac{\rho_3}{h_2 h_3}$	$\frac{\rho_2}{\rho_1 h_1 h_2}$				6	4049.9766	4049.9465	4050.0066	0

Effective parameter: 4.146

4.2.3 Independent cross check (Forward modeling)

The above inversion result both smooth and layered model was cross-checked with forward calculation. In inversion, EMUPLUS is used to run Occam's and Marquardt inversion while for the forward calculation is used to verify the processing using a different program, LOTEM suite, complied with different codes. Nevertheless, the forward calculations of two models, Occam's and Marquardt inversion, show the similarity to the measured data (Figure 4.11). This indicate that all procedures and used parameters, such as transmitter and receiver dipole moment, are correct during inversion. To support the processing, the time-lapse and the feasibility study are included in Appendix F.

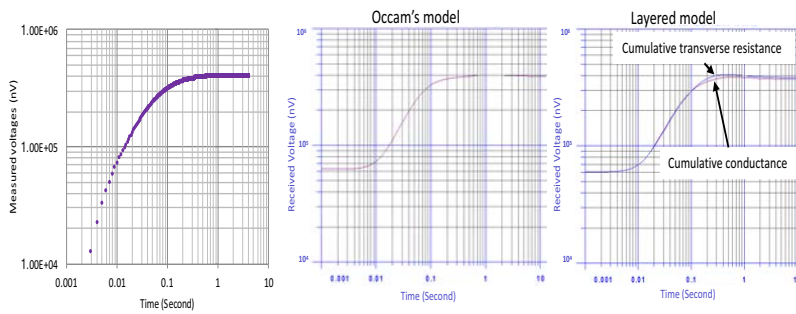


Figure 4.9 Comparison between measured signal (left) and forward calculation of Occam's model (middle) and layered model (right) showing the similarity.

4.2.4 Reconciliation with KMS 3D results

To understand the geology correctly, the 1D inversion results are further compared with 3D model of FSEM by Davydycheva (personal communication, 2018). Meanwhile, Interpolation of 1D inversion results of best fit Occam's and Marquardt model, with the resolved layer of three stations are plotted in 3D visualization (Figure 4.10 and Figure 4.11).

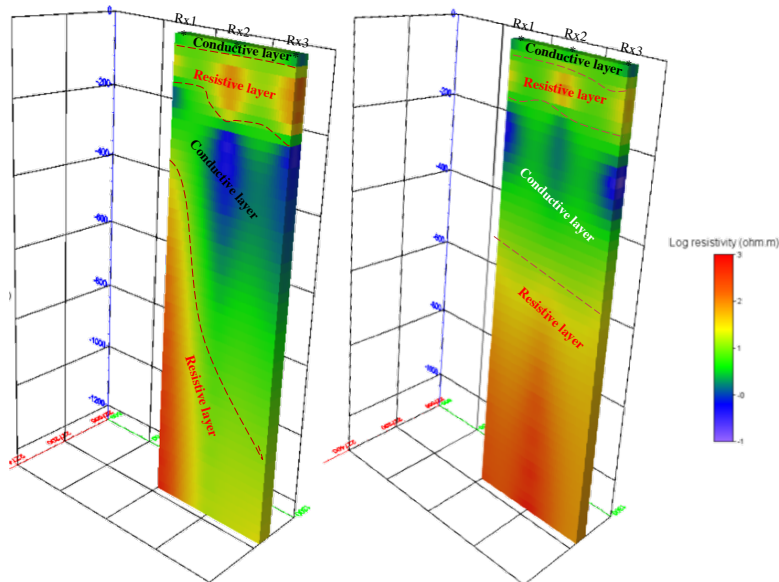


Figure 4.10 3D visualization of Occam model, broadside transmitter (left) and inline transmitter (right).

From the Figure 4.10 above, the resistivity contrast between conductive layer and resistive layer can be clearly distinguished from two images. The conductive layer in the near surface is recondite because this thin layer is covered from the strong resistive layer. Second layer is defined as the resistive layer and underlined by the conductive layer. Meanwhile, the fourth layer show the high resistivity to the bottom. Although, the both inversion give a similar display until the layer 3, but the resistivity layer underlined by second conductive layer are dissimilar. This need to compare with the result from Marquardt inversion.

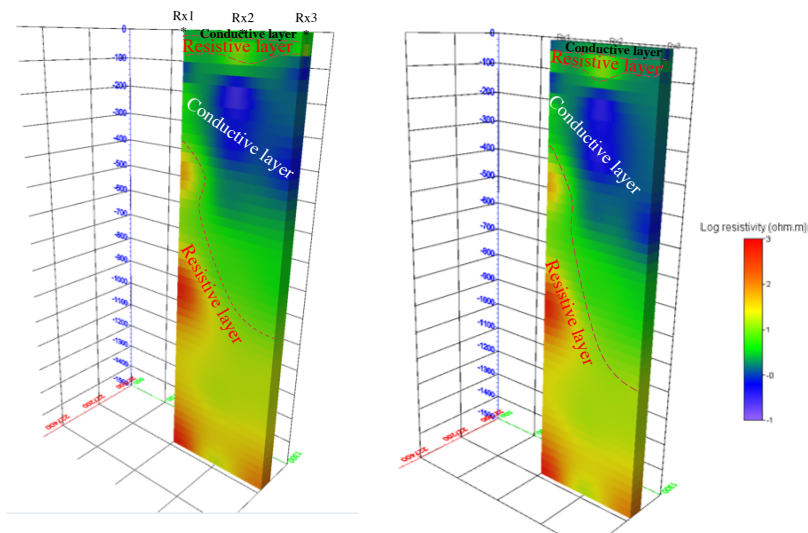


Figure 4.11 3D visualization of Marquardt inversion result, broadside transmitter (left) and inline transmitter (right).

The similar results for broadside and inline are finally obtained from Marquardt inversion. Figure 4.11 show the increased thickness of second conductive layer from the station 1 to the station 3. This is also similar to the Occam' model from broadside transmitter configuration. This indicate that the station may closed to the edge of the salt body.

The result is compared with 3D forward model from Sofia Davydycheva (KMS Technologies, 2016) as shown in Figure 4.12. The result only shows an overhang closed to the transmitter. The low resistivity layer in the depth of 400 m approximately is shown from all 3D model. Furthermore, the low resistivity structure above the salt body can be seen start from part 3 (closed to south transmitter) until part 7 (southern part of Rx3) indicated wet area (Sofia Davydycheva, personal communication).

Deleted: 2018

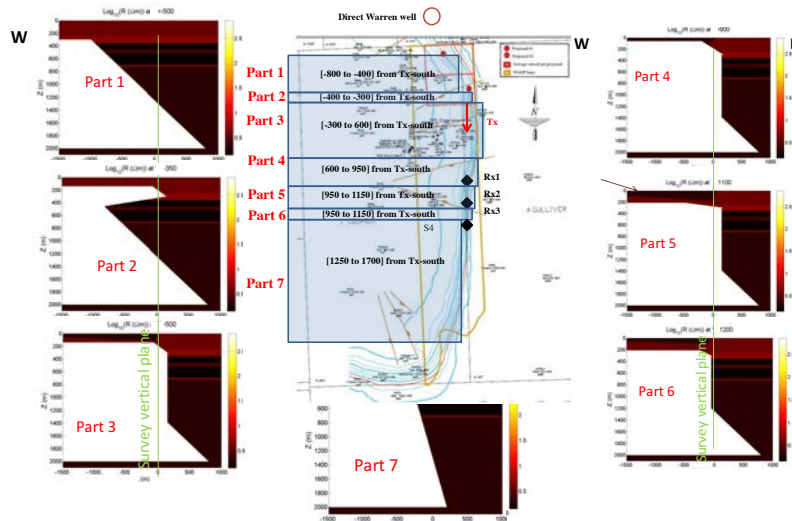


Figure 4.12 Cross section of 3D model of the salt dome, best matching to the data showing the overhang in the part 2 closed to transmitter (Sofia Davydycheva, personal communication).

4.3 Interpretation

In the following, the inversion models of the 1D-inversion and 3D visualization in conjunction with the performed modeling studies, are interpreted by incorporating geological information obtained from the previous study and direct Warren log. The following geological interpretation is based on their suggestions.

Warren well situated to the North-East from the salt dome as depicted in Figure 4.13 (right). The resistivity of the upper part of the formation is believed to be a conductive layer. The conductive layer is also predicted at a depth of 250 m approximately; at the depth above 250 m several more resistive beds are situated. The resistive increase in the depth about 750 m (KMS Technologies, personal communication, 2017).

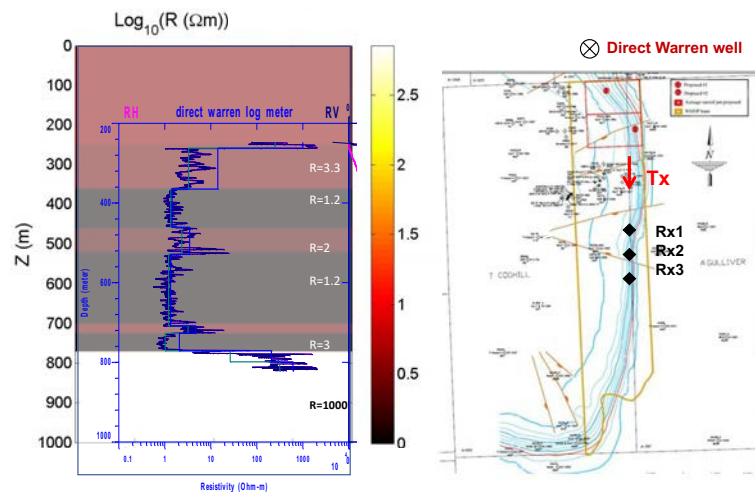


Figure 4.13 Direct Warren log (left) and its location (right). Anisotropic reduced well log model showing the horizontal resistivity (generated from cumulative conductance) and vertical resistivity (generated from cumulative transfer resistance) (KMS Technologies, personal communication, 2017).

From the resistivity models obtained from the best fit 1D inversion, following geological setting is suggested:

4.3.1 The conductive layer, below 1 Ωm , consisting of sediment from Lissie or Wills formation. It extends to a depth of approximately 50 m. Very low resistivity layer may imply the static shift effects in surface. Davydycheva already observed that near surface conductive anomalies are needed that could be real or static shift effects.

4.3.2 The resistive layer, from 30 to 100 Ωm approximately, has the variable thickness up to 30 m in 30 m to 70 m depth from the subsurface. The 1D inversion results show that this layer is possible interrupted by salt overhang. This is supported by the direct warren log where the resistivity value is similar to the forth layer.

4.3.3 A low resistivity characterizes the third layer below 10 Ωm . According to the geological information, it mainly consists of sediment with a depth interval of 70 m.

4.3.4 The resistivity increase characterizes the fourth layer up to 300 m approximately indicating a salt body. It represents a resistive layer and similar to Direct Warren log interpretation.

By linking the eighth-layer resistivity model to previous study and geological information in the study area (Figure 4.14), an improvement of the geological model is obtained. The depth and thickness of each geological formation, not explicitly known, is now restricted to certain depth intervals. These boundaries are obliged to a certain degree of variation due to the equivalent models.

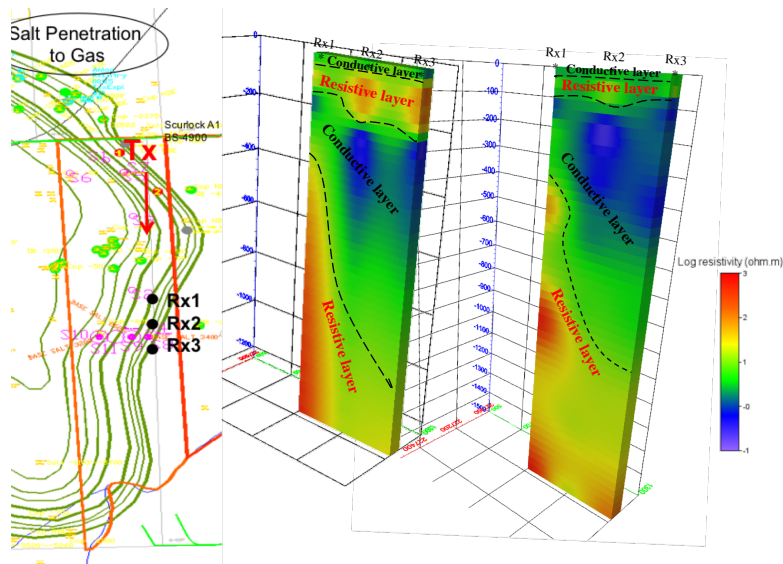


Figure 4.14 Interpretation with the previous study. In the left showing the cap-rock contour from gravity result (Halbouty, 1967) and the 3D visualization from best fits Occam' model (middle) Marquardt model (right) of broadside transmitter configuration.

CHAPTER V

CONCLUSION AND RECOMMENDATION

5.1 Conclusion

This research “An application of long-offset transient electromagnetic (LOTEM) around a salt dome near Houston, Texas” aimed at resolving the inner layer of salt dome by applying electromagnetic methods. The individual test-field surveys were conducted to resolve successively overhang zone of the subsurface of the salt dome. An interpretation of the obtained data should give information about the electrical resistivity distribution with depth. For this, the electromagnetic methods LOTEM were applied. The results of the latter were subject of this thesis.

The results here and the analysis are more reliable than the 3D model run by Davydycheva because the 3D model is highly equivalent. Having found the overhang with these workflows described here, Davydycheva calculate the respective 3D model and it is consistent with the results.

The LOTEM data were obtained during a field survey conducted in May 2015 and the processing is begun on 2017. In the extent of this thesis, the data are processed to produce transient as smooth as possible, and then the processed data were subsequently inverted using 1D inversion/modeling tools, both Occam’ and Marquardt inversion. Particularly, the program EMUPLUS was utilized for the 1D inversion. Finally, for the data interpretation, the 1D model interpolated to get the 3D visualization in order to better understand the geology and this can clearly show the layer from three stations.

The layered model is derived ranging from the surface up to a depth of approximately 4000 m. The subsurface consists of a seven-layer to eight-layer resistivity structure, nevertheless, according to statistical analysis, the resolved parameters only until third layer. 3D visualizations display the resistivity profile clearly. This led to the better image for the geologic interpretation.

The top layer is very conductive comprising a resistivity below 1 Ωm and a thickness of 20 to 50 m. The following layer is resistive with resistivity up to 30 Ωm predicted as the salt flank and extending to a thickness of 20 m to 120 m. This resistive layer is needing to be corrected with another due to the static shift effect may still influence to the data. The third layer is conductor with approximately <1 Ωm to 10 Ωm . This layer consists of 70 to 500 m thick of sediment. Nonetheless, since all 1D inversion models show a resistivity increase at a depth up to 300 m approximately to the base, it is considered as the salt body.

The considerations for interpretation are described as follow:

5.1.1 All results from both Occam' and layered models consistent showing the resistive layer interbedded with two conductive layers.

5.1.2 The layered model with Eigenparameter as well as the importance resolves the parameter combinations where the section can be resolved to below the salt overhang.

5.1.3 Results correspond to the vintage interpretation of gravity result.

5.1.4 From the gravity contour show the oil fields under the salt dome in the northeast and southern part of the salt dome that relate to the salt overhang.

The forward calculations were conducted from various resistivity models of Occam and Marquardt inversion result. The best-fit models are obtained corresponding to the measured data. Fortunately, the obtained models demonstrate that the processing is reliable, the models are consistent with the 1D inversion models, and satisfying a 1D resistivity structure.

The result from time-lapse support the appropriateness of the processing. The smoother signals were obtained and calculate the transient differences which is directly related to resistivity changes. The resistivity changes are correlated with the presence of water injection during the survey.

Key element in the derivation of the different models was the upscaling derived in the appendix for a sample feasibility study. It is based the Earth being anisotropic and deriving end members for the models, which then lead us to the most plausible models.

5.2 Recommendation

Since the processing of the data was the key element this thesis stops at this. There is more data available from KMS Technologies that could be integrated at a later stage.

5.2. Three sites with the maximum offset of 1300 m cause minimum interpretation. It is required more data with the offset up to 2 km.

5.2.1 Magnetotellurics data: This data was acquired over the years and processed with various vintage software. All of this would have to be re-processed and inverted and then jointly inverted with the LOTEM. This is now possible as here we obtain a stable model.

5.2.2 Integration of the 3D requires more measurements. Davdycheva only had 3 sites and resulting 3D model which was highly equivalent. A larger data base is necessary.

5.2.3 Shallow near surface control measurements with loop source TEM. The data set shows near surface resistive anomalies that are typical for static effects. They need to be controlled adding TEM measurements and jointly invert them.

REFERENCES

- Allen, W. E., Caillouet, H. J., & Stanley, L. (1955). Gravity Investigations in The Hockley Salt Dome, Harris County, Texas. **Geophysics**, 20(4). 829-840;
- Anderson, R. E., Eargle, D. H., & Davis, B. O. (1973). **Geologic and Hydrologic summary of salt domes in Gulf Coast region of Texas, Louisiana, Mississippi, and Alabama**. Denver: U.S. Dept. of the Interior, Geological Survey;
- Amin, A., & Deriche, M. (2016). Salt-Dome Detection Using a Codebook-Based Learning Model. **IEEE Geoscience and Remote Sensing Letters**, 13(11). 1636-1640;
- Avdeeva, A., Avdeev, D., & Jegen, M. (2012). Detecting a salt dome overhang with magnetotellurics: 3D inversion methodology and synthetic model studies. **Geophysics**, 77(4). E251–E263;
- Ayten, U. E., Vural, R. A., & Yildirim T. (2011). Low-pass Filter Approximation with Evolutionary Techniques, **The 7th International Conference on Electrical and Electronics Engineering, ELECO 2011**, Bursa, Turkey. 125-129;
- Baker, [E. T.](#) (1995). **Stratigraphic nomenclature and geologic sections of the Gulf Coastal Plain of Texas** Austin, Texas: U.S. Department of the Interior, U.S. Geological Survey. 94–461;
- Beamish, D., & Travassos, J. M. (1992). Magnetotelluric imaging of basalt-covered sediments. **First Break**, 10. 345-357;
- Beckman, J. D., & Williamson, A. K. (1990). **Salt-dome locations in the gulf coastal plain, South-Central United States**. Texas: U.S. Geological Survey - Water-Resources Investigations Report 90-4060;
- Buehnemann, J., Henke, C.H., Mueller, C., Krieger, M.H., Zerilli, A., & Strack, K.M. (2002) Bringing complex salt structures into focus—a novel integrated approach: **SEG technical program expanded abstracts**. 446–449;

Deleted: ET

Deleted: Jr.

- Cagniard, L. (1953). Basic theory of the magnetotelluric method of geophysical prospecting. **Geophysics**, 18. 605–635;
- Canada, W. R. (1953). Hockley Field: Harris County, Texas. Houston, Texas: Houston Geological Society;
- Ceia, M. A., Carrasquilla, A. A., Sato, H. K., & Lima, O. (2007). Long Offset Transient Electromagnetic (LOTEM) for monitoring fluid injection in petroleum reservoirs – Preliminary results of Fazenda Alvorada Field (Brazil). **10th International Congress of the Brazilian Geophysical Society & EXPOGEF 2007**, Rio de Janeiro, Brazil;
- Claerbout, J.F. (1985). **Fundamentals of Geophysical Data Processing with Applications to Petroleum Prospecting**. Oxford: Blackwell Scientific Publications;
- Coburn, G. W. (2002). A Methodology for Defining the Base and Geometry of Salt Bodies in the Deep-Water Gulf of Mexico. **Gulf Coast Association of Geological Societies Transactions**, 52. 123–133;
- Colombo, D., Keho, T., & McNeice, G. (2012). Integrated seismic-electromagnetic workflow for sub-basalt exploration in northwest Saudi Arabia. **The Leading Edge**, 31(1), 42-52;
- Colombo, D., Dasgupta, S., Strack, K.M., & Yu, G. (2010). Feasibility study of surface-to-borehole CSEM for oil-water fluid substitution in Ghawar field, Saudi Arabia, **AAPG GEO 2010 Middle East: Innovative Geoscience Solutions – Meeting Hydrocarbon Demand in Changing Times**, Manama, Bahrain;
- Commer, M., (1999). *Ein spezielles Verfahren der eindimensionalen kombinierten Inversion von Long-Offset Transient Electromagnetic (LOTEM)- und Magne- totellurik (MT)-Daten*: Master's thesis, University of Cologne, Institute for Geophysics and Meteorology.
- Constable, S. (2010). Ten years of marine CSEM for hydrocarbon exploration. **Geophysics**, 75(5). 75A67-75A81;
- Constable, S. C., Parker, R. L., & Constable, C. G. (1987). Occam's inversion: A practical algorithm for generating smooth models from electromagnetic sounding data. **Geophysics**, 52(3). 289-300;

Formatted: Font: Bold, Italic, Complex Script Font: Bold, Italic

Deleted: Constable, S. C., Parker, R. L., & Constable, C. G. (1987). Occam's inversion: A practical algorithm for generating smooth models from electromagnetic sounding data. **Geophysics**, 52(3). 289-300;

Formatted: Font: Bold, Complex Script Font: Bold

- Darton, N.H., Stephenson, L.W., & Gardner, J., (1937), **Geologic map of Texas**. Texas: U.S. Geological Survey, scale 1: 500.000;
- Davydycheva, S., Rykhliniski, N., & Legeido, P. (2006). Electrical-prospecting method for hydrocarbon search using the induced-polarization effect. **Geophysics**, 71(4). G179- G189;
- Davydycheva, S., & Rykhliniski, N. (2009). Focused Source EM Survey – New Solution for Both Shallow and Deep Water. **71st EAGE Conference and Exhibition incorporating SPE EUROPEC 2009**. Amsterdam: EAGE
- Deri, C. P., & Sparlin, M. A. (1990). Salt dome seismic profiling from the inside out. **The Leading Edge**, 9(8). 64-68;
- Deussen, A., & Lane, L. L. (1925). Hockley Salt Dome, Harris County, Texas. **Bulletin AAPG Bulletin**, 9. 570-599;
- [Donoho, D. L., & Johnstone, J. M. \(1994\). Ideal spatial adaptation by wavelet shrinkage. **Biometrika**, 81\(3\), 425-455;](#)
- Fleisch, D. A. (2008). **A student's guide to Maxwell's equations**. New York: Cambridge University Press;
- [Halbouty, M.T. \(1967\). **Salt domes – Gulf region, United States and Mexico**. Houston, TX: Gulf Pub. Co.;](#)
- [Haroon, A. Yogeshwar, P., Bockmann, J., & Ossen, D. \(2015\). **EMUPLUS Manual**. Cologne: Institute of Geophysics and Meteorology, University of Cologne;](#)
- Haroon, A. (2012). **The application of the Long Offset Transient Electromagnetic Method in Perekishkul, Azerbaijan**. Master's thesis, Faculty of Mathematics and Natural Sciences, University of Cologne;
- [Hawkins, M. E., & Jirik, C. J. \(1966\). **Salt domes in Texas, Louisiana, Mississippi, Alabama, and offshore tidelands; a survey**. Washington, D.C.: U.S. Dept. of the Interior, Bureau of Mine;](#)
- Hawwar, Y.M., & Turney, R.D. (2000). Filtering (Denoising) in the Wavelet Transform Domain;
- He, C., Xing, J., Li, J., Yang, Q. & Wang, R. (2015). A New Wavelet Threshold Determination Method Considering Interscale Correlation in Signal Denoising. **Mathematical Problems in Engineering**.1-9;

Formatted: Font color: Auto, Pattern: Clear

Formatted: References list

Deleted: ¶

Deleted: Grubb, H. F. (1984). **Planning report for the Gulf Coast regional aquifer-system analysis in the Gulf of Mexico coastal plain, United States**. Austin, TX: U.S. Geological Survey;

Formatted: Font: (Default) Times New Roman, 12 pt, Font color: Auto, Complex Script Font: Times New Roman, 12 pt, (Complex) Arabic

Formatted: Font: Bold, Complex Script Font: Bold

Formatted: Font: (Default) Times New Roman, Font color: Auto, Complex Script Font: Times New Roman, Pattern: Clear

Formatted: Font: Bold, Complex Script Font: Bold

Formatted: Font: Bold, Complex Script Font: Bold

Hoerdt, A., & Scholl, C. (2004). The effect of local distortions on time-domain electromagnetic measurements. *Geophysics*, 69(1), 87–96;

Moved (insertion) [2]

Hoerdt, A., 1989. *Ein Verfahren zur 'Joint Inversion' angewandt auf 'Long Offset Electromagnetics' (LOTEM) und Magnetotellurik (MT)*; Master's thesis, Univer- sity of Cologne, Institute for Geophysics and Meteorology.

Formatted: Font: (Default) Times New Roman, 12 pt, Font color: Auto, Complex Script Font: Times New Roman, 12 pt

Formatted: References list, Space After: 0 pt, Line spacing: single, Adjust space between Latin and Asian text, Adjust space between Asian text and numbers

Hosman, R.L. (1996). **Regional stratigraphy and subsurface geology of Cenozoic deposits, Gulf Coastal Plain, South-Central United States.** Texas: U.S. Geological Survey professional paper; 1416-G;

Formatted: Font: (Default) Times New Roman, 12 pt, Bold, Italic, Font color: Auto, Complex Script Font: Times New Roman, 12 pt, Bold, Italic

Formatted: Font: (Default) Times New Roman, 12 pt, Font color: Auto, Complex Script Font: Times New Roman, 12 pt

Hosman, R. L., & Weiss, J. S. (1991). **Geohydrologic units of the Mississippi embayment and Texas coastal uplands aquifer systems, South-Central United States.** Washington: U.S. Dept. of the Interior, U.S. Geological Survey;

Formatted: Font: (Default) Times New Roman, Font color: Auto, Complex Script Font: Times New Roman

Deleted: ¶

Hussain, N., Karsiti, M. N., Yahya, N., & Yahya, N. (2012). 2D forward modeling of marine Controlled Source Electromagnetic (CSEM) data for salt-dome and stratigraphy trap reservoir. **2012 4th International Conference on Intelligent and Advanced System**, Kuala Lumpur. 616–621;

Moved up [2]: Hoerdt, A., & Scholl, C. (2004). The effect of local distortions on time-domain electromagnetic measurements. *Geophysics*, 69(1), 87–96;

Deleted: ¶

Jackson, M. P., & Seni, S. J. (1984). **Atlas of salt domes in the East Texas Basin.** Austin, TX: Bureau of Economic Geology, University of Texas at Austin;

Moved down [3]: Jegen, M. D., Hobbs, R. W., Tarits, P., & Chave, A. (2009). Joint inversion of marine magnetotelluric and gravity data incorporating seismic constraints: Preliminary results of sub-basalt imaging off the Faroe Shelf. *Earth and Planetary Science Letters*, 282, 1-4,

Deleted: ¶

Jegen, M. D., Hobbs, R. W., Tarits, P., & Chave, A. (2009). Joint inversion of marine magnetotelluric and gravity data incorporating seismic constraints: Preliminary results of sub-basalt imaging off the Faroe Shelf. *Earth and Planetary Science Letters*, 282, 1-4.

Moved (insertion) [3]

Jupp, D. L. B., and Vozoff, K., 1977, Resolving anisotropy in layered media by joint inversion: *Geophysical Prospecting*, 25, 460-470;

Jupp, D. L. B. & Vozoff, K. (1975), Stable Iterative Methods for the Inversion of Geophysical Data. *Geophysical Journal of the Royal Astronomical Society*, 42, 957–976;

Karki, J. (2000). **Active low-pass filter design.** Texas: Texas Instruments;

Deleted: 2002

Deleted: ,

Keller, G. V., & Frischknecht, F. C. (1966). **Electrical methods in geophysical prospecting.** Oxford: Pergamon Press.

Formatted: Font color: Auto, Pattern: Clear

Formatted: References list

- Khan, S. D., Stewart, R. R., Otoum, M., & Chang, L. (2013). A geophysical investigation of the active Hockley Fault System near Houston, Texas. **Geophysics**, 78(4). 177-184;
- KMS Technologies (2016). Focused time-domain EM (FSEM) demonstration over a 3D structure (salt dome), www.KMSTechnologies.com (confidential);
- Lanczos, C. (1964). A Precision Approximation of the Gamma Function. **Journal of the Society for Industrial and Applied Mathematics: Series B, Numerical Analysis**, 1. 86-96;
- Levenberg, K. (1944). A method for the solution of certain non-linear problems in least squares. **Quarterly of Applied Mathematics**, 2(2). 164-168;
- Lines, L. & Treitel, S. (1984). A Review of Least-Squares Inversion and Its Application to Geophysical Problems. **Geophysical Prospecting**, 32(2).159-186;
- Linville, A. F., & Dablain, M. A. (1985). A case study in seismic diffraction near a Gulf Coast salt dome. **Geophysics**, 50(7). 1077-1082;
- MacGregor, L., & Sinha, M. (2000). Use of marine controlled-source electromagnetic sounding for sub-basalt exploration. **Geophysical Prospecting**, 48(6). 1091-1106;
- Marquardt, D. (1963). An Algorithm for Least-Squares Estimation of Nonlinear Parameters. **SIAM Journal on Applied Mathematics**. 11 (2). 431-441;
- Mayne, W.H, (1967). Practical Considerations in The Use of Common Reflection Point Techniques, **Geophysics**, 32(2). 225-229;
- Mayne, W.H, (1962). Common Reflection Point Horizontal Data Stacking Techniques. **Geophysics**, 27(6). 927-938;
- McClintock, W. R., Galloway, T. L., Stringer, B. R., & Andrew, L. E. (1972). **Soil survey of Montgomery County, Texas**. Washington: U.S. Soil Conservation Service;
- [Menke, W. \(1984\). **Geophysical data analysis: Discrete inverse theory**. Orlando: Academic Press.](#)
- Mishra, U., & Verma, L. (2013). Denoising of ECG signal using thresholding techniques with comparison of different types of wavelet. **International Journal of Electronics and Computer Science Engineering**. ISSN 2277-1956/V2N2-1143-1148;

Formatted: References list

Deleted: ¶

Page Break

Formatted: Font color: Auto, Pattern: Clear

Formatted: References list

Deleted: ¶

- Morrison, H. F., Shoham, Y., Hoversten, G. M., & Torres-Verdin, C. (1996). Electromagnetic mapping of electrical conductivity beneath the Columbia basalts. **Geophysical Prospecting**, 44(6). 963-986;
- Mussett, A. E. & Khan, M. A. (2000). **Looking into the Earth: An Introduction to Geological Geophysics**. Cambridge: Cambridge University Press;
- Naidu, G. D. (2012). **Deep crustal structure of the Son-Narmada-Tapti Lineament, central India**. Berlin: Springer;
- Nettleton, L. L. (1947). Geophysical history of typical Mississippi Piedmont salt-domes. **Geophysics**, 12(1). 30–42;
- Newman, G. A. (1989). Deep transient electromagnetic soundings with a grounded source over near-surface conductors. **Geophysical Journal International**, 98(3). 587-601;
- Paembonan, A. Y., Arjwech, R., Davydycheva, S., Smirnov, M., & Strack, K. M. (2017). An application of LOTEM around salt dome near Houston, Texas. **AIP Conference Proceedings** 186;
- Petersen, U., Andersen, M. & White, R. (2006). Seismic imaging of basalts at Glyvursnes, Faroe Islands: hunting for future exploration methods in basalt covered areas. **First Break**, 24(1093);
- Peterst, J. W., & Dugan, A. F. (1945). Gravity and Magnetic Investigations at The Grand Saline Salt Dome, Van Zandt CO., Texas. **Geophysics**. 376–393;
- [Poularikas, A. D. \(1999\). **The handbook of formulas and tables for signal processing**. Boca Raton \(Florida\): CRC Press.;](#)
- [Raiche, A. P., Jupp, D. L., Rutter, H., & Vozoff, K. \(1985\). **The joint use of coincident loop transient electromagnetic and Schlumberger sounding to resolve layered structures**. **Geophysics**, 50\(10\);](#)
- Ruckemann, C. P., (2012), Comparison of stacking methods regarding processing and computing of geoscientific depth data. **Geoprocessing 2012: The Fourth International Conference on Advanced Geographic Information Systems, Applications and Services**. 35–40;
- [Saribudak, M. \(2011\). **Geophysical mapping of the Hockley growth fault in northwest Houston, USA, and recent surface observations**. **The Leading Edge**, 30\(2\). 172-180;](#)

Formatted: Font color: Auto, Pattern: Clear

Formatted: References list

Formatted: Font color: Auto, Pattern: Clear

Deleted: ¶

Moved (insertion) [4]

Shafiq, M. A., Alshawi, T., Long, Z., & AlRegib, G. (2016). SalSi: A new seismic attribute for salt dome detection. **2016 IEEE International Conference on Acoustics, Speech and Signal Processing (ICASSP)**;

Shah, J., Fainstein, R., J. Broetz, R., & Wygrala, B. (2009). Hydrocarbons in Sub-Basalt Sediments – Basin Modeling of Kerala-Konkan Basin, Offshore West India. **71st EAGE Conference and Exhibition incorporating SPE EUROPEC 2009**;

Sheriff, R. E., (2002). **Encyclopedic dictionary of applied geophysics**. Tulsa, Oklahoma; Society of Exploration Geophysicists;

Siever, K., & Elsen, R. (2010). Salt dome exploration by directional borehole radar wireline service. **Proceedings of the XIII International Conference on Ground Penetrating Radar**;

Smith, S. W. (1997). **The scientist and engineer's guide to digital signal processing**. San Diego, California: California Technical Publishing;

Starich, P. J., Lewis, G. G., Faulkner, J., Standley, P. G., & Setterquist, S. (1994). **Integrated geophysical study of an onshore salt dome. *The Leading Edge*, (8), 880–884;**

Stewart, R. D., & Unterberger, R. R. (1976). **Seeing through rock-salt with radar. *Geophysics*, 41(1), 123–132;**

Strack, K.M., and Aziz, A.A. (2012). Full Field Array Electromagnetics: Advanced EM from the surface to the borehole, exploration to reservoir monitoring, in Lane, R. (Editor), **Natural Fields EM Forum 2012, Geoscience Australia Record 2012/04**, 176-198. Canberra: Geoscience Australia;

Strack, K., & Pandey, P. B. (2007). Exploration with controlled-source electromagnetics under basalt cover in India. **The Leading Edge**, 26(3), 360-363;

Strack, K. M. (1992). **Exploration with deep transient electromagnetics**. Amsterdam: Elsevier;

Strack, K. M., Seara, J. L., Vozoff, K., & Woflgram, P. A. (1990). LOTEM case histories in frontier areas of hydrocarbon exploration in Asia. **SEG Technical Program Expanded Abstracts 1990**. 495-497;

Deleted: Scholl, C. (2005). **The influence of multidimensional structures on the interpretation of LOTEM data with one-dimensional models and the application to data from Israel**. Ph.D. thesis, Faculty of Mathematics and Natural Sciences, University of Cologne;

Formatted: Font: Bold, Not Italic, Font color: Auto, Complex Script Font: Bold, Not Italic, Pattern: Clear (White)

Deleted: Sheriff, R. E. (2006). **Encyclopedic dictionary of applied geophysics**. Tulsa, OK: Society of Exploration Geophysicists

Formatted: Font color: Auto, Pattern: Clear (White)

Formatted: Pattern: Clear (White)

Moved up [4]: Saribudak, M. (2011). Geophysical mapping of the Hockley growth fault in northwest Houston, USA, and recent surface observations. **The Leading Edge**,30(2). 172-180;

Moved (insertion) [1]

Deleted: ¶

- Strack, K. M., Hanstein, T., Newman, G. A., & Wolfgram, P. A. (1989). **Basic theory and data processing principles: LOTEM training program. Vol. 1.** Germany: University of Cologne;
- Strack, K.-M., LeBrocq, K., Moss, D.C., Petry, H., Vozoff, K., & Wolfgram, P.A. (1988) Resolving resistive layers with LOTEM in hydrocarbon exploration: case histories: paper 4-23, **50th Annual Meeting, European Association for Exploration Geophysicists**, The Hague;
- Thede, L. (2004). **Practical analog and digital filter design.** Boston: Artech House, Inc.;
- Tikhonov, A. N., (1950), Determination of the electrical characteristics of the deep strata of the earth's crust. **Doklady Akademia Nauk**, 73. 295–297;
- Vozoff, K., 1990, Magnetotellurics: Principles and practice: **Proc. Indian Acad. Soc.**, 99, 441-471
- Vozoff, K., 1972, The magnetotelluric method in the exploration of sedimentary basins: **Geophysics**, 37, 98-141
- Weiss, J.S. (1992). Geohydrologic units of the coastal lowlands aquifer system, south-central United States. Washington: U.S. Geological Survey Professional Paper 1416-C;
- Whitmore, N. D., & Lines, L. R. (1986). Vertical seismic profiling depth migration of a salt dome flank. **Geophysics**, 51(5);
- Wilson, G., Donderici, B., & Fouda, A. (2015). **World Intellectual Property Organization** No. WO 2015160347 A1. TX, U.S: World Intellectual Property Organization International Bureau
- Yan, L, Chen, X., Xie, X.,2, Zhou, L., Wang, Z., & Hu, W. (2017). **Continuous TDEM monitoring for shale gas fracturing.** Paper presented in The 13th China International Geo-Electromagnetic Workshop 2017. Wuhan: Chinese Geophysical Society Geo-Electromagnetic Professional Committee;
- Yan, L., Su, Z., Hu, J., & Hu, W. (1997). Field trials of LOTEM in a very rugged area. **The Leading Edge**, 16(4), 379-380;
- Zerilli A., Bühnenmann, J., Henke, C.H., Krieger, M.H., Müller, C., & Strack, K.M. (2002). A novel integrated approach to subsalt imaging. **72nd SEG meeting**, Salt Lake City.

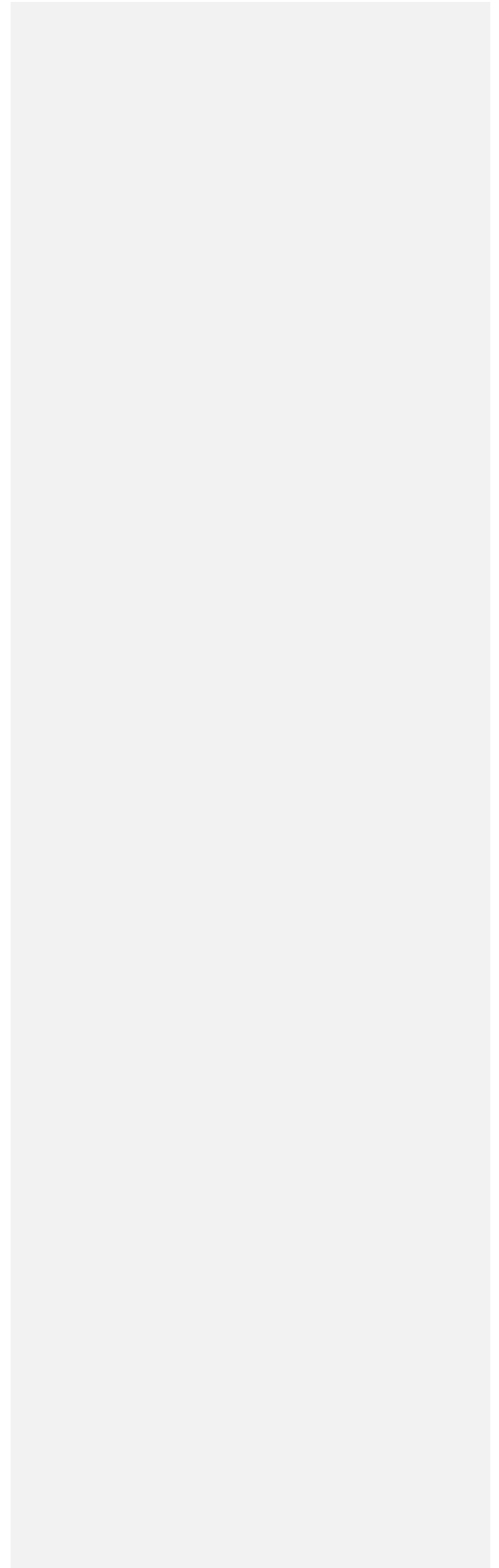
Moved up [1]: Starich, P. J., Lewis, G. G., Faulkner, J., Standley, P. G., & Setterquist, S. (1994). Integrated geophysical study of an onshore salt dome. **The Leading Edge**, (8). 880–884;†

Stewart, R. D., & Unterberger, R. R. (1976). Seeing through rock-salt with radar. **Geophysics**, 41(1). 123–132;†

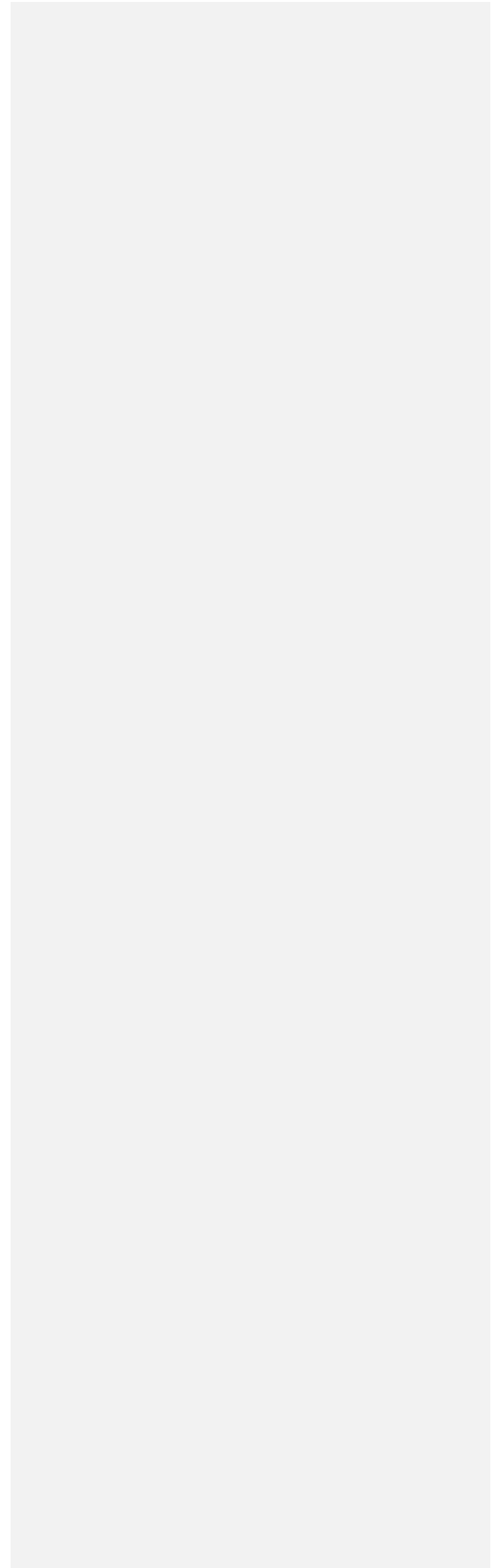
Deleted: 2005

Deleted: †

APPENDICES



APPENDIX A
Software Workflow Diagrams and Data Output



In this appendix, all flow diagrams of the processing software and output file are displayed. The processing consists of data quality assurance using KMSProQA, data merge with KMSProDM, and the quality control under KMSProQC. Following flow diagram of each step is provided.

A.1 Flow diagram of KMSProQA

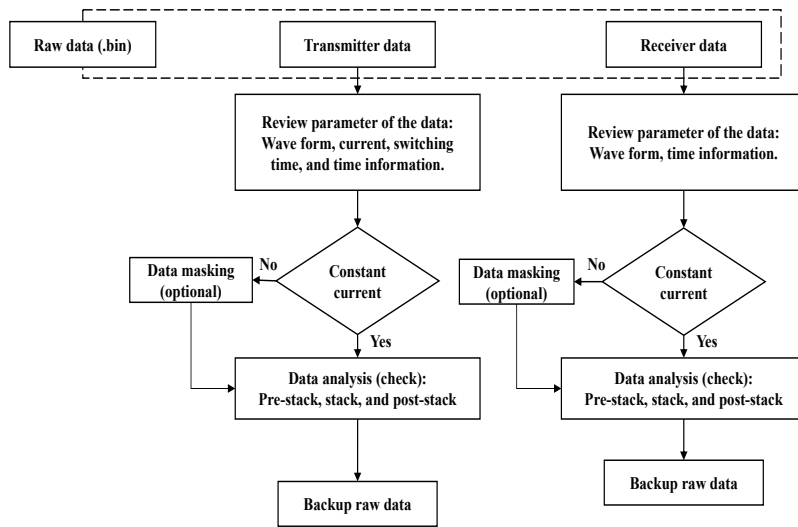


Figure A. 1 Flow of Quality Assurance (QA) for both receiver and transmitter data.

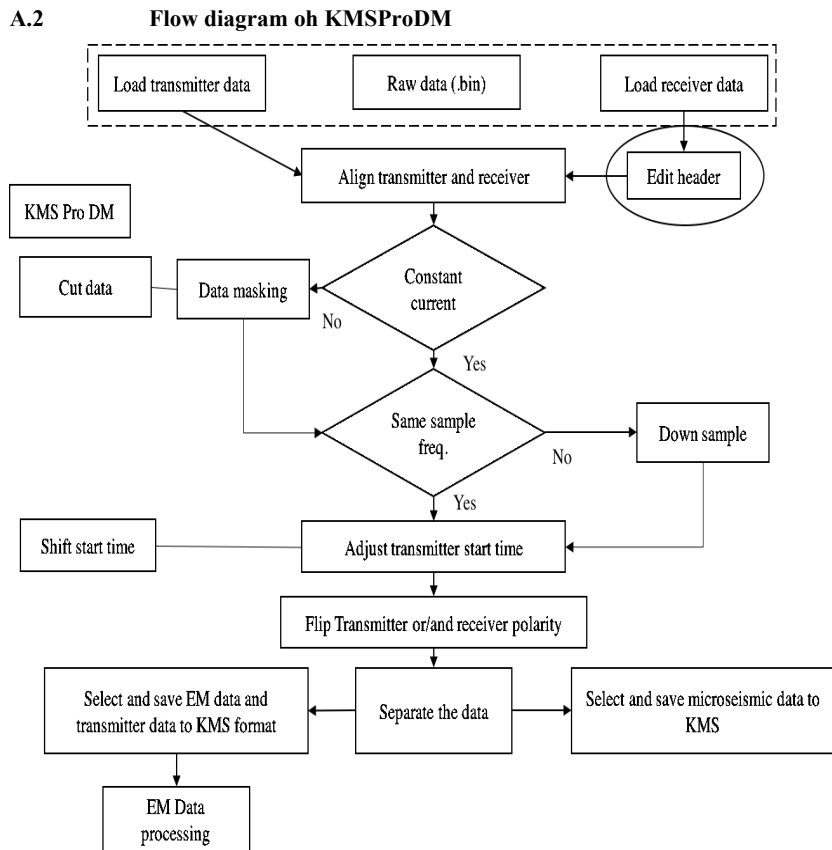


Figure A. 2 Flow diagram of data merge, including all additional procedure until the data ready to be processed.

A.3 KMS PRO QC

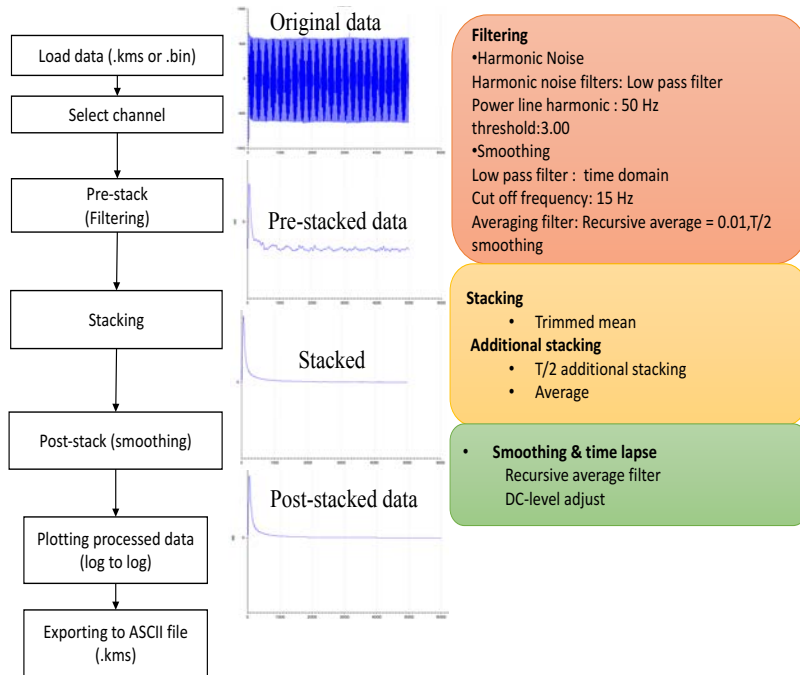


Figure A. 3 Flow diagram of data processing using KMS Pro QC. Including an example and details for each step.

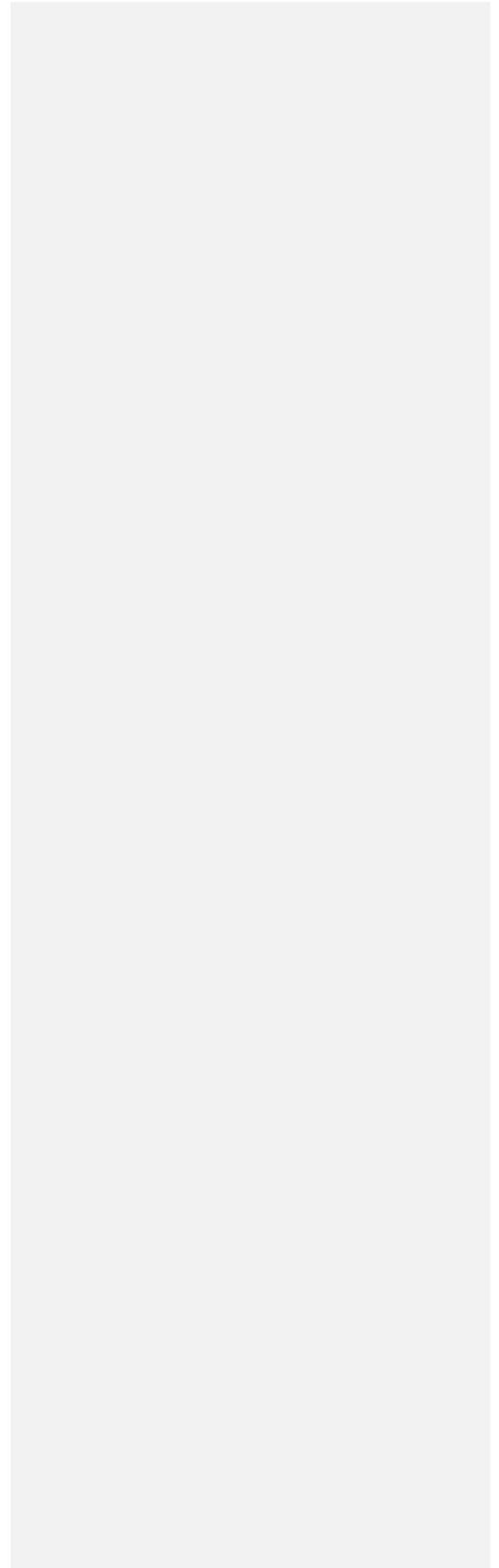
```

//time, ms  tr1 err tr1 .....
0  0.00000E+00 0.0
1  3.37835E-02 0.0
2  1.53289E-01 0.0
3  2.53829E-01 0.0
4  3.44160E-01 0.0
5  4.19508E-01 0.0
6  4.72385E-01 0.0
7  5.22115E-01 0.0
8  5.60683E-01 0.0
9  5.89696E-01 0.0
10 6.04334E-01 0.0
11 6.20475E-01 0.0
12 6.31504E-01 0.0
13 6.35017E-01 0.0
14 6.40540E-01 0.0
15 6.44097E-01 0.0
16 6.45853E-01 0.0
17 6.48638E-01 0.0
18 6.51186E-01 0.0
19 6.53911E-01 0.0
20 6.58872E-01 0.0
21 6.62978E-01 0.0
22 6.67710E-01 0.0
23 6.75074E-01 0.0
24 6.80997E-01 0.0
25 6.87488E-01 0.0
26 6.95379E-01 0.0
27 7.02218E-01 0.0
28 7.09316E-01 0.0
29 7.16591E-01 0.0
30 7.23626E-01 0.0
31 7.30730E-01 0.0
32 7.37844E-01 0.0
33 7.44149E-01 0.0
34 7.51096E-01 0.0
35 7.57980E-01 0.0
36 7.63914E-01 0.0
37 7.70528E-01 0.0
38 7.76952E-01 0.0
39 7.83120E-01 0.0
40 7.88161E-01 0.0
... ..
3999 1.01848E+00 0.0

```

Figure A. 4 Output ASCII data from KMSProQC showing time in millisecond and Voltage in millivolt.

APPENDIX B
Processing Description



As the main part in this research, the order of data processing is described, starting with data quality assurance using KMSProQA to verify the data integrity, and ensured all the measured data for the further processing. In KMSProDM the data are merged with transmitter records and the microseismic data is separated. Using a new processing system with the new software KMSPro family, the processing is performed. Finally, the data normalization following by 1D inversion are performed to get the Earth model. The quality assurance (QA) is reviewed in B.1. followed by data merge in B.2. and B.3 for quality assurance. Furthermore, the data normalizations are explained in B.4. followed by inversion and interpretation B.5.

B.1 Quality Assurance (QA)

Before data processing, we must review all the data, called quality assurance, to avoid the time-consuming problems in processing caused by operational data integrity issues. First, we review quality of all raw data from the field, both transmitter and receiver data and observer records, with KMSProQA where each data must be in accordance of the set standard. We sort the data by quality for further processing.

Several criteria to review the quality of transmitter data are:

- i. Wave form, 50% and 100% duty-cycle waveform,
- ii. Switching time, e.g. 4, 8 second,
- iii. Current, most of data uses 70A,
- iv. Time information, start time, end time, and duration
- v. Transmitter geographic direction

Several criteria to review the quality of receiver data are:

- i. Wave form, 50% and 100% duty-cycle waveform
- ii. Time information, start time, end time, and duration

The data are reviewed using KMSProQA by the following steps:

B.1.1 The file data (neither receiver or transmitter data) is loaded as displayed in Figure B.1. In addition, we can select the number of the channels to be plotted.

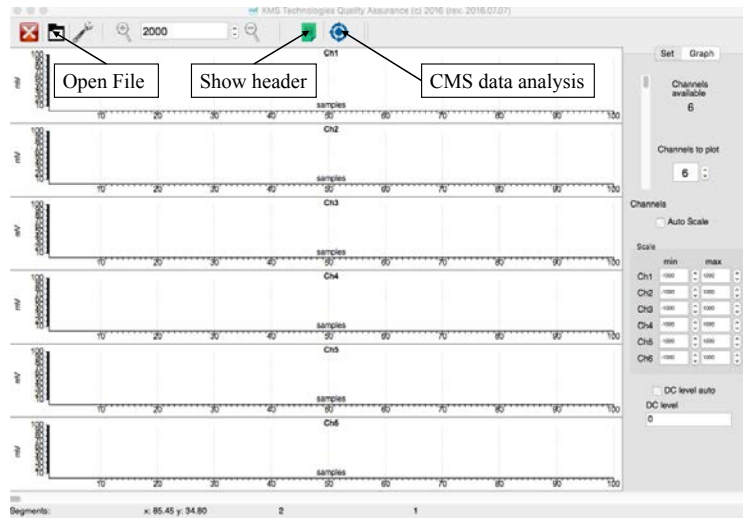


Figure B. 1 The main window of KMSProQA, showing the signal for each sensor showing the signal for each sensor, magnetic and electric signal as well as microseismic signal.

B.1.2 The icon header is showed in the Figure B.1, containing all the information of the data such as date and time, coordinate information, sampling frequency etc.

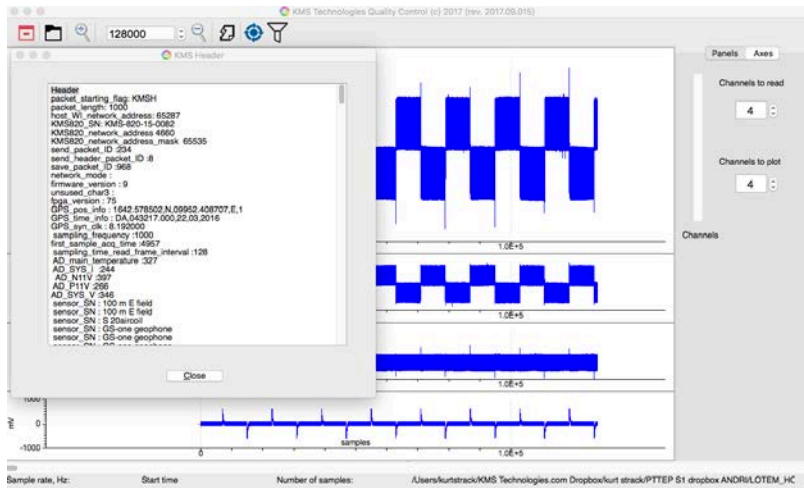


Figure B.2 The header showing all information of the data.

B.1.3 Data analysis is used to simulate the processing for each channel. The following figures show the processing in order, start from filtering the noise (Figure B.3), stacking (Figure B.5), and smoothing (Figure B.6). All the processing in details, including the filter, staking method and recursive average filter for smoothing data, will be explained in the next stage.

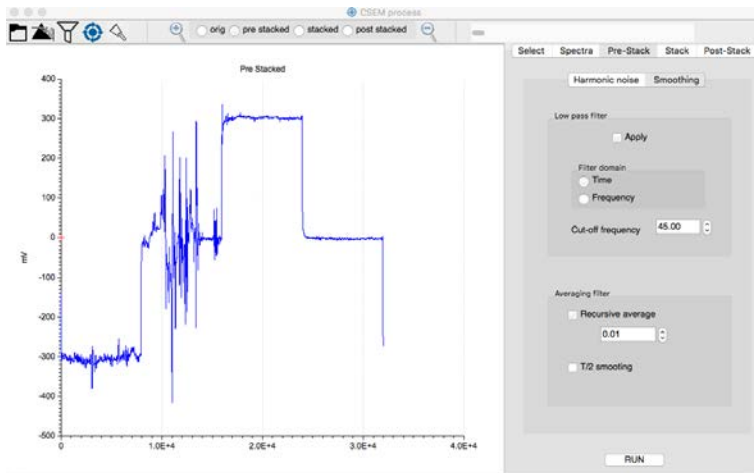


Figure B.3 Example of filtered data of electric field still including noise. On the right-side filtering method selection menu.

B.1.4 Using Fast Fourier Transform (FFT), the signals frequency of the data is displayed (Figure B.4).

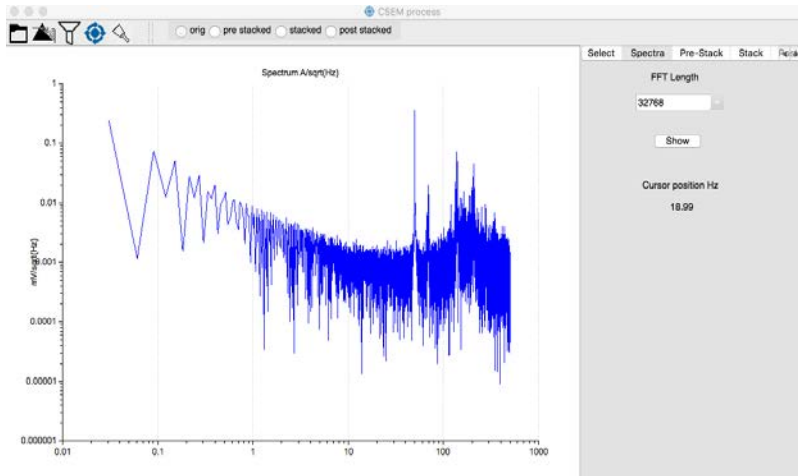


Figure B. 4 The spectrum of the signal frequencies is displayed after Fast Fourier Transform (FFT).

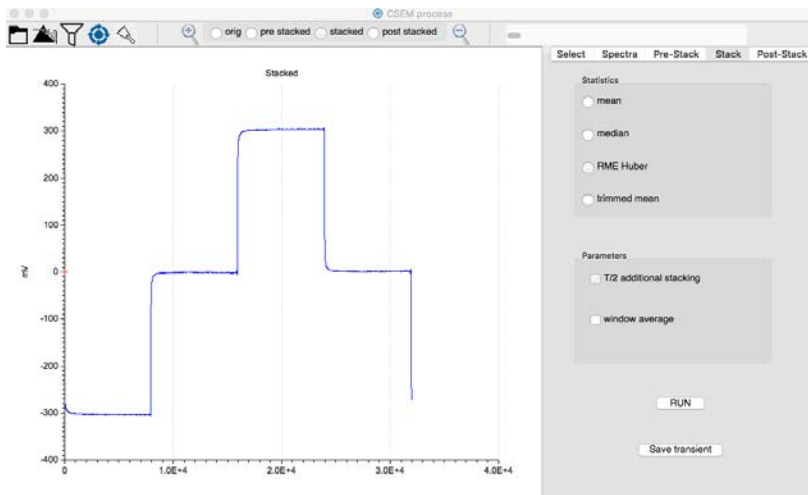


Figure B. 5 The curve showing the signal after staking, the remaining noise from filtering is reduced.

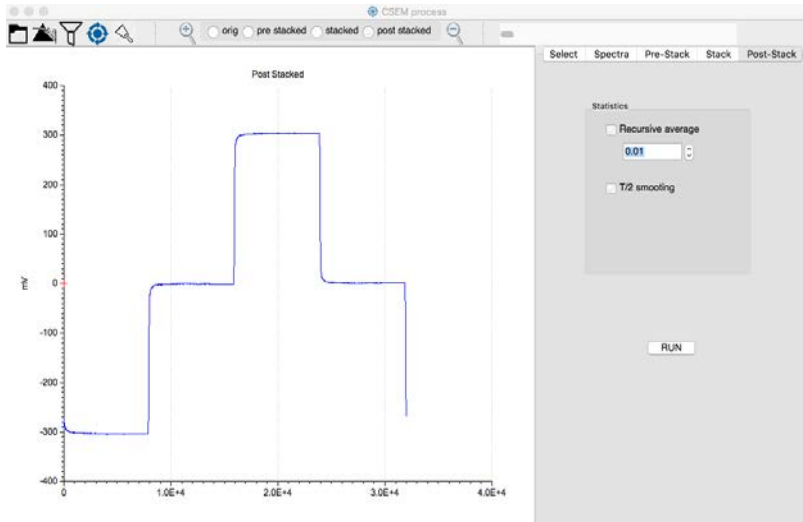


Figure B. 6 The application of recursive average filter to produce smooth signal. The different value of the filter applied to get the smoothest data.

B.1.5 Table B.1 to B.3 are the reviews of transmitter and receiver data compared to the field operator notes using the information from the data' header. This is necessary to ensure that the data used is correct.

Table B. 1 An example of transmitter data review including current, configuration, time compared with the field note.

Transmitter file name	Start time from header	File time	Configuration	Wave form	switching time	current
data_S1000Hz_15	21:32:56	10:05	inline	100%	4	10
data_S1000Hz_16	22:16:48	10:50	inline	100%	4	10

Table B. 2 Review of receiver data from 1st day (1st May 2015), consisting of time information, and kind of sensors.

File name	Start time from header	File time	Remarks
t01a 1204 1kHz 1	22:01:12	5:25	Electric Field only
KMS-820-15-0087_1 Rx0c	21:44:45	9:59	Electric Field only
t01a 1208 1	22:18:56	10:19	Electric Field only
t01a 1208 2	22:20:05	10:21	Electric Field only
t01a 1208 3	22:21:47	10:27	Electric Field only
t01a 1208 4	22:28:55	10:31	Electric Field only
t01a 1208 01 1	22:32:02	10:33	Electric Field only
t01a 1208 01 2	22:34:20	10:49	Electric Field only

Table B. 3 Location of the transmitter electrodes and receiver units.

Name	Label	Actual location					Elevation [m]
		Easting [m]	Northing [m]	UTM zone	Latitude	Longitude	
North Tx electrode	Tx north	227149	3318368	15 R	29.965870	-95.827458	53
South Tx electrode	Tx south	227151	3318027	15 R	29.962798	-95.827350	52
West Tx electrode	Tx west	226747	3318027	15 R	29.962709	-95.831534	53
Near-offset receiver	Rx0a	227149	3317987	15 R	29.962433	-95.827360	53
Middle-offset receiver	Rx0b	227161	3317766	15 R	29.960448	-95.827183	51
Inter Tx electrode receiver	Rx0c	227153	3318109	15 R	29.963699	-95.827350	52
1st receiver	Rx1	227141	3317127	15 R	29.954687	-95.827225	50
2nd receiver	Rx2	227142	3316929	15 R	29.952898	-95.827162	50
3rd receiver	Rx3	227146	3316720	15 R	29.951014	-95.827069	50

B.2 Data merge with KMSProDM

The second section of data processing is the data merge. An example is shown in Figure B. 7. This step includes editing the header of receiver data, merging the transmitter and the receiver data, saving both transmitter and receiver data together in KMS file format. If the data contain microseismic data, they are separated by saving microseismic data to SEG Y or KMS file format. In order to merge the data, several analyses must be included due to the time, current, and sample frequency issue. Time shift is added to fix the time issue, while the resample frequency handle the data that have different sample frequency and data cutting if the transmitter has different current during data measurement. The flip polarity is applied to flip the direction of the either transmitter or receiver polarity.

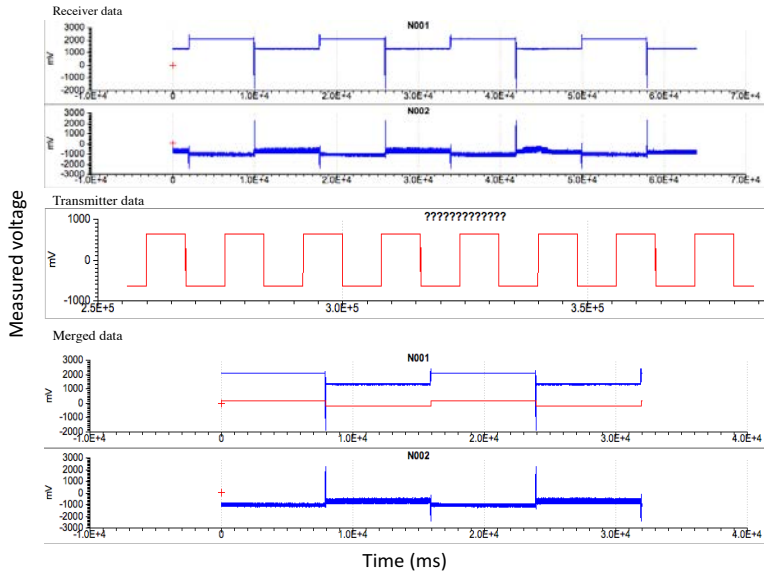


Figure B.7 Example of data merge. showing receiver data on the top, transmitter data in the middle, and the data after merged (below).

If the time and sample issue does not exist in the data, we can merge the transmitter and receiver data by using menu align only, as show in the figure below:

B.2.1 Flip polarity

In data merge, the transmitter and receiver are required in the same start time and for this case either transmitter signal or receiver signal must be flipped. This can ease to determine the start time matching of transmitter and receiver signal (Figure B.8).

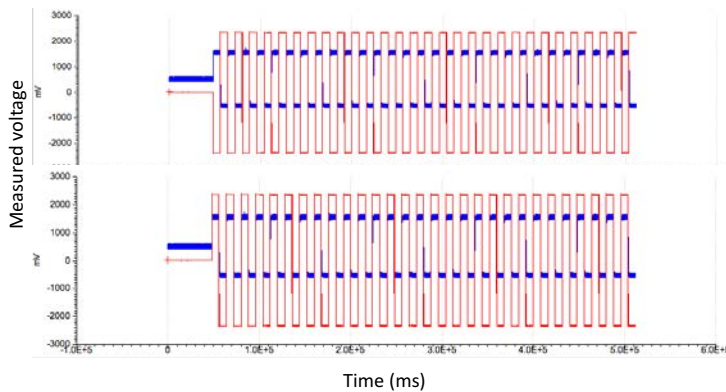


Figure B. 8 The example of data using flip polarity, above showing the data before flipping, below showing the data after flipping.

B.2.1 Data separation (cutting)

During data measurement, sometimes the transmitter has different current because of the hardware issue. This can change the amplitude in receiver signal as shown in the following Figure B9. The data recorded four different currents: 30, 40, 50 and 60 A and this need to be separate. KMSProDM has an option to cut the data direct from the displayed curve.

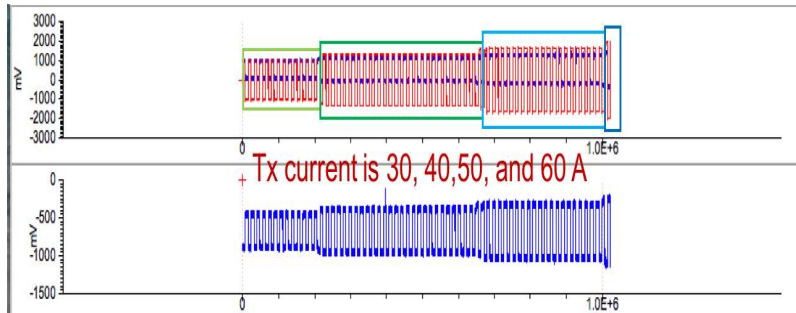


Figure B. 9 The response of four different amplitudes due to current change from 30 A to 60 A.

Other issue in data acquisition is when the transmitter data is turned off while receiver still record the data. Hence, the data with unnecessary signal must be removed. It also is done by menu cut in the KMSProDM. An example is displayed in the Figure B.10.

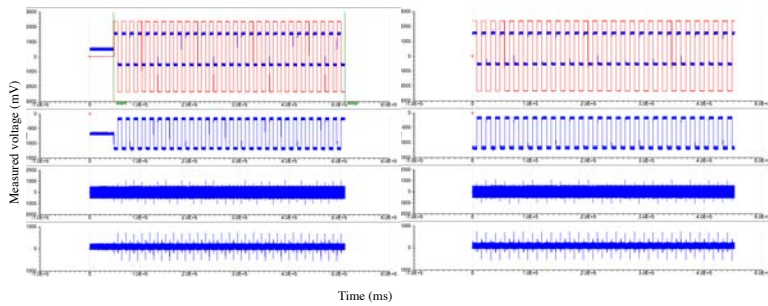


Figure B.10 Removing unnecessary signal from the data. The merged data containing unnecessary signal (left) have to be removed obtain the required signal.

B.2.3 Resampling frequency

The measured data at Hockley salt dome include several sample frequencies. Before we merge the transmitter and receiver data, we must resample frequencies either transmitter or receiver data. In our data, we only resample the transmitter data. In the Figure B.11, sample frequency of transmitter is 40 kHz, and receiver sample frequency is 1 kHz. This can be easily done by calculating the differences factor; sample frequency of transmitter data is divided by sample frequency of receiver data.

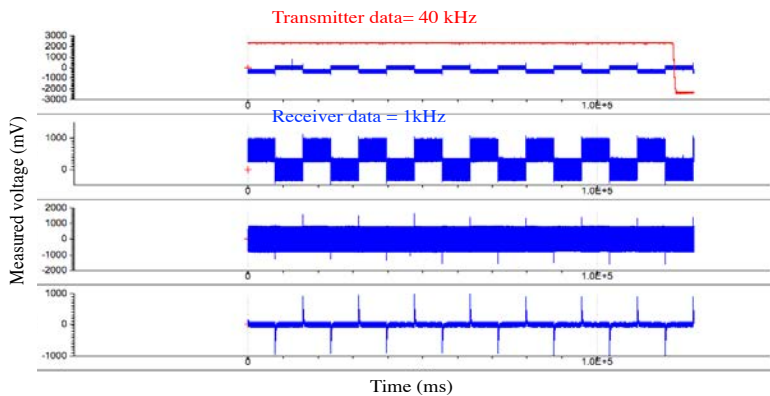


Figure B.11 Receiver and transmitter data with different sample frequency. The blue curve is the receiver signal with sample frequency of 1 kHz, and the red curve is the transmitter signal with sample frequency of 40 kHz.

B.2.4 Time shift

Due to errors in GPS, the different time stamps between receiver and transmitter signal may be occurred, and it needs to be shifted. Using time shift method (Figure B.12), the value of the time shift between transmitter and receiver signal is determined and adjusted in the same onset. The example of time shift result is shown in the following Table B.4.

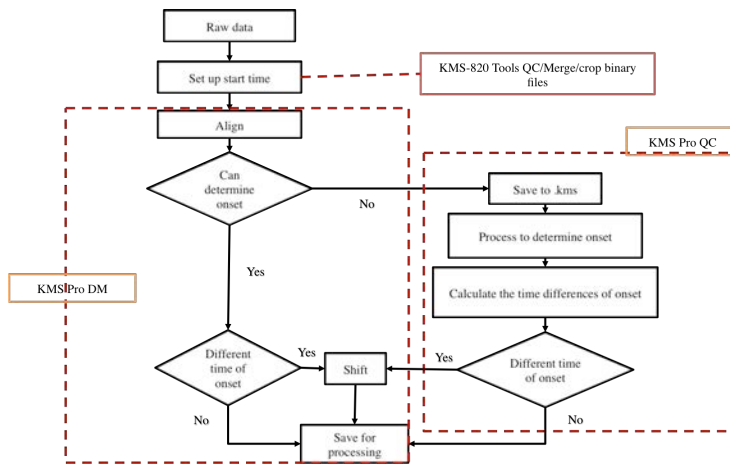


Figure B.12 The flow diagram showing how to obtain the time shift between transmitter and receiver.

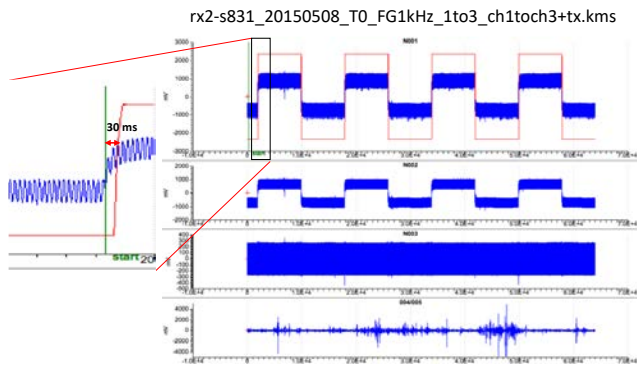


Figure B.13 An example of the time shift. Showing the difference start time of the transmitter and receiver

Table B. 4 Time shift from data measurement on 5th May 2015, with sample frequency 1 kHz, switching time 8 s, wave form 100% duty circle (processed data).

Station	Tx onset (ms)	Rx onset (ms)	Time shift (ms)	Start time	End time	Remarks
Rx1a	8009	8023	14	17:39:00	17:48:00	Tx 40 kHz
Rx1b				19:39:00	19:32:00	Tx 40 kHz
Rx2	10009	10005	-4	19:39:00	19:32:00	Tx 40 kHz
Rx3	8009	8053	44	17:39:00	17:48:00	Tx 40 kHz

B.2.5 Archive the data

The final step in data merge is to archive the EM data for data quality control. If data include the microseismic, it must be saved separately to the SEGY format. The following procedure is to save both EM and microseismic.

The EM data include electric field (generally in channel 1 and 2), magnetic field (channel 3), and transmitter data (channel 7), if consisting two (2) sensor of magnetic field (magnetic coil and loop) and then the transmitter should be in the channel 8. The data must be selected in order to separate the EM data from microseismic data. The data is converted to the kms format (**.kms**) for receiver transmitter data, while the header file is automatically saved in **.inf** format in the same folder. The geophone data must be selected carefully, usually in channel 4,5,6 or 5,6, and 7 and saved them to SEGY or KMS format.

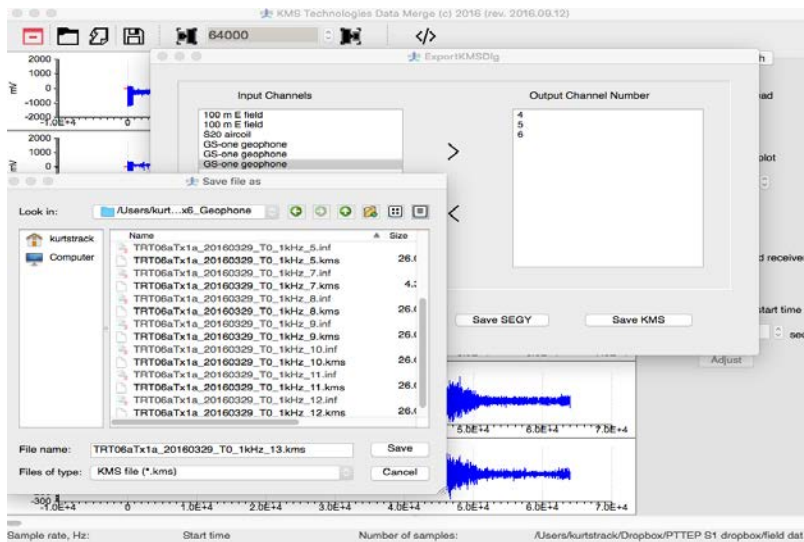


Figure B. 14 An example to export (save) the data. First, selecting the channel of either EM or microseismic and save them in KMS format for EM and SGY or KMS for microseismic.

B.3 Data Quality Control Using KMSProQC

Because most of the electromagnetic noise is much bigger than the signals, the recorded time series must be processed before inversion. The quality control processing consists of pre-stacking, stacking, and post-stacking, using KMSProQC software. This is the same procedure of using KMSProQA. The only difference is; KMSProQC allow to save the processed data, while the menu to save the data in KMSProQA is not available. This processing includes following certain steps:

1. Each time series is filtered separately to reduce periodic noise, mostly from the power line
2. To reduce aperiodic noise, all time series are selectively stacked
3. The stacked data is smoothed with recursive average filter
4. The data is saved to ASCII file for inversion.

The following is the detail of Data Quality Control processing:

B.3.1 Filtering (Pre-stack)

In this step, several filters such as first differences filter, lock in filter, time domain notch filter, frequency notch filter, and low pass filter, is applied to reduce the noise. For the power line harmonics noise can be selected 50 Hz or 60 Hz depending on where the data is measured (USA using 50Hz). The threshold is an addition option to detect the noise automatically depend on their magnitude for each the center frequency and their width (usually 10 Hz).

The Low pass filter, either time or frequency domain, includes the cut-off frequency and the order N (in this data we use 5th order). The recursive average filter and T/2 smoothing can be included. The example of two different filtering is shown in the Figure B.14.

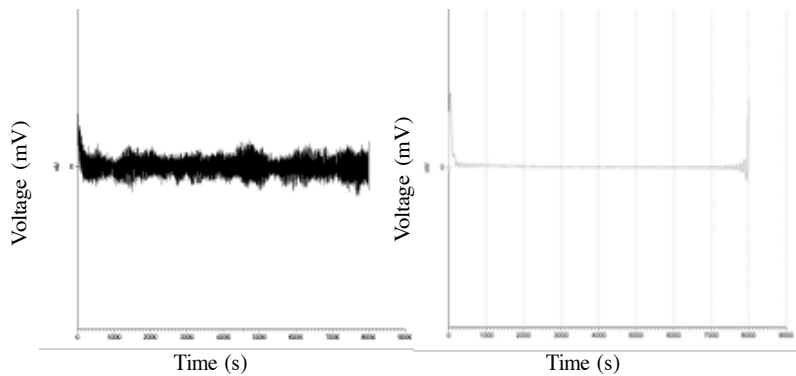


Figure B. 15 The comparison of two different filters. In the left showing time domain notch filter result and low pass filter application in the right.

B.3.2 Stacking

The main purpose of using stacking statistic is to compensate the unrecognized sporadic noise that could not be eliminated using filter (Figure B.15). Five (5) different statistic method including mean, median, RME Hampel, trimmed mean, and selective stacking, can be applied. T/2 additional stacking, and window average are the optional. The T/2 additional stacking is usually used for 50% duty circle wave form.

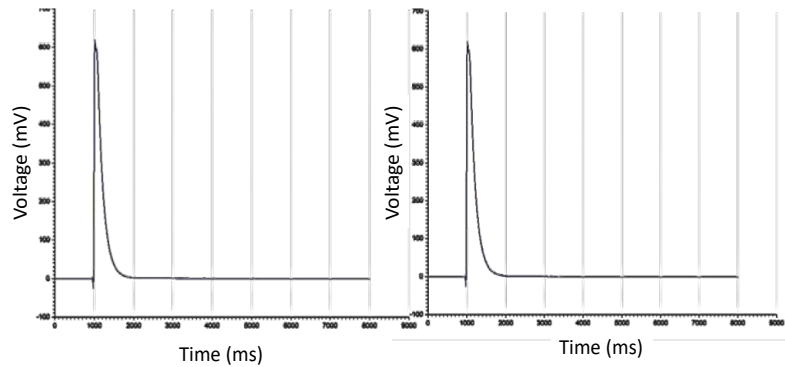


Figure B.16 Two different statistic methods, mean (left) and trimmed mean (right) stacking to compensate the unrecognized sporadic noise that could not be eliminated by filter.

B.3.3 Smoothing (Post-stack)

The last processing is to smooth the data after stacking, so called post-stack. In this research, the value from 0.1 to 0.8 are used, depending on the result from stacking, if the stacked data is smooth enough, the value of 0.1 is usually used, but if the data still contain the noise, higher number is required. The example of recursive average filter application is displayed in Figure B.16.

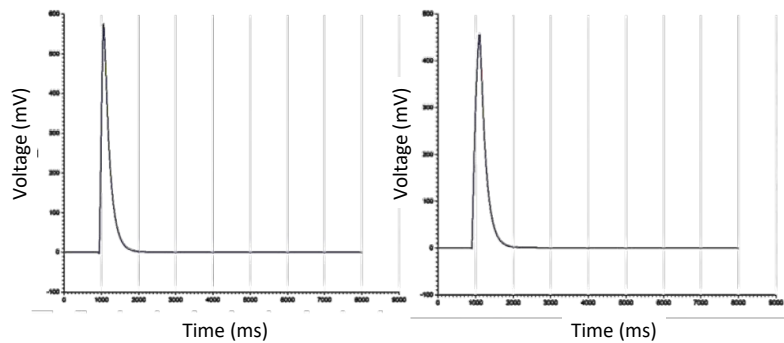


Figure B.17 The data after smoothing with 0.6 of recursive average filter.

B.4 Normalization or apparent resistivity calculation

After the processing, now the data are converted to the ASCII file. This allow us to copy the data to MS. Excel to be normalized or calculated late and early time resistivity for inversion. As input for the EMUPLUS, data are normalized by transmitter and receiver moment; for electric field (Figure B.5), the data are normalized by transmitter current and transmitter length, and electrode space (V/Am^2), for magnetic field using transmitter current and transmitter length, and receiver area (V/Am^3). It not required to distinguish between ET and LT for normalization. For the magnetic field, it is possible to use either normalized data or apparent resistivity conversion.

Table B. 5 The example of the E-filed data after normalization.

Point	Time (s)	Normalized E-field ((V/Am ²))	% STD
1	5.0000E-03	2.9965E-10	4.4184E-21
2	1.0000E-02	4.3167E-10	2.0786E-21
3	1.5000E-02	4.6007E-10	1.6892E-21
4	2.0000E-02	4.7062E-10	1.5548E-21
5	2.5000E-02	4.9106E-10	1.3103E-21
6	3.0000E-02	5.1688E-10	1.0314E-21
7	3.5000E-02	5.4141E-10	7.9720E-22
8	4.0000E-02	5.6297E-10	6.1630E-22
10	5.0000E-02	5.9590E-10	3.8483E-22
12	6.0000E-02	6.2038E-10	2.4793E-22
14	7.0000E-02	6.3893E-10	1.6418E-22
17	8.5000E-02	6.5917E-10	9.2383E-23
20	1.0000E-01	6.7298E-10	5.5165E-23
24	1.2000E-01	6.8592E-10	2.8944E-23
29	1.4500E-01	6.9637E-10	1.3898E-23
35	1.7500E-01	7.0417E-10	6.2242E-24
42	2.1000E-01	7.1012E-10	2.4136E-24
50	2.5000E-01	7.1419E-10	8.2895E-25
60	3.0000E-01	7.1741E-10	1.6070E-25
72	3.6000E-01	7.1958E-10	3.3012E-27
86	4.3000E-01	7.2107E-10	3.1914E-26
103	5.1500E-01	7.2229E-10	1.3741E-25
124	6.2000E-01	7.2311E-10	2.5173E-25
149	7.4500E-01	7.2376E-10	3.6409E-25
179	8.9500E-01	7.2425E-10	4.6423E-25
215	1.0750E+00	7.2467E-10	5.5950E-25
258	1.2900E+00	7.2500E-10	6.3994E-25
310	1.5500E+00	7.2535E-10	7.3156E-25
372	1.8600E+00	7.2565E-10	8.1498E-25
446	2.2300E+00	7.2594E-10	8.9860E-25
535	2.6750E+00	7.2616E-10	9.6622E-25
642	3.2100E+00	7.2446E-10	5.1156E-25
770	3.8500E+00	7.2699E-10	1.2410E-24

The next procedure is to input the data in the input file of EMUPLUS including header such as offset, date and time information, coordinate of transmitter and receiver, etc.

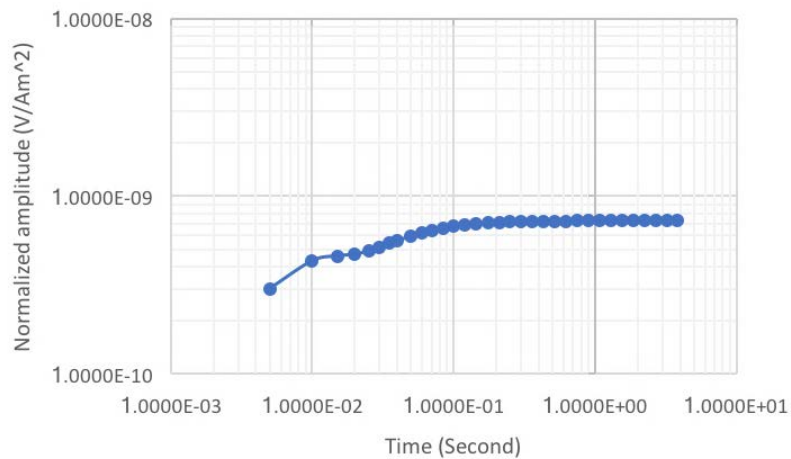


Figure B. 18 An example graph of the E-field data after normalization.

B.5 Inversion and interpretation

The last procedure to obtain the result is to invert the data to the Earth model. Using EMUPLUS, both electric and magnetic field are inverted. First, the normalized data must be load, and before inverting the data, the parameter must be set, and ensure the information is corrected. The stating model uses the homogenous half-space to yield the 1D model of Occam's inversion. The result of data fitting is shown in Figure B.18, and B.19 for the Earth model.

The result from the Occam' inversion is further analysis using cumulative conductance and transverse resistance to generate the starting model for Marquardt inversion (layered model). Before running the layered model, the parameters must be set and a seven to eighth-layer starting model for all the data is performed.

The final step is to interpret the model comparing to the previous study and other result. In this research,]the resolution from the eigenparameter or V matrix is analyzed to see the resolved layer and the importance of parameter for every layer. To compare the result (model) and for better understand of the geology, the 1D models are converted to 3D visualization by interpolating the models. Finally, all the result is compare with the previous study and geologic information.

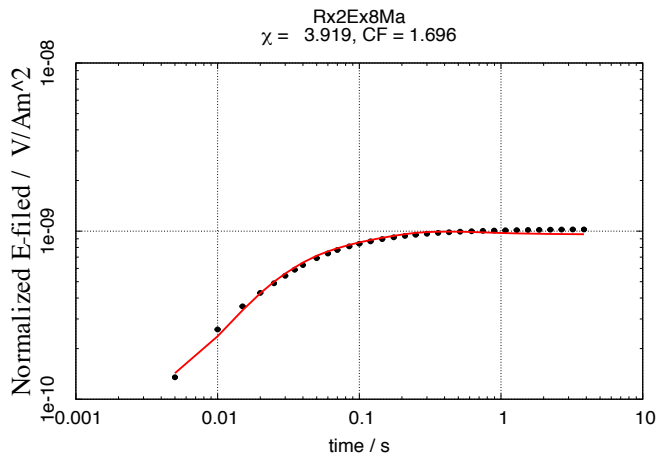


Figure B. 19 Inversion data fits corresponding. The curve showing the measured data (black dot), and calculated data (red line).

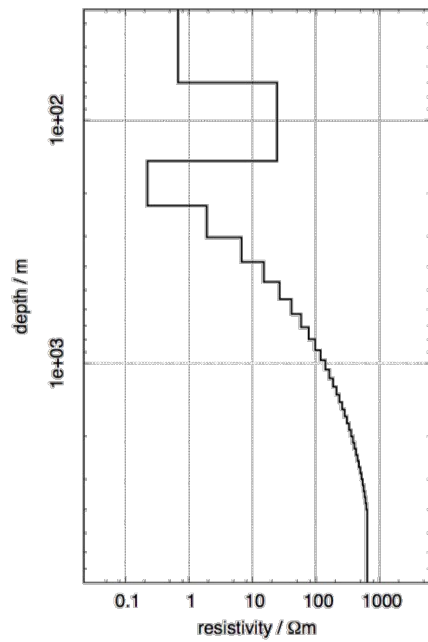
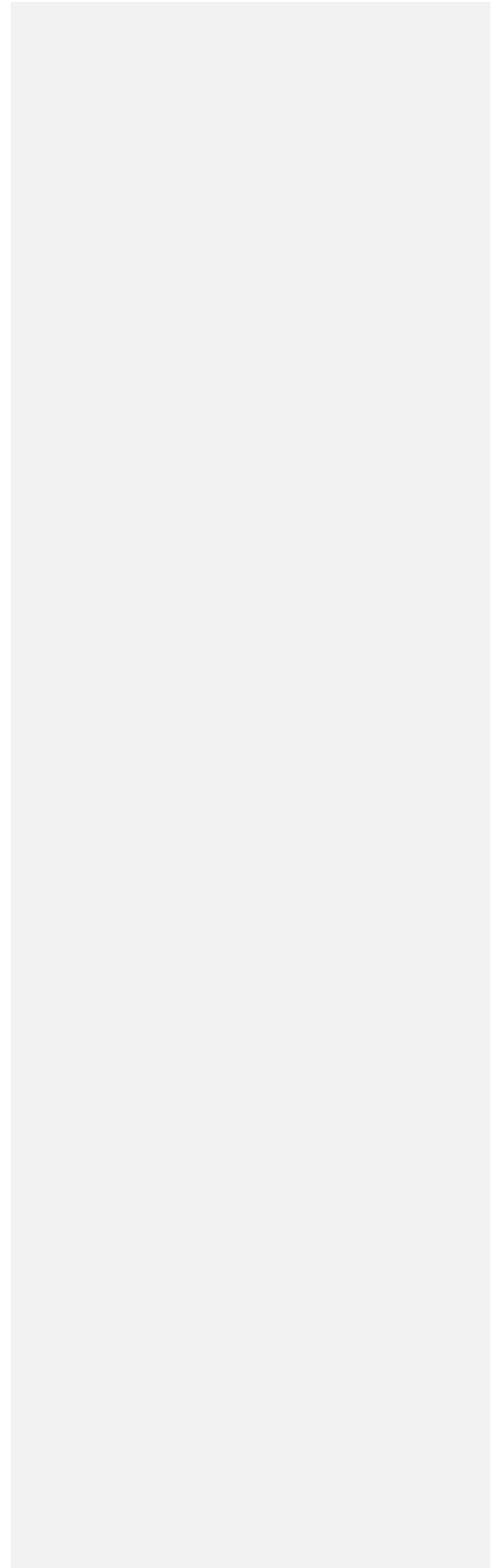


Figure B. 20 Result of data inversion, showing the depth and resistivities of the layer.

APPENDIX C
Processing Results



The result from all stations (Rx1, Rx2, and Rx3) and fields (electric and magnetic field) are shown in this appendix. All magnetic signals, both measured data and second derivative of fluxgate data, show the reversal due to the 3D effect. The 1D inversion could not perform for distorted transient and need to perform any approach to solve it. The reversal solution is suggested by Strack (1992) and also 3D modeling may be useful for this case (Strack, personal communication)

C.1 Data Processing result, 1st May, 2015

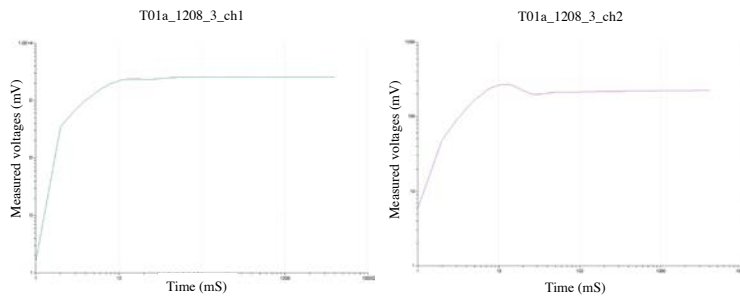


Figure C. 1 Processing result of Rx0a E-field signal; Ex (left) and Ey (right) output from KMSProQC.

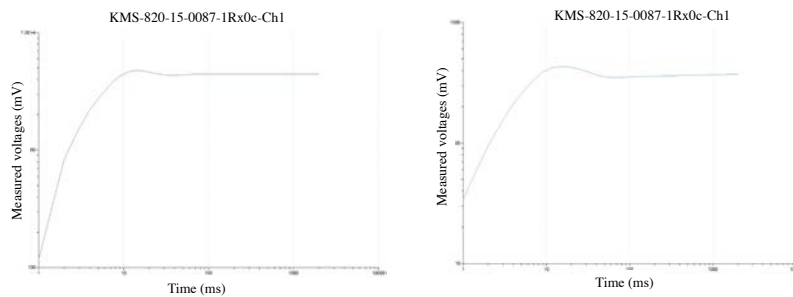


Figure C. 2 Processing result of Rx0c E-field signal; Ex (left) and Ey (right) output from KMSProQC.

C.2 Data Processing result, 3rd May, 2015

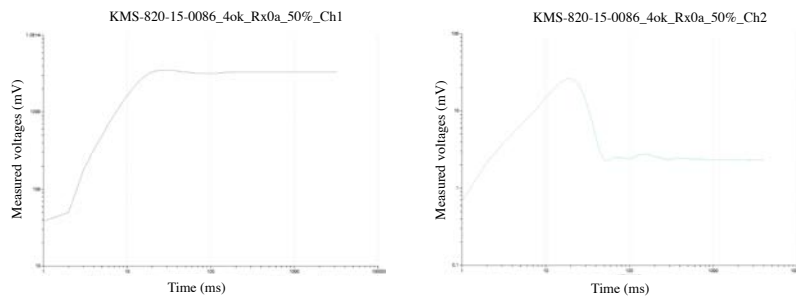


Figure C. 3 Processing result of Rx0a E-field signal; Ex (left) and Ey (right) output from KMSProQC.

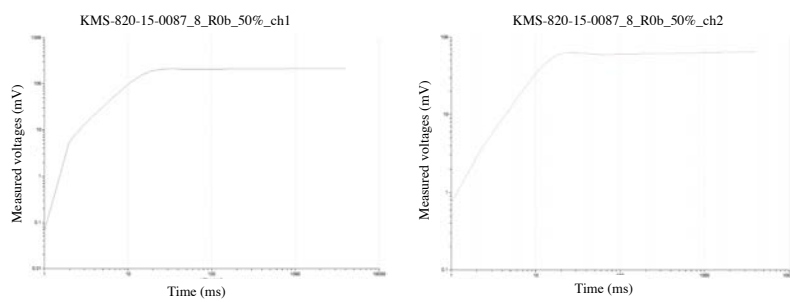


Figure C. 4 Processing result of Rx0b E-field signal; Ex (left) and Ey (right) output from KMSProQC.

C.3 Data Processing result, 5th May, 2015

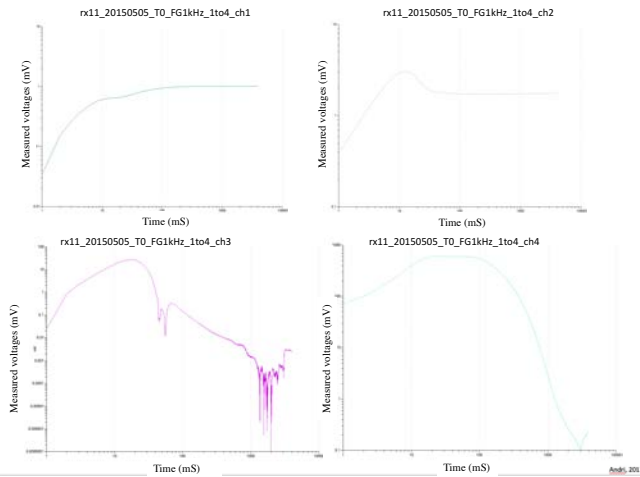


Figure C.5 Processing result of Rx11 E-field signal; Ex (top-left) and Ey (top-right), and H-field; loop (bottom-left) and coil (bottom-right) output from KMSProQC.

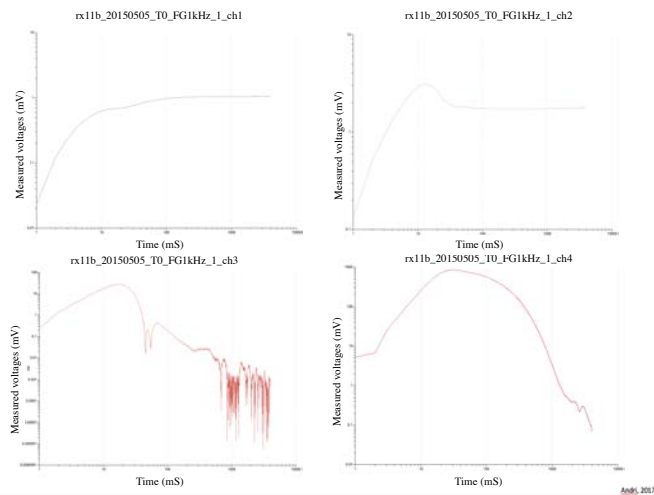


Figure C.6 Processing result of Rx11b E-field signal; Ex (top-left) and Ey (top-right), and H-field; loop (bottom-left) and coil (bottom-right), output from KMSProQC.

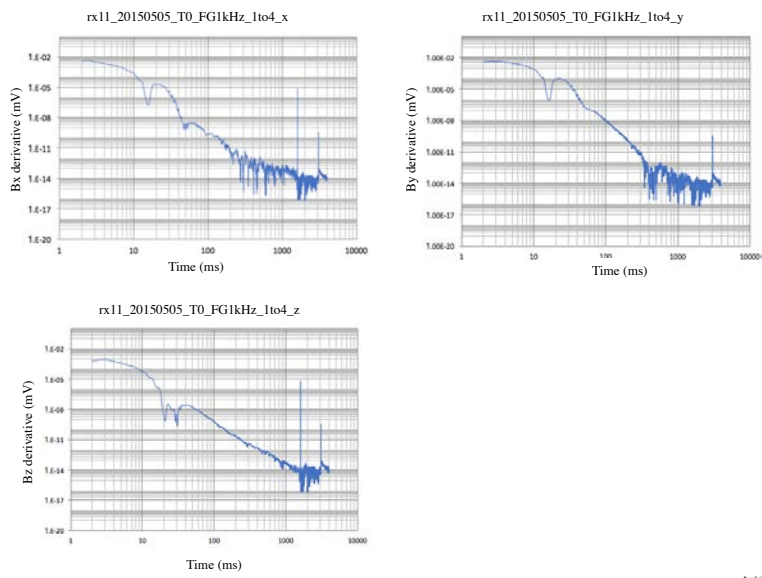


Figure C. 7 Second derivative of Rx11 magnetic field (Fluxgate sensor); Bx (top-left), By (top-right), and Bz (bottom-left). Processed data from KMSProQC and manual derivative calculation in Ms. Excel.

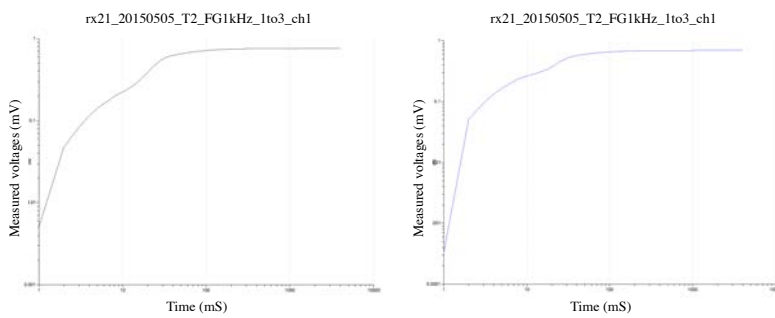


Figure C. 8 Processing result of Rx21 E-field signal; Ex (top-left) and Ey (top-right), output from KMSProQC.

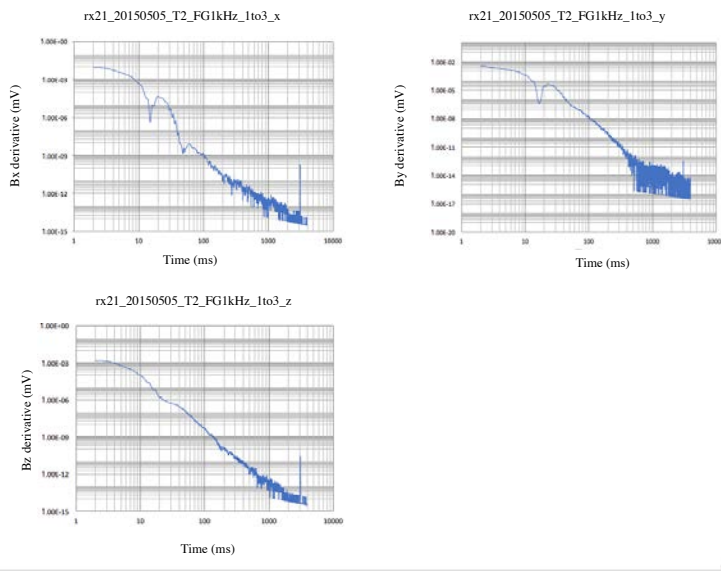


Figure C. 9 Second derivative of Rx21 magnetic field (Fluxgate sensor); Bx (top-left), By (top-right), and Bz (bottom-left). Processed data from KMSProQC and manual derivative calculation in Ms. Excel.

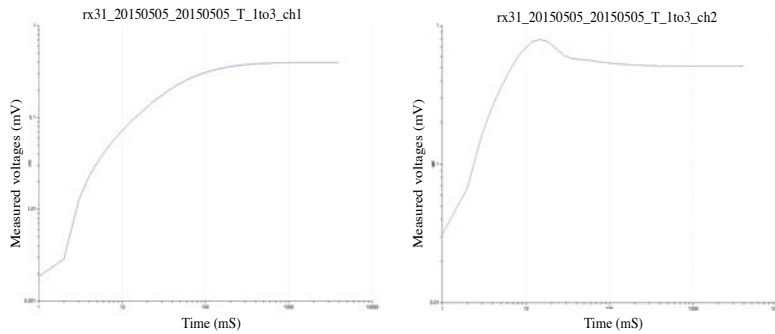


Figure C. 10 Processing result of Rx31 E-field signal; Ex (top-left) and Ey (top-right), output from KMSProQC.

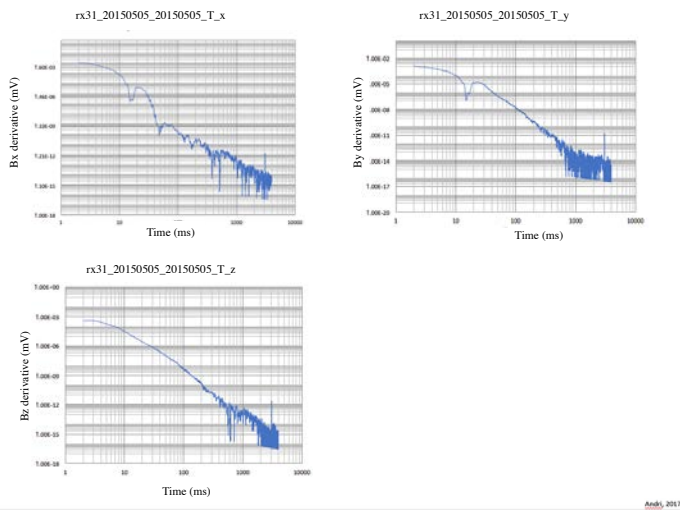


Figure C.11 Second derivative of Rx31 magnetic field (Fluxgate sensor); Bx (top-left), By (top-right), and Bz (bottom-left). Processed data from KMSProQC and manual derivative calculation in Ms. Excel.

C.4 Data Processing result, 7^h May 2015

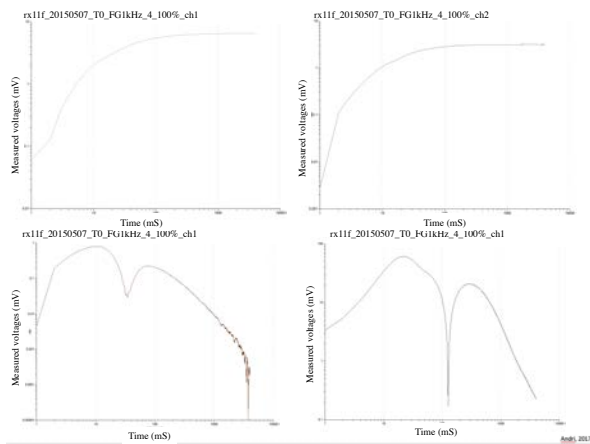


Figure C.12 Processing result of Rx11f E-field signal; Ex (top-left) and Ey (top-right), and H-field; loop (bottom-left) and coil (bottom-right), output from KMSProQC.

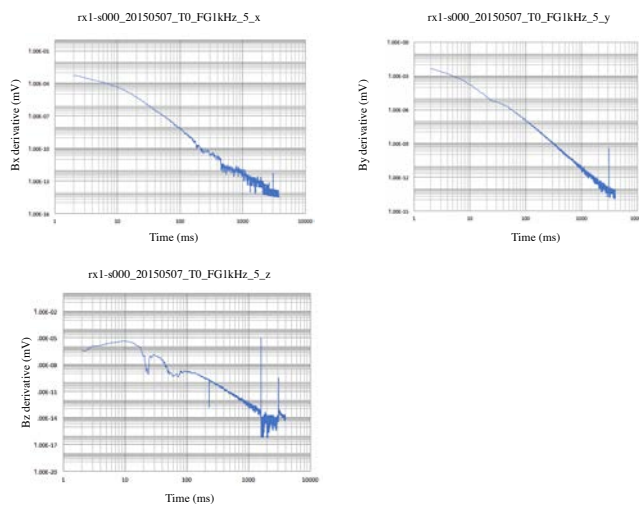


Figure C. 13 Second derivative of Rx1 magnetic field (Fluxgate sensor); Bx (top-left), By (top-right), and Bz (bottom-left). Processed data from KMSProQC and manual derivative calculation in Ms. Excel.

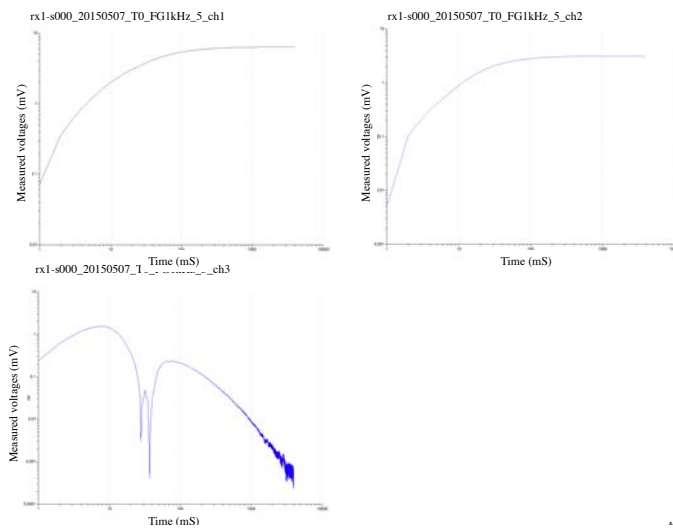


Figure C. 14 Processing result of Rx1lf E-field signal; Ex (top-left) and Ey (top-right), and H-field; loop (bottom-left), output from KMSProQC.

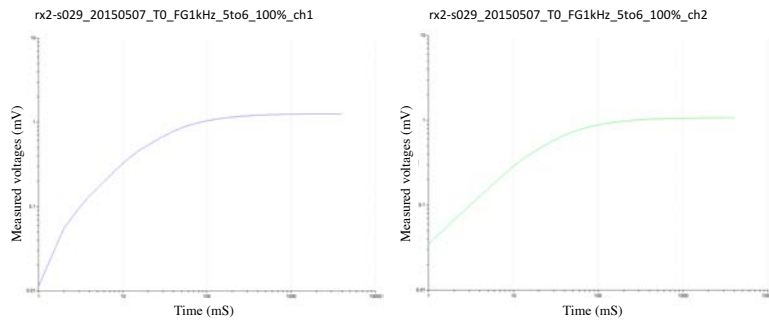


Figure C. 15 Processing result of Rx2-s029 E-field signal; Ex (top-left) and Ey (top-right), output from KMSProQC.

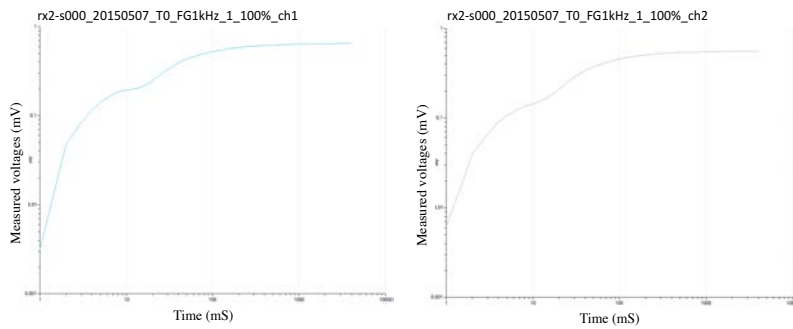


Figure C. 16 Processing result of Rx2 E-field signal; Ex (top-left) and Ey (top-right), output from KMSProQC.

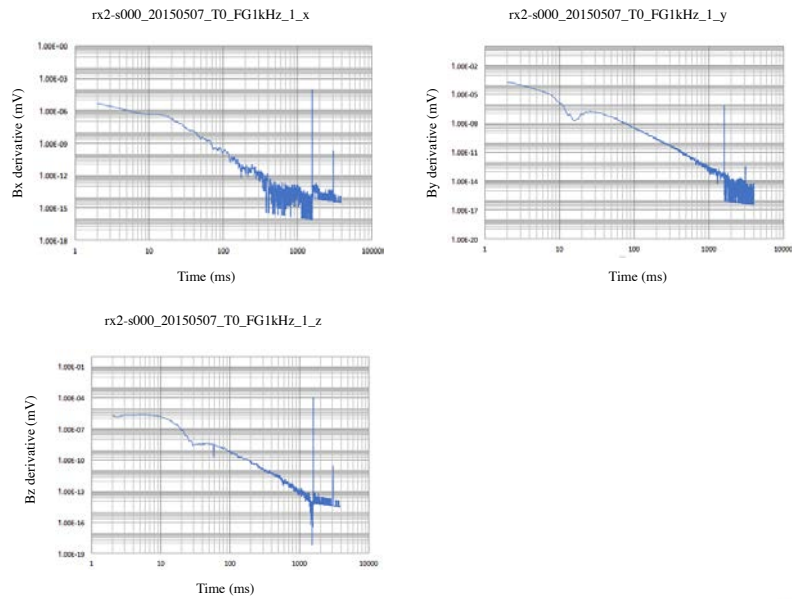


Figure C. 17 Second derivative of Rx2 magnetic field (Fluxgate sensor); Bx (top-left), By (top-right), and Bz (bottom-left). Processed data from KMSPProQC and manual derivative calculation in Ms. Excel.

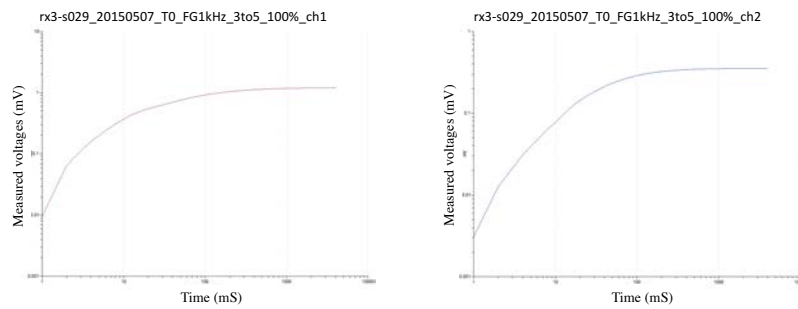


Figure C. 18 Processing result of Rx3-s029 E-field signal; Ex (top-left) and Ey (top-right), output from KMSPProQC.

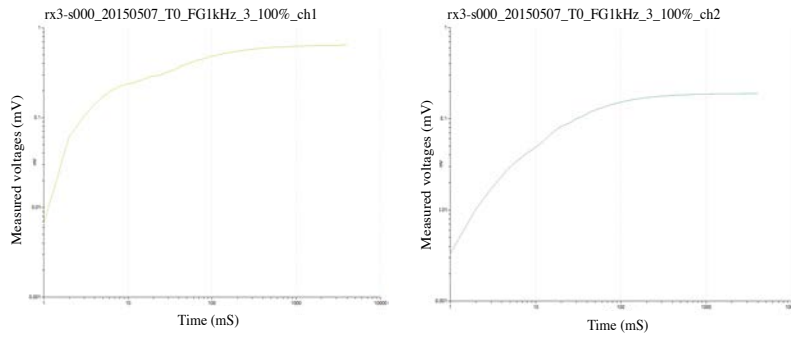


Figure C. 19 Processing result of Rx3 E-field signal; Ex (top-left) and Ey (top-right), output from KMSProQC.

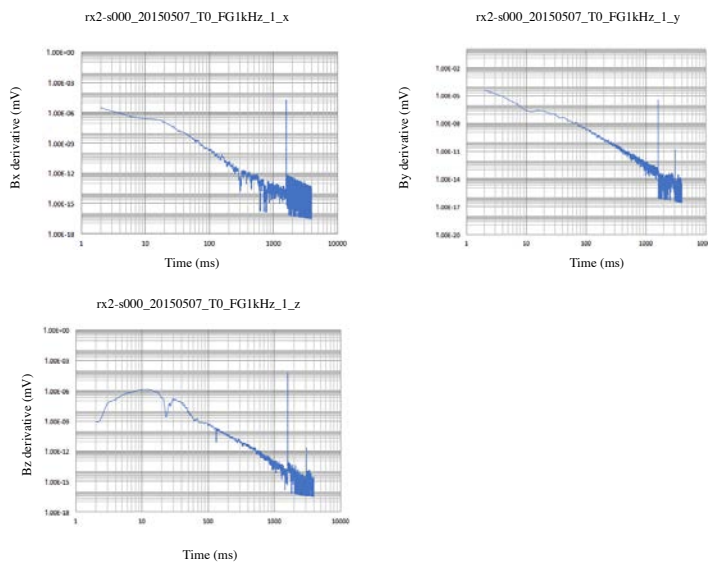


Figure C. 20 Second derivative of Rx3 magnetic field (Fluxgate sensor); Bx (top-left), By (top-right), and Bz (bottom-left). Processed data from KMSProQC and manual derivative calculation in Ms. Excel.

C.5 Data Processing result, 8^h May 2015

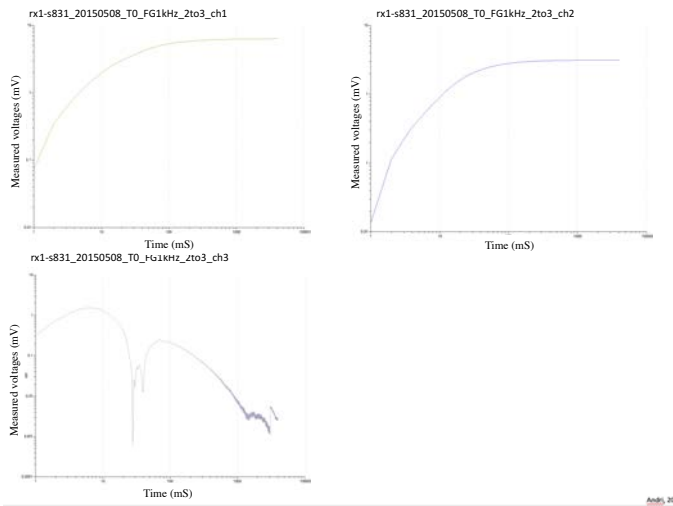


Figure C. 21 Processing result of Rx1-A E-field signal; Ex (top-left) and Ey (top-right), and H-field; loop (bottom-left), output from KMSPProQC.

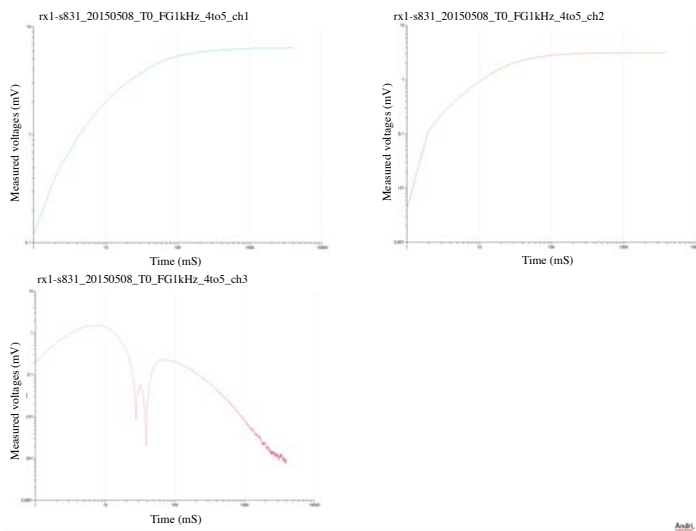


Figure C. 22 Processing result of Rx1-B E-field signal; Ex (top-left) and Ey (top-right), and H-field; loop (bottom-left), output from KMSPProQC.

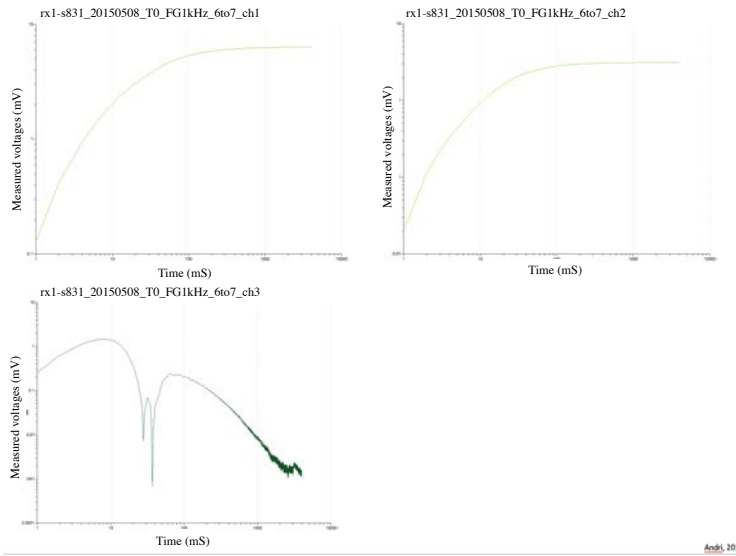


Figure C. 23 Processing result of Rx1-C E-field signal; Ex (top-left) and Ey (top-right), and H-field; loop (bottom-left), output from KMSProQC.

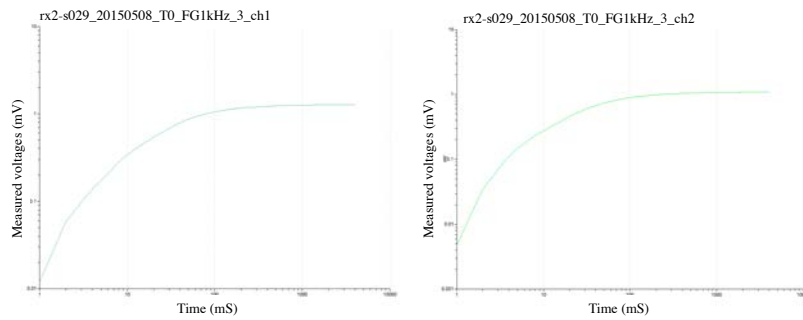


Figure C. 24 Processing result of Rx2-A E-field signal; Ex (top-left) and Ey (top-right), output from KMSProQC.

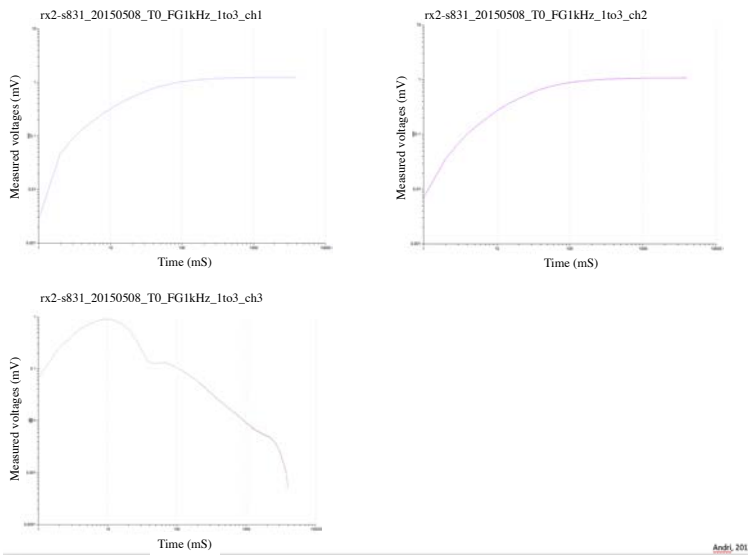


Figure C. 25 Processing result of Rx2-B E-field signal; Ex (top-left) and Ey (top-right), and H-field; loop (bottom-left), output from KMSProQC.

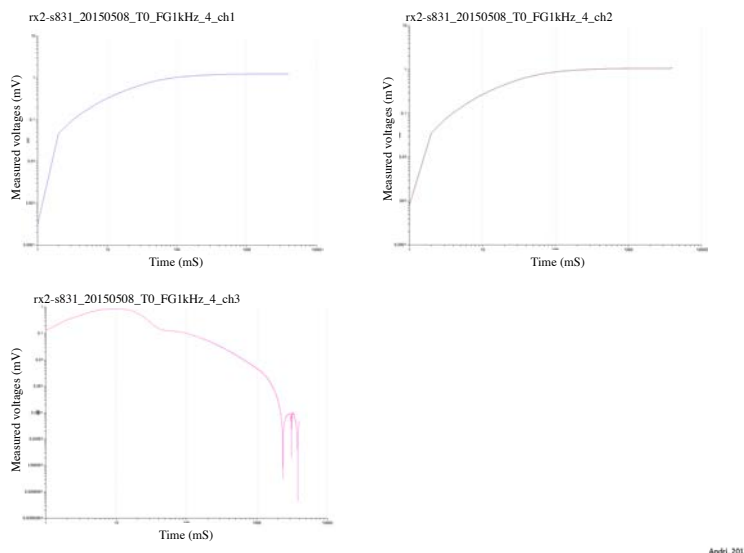


Figure C. 26 Processing result of Rx2-C E-field signal; Ex (top-left) and Ey (top-right), and H-field; loop (bottom-left), output from KMSProQC.

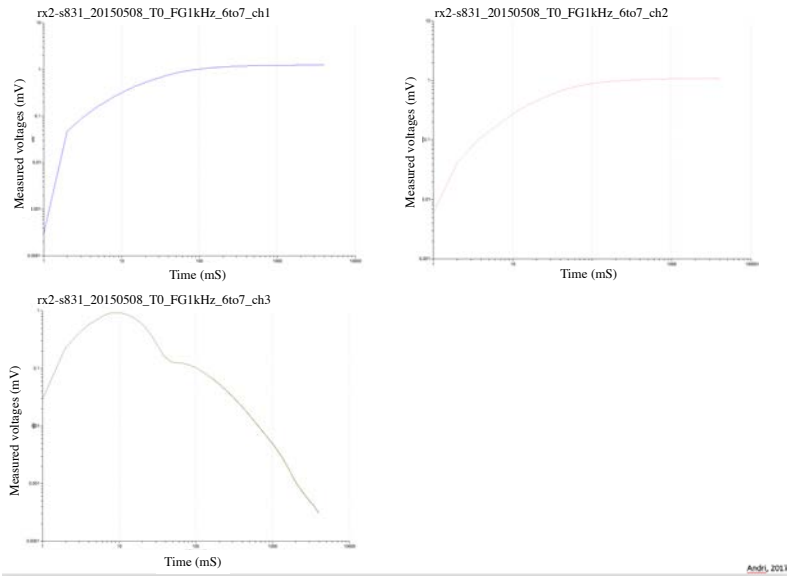


Figure C. 27 Processing result of Rx2-C E-field signal; Ex (top-left) and Ey (top-right), and H-field; loop (bottom-left), output from KMSProQC.

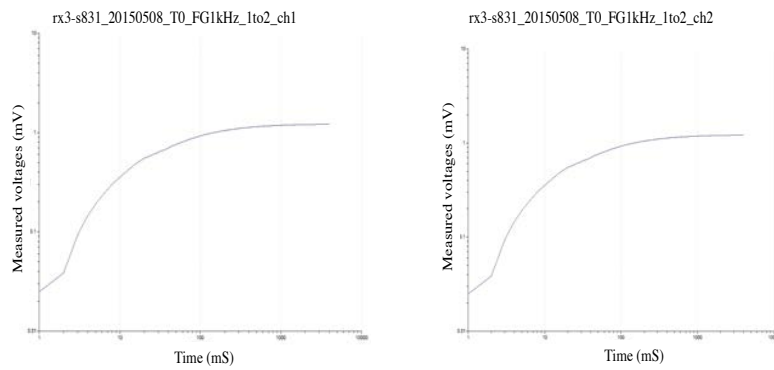


Figure C. 28 Processing result of Rx3-A E-field signal; Ex (top-left) and Ey (top-right), output from KMSProQC.

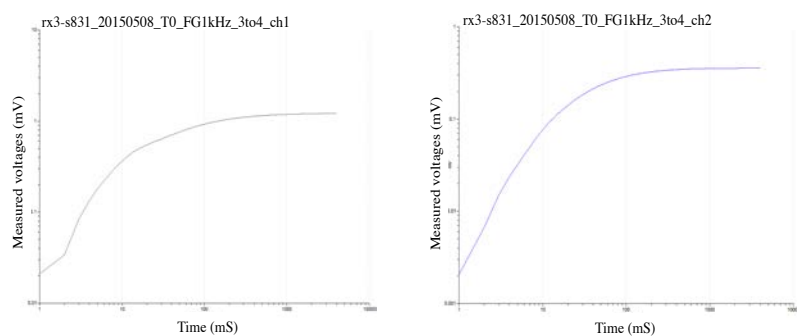


Figure C. 29 Processing result of Rx3-B E-field signal; Ex (top-left) and Ey (top-right), output from KMSPProQC.

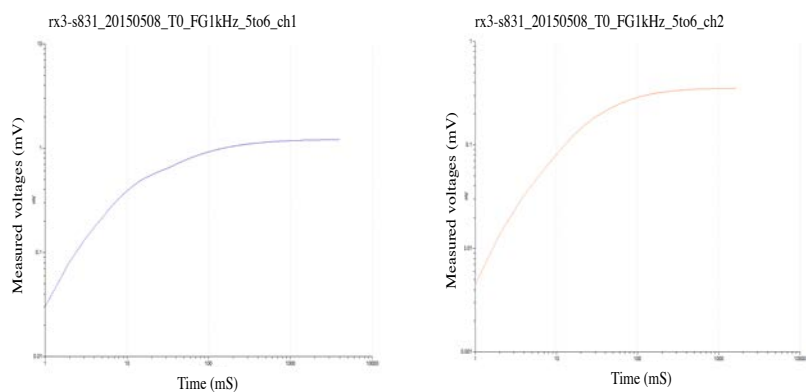
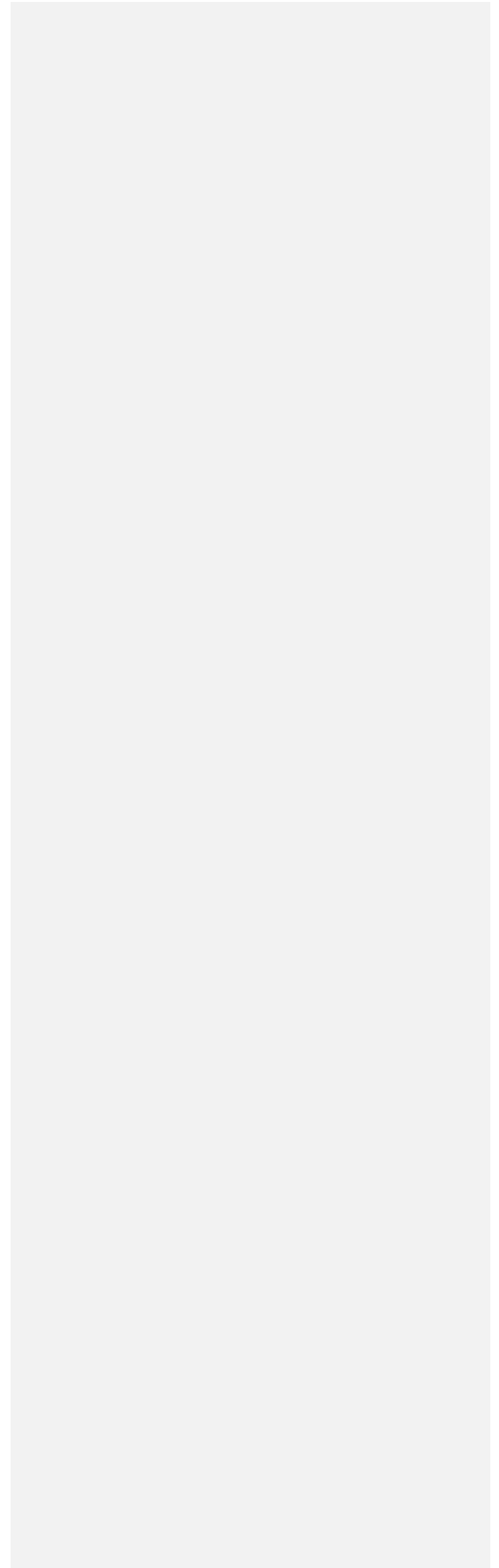


Figure C. 30 Processing result of Rx3-C E-field signal; Ex (top-left) and Ey (top-right), output from KMSPProQC.

APPENDIX D
Cumulative Conductance and Transverse Resistance Analysis



Cumulative conductance and transverse resistance analysis are carried out for two proposes. First propose is to analyze Occam' model to generate the starting model for Marquardt inversion and other is to analyze to get the vertical and horizontal resistivity from the well log data.

D.1 Generate Layered Model from Occam' Model

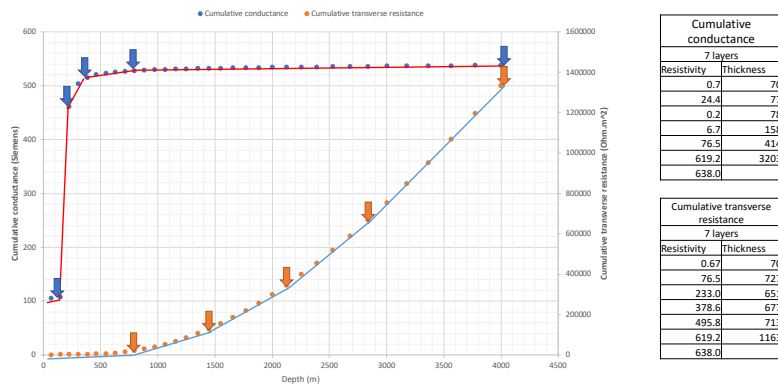


Figure D. 1 Cumulative conductance (blue) and transverse resistance (orange) analysis to generate starting model for Marquardt inversion of Rx1.

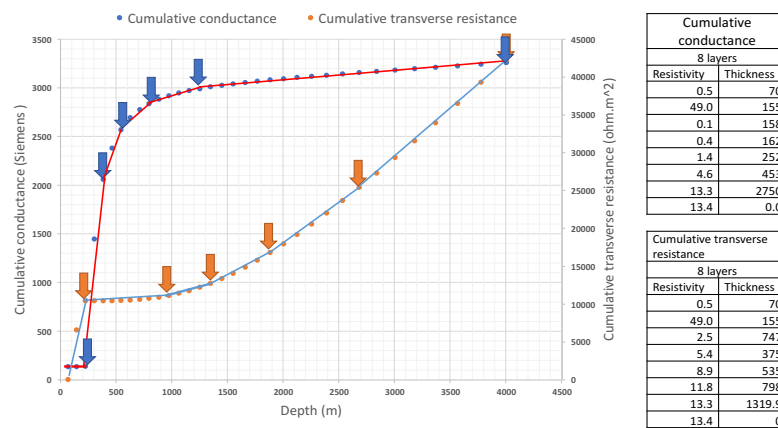


Figure D. 2 Cumulative conductance (blue) and transverse resistance (orange) analysis to generate starting model for Marquardt inversion of Rx2.

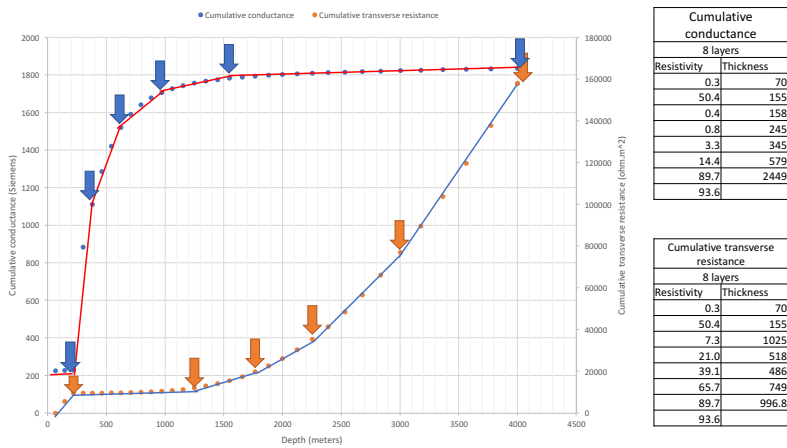


Figure D.3 Cumulative conductance (blue) and transverse resistance (orange) analysis to generate starting model for Marquardt inversion of Rx3.

D.3 An example of using the cumulative conductance and transverse resistance analysis for Direct Warren

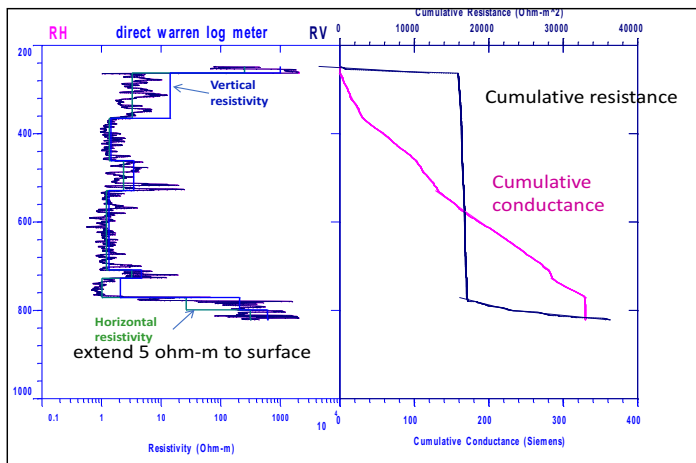
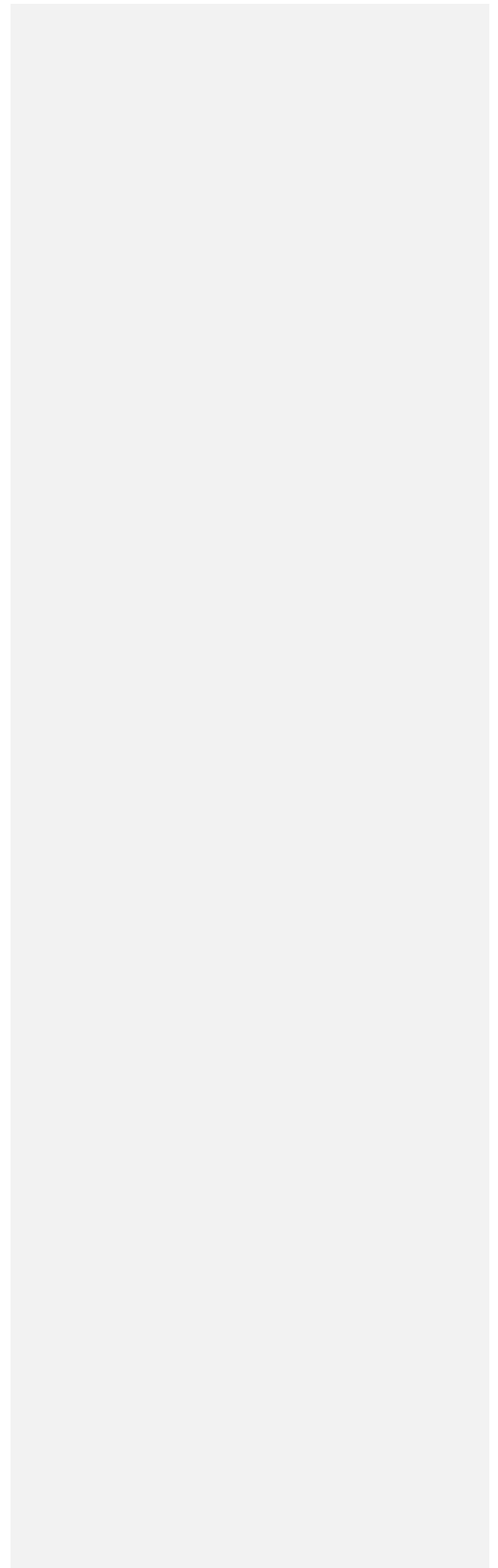


Figure D.4 Direct Warren: anisotropic reduced well log model showing the horizontal resistivity (generated from cumulative conductance) and vertical resistivity (generated from cumulative transverse resistance) (KMS Technologies, personal communication, 2017).

APPENDIX E
Inversion Result, Statistical Analysis and Interpretation



The statistical analysis of the inversion is based on the literature (mostly Jupp and Vozoff, 1976) and the workflow described in Chapter III. Here, the results for each station are reported.

Table E.1, E.2 and E.3 show the resolved combination for each layer (layer 1 to 3) from all station. The result show that the layer 1 to 3 are resolved mostly in E-field Ex. The importance also confirms the resistivity and the depth mostly until layer 3.

Table E. 1 Statistical analysis for all station of broadside transmitter (5th May 2017). The result analyzed from V-Matrix.

No.	Station/ sensor	Starting model from cumulative conductance analysis			Starting model from cumulative trans. resistance analysis		
		Resolved combination for Layer 1	Resolved combination for Layer 2	Resolved combination for Layer 3	Resolved combination for Layer 1	Resolved combination for Layer 2	Resolved combination for Layer 3
1	Rx1Ex	$\frac{\rho_3 h_1}{\rho_1 h_3} (P2)$	$\frac{\rho_1 \rho_2 \rho_3 h_2}{h_1 h_3} (P1)$	$\frac{\rho_1 \rho_3}{\rho_2 h_2 h_3} (P3)$	$\frac{\rho_1}{h_1} (P1)$		
2	Rx2Ex	$\frac{\rho_1 \rho_2 h_2}{h_1} (p2)$	$\frac{\rho_2 h_2}{\rho_1} (P1)$	$\frac{h_2 h_3}{\rho_2 \rho_3} (P4)$	$\frac{\rho_1 \rho_2 h_2}{h_1} (P2)$	$\frac{\rho_2 h_2}{\rho_1} (P1)$	$\frac{\rho_1 h_2 h_3}{\rho_2 \rho_3 h_1} (P4)$
3	Rx3Ex	$\frac{\rho_1 \rho_2}{h_1} (P2)$	$\frac{\rho_2 \rho_3 h_2}{\rho_1} (P1)$		$\frac{\rho_1}{h_1} (P2)$	$\rho_3 \rho_2 h_2 (P1)$	
4	Rx1Ey	$\frac{\rho_2 h_1}{\rho_1 h_2 h_3}$				$\frac{1}{\rho_2 h_2}$	
5	Rx2Ey	$\frac{\rho_1}{h_1}$			$\frac{h_1 h_2}{\rho_1}$		
6	Rx3Ey	$\frac{h_1 h_2}{\rho_1}$	$\frac{1}{\rho_2 h_2}$		$\frac{h_1}{\rho_1 h_2}$	$\frac{1}{\rho_2 h_2}$	

Table E. 2 Statistical analysis for all station of inline transmitter (7th May 2017). The result analyzed from V-Matrix.

No.	Station/ sensor	Starting model from cumulative conductance analysis			Starting model from cumulative trans. resistance analysis		
		Resolved combination for Layer 1	Resolved combination for Layer 2	Resolved combination for Layer 3	Resolved combination for Layer 1	Resolved combination for Layer 2	Resolved combination for Layer 3
1	Rx1Ex	$\frac{h_1 h_2}{\rho_1}$ (P2)		$\frac{\rho_1 \rho_3 h_1}{h_2 h_3}$ (P3)	$\frac{h_1}{\rho_1}$ (P3)		
2	Rx2Ex	$\frac{h_1 h_2}{\rho_1}$ (P2)			$\frac{h_1 h_2}{\rho_1}$ (P2)		$\frac{\rho_2 \rho_3}{\rho_1 h_1 h_2 h_3}$ (P4)
3	Rx3Ex	$\frac{h_1 h_2}{\rho_1}$ (P2)	$\frac{\rho_2 h_2}{\rho_1}$ (P1)	$\frac{h_1 h_3}{\rho_3}$ (P5)			$\frac{h_3}{\rho_3 h_1}$ (P3)
4	Rx1Ey	$\frac{\rho_1}{h_1}$ (P1)			$\frac{h_1}{\rho_1}$ (P2)		
5	Rx2Ey	$\frac{h_1}{\rho_1}$ (P2)			$\frac{h_1}{\rho_1}$ (P2)		
6	Rx3Ey	$\frac{h_1}{\rho_1}$ (P2)	$\frac{\rho_2 h_2}{h_1}$ (P1)	$\frac{\rho_2 h_3}{\rho_1 \rho_3 h_2}$ (P4)	$\frac{\rho_3 h_1}{\rho_1}$ (P2)		

Table E. 3 Statistical analysis for all station of inline transmitter (8th May 2017). The result analyzed from V-Matrix.

No.	Station/ sensor	Starting model from cumulative conductance analysis			Starting model from cumulative trans. resistance analysis		
		Resolved combination for Layer 1	Resolved combination for Layer 2	Resolved combination for Layer 3	Resolved combination for Layer 1	Resolved combination for Layer 2	Resolved combination for Layer 3
1	Rx1Ex	$\frac{h_1 h_2}{\rho_1}$ (P2)			$\frac{\rho_1}{h_1}$ (P1)		
2	Rx2Ex	$\frac{h_1 h_2}{\rho_1}$ (P2)			$\frac{h_1}{\rho_2}$ (P2)	$\frac{\rho_1 h_1}{\rho_2 h_2}$ (P3)	$\frac{\rho_3}{h_1 h_2 h_3}$ (P4)
3	Rx3Ex	$\frac{h_1 h_2 \rho_3}{\rho_1}$ (P2)	$\frac{\rho_2 h_2}{h_1}$ (P1)	$\frac{\rho_1 \rho_3}{h_2 h_3}$ (P3)	$\frac{h_1 h_2 \rho_3}{\rho_1}$ (P2)		$\frac{\rho_1 \rho_3}{h_2 h_3}$ (P3)
4	Rx1Ey	$\frac{\rho_1}{h_1}$ (P1)			$\frac{\rho_1}{h_1}$ (P1)		
5	Rx2Ey	$\frac{\rho_1}{h_1}$ (P1)			$\frac{h_1}{\rho_1}$ (P2)		$\frac{\rho_2}{\rho_1 \rho_3 h_1 h_2}$ (P4)
6	Rx3Ey	$\frac{h_1 h_2}{\rho_1}$ (P2)	$\frac{\rho_2 \rho_4}{\rho_1 h_1 h_2 h_4}$ (P4)	$\frac{\rho_3}{h_3}$ (P5)	$\frac{\rho_1}{h_1}$ (P1)	$\frac{\rho_2}{\rho_1 \rho_3 h_1 h_2}$ (P4)	

E.1 Occam inversion

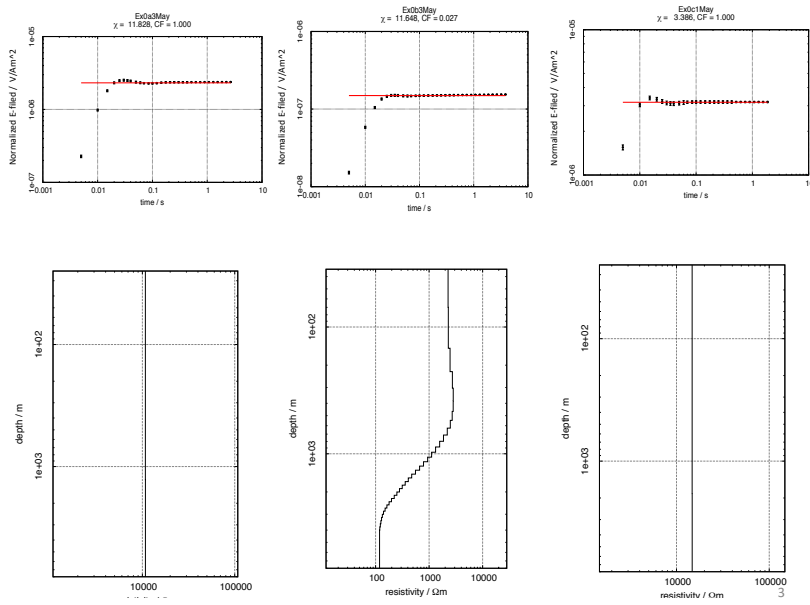


Figure E. 1 Occam' model of E-field (Ex) near offset. From left to the right, Rx0a to Rx0c.

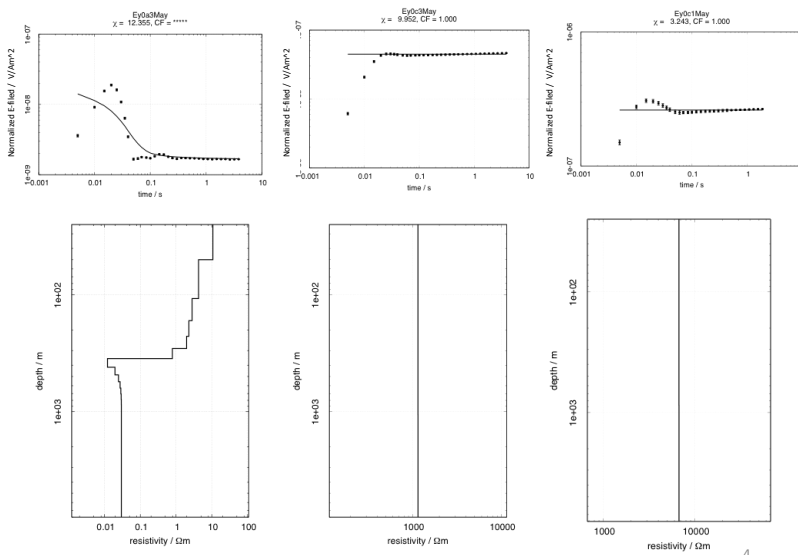


Figure E. 2 Occam' model of E-field (E_y) near offset. From left to the right, Rx0a to Rx0c.

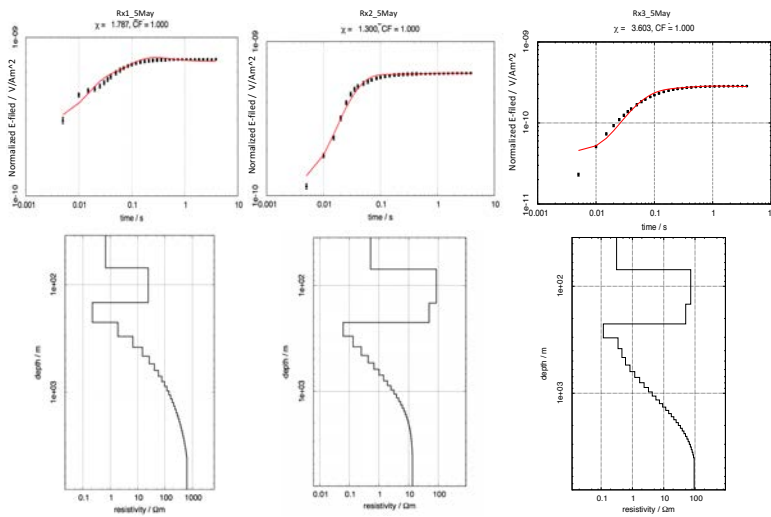


Figure E. 3 Occam' model of E-field (E_x), broadside transmitter configuration, data measured on 5th May 2015. From left to the right, Rx1 to Rx3.

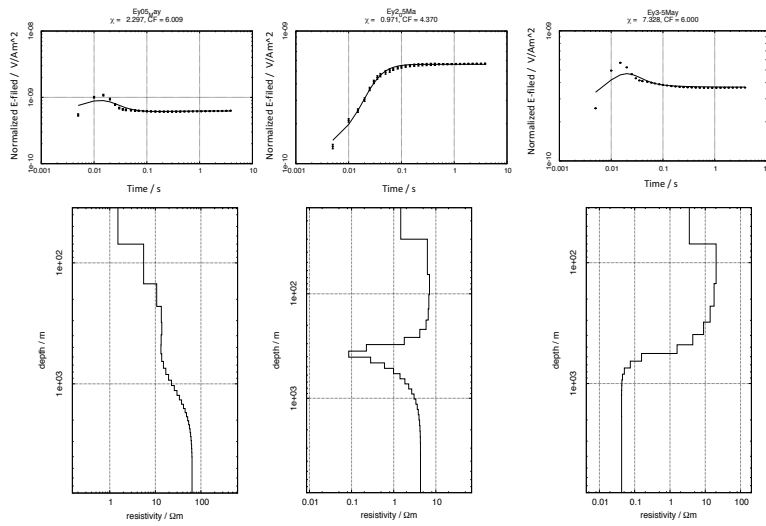


Figure E. 4 Occam' model of E-field (E_y), broadside transmitter configuration, data measured on 5th May 2015. From left to the right, Rx1 to Rx3.

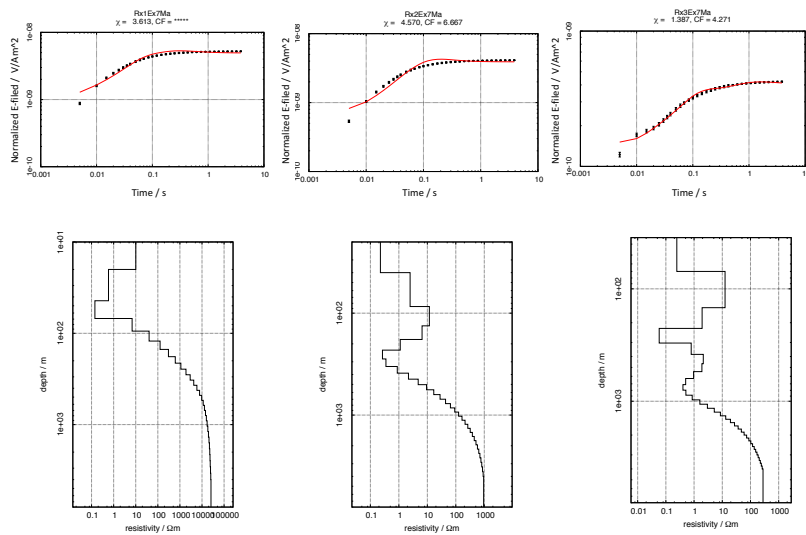


Figure E. 5 Occam' model of E-field (E_x), inline transmitter configuration, data measured on 7th May 2015. From left to the right, Rx1 to Rx3.

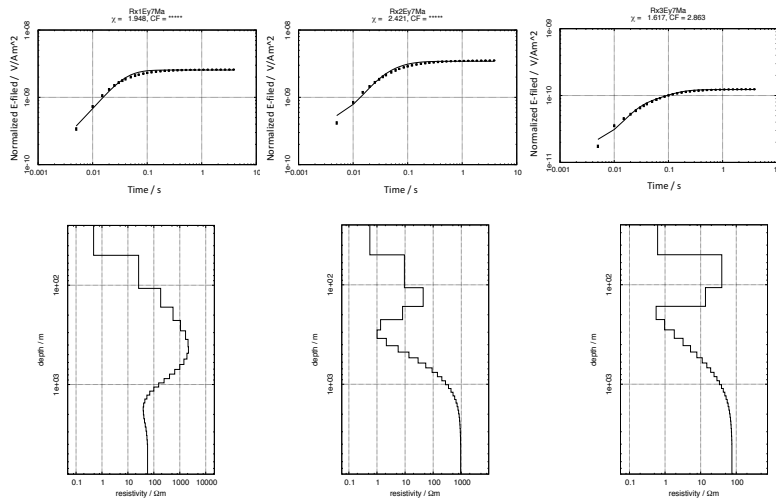


Figure E. 6 Occam' model of E-field (E_y), inline transmitter configuration, data measured on 7th May 2015. From left to the right, Rx1 to Rx3.

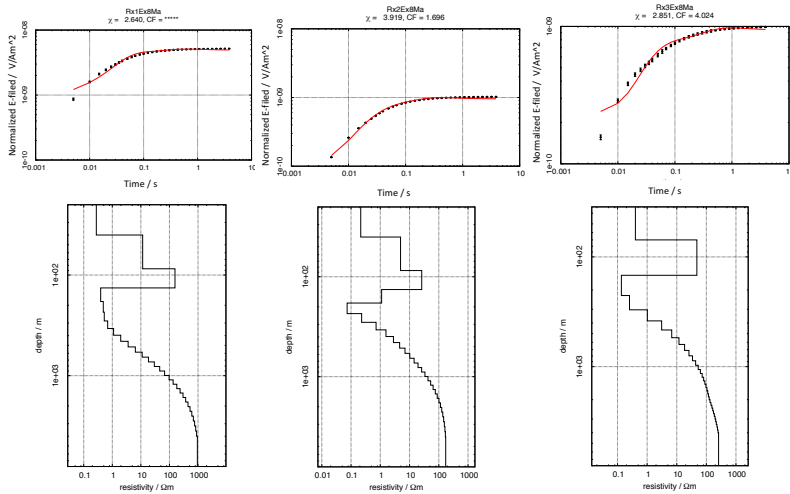


Figure E. 7 Occam' model of E-field (E_x), inline transmitter configuration, data measured on 8th May 2015. From left to the right, Rx1 to Rx3.

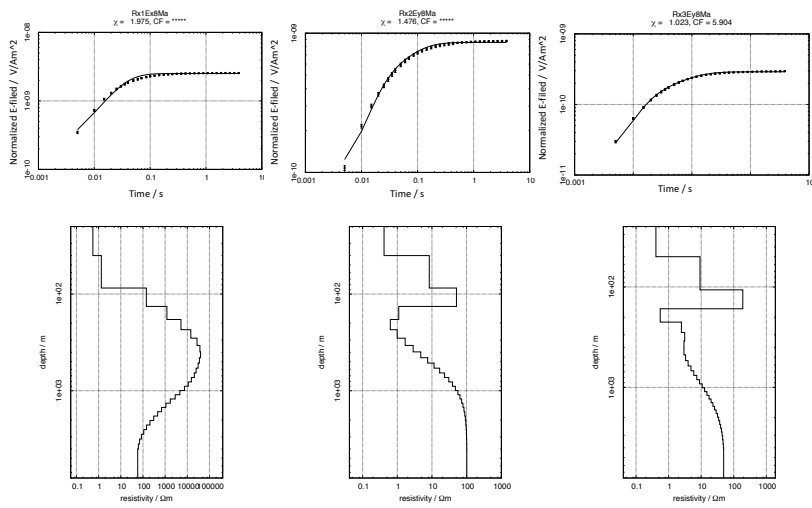


Figure E. 8 Occam' model of E-field (E_y), inline transmitter configuration, data measured on 8th May 2015. From left to the right, Rx1 to Rx3.

E.1 Marquardt inversion and its statistical analysis

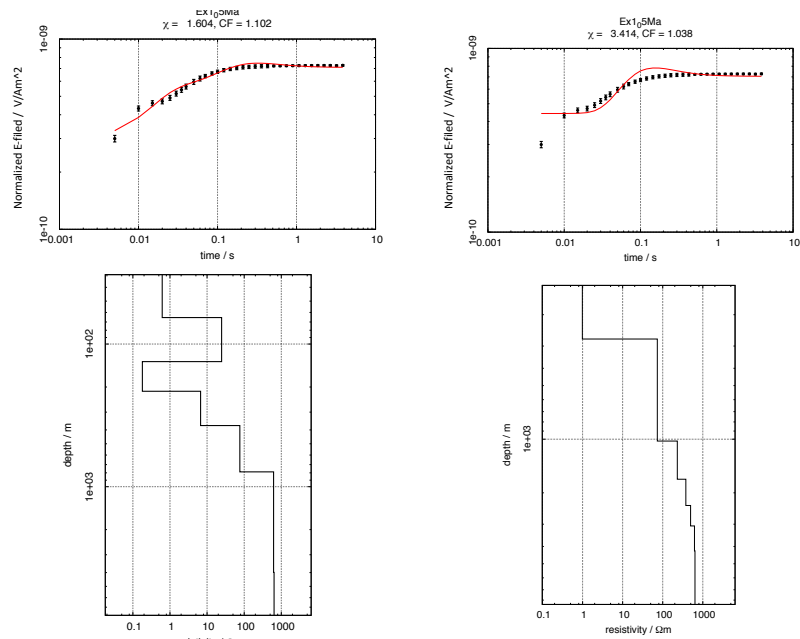


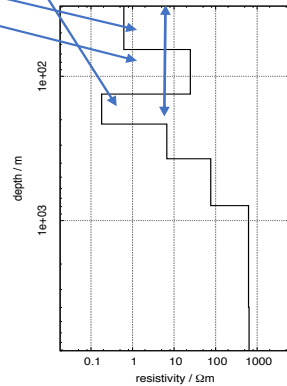
Figure E. 9 Marquardt inversion of Rx2 E-field (E_x) broadside transmitter configuration, data measured on 5th May 2015. The starting models generated using cumulative conductance (left) and transverse resistance (right).

Transform Original par.	P1	P2	P3	P4	P5	P6	P7	P8	P9	P10	P11	P12	P13
ρ_1	0.3	-0.8	0.3	-0.3	0.3	0.0	0.1	0.0	0.0	0.0	0.0	0.0	0.0
ρ_2	0.6	0.2	-0.3	0.4	0.5	0.1	0.4	0.0	0.0	0.0	0.0	0.0	0.0
ρ_3	0.3	0.3	0.5	-0.3	-0.4	0.3	0.5	0.0	0.0	0.0	0.0	0.0	0.0
ρ_4	0.0	0.0	0.0	0.0	0.1	0.5	-0.3	0.8	-0.2	0.1	0.0	0.0	-0.1
ρ_5	0.0	0.0	0.0	0.0	0.0	0.1	-0.1	-0.1	-0.5	-0.7	-0.3	0.3	0.4
ρ_6	0.0	0.0	0.0	0.0	0.0	0.0	0.0	-0.3	-0.7	0.0	0.6	-0.3	-0.1
ρ_7	0.0	0.0	0.0	0.0	0.0	0.0	0.0	-0.1	-0.1	-0.2	-0.2	0.3	-0.9
h_1	-0.3	0.3	-0.2	-0.7	0.6	0.0	0.1	0.0	0.0	0.0	0.0	0.0	0.0
h_2	0.6	0.1	-0.4	-0.4	-0.3	-0.1	-0.3	0.0	0.0	0.0	0.0	0.0	0.0
h_3	-0.2	-0.3	-0.6	-0.1	-0.3	0.4	0.5	0.0	0.0	0.0	0.0	0.0	0.0
h_4	0.0	0.0	0.0	0.0	-0.1	-0.7	0.4	0.5	-0.3	0.1	-0.1	0.0	0.0
h_5	0.0	0.0	0.0	0.0	0.0	-0.1	0.0	0.3	0.4	-0.7	0.5	-0.1	0.0
h_6	0.0	0.0	0.0	0.0	0.0	0.0	0.0	0.0	0.0	-0.2	-0.5	-0.8	-0.1
Damping Factor	1.0	1.0	1.0	1.0	0.2	0.0	0.0	0.0	0.0	0.0	0.0	0.0	0.0
Resolved combination	$\frac{\rho_1 \rho_2 \rho_3 h_2}{h_1 h_3}$	$\frac{\rho_3 h_1}{\rho_1 h_3}$	$\frac{\rho_1 \rho_3}{\rho_2 h_2 h_3}$	$\frac{\rho_2}{\rho_1 \rho_3 h_1 h_2}$									

Effective parameter: 4.2

Layer	Resistivity	Thickness
1	0.61	53.79
2	32.76	55.74
3	0.17	70.3
4	7.08	254.21
5	77.19	413
6	620.15	3202.95
7	638.44	0

Calibration factor: 1.1
Error: 1.6



Layer resistivities - 68 percent confidence interval (damped)				
I	RO(I)	BOUND(1)	BOUND(2)	IMPORTANCE
1	0.6108	0.5674	0.6576	0.9204
2	32.755	29.1352	36.8245	0.5371
3	0.1678	0.1576	0.1787	0.3797
4	7.0767	7.0623	7.091	0.0246
5	77.1895	77.1704	77.2086	0.0025
6	620.1487	619.9661	620.3313	0.0011
7	638.4388	638.3203	638.5574	0.0006

Layer depths (to base) - 68 percent confidence interval (damped)				
I	Z(I)	BOUND(1)	BOUND(2)	IMPORTANCE
1	53.7853	48.8847	59.1772	0.6708
2	109.524	98.3298	121.9926	0.8919
3	179.823	164.155	196.9864	0.9333
4	434.0316	432.3493	435.7203	0.0339
5	847.0286	846.6716	847.3857	0.0039
6	4049.9766	4049.9465	4050.0066	0

Figure E. 10 Resolved combination and importance analyzed using Eigenparameter for Marquardt inversion of Rx1 E-field (Ex), broadside transmitter configuration (5th May 2015). Starting model generated using cumulative conductance.

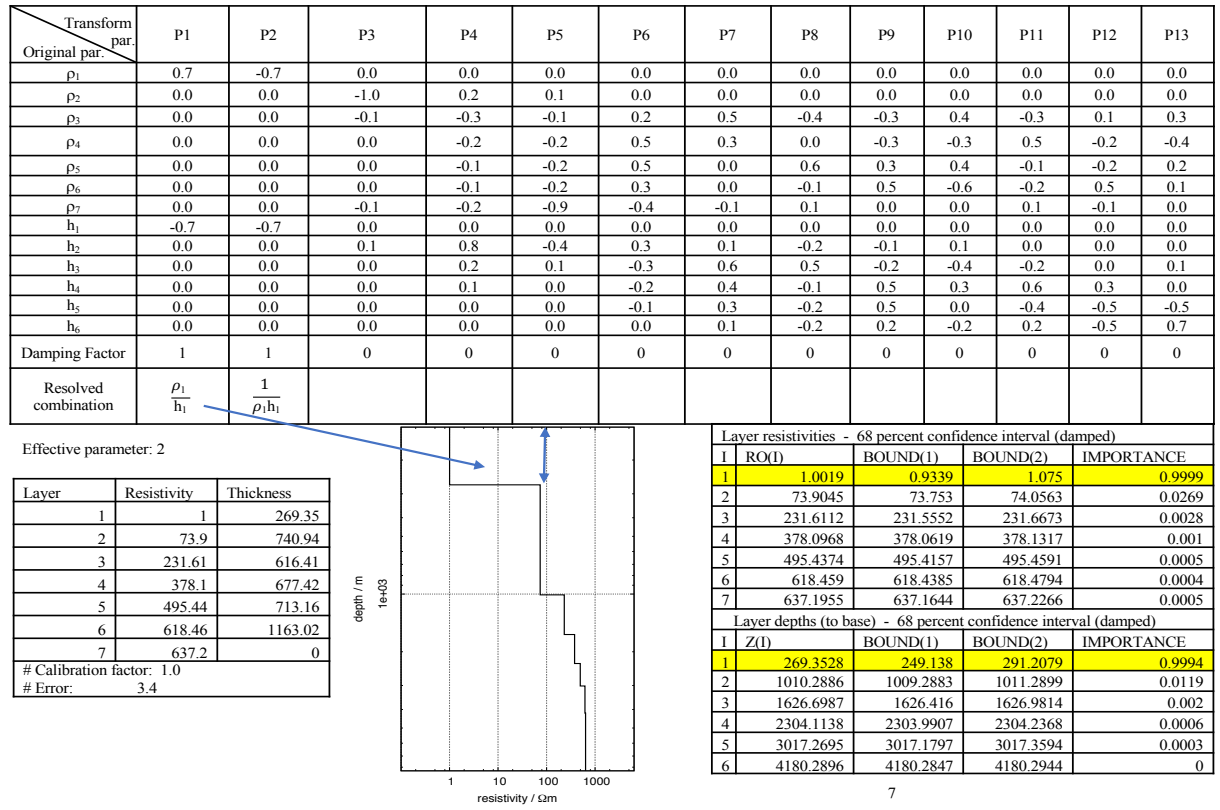


Figure E. 11 Resolved combination and importance analyzed using Eigenparameter for Marquardt inversion of Rx1 E-field (Ex), broadside transmitter configuration (5th May 2015). Starting model generated using cumulative transverse resistance.

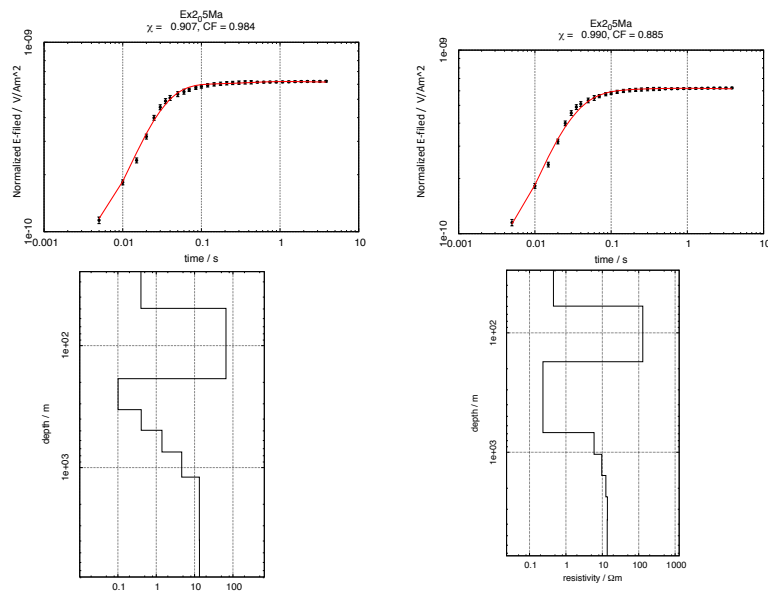
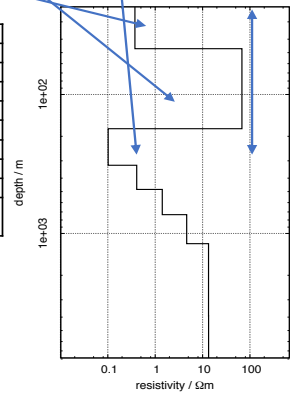


Figure E.12 Marquardt inversion of Rx2 E-field (Ex) broadside transmitter configuration, data measured on 5th May 2015. The starting models generated using cumulative conductance (left) and transverse resistance (right).

Transform Original par.	P1	P2	P3	P4	P5	P6	P7	P8	P9	P10	P11	P12	P13	P14	P15
ρ_1	0.6	-0.4	0.6	-0.1	0.2	0.0	0.0	0.0	0.0	0.0	0.0	0.0	0.0	0.0	0.0
ρ_2	0.3	0.4	-0.3	-0.4	0.6	0.0	0.0	0.0	0.0	0.0	0.0	0.0	0.0	0.0	0.0
ρ_3	0.0	0.1	0.1	-0.6	-0.4	0.6	0.1	0.0	0.0	0.0	0.0	0.0	0.0	0.0	0.0
ρ_4	0.0	0.0	0.0	-0.1	-0.1	-0.2	0.2	0.6	-0.5	0.3	0.1	-0.3	0.1	0.2	0.0
ρ_5	0.0	0.0	0.0	0.0	0.0	-0.1	0.3	0.0	-0.1	-0.5	0.4	0.0	0.6	-0.4	0.1
ρ_6	0.0	0.0	0.0	0.0	0.0	-0.1	0.2	-0.3	0.0	-0.3	0.2	-0.7	-0.5	0.0	-0.1
ρ_7	0.0	0.0	0.0	0.0	0.0	0.0	0.1	-0.6	-0.6	0.2	0.3	0.3	-0.2	0.0	0.0
ρ_8	0.0	0.0	0.0	0.0	0.0	0.0	0.0	0.0	-0.5	-0.5	-0.7	0.0	0.0	0.0	0.0
h_1	-0.6	0.2	0.6	-0.2	0.4	-0.1	0.0	0.0	0.0	0.0	0.0	0.0	0.0	0.0	0.0
h_2	0.3	0.8	0.4	0.3	-0.3	0.0	0.0	0.0	0.0	0.0	0.0	0.0	0.0	0.0	0.0
h_3	0.0	0.0	0.0	0.5	0.4	0.7	0.3	0.1	-0.1	0.0	0.0	0.0	0.0	0.0	0.0
h_4	0.0	0.0	0.0	0.1	0.0	0.2	-0.7	-0.2	-0.3	0.0	0.2	-0.4	0.4	0.1	0.0
h_5	0.0	0.0	0.0	0.0	0.0	0.1	-0.4	0.4	-0.2	-0.1	0.1	0.1	-0.4	-0.7	0.1
h_6	0.0	0.0	0.0	0.0	0.0	0.0	-0.1	0.3	-0.1	-0.5	0.4	0.3	-0.3	0.5	-0.1
h_7	0.0	0.0	0.0	0.0	0.0	0.0	0.0	0.0	0.0	0.0	0.0	0.0	0.0	-0.2	-1.0
Damping Factor	1.0	1.0	0.9	0.6	0.0	0.0	0	0	0	0	0	0	0	0	0
Resolved combination	$\frac{\rho_1 \rho_2 h_2}{h_1}$	$\frac{\rho_2 h_2}{\rho_1}$	$\frac{\rho_1 h_1 h_2}{\rho_2}$	$\frac{h_2 h_3}{\rho_2 \rho_3}$											

Effective parameter: 3.5

Layer	Resistivity	Thickness
1	0.37	46.81
2	67.69	129.39
3	0.1	146.76
4	0.41	159.26
5	1.41	250.46
6	4.62	452.09
7	13.33	2750
8	13.4	0
# Calibration factor:	0.98	
# Error:	0.9	



Layer resistivities - 68 percent confidence interval (damped)				
I	RO(I)	BOUND(1)	BOUND(2)	IMPORTANCE
1	0.3738	0.3417	0.4089	0.9312
2	67.6861	62.3609	73.466	0.5513
3	0.1017	0.0943	0.1097	0.3279
4	0.4075	0.4006	0.4145	0.0684
5	1.4104	1.4023	1.4186	0.0232
6	4.6158	4.6058	4.6258	0.0087
7	13.3332	13.3192	13.3472	0.0039
8	13.403	13.4017	13.4042	0.0003
Layer depths (to base) - 68 percent confidence interval (damped)				
I	Z(I)	BOUND(1)	BOUND(2)	IMPORTANCE
1	46.812	42.6438	51.3877	0.8421
2	176.198	163.4458	189.9452	0.9528
3	322.9593	286.2776	364.3411	0.4834
4	482.2189	466.6384	498.3196	0.1321
5	732.6812	725.0999	740.3417	0.0418
6	1184.767	1181.2911	1188.2531	0.0117
7	3934.7676	3934.762	3934.7732	0

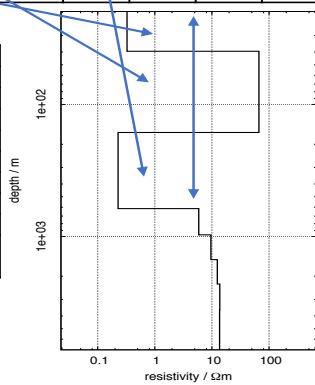
Figure E. 13 Resolved combination and importance analyzed using Eigenparameter for Marquardt inversion of Rx2 E-field (Ex), broadside transmitter configuration (5th May 2015). Starting model generated using cumulative conductance.

Transform Original par.	par.	P1	P2	P3	P4	P5	P6	P7	P8	P9	P10	P11	P12	P13	P14	P15
ρ_1		0.6	-0.4	-0.5	0.3	0.2	-0.2	0.0	0.0	0.0	0.0	0.0	0.0	0.0	0.0	0.0
ρ_2		0.3	0.5	-0.5	-0.5	0.1	-0.4	0.0	0.0	0.0	0.0	0.0	0.0	0.0	0.0	0.0
ρ_3		0.0	0.1	0.1	-0.5	-0.8	0.3	0.0	0.0	0.0	0.0	0.0	0.0	0.0	0.0	0.0
ρ_4		0.0	0.0	0.0	0.0	0.0	0.0	-0.2	0.4	-0.8	0.0	-0.3	-0.1	0.0	-0.2	-0.1
ρ_5		0.0	0.0	0.0	0.0	0.0	0.0	-0.5	-0.1	0.0	-0.4	0.0	-0.6	0.3	0.2	0.3
ρ_6		0.0	0.0	0.0	0.0	0.0	0.0	-0.6	-0.1	0.1	-0.1	-0.2	0.3	-0.7	-0.1	-0.2
ρ_7		0.0	0.0	0.0	0.0	0.0	0.0	-0.4	0.1	0.0	-0.1	0.5	0.6	0.5	-0.2	-0.1
ρ_8		0.0	0.0	0.0	0.0	0.0	0.0	-0.1	0.8	0.4	0.3	-0.1	-0.1	0.0	0.2	0.1
h_1		-0.6	0.2	0.5	-0.5	0.3	-0.3	0.0	0.0	0.0	0.0	0.0	0.0	0.0	0.0	0.0
h_2		0.3	0.7	0.5	0.3	0.1	0.2	0.0	0.0	0.0	0.0	0.0	0.0	0.0	0.0	0.0
h_3		0.0	0.0	0.1	0.4	-0.5	-0.8	0.0	0.0	0.0	0.0	0.0	0.0	0.0	0.0	0.0
h_4		0.0	0.0	0.0	0.0	0.0	0.0	0.3	0.2	0.2	-0.8	-0.3	0.2	0.1	-0.1	0.0
h_5		0.0	0.0	0.0	0.0	0.0	0.0	0.2	0.2	-0.3	-0.3	0.6	0.0	-0.4	0.4	0.0
h_6		0.0	0.0	0.0	0.0	0.0	0.0	0.1	0.1	0.2	-0.1	0.4	-0.4	-0.2	-0.8	0.0
h_7		0.0	0.0	0.0	0.0	0.0	0.0	0.0	0.0	0.1	0.0	0.1	-0.3	0.2	0.1	-0.9
Damping Factor		1.0	1.0	0.9	0.8	0.1	0.0	0.0	0.0	0.0	0.0	0.0	0.0	0.0	0.0	0.0
Resolved combination		$\frac{\rho_1 \rho_2 h_2}{h_1}$	$\frac{\rho_2 h_2}{\rho_1}$	$\frac{h_1 h_2}{\rho_1 \rho_2}$	$\frac{\rho_1 h_2 h_3}{\rho_2 \rho_3 h_1}$											

Effective parameter: 3.9

Layer	Resistivity	Thickness
1	0.33	39.49
2	66.48	123.31
3	0.23	451.56
4	5.87	357.19
5	9.59	525.67
6	12.44	795.06
7	13.71	1319.02
8	13.6	0

Calibration factor: 0.8846
Error: 0.990



Layer resistivities - 68 percent confidence interval (damped)			
RO(l)	BOUND(1)	BOUND(2)	IMPORTANCE
0.3259	0.2877	0.3691	0.9277
66.48	56.8252	77.7752	0.7924
0.2272	0.2011	0.2566	0.4085
5.869	5.8519	5.8861	0.0099
9.5912	9.5746	9.6079	0.0056
12.4364	12.4232	12.4497	0.0031
13.7118	13.7036	13.7201	0.0015
13.5981	13.5938	13.6024	0.0007
Layer depths (to base) - 68 percent confidence interval (damped)			
Z(l)	BOUND(1)	BOUND(2)	IMPORTANCE
39.4874	34.3217	45.4305	0.8481
162.7975	146.3484	181.0955	0.9688
614.3573	541.1373	697.4845	0.4329
971.5522	969.0604	974.0505	0.0086
1497.2185	1495.8757	1498.5625	0.0027
2292.2827	2291.782	2292.7837	0.0006
3611.2993	3611.2507	3611.3479	0

Figure E. 14 Resolved combination and importance analyzed using Eigenparameter for Marquardt inversion of Rx2 E-field (Ex), broadside transmitter configuration (5th May 2015). Starting model generated using cumulative transverse resistance.

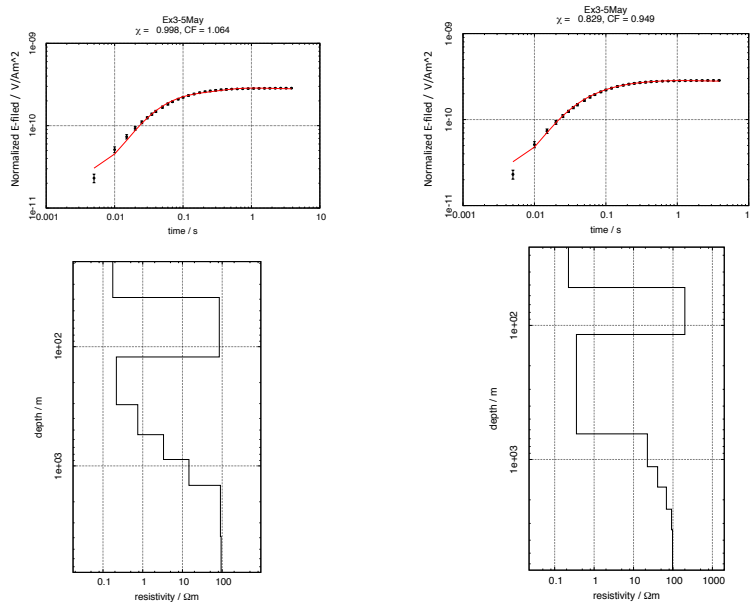


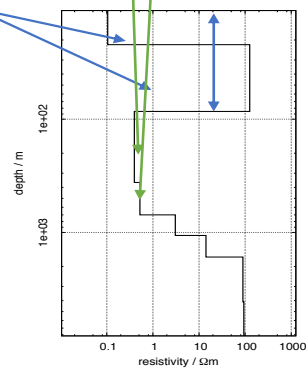
Figure E.15 Marquardt inversion of Rx3 E-field (Ex) broadside transmitter configuration, data measured on 5th May 2015. The starting models generated using cumulative conductance (left) and transverse resistance (right).

Transform Original par.	par.	P1	P2	P3	P4	P5	P6	P7	P8	P9	P10	P11	P12	P13	P14	P15
ρ_1		0.7	-0.3	0.3	-0.3	0.4	-0.3	0.1	0.0	0.0	0.0	0.0	0.0	0.0	0.0	0.0
ρ_2		0.3	0.3	0.1	0.7	0.0	-0.5	0.1	0.0	0.0	0.0	0.0	0.0	0.0	0.0	0.0
ρ_3		0.0	0.4	0.8	-0.2	-0.4	0.1	-0.1	0.0	0.0	0.0	0.0	0.0	0.0	0.0	0.0
ρ_4		0.0	0.1	0.2	0.3	0.4	0.5	0.4	-0.6	-0.1	0.0	0.0	0.0	0.0	0.0	0.0
ρ_5		0.0	0.0	0.0	0.0	0.1	0.0	-0.1	0.0	-0.3	0.4	0.7	0.2	-0.5	-0.1	0.1
ρ_6		0.0	0.0	0.0	0.0	0.0	0.0	0.0	0.0	-0.3	0.6	-0.2	-0.6	0.2	-0.2	0.1
ρ_7		0.0	0.0	0.0	0.0	0.0	0.0	0.0	0.0	-0.2	0.4	-0.2	0.2	0.0	0.8	-0.3
ρ_8		0.0	0.0	0.0	0.0	0.0	0.0	0.0	0.0	0.0	0.3	-0.5	0.7	0.0	-0.4	0.1
h_1		-0.6	0.1	0.2	-0.2	0.5	-0.5	0.1	0.0	0.0	0.0	0.0	0.0	0.0	0.0	0.0
h_2		0.2	0.8	-0.4	-0.4	0.2	0.1	0.0	0.0	0.0	0.0	0.0	0.0	0.0	0.0	0.0
h_3		0.0	-0.1	-0.1	-0.3	-0.4	-0.4	-0.1	-0.8	-0.1	0.0	0.0	0.0	0.0	0.0	0.0
h_4		0.0	-0.1	-0.1	-0.2	-0.4	-0.1	0.8	0.2	-0.2	0.0	0.1	0.0	0.0	0.0	0.0
h_5		0.0	0.0	0.0	0.0	-0.1	0.0	0.1	-0.1	0.8	0.4	0.0	-0.1	-0.4	0.1	0.1
h_6		0.0	0.0	0.0	0.0	0.0	0.0	0.0	0.0	0.3	0.3	0.5	0.3	0.7	-0.1	-0.2
h_7		0.0	0.0	0.0	0.0	0.0	0.0	0.0	0.0	0.0	0.0	0.0	0.1	0.2	0.3	0.9
Damping factor		1.0	1.0	1.0	0.9	0.4	0.1	0.0	0.0	0.0	0.0	0.0	0.0	0.0	0.0	0.0
Resolved combination		$\frac{\rho_1 \rho_2}{h_1}$	$\frac{\rho_2 \rho_3 h_2}{\rho_1}$	$\frac{\rho_1 \rho_3}{h_2}$	$\frac{\rho_2 \rho_4}{\rho_1 h_1 h_3}$	$\frac{\rho_1 \rho_4 h_1}{\rho_3 h_3 h_4}$										

Effective parameter = 4.4

Layer	Resistivity	Thickness
1	0.1	22
2	125.84	63.46
3	0.39	276.61
4	0.52	337.52
5	3.06	364.21
6	14.16	584.97
7	89.47	2449.07
8	93.74	0

Calibration factor: 1.1
Error: 0.998



Layer resistivities - 68 percent confidence interval (damped)				
I	RO(I)	BOUND(1)	BOUND(2)	IMPORTANCE
1	0.1044	0.0954	0.1143	0.859
2	125.8368	110.7722	142.9502	0.7459
3	0.3948	0.3435	0.4537	0.8915
4	0.5216	0.4876	0.5581	0.3071
5	3.0577	3.0278	3.0878	0.0421
6	14.16	14.1212	14.199	0.0115
7	89.4706	89.3751	89.5663	0.0043
8	93.7395	93.7058	93.7732	0.0013

Layer depths (to base) - 68 percent confidence interval (damped)				
I	Z(I)	BOUND(1)	BOUND(2)	IMPORTANCE
1	22.0005	20.3388	23.7979	0.7452
2	85.4634	79.1567	92.2726	0.9533
3	362.0731	351.8933	372.5472	0.1432
4	699.5906	630.4316	776.3364	0.4461
5	1063.7968	1041.4006	1086.6744	0.0899
6	1648.77	1638.6187	1658.9843	0.0253
7	4097.8442	4097.71	4097.9785	0.0001

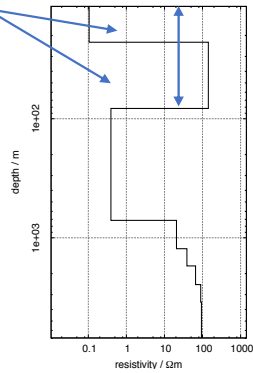
Figure E. 16 Resolved combination and importance analyzed using Eigenparameter for Marquardt inversion of Rx3 E-field (Ex), roadside transmitter configuration (5th May 2015). Starting model generated using cumulative conductance.

Transform Original par. \ par.	P1	P2	P3	P4	P5	P6	P7	P8	P9	P10	P11	P12	P13	P14	P15
ρ_1	0.7	-0.3	0.2	-0.4	0.4	-0.3	0.0	0.0	0.0	0.0	0.0	0.0	0.0	0.0	0.0
ρ_2	0.3	0.3	0.2	0.7	0.0	-0.6	0.0	0.0	0.0	0.0	0.0	0.0	0.0	0.0	0.0
ρ_3	0.0	0.5	0.8	-0.3	-0.3	0.2	0.0	0.0	0.0	0.0	0.0	0.0	0.0	0.0	0.0
ρ_4	0.0	0.0	0.0	0.0	0.0	0.0	0.8	0.4	-0.4	-0.1	-0.1	-0.1	0.0	-0.1	-0.2
ρ_5	0.0	0.0	0.0	0.0	0.0	0.0	-0.1	0.5	-0.1	0.5	0.6	-0.2	0.3	0.2	0.2
ρ_6	0.0	0.0	0.0	0.0	0.0	0.0	-0.1	0.1	-0.1	0.7	-0.4	0.1	-0.4	0.1	-0.3
ρ_7	0.0	0.0	0.0	0.0	0.0	0.0	-0.3	0.1	-0.2	-0.2	-0.3	0.0	0.7	0.1	-0.5
ρ_8	0.0	0.0	0.0	0.0	0.0	0.0	-0.5	0.2	-0.7	-0.2	0.1	-0.1	-0.3	-0.2	0.1
h_1	-0.7	0.1	0.1	-0.3	0.5	-0.5	0.0	0.0	0.0	0.0	0.0	0.0	0.0	0.0	0.0
h_2	0.2	0.8	-0.5	-0.3	0.1	0.0	0.0	0.0	0.0	0.0	0.0	0.0	0.0	0.0	0.0
h_3	0.0	-0.1	-0.2	-0.4	-0.7	-0.5	0.0	0.0	0.0	0.0	0.0	0.0	0.0	0.0	0.0
h_4	0.0	0.0	0.0	0.0	0.0	0.0	0.1	-0.6	-0.3	0.1	0.0	-0.7	0.1	0.2	-0.1
h_5	0.0	0.0	0.0	0.0	0.0	0.0	0.2	-0.2	-0.4	0.3	-0.2	0.5	0.3	0.1	0.5
h_6	0.0	0.0	0.0	0.0	0.0	0.0	0.1	-0.2	-0.3	0.0	0.5	0.5	-0.1	0.3	-0.5
h_7	0.0	0.0	0.0	0.0	0.0	0.0	0.0	-0.2	0.0	0.3	0.2	0.1	0.2	-0.8	-0.2
Damping Factor	1.0	1.0	1.0	0.9	0.4	0.0	0.0	0.0	0.0	0.0	0.0	0.0	0.0	0.0	0.0
Resolved combination	$\frac{\rho_1 \rho_2}{h_1}$	$\frac{\rho_2 \rho_3 h_2}{\rho_1}$	$\frac{\rho_3}{h_2}$	$\frac{\rho_2}{\rho_1 \rho_3 h_1 h_2 h_3}$	$\frac{\rho_1 h_1}{\rho_2 h_3}$										

Effective parameter 4.3

Layer	Resistivity	Thickness
1	0.11	22.79
2	142.04	59.23
3	0.39	631.69
4	20.68	521.23
5	38.92	486.66
6	65.56	749.19
7	89.63	996.74
8	93.66	0

Calibration factor: 0.9486
Error: 0.82



Layer resistivities - 68 percent confidence interval (damped)				
I	RO(I)	BOUND(1)	BOUND(2)	IMPORTANCE
1	0.1052	0.0952	0.1163	0.8601
2	142.0448	124.3256	162.2894	0.6904
3	0.3921	0.3422	0.4492	0.9104
4	20.6774	20.6414	20.7135	0.0068
5	38.917	38.8905	38.9436	0.0025
6	65.5634	65.531	65.5958	0.0018
7	89.6313	89.6015	89.6612	0.0012
8	93.6648	93.6196	93.7101	0.0017

Layer depths (to base) - 68 percent confidence interval (damped)				
I	Z(I)	BOUND(1)	BOUND(2)	IMPORTANCE
1	22.7921	21.0183	24.7155	0.7485
2	82.0222	75.5315	89.0707	0.9551
3	713.7148	623.0542	817.5676	0.5234
4	1234.9403	1232.9392	1236.9447	0.0063
5	1721.6045	1720.0419	1723.1686	0.0036
6	2470.7915	2469.875	2471.7085	0.0012
7	3467.5288	3467.2659	3467.7917	0.0003

anisotropy coefficients - 68 percent confidence interval (damped)				
---	--	--	--	--

Figure E. 17 Resolved combination and importance analyzed using Eigenparameter for Marquardt inversion of Rx3 E-field (Ex), roadside transmitter configuration (5th May 2015). Starting model generated using cumulative transverse resistance.

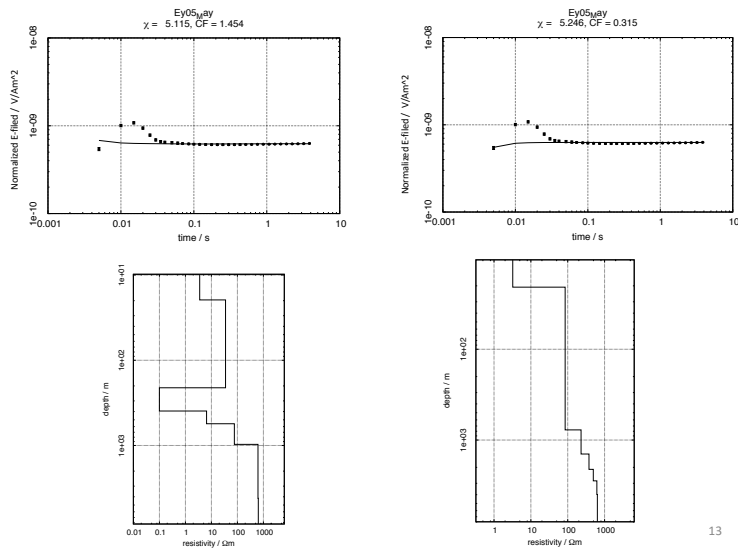
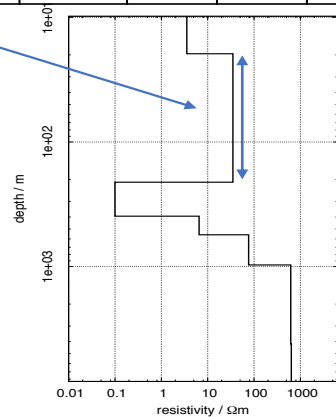


Figure E. 18 Marquardt inversion of Rx1 E-field (E_y) broadside transmitter configuration, data measured on 5th May 2015. The starting models generated using cumulative conductance (left) and transverse resistance (right).

Transform Original par	P1	P2	P3	P4	P5	P6	P7	P8	P9	P10	P11	P12	P13
ρ_1	0.2	-0.3	0.1	-0.1	0.4	-0.4	0.7	-0.2	0.1	-0.1	0.0	0.0	0.0
ρ_2	-0.6	0.5	-0.4	-0.3	0.3	-0.4	0.0	0.0	0.0	0.0	0.0	0.0	0.0
ρ_3	0.0	0.0	0.3	-0.1	0.8	0.5	-0.3	0.1	-0.1	0.0	0.0	0.0	0.0
ρ_4	0.0	0.0	0.0	0.0	0.0	0.0	-0.1	-0.6	-0.7	-0.3	-0.1	0.0	0.0
ρ_5	0.0	0.0	0.0	0.0	0.0	0.0	0.0	0.1	-0.1	-0.1	0.7	-0.7	0.1
ρ_6	0.0	0.0	0.0	0.0	0.0	0.0	0.0	0.0	0.0	0.1	-0.5	-0.6	-0.6
ρ_7	0.0	0.0	0.0	0.0	0.0	0.0	0.0	0.0	0.0	0.0	-0.5	-0.4	0.6
h_1	-0.1	0.4	-0.1	0.0	-0.2	0.6	0.6	-0.2	0.1	-0.1	0.0	0.0	0.0
h_2	-0.7	-0.3	0.2	0.6	0.0	0.0	0.1	0.0	0.0	0.0	0.0	0.0	0.0
h_3	0.0	-0.5	-0.8	0.1	0.2	0.2	-0.1	0.0	0.0	0.0	0.0	0.0	0.0
h_4	0.0	0.0	0.0	0.0	0.0	0.0	-0.3	-0.7	0.7	-0.1	0.1	-0.1	0.0
h_5	0.0	0.0	0.0	0.0	0.0	0.0	0.1	-0.2	-0.2	0.9	0.1	0.0	0.0
h_6	0.0	0.0	0.0	0.0	0.0	0.0	0.0	0.0	0.0	0.0	-0.2	-0.1	0.4
Damping Factor	1.0	0.1	0.0	0.0	0.0	0.0	0.0	0.0	0.0	0.0	0.0	0.0	0.0
Resolved combination	$\frac{1}{\rho_2 h_2}$												

Effective parameter: 1.1

Layer_No.	Resistivity	Thickness
1	3.19	17.06
2	39.07	166.27
3	0.09	186.97
4	6.51	161.79
5	76.22	414.69
6	619.09	3202.95
7	638.08	0.00
# Calibration factor:	1.5826	
# Error:	5.106	



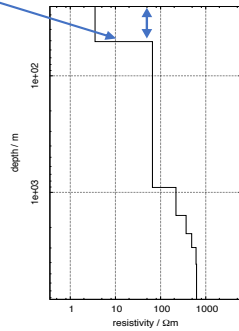
Layer resistivities - 68 percent confidence interval (damped)				
l	RO(l)	BOUND(1)	BOUND(2)	IMPORTANCE
1	3.1877	3.0639	3.3165	0.1699
2	39.0706	36.64	41.67	0.56
3	0.0898	0.09	0.09	0.01
4	6.5132	6.51	6.52	0.00
5	76.2171	76.21	76.22	0.00
6	619.093	619.09	619.10	0.00
7	638.077	638.08	638.08	0.00
Layer depths (to base) - 68 percent confidence interval (damped)				
l	Z(l)	BOUND(1)	BOUND(2)	IMPORTANCE
1	17.064	16.3602	17.7981	0.105
2	183.33	176.11	190.85	0.71
3	370.299	343.61	399.06	0.04
4	532.0936	531.46	532.73	0.00
5	946.7877	946.74	946.84	0.00
6	4149.7417	4149.74	4149.75	0.00

Figure E. 19 Resolved combination and importance analyzed using Eigenparameter for Marquardt inversion of Rx1 E-field (E_y), broadside transmitter configuration (5th May 2015). Starting model generated using cumulative conductance.

Transform Original par.	P1	P2	P3	P4	P5	P6	P7	P8	P9	P10	P11	P12	P13
ρ_1	0.4	-0.6	0.0	-0.6	-0.2	0.2	0.0	0.0	0.0	0.0	0.0	-0.012	-0.008
ρ_2	0.3	0.2	0.8	0.2	0.1	-0.4	0.0	0.0	0.0	-0.1	0.0	0.014	-0.019
ρ_3	0.0	0.0	0.2	-0.2	-0.4	0.1	0.0	0.1	-0.1	0.3	-0.1	0.689	-0.378
ρ_4	0.0	0.0	0.1	-0.1	-0.4	0.0	0.1	0.0	0.0	0.2	-0.4	-0.608	-0.138
ρ_5	0.0	0.0	0.0	0.0	-0.3	-0.1	0.1	-0.2	0.1	0.0	-0.4	0.26	0.811
ρ_6	0.0	0.0	0.0	0.0	-0.2	-0.1	0.1	-0.2	0.0	0.2	-0.3	-0.138	-0.293
ρ_7	0.0	0.0	0.0	0.0	0.2	0.2	0.2	-0.8	0.4	0.0	0.0	0.098	-0.16
h_1	-0.4	0.5	0.0	-0.7	0.2	-0.4	0.0	0.0	0.0	0.0	0.0	-0.009	0.002
h_2	-0.1	-0.2	-0.5	0.3	-0.1	-0.8	0.1	0.0	0.1	-0.1	0.0	0.169	-0.148
h_3	0.0	0.0	-0.1	0.2	0.6	-0.1	0.2	-0.1	-0.4	0.6	-0.2	0.009	0.057
h_4	0.0	0.0	0.0	0.0	0.3	0.1	-0.6	0.1	0.2	-0.3	-0.6	0.145	-0.161
h_5	0.0	0.0	0.0	0.0	0.2	0.1	0.7	0.4	0.4	-0.2	-0.2	0.093	-0.075
h_6	0.0	0.0	0.0	0.0	0.0	0.0	0.3	-0.2	-0.7	-0.6	-0.2	0.034	-0.106
Damping Factor	1.0	0.3	0.0	0.0	0.0	0.0	0.0	0.0	0.0	0	0	0	0
Resolved combination	$\frac{\rho_1}{h_1}$	$\frac{h_1}{\rho_1}$											

Effective parameter: 1.3

Layer No.	Resistivity	Thickness
1	3.53	50.88
2	66	856.37
3	218.8	670.46
4	367.36	682.96
5	487.63	715.14
6	610.71	1163.34
7	625.78	0
# Calibration factor:	3.963	
# Error:	5.246	



Layer resistivities - 68 percent confidence interval (damped)				
I	RO(I)	BOUND(1)	BOUND(2)	IMPORTANCE
1	3.5349	3.2726	3.8182	0.4739
2	65.9977	64.7305	67.2898	0.2851
3	218.7983	217.7605	219.841	0.0197
4	367.3606	366.8895	367.8323	0.0051
5	487.6287	487.3958	487.8617	0.0019
6	610.7118	610.5428	610.8807	0.0012
7	625.7784	625.6442	625.9126	0.0011
Layer depths (to base) - 68 percent confidence interval (damped)				
I	Z(I)	BOUND(1)	BOUND(2)	IMPORTANCE
1	50.8832	48.0286	53.9074	0.4453
2	907.2534	890.7225	924.0911	0.0805
3	1577.718	1573.3517	1582.0964	0.011
4	2260.6787	2259.1406	2262.2178	0.0027
5	2975.8184	2974.9761	2976.6609	0.0012
6	4139.1572	4139.0903	4139.2241	0.0001

Figure E. 20 Resolved combination and importance analyzed using Eigenparameter for Marquardt inversion of Rx1 E-field (E_y), broadside transmitter configuration (5th May 2015). Starting model generated using cumulative transverse resistance.

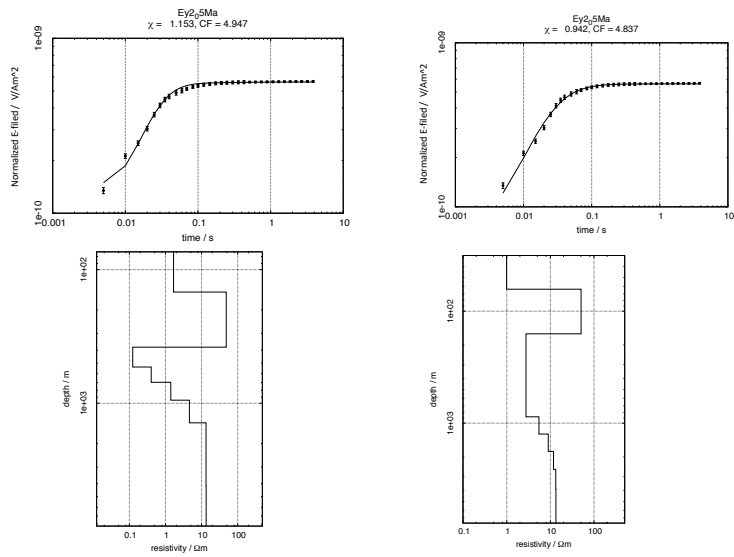
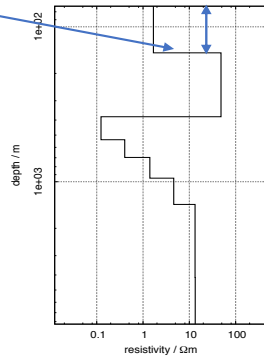


Figure E. 21 Marquardt inversion of Rx2 E-field (Ey) broadside transmitter configuration, data measured on 5th May 2015. The starting models generated using cumulative conductance (left) and transverse resistance (right).

Transform par Original par	P1	P2	P3	P4	P5	P6	P7	P8	P9	P10	P11	P12	P13	P14	P15
ρ_1	0.5	-0.7	0.4	-0.3	0.3	0.0	0.1	0.0	0.0	0.0	0.0	0.0	0.0	0.0	0.0
ρ_2	0.1	0.1	-0.2	0.2	0.3	0.7	0.5	-0.1	0.0	0.0	0.0	0.0	0.0	0.0	0.0
ρ_3	0.0	0.0	0.0	0.3	0.6	0.2	-0.7	0.1	0.0	0.0	0.0	0.0	0.0	0.0	0.0
ρ_4	0.0	0.0	0.0	0.0	0.0	-0.1	0.1	0.2	-0.2	0.6	-0.7	-0.2	0.1	-0.1	0.0
ρ_5	0.0	0.0	0.0	0.0	0.0	0.0	0.0	0.1	0.2	0.0	0.3	-0.9	0.3	0.1	0.0
ρ_6	0.0	0.0	0.0	0.0	0.0	0.0	0.0	0.0	0.2	0.0	0.1	-0.2	-0.5	-0.8	0.0
ρ_7	0.0	0.0	0.0	0.0	0.0	0.0	0.0	0.0	0.1	0.0	0.0	-0.2	-0.7	0.5	-0.4
ρ_8	0.0	0.0	0.0	0.0	0.0	0.0	0.0	0.0	0.0	0.0	0.0	-0.1	-0.3	0.0	0.3
h_1	-0.5	0.1	0.8	-0.1	0.2	0.1	0.2	0.0	0.0	0.0	0.0	0.0	0.0	0.0	0.0
h_2	0.2	0.5	-0.1	-0.7	0.5	-0.2	0.1	0.0	0.0	0.0	0.0	0.0	0.0	0.0	0.0
h_3	0.0	0.0	0.0	-0.5	-0.4	0.6	-0.3	0.3	0.0	0.0	0.0	0.0	0.0	0.0	0.0
h_4	0.0	0.0	0.0	-0.1	-0.1	0.1	-0.2	-0.9	0.2	0.2	-0.1	-0.1	0.0	0.0	0.0
h_5	0.0	0.0	0.0	0.0	0.0	0.0	0.0	-0.3	-0.9	-0.3	0.0	-0.3	-0.1	-0.1	0.0
h_6	0.0	0.0	0.0	0.0	0.0	0.0	0.0	0.0	-0.3	0.7	0.6	0.1	0.0	0.0	0.0
h_7	0.0	0.0	0.0	0.0	0.0	0.0	0.0	0.0	0.0	0.0	0.0	-0.1	-0.3	0.2	0.8
Damping Factor	1.0	0.1	0.0	0.0	0.0	0.0	0.0	0.0	0.0	0.0	0.0	0.0	0.0	0.0	0.0
Resolved combination	$\frac{\rho_1}{h_1}$	$\frac{h_2}{\rho_1}$													

Effective parameter: 2

Layer_No.	Resistivity	Thickness
1	1.68	147.24
2	48.35	233.54
3	0.12	154.8
4	0.4	161.45
5	1.4	251.74
6	4.6	452.9
7	13.3	2749.97
8	13.4	0
# Calibration factor:	4.9468	
# Error:	1.153	



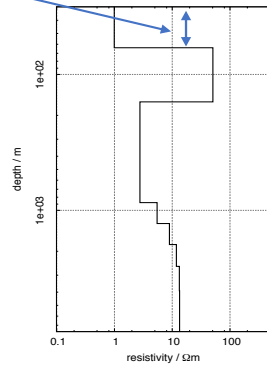
Layer resistivities - 68 percent confidence interval (damped)				
I	RO(I)	BOUND(1)	BOUND(2)	IMPORTANCE
1	1.6758	1.5967	1.7588	0.9286
2	48.3491	47.3291	49.391	0.2455
3	0.1236	0.123	0.1242	0.0312
4	0.402	0.4017	0.4022	0.0013
5	1.4019	1.4016	1.4021	0.0004
6	4.6019	4.6016	4.6021	0.0001
7	13.3007	13.3005	13.301	0
8	13.3999	13.3998	13.3999	0
Layer depths (to base) - 68 percent confidence interval (damped)				
I	Z(I)	BOUND(1)	BOUND(2)	IMPORTANCE
1	147.2371	135.4278	160.0763	0.9557
2	380.7753	370.9402	390.8711	0.5537
3	535.5708	531.6244	539.5465	0.012
4	697.0256	695.9119	698.141	0.0033
5	948.7689	948.4048	949.1331	0.001
6	1401.6702	1401.5631	1401.7772	0.0002
7	4151.6431	4151.6392	4151.647	0

Figure E. 22 Resolved combination and importance analyzed using Eigenparameter for Marquardt inversion of Rx2 E-field (Ey), broadside transmitter configuration (5th May 2015). Starting model generated using cumulative conductance.

Transform Original par	par	P1	P2	P3	P4	P5	P6	P7	P8	P9	P10	P11	P12	P13	P14	P15
ρ_1		0.4	-0.7	0.3	-0.2	0.1	-0.2	0.3	-0.2	0.0	0.0	0.0	0.0	0.0	0.0	0.0
ρ_2		0.2	0.1	-0.2	0.6	-0.4	-0.3	0.4	-0.3	0.1	0.0	0.1	0.0	0.0	0.0	0.0
ρ_3		0.1	0.2	0.0	-0.6	-0.7	0.2	0.1	-0.1	0.0	0.0	0.0	0.0	0.0	0.0	0.0
ρ_4		0.0	0.0	0.0	0.0	0.1	0.3	0.0	-0.3	0.5	0.1	-0.7	0.1	-0.3	0.1	0.2
ρ_5		0.0	0.0	0.0	0.0	0.0	0.1	-0.2	-0.3	0.4	0.0	0.0	0.3	0.6	-0.2	-0.4
ρ_6		0.0	0.0	0.0	0.0	0.0	0.0	-0.1	0.0	0.5	-0.2	0.5	-0.2	0.2	0.2	0.6
ρ_7		0.0	0.0	0.0	0.0	0.0	0.0	-0.1	0.1	0.5	0.2	0.4	-0.1	-0.4	0.0	-0.5
ρ_8		0.0	0.0	0.0	0.0	0.0	0.0	0.0	0.0	0.1	0.3	0.1	0.0	-0.3	0.0	0.0
h_1		-0.5	0.4	0.4	-0.2	0.2	-0.3	0.4	-0.3	0.1	0.0	0.1	0.0	0.0	0.0	0.0
h_2		0.4	0.3	-0.6	-0.4	0.4	-0.2	0.2	-0.2	0.0	0.0	0.0	0.0	0.0	0.0	0.0
h_3		0.0	0.0	0.0	-0.1	-0.2	-0.7	-0.6	-0.1	0.0	0.1	-0.2	0.0	-0.1	0.0	0.1
h_4		0.0	0.0	0.0	0.0	-0.1	-0.3	0.3	0.7	0.4	-0.1	-0.3	0.3	0.1	0.1	0.0
h_5		0.0	0.0	0.0	0.0	0.0	0.0	0.2	0.1	0.1	0.6	-0.2	-0.6	0.4	-0.2	0.1
h_6		0.0	0.0	0.0	0.0	0.0	0.0	0.0	0.0	-0.1	0.6	0.2	0.6	0.1	0.3	0.3
h_7		0.0	0.0	0.0	0.0	0.0	0.0	0.0	0.0	0.1	0.0	0.1	0.3	-0.2	-0.9	0.3
Damping Factor		1.0	1.0	0.6	0.0	0.0	0.0	0.0	0.0	0.0	0.0	0.0	0.0	0.0	0.0	0.0
Resolved combination		$\frac{\rho_1}{h_1}$	$\frac{h_1 h_2}{\rho_1}$	$\frac{\rho_1 h_1}{h_2}$												

Effective parameter: 2.6

Layer No.	Resistivity	Thickness
1	0.99	63.65
2	50.59	95.53
3	2.76	717.97
4	5.47	373.64
5	8.94	534.65
6	11.82	797.94
7	13.3	1319.9
8	13.4	0
# Calibration factor: 4.8373		



Layer resistivities - 68 percent confidence interval (damped)				
l	RO(l)	BOUND(1)	BOUND(2)	IMPORTANCE
1	0.9923	0.9572	1.0286	0.839
2	50.5935	49.6564	51.5482	0.2835
3	2.7623	2.7422	2.7827	0.1875
4	5.4678	5.4625	5.4732	0.0101
5	8.9401	8.9372	8.943	0.0033
6	11.8171	11.816	11.8181	0.0009
7	13.305	13.3047	13.3053	0.0002
8	13.4009	13.4008	13.4009	0.0001
Layer depths (to base) - 68 percent confidence interval (damped)				
l	Z(l)	BOUND(1)	BOUND(2)	IMPORTANCE
1	63.6541	61.3532	66.0414	0.6754
2	159.1852	151.5704	167.1826	0.5925
3	877.1567	874.5564	879.7648	0.0313
4	1250.8003	1249.774	1251.8274	0.0081
5	1785.4509	1785.213	1785.6888	0.0013
6	2583.3901	2583.3535	2583.4268	0.0001
7	3903.2866	3903.2852	3903.2881	0

Figure E. 23 Resolved combination and importance analyzed using Eigenparameter for Marquardt inversion of Rx2 E-field (Ey), broadside transmitter configuration (5th May 2015). Starting model generated using cumulative transverse resistance.

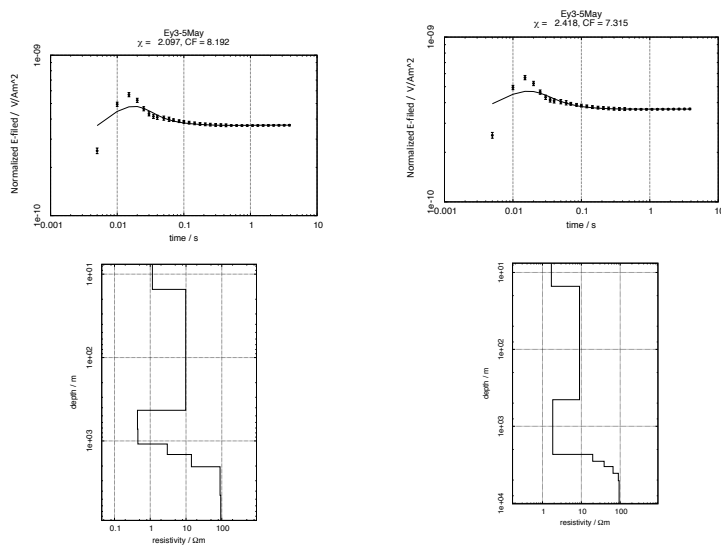
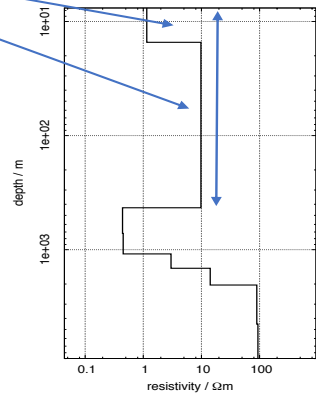


Figure E.24 Marquardt inversion of Rx3 E-field (Ey) broadside transmitter configuration, data measured on 5th May 2015. The starting models generated using cumulative conductance (left) and transverse resistance (right).

Transform Original par.	par.	P1	P2	P3	P4	P5	P6	P7	P8	P9	P10	P11	P12	P13	P14	P15
ρ_1		0.1	-0.6	0.1	-0.1	0.6	-0.1	-0.1	-0.5	0.0	0.0	0.0	0.0	0.0	0.0	0.0
ρ_2		-0.6	-0.1	0.8	0.3	-0.1	-0.1	0.0	0.0	0.0	0.0	0.0	0.0	0.0	0.0	0.0
ρ_3		0.0	0.0	-0.2	0.2	0.1	-0.8	0.5	0.1	-0.1	0.0	0.0	0.0	0.0	0.0	0.0
ρ_4		0.0	0.0	0.1	-0.4	0.0	0.3	0.8	-0.2	-0.1	0.1	0.0	0.0	0.0	0.0	0.0
ρ_5		0.0	0.0	0.0	0.0	0.0	0.0	0.0	0.0	-0.1	0.1	0.1	0.6	-0.8	-0.1	-0.1
ρ_6		0.0	0.0	0.0	0.0	0.0	0.0	0.0	0.0	-0.1	0.0	-0.2	0.8	0.6	0.0	0.3
ρ_7		0.0	0.0	0.0	0.0	0.0	0.0	0.0	0.0	0.0	0.0	0.1	0.2	0.3	0.0	-0.8
ρ_8		0.0	0.0	0.0	0.0	0.0	0.0	0.0	0.0	0.0	0.0	0.0	0.1	0.0	0.7	0.3
h_1		-0.1	0.5	-0.1	0.1	-0.2	-0.2	-0.1	-0.8	0.0	0.0	0.0	0.0	0.0	0.0	0.0
h_2		-0.6	0.4	-0.3	-0.2	0.5	0.1	0.0	0.1	0.0	0.0	0.0	0.0	0.0	0.0	0.0
h_3		0.0	0.0	0.0	0.0	0.0	-0.1	-0.1	0.0	0.3	0.9	0.2	0.0	0.0	0.0	0.0
h_4		0.0	0.0	-0.2	0.8	0.2	0.4	0.2	-0.1	-0.2	0.1	0.0	0.0	0.0	0.0	0.0
h_5		0.0	0.0	0.0	0.1	0.0	0.1	0.2	0.0	0.9	-0.3	-0.2	0.1	-0.1	0.0	-0.1
h_6		0.0	0.0	0.0	0.0	0.0	0.0	0.1	0.0	0.1	-0.2	0.9	0.1	0.1	0.0	0.1
h_7		0.0	0.0	0.0	0.0	0.0	0.0	0.0	0.0	0.0	0.0	0.0	0.0	0.0	0.7	-0.3
Damping Factor		1.0	1.0	0.9	0.2	0.0	0.0	0.0	0.0	0.0	0.0	0.0	0.0	0.0	0.0	0.0
Resolved combination		$\frac{1}{\rho_2 h_2}$	$\frac{h_1 h_2}{\rho_1}$	$\frac{\rho_2}{h_2}$												

Effective parameter: 3.1

Layer No.	Resistivity	Thickness
1	1.15	15.24
2	9.8	413.99
3	0.44	291.4
4	0.45	368.19
5	3	365.96
6	14.16	583.74
7	89.52	2448.84
8	93.6	0
# Calibration factor:	8.1924	
# Error:	2.097	



Layer resistivities - 68 percent confidence interval (damped)				
I	RO(I)	BOUND(1)	BOUND(2)	IMPORTANCE
1	1.15	1.09	1.21	0.58
2	9.80	7.98	12.05	0.91
3	0.44	0.42	0.46	0.15
4	0.45	0.42	0.48	0.15
5	3.00	2.98	3.02	0.01
6	14.16	14.14	14.17	0.00
7	89.52	89.51	89.53	0.00
8	93.60	93.60	93.60	0.00
Layer depths (to base) - 68 percent confidence interval (damped)				
I	Z(I)	BOUND(1)	BOUND(2)	IMPORTANCE
1	15.24	14.65	15.85	0.50
2	429.22	395.35	466.00	0.79
3	720.63	717.42	723.85	0.01
4	1088.82	953.46	1243.38	0.27
5	1454.78	1432.88	1477.01	0.03
6	2038.52	2034.48	2042.56	0.00
7	4487.36	4487.33	4487.39	0.00

Figure E. 25 Resolved combination and importance analyzed using Eigenparameter for Marquardt inversion of Rx3 E-field (Ey), broadside transmitter configuration (5th May 2015). Starting model generated using cumulative conductance.

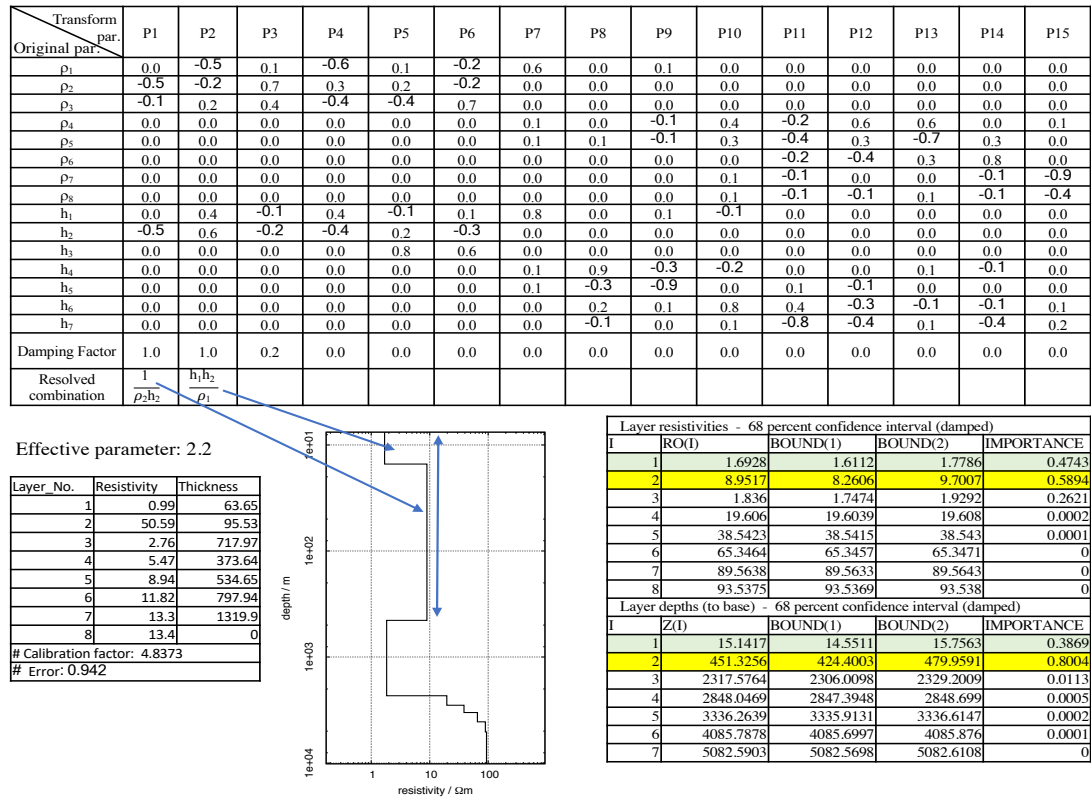


Figure E. 26 Resolved combination and importance analyzed using Eigenparameter for Marquardt inversion of Rx3 E-field (Ey), broadside transmitter configuration (5th May 2015). Starting model generated using cumulative transverse resistance.

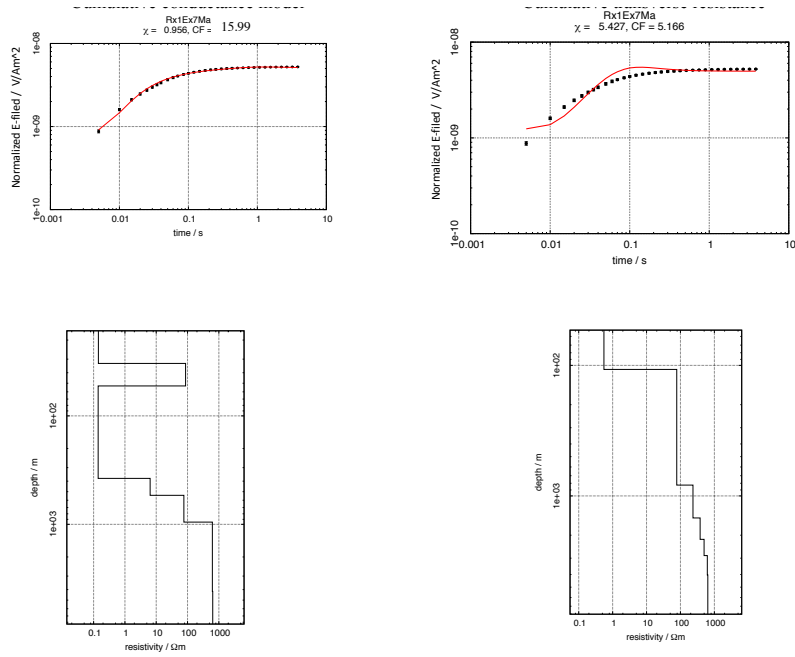


Figure E. 27 Marquardt inversion of Rx1 E-field (Ex) inline transmitter configuration, data measured on 7th May 2015. The starting models generated using cumulative conductance (left) and transverse resistance (right).

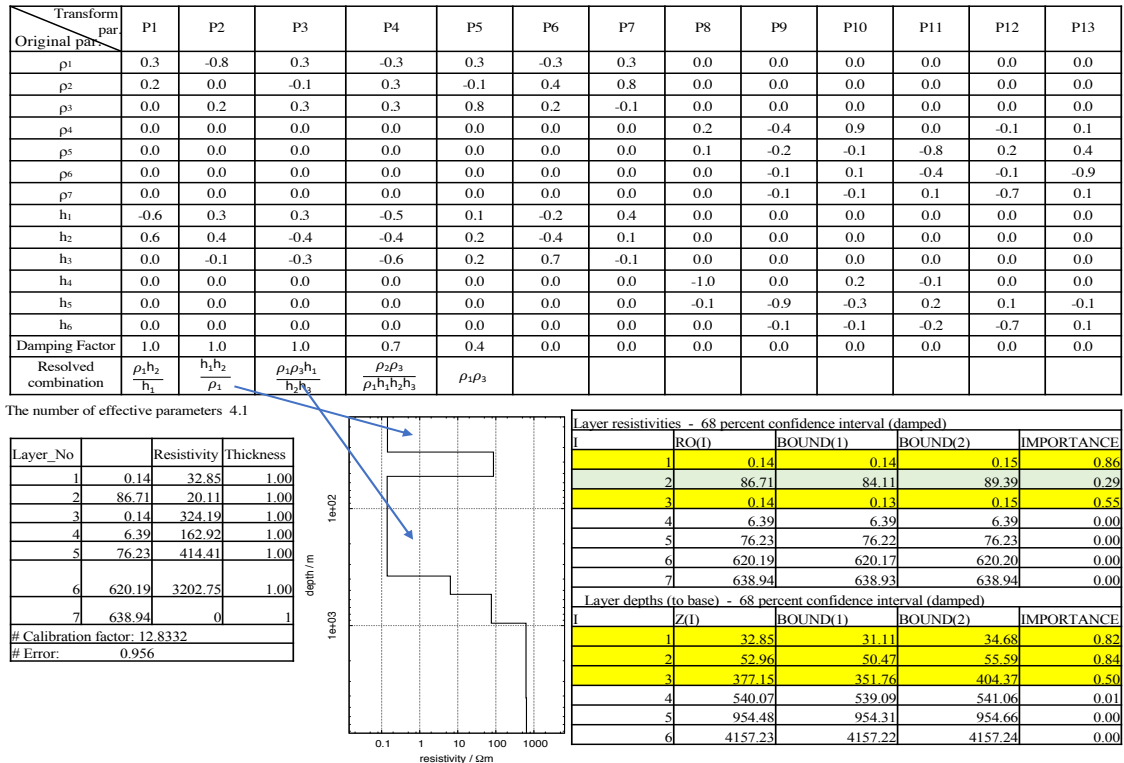
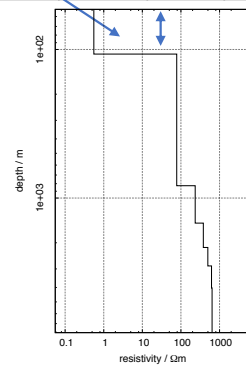


Figure E. 28 Resolved combination and importance analyzed using Eigenparameter for Marquardt inversion of Rx1 E-field (Ex), inline transmitter configuration (7th May 2015). Starting model generated using cumulative conductance.

Transform Original par.	P1	P2	P3	P4	P5	P6	P7	P8	P9	P10	P11	P12	P13
ρ^1	0.6	-0.6	0.5	0.0	0.0	0.0	0.0	0.0	0.0	0.0	0.0	0.0	0.0
ρ^2	0.0	0.0	0.0	1.0	-0.2	0.0	0.1	0.0	0.0	0.0	0.0	0.0	0.0
ρ^3	0.0	0.0	0.0	0.0	0.3	-0.3	0.3	-0.1	0.1	-0.1	0.4	0.7	0.2
ρ^4	0.0	0.0	0.0	0.0	0.1	-0.2	0.3	-0.1	0.1	-0.2	0.3	-0.1	-0.6
ρ^5	0.0	0.0	0.0	0.0	0.0	-0.1	0.1	0.0	0.3	-0.3	0.4	-0.6	0.0
ρ^6	0.0	0.0	0.0	0.0	0.0	-0.1	0.0	0.2	0.3	-0.1	0.1	-0.2	0.7
ρ^7	0.0	0.0	0.0	0.0	0.0	-0.8	-0.5	0.1	-0.2	0.1	-0.1	0.0	-0.1
h_1	-0.6	0.2	0.8	0.0	0.0	0.0	0.0	0.0	0.0	0.0	0.0	0.0	0.0
h_2	0.0	0.0	0.0	-0.2	-0.9	-0.2	0.2	0.0	0.0	0.0	0.1	0.2	0.0
h_3	0.0	0.0	0.0	0.0	-0.2	0.3	-0.6	-0.1	0.0	-0.5	0.4	0.2	-0.1
h_4	0.0	0.0	0.0	0.0	0.0	0.1	-0.2	0.1	0.4	0.7	0.5	0.1	-0.2
h_5	0.0	0.0	0.0	0.0	0.0	0.1	0.1	0.9	-0.3	-0.1	0.2	0.1	-0.1
h_6	0.0	0.0	0.0	0.0	0.0	0.0	-0.1	0.3	0.7	-0.2	-0.5	0.2	-0.2
Damping Factor	1.0	1.0	1.0	0.0	0.0	0.0	0.0	0.0	0.0	0.0	0.0	0.0	0.0
Resolved combination	$\frac{\rho_1}{h_1}$	$\frac{1}{\rho_1}$	$\frac{h_1}{\rho_1}$										

The number of effective parameters : 4.6

Layer No.	Resistivity	Thickness
1	0.55	107.4
2	77.64	718.34
3	234.21	649.31
4	379.67	676.4
5	496.66	712.76
6	620.17	1162.95
7	639.64	0
# Calibration factor:	5.1661	
# Error:	5.427	



Layer resistivities - 68 percent confidence interval (damped)				
I	RO(I)	BOUND(1)	BOUND(2)	IMPORTANCE
1	0.5547	0.4496	0.6843	0.9985
2	77.6409	77.1124	78.173	0.0301
3	234.2132	233.8818	234.545	0.0046
4	379.67	379.4726	379.8675	0.0017
5	496.6624	496.5424	496.7824	0.0009
6	620.1744	620.0669	620.282	0.0007
7	639.6394	639.4937	639.7851	0.0011
Layer depths (to base) - 68 percent confidence interval (damped)				
I	Z(I)	BOUND(1)	BOUND(2)	IMPORTANCE
1	107.4047	81.1548	142.1452	0.9967
2	825.7457	822.3566	829.1487	0.0139
3	1475.0583	1473.734	1476.3838	0.0029
4	2151.4587	2150.8425	2152.075	0.001
5	2864.2212	2863.7139	2864.7285	0.0006
6	4027.1699	4027.1516	4027.1882	0

Figure E. 29 Resolved combination and importance analyzed using Eigenparameter for Marquardt inversion of Rx1 E-field (Ex), inline transmitter configuration (7th May 2015). Starting model generated using cumulative transverse resistance.

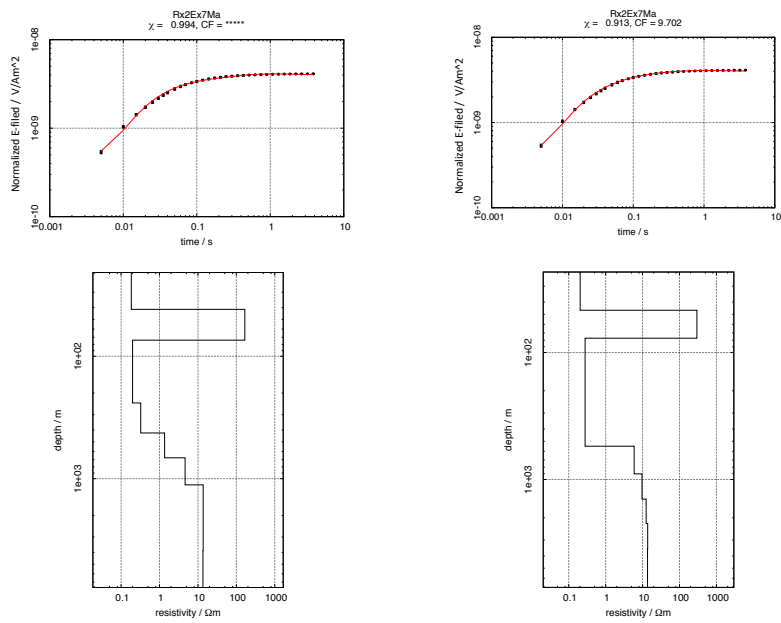
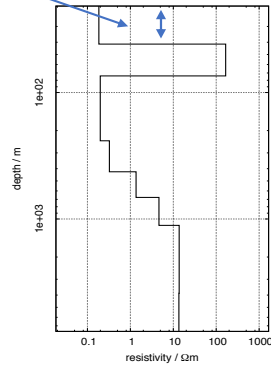


Figure E. 30 Marquardt inversion of Rx2 E-field (Ex) inline transmitter configuration, data measured on 7th May 2015. The starting models generated using cumulative conductance (left) and transverse resistance (right).

Transform Original par.	P1	P2	P3	P4	P5	P6	P7	P8	P9	P10	P11	P12	P13
ρ_1	0.4	-0.7	0.3	-0.5	0.2	-0.1	0.0	-0.2	0.0	0.0	0.0	0.0	0.0
ρ_2	0.2	0.0	-0.1	0.3	-0.1	0.2	0.2	-0.9	0.1	0.1	0.1	0.0	0.0
ρ_3	0.0	0.2	0.2	0.1	0.9	0.3	-0.1	0.0	0.0	0.0	0.0	0.0	0.0
ρ_4	0.0	0.0	0.1	0.2	0.1	-0.4	0.1	-0.1	-0.8	0.3	0.0	-0.1	0.0
ρ_5	0.0	0.0	0.0	0.0	0.0	-0.1	-0.1	0.0	0.1	0.1	0.0	-0.2	0.7
ρ_6	0.0	0.0	0.0	0.0	0.0	0.0	0.0	0.0	0.1	0.1	0.2	-0.3	0.5
ρ_7	0.0	0.0	0.0	0.0	0.0	0.0	0.0	0.0	-0.1	-0.4	0.6	-0.3	0.1
ρ_8	0.0	0.0	0.0	0.0	0.0	0.0	0.0	0.0	-0.1	-0.4	0.5	-0.1	-0.3
h_1	-0.6	0.3	0.5	-0.5	0.0	-0.1	0.1	-0.3	0.0	0.0	0.0	0.0	0.0
h_2	0.4	0.5	-0.5	-0.5	0.2	-0.2	0.0	-0.1	0.0	0.0	0.0	0.0	0.0
h_3	0.0	0.0	-0.1	-0.2	-0.2	0.4	-0.8	-0.1	-0.3	0.1	0.0	0.0	0.0
h_4	0.0	0.0	-0.1	-0.3	-0.1	0.6	0.6	0.2	-0.2	0.3	0.1	-0.1	0.0
h_5	0.0	0.0	0.0	-0.1	0.0	0.1	0.1	-0.1	-0.4	-0.6	-0.3	0.4	0.4
h_6	0.0	0.0	0.0	0.0	0.0	0.0	0.0	-0.1	-0.1	-0.3	-0.5	-0.8	-0.1
h_7	0.0	0.0	0.0	0.0	0.0	0.0	0.0	0.0	0.0	0.0	0.0	0.0	-0.1
Damping Factor	1.0	1.0	1.0	0.7	0.6	0.1	0.0	0.0	0.0	0.0	0.0	0.0	0.0
Resolved combination	$\frac{\rho_1 h_2}{h_1}$	$\frac{h_1 h_2}{\rho_1}$	$\frac{\rho_2 h_1}{h_2}$	$\frac{\rho_2}{\rho_1 h_1 h_2 h_4}$	ρ_3								

The number of effective parameters: 4.4

Layer_No.	Resistivity	Thickness
1	0.18	41.37
2	166.1	32.5
3	0.2	166.86
4	0.32	182.5
5	1.36	252.15
6	4.63	448.61
7	13.69	2750.22
8	13.48	0
# Calibration factor:	11.0432	
# Error:	0.994	



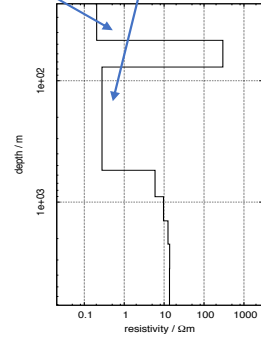
Layer resistivities - 68 percent confidence interval (damped)				
I	RO(I)	BOUND(1)	BOUND(2)	IMPORTANCE
1	0.1844	0.1699	0.2002	0.9096
2	166.1007	158.2198	174.3741	0.3007
3	0.1989	0.175	0.2261	0.577
4	0.3247	0.3128	0.3371	0.1724
5	1.356	1.3465	1.3654	0.0347
6	4.6296	4.6174	4.6418	0.0136
7	13.6882	13.651	13.7255	0.0122
8	13.4809	13.4756	13.4861	0.0016
Layer depths (to base) - 68 percent confidence interval (damped)				
I	Z(I)	BOUND(1)	BOUND(2)	IMPORTANCE
1	41.3696	38.1346	44.8791	0.8785
2	73.869	67.0935	81.3288	0.8823
3	240.731	230.0194	251.9414	0.2083
4	423.2358	403.4935	443.9441	0.2284
5	675.3889	667.7321	683.1336	0.0588
6	1124.0015	1099.1478	1128.8762	0.0214
7	3874.2236	3874.1331	3874.3142	0.0001

Figure E. 31 Resolved combination and importance analyzed using Eigenparameter for Marquardt inversion of Rx2 E-field (Ex), inline transmitter configuration (7th May 2015). Starting model generated using cumulative conductance.

Transform Original par. \ par.	P1	P2	P3	P4	P5	P6	P7	P8	P9	P10	P11	P12	P13
ρ^1	0.5	-0.6	0.4	-0.4	0.2	-0.1	0.1	0.0	0.0	0.0	0.0	0.0	0.0
ρ^2	0.1	0.0	-0.1	0.3	-0.1	0.1	0.9	0.0	0.0	0.0	0.0	0.0	0.0
ρ^3	0.0	0.2	0.2	0.3	0.9	0.1	0.0	0.0	0.0	0.0	0.0	0.0	0.0
ρ^4	0.0	0.0	0.0	0.0	0.0	0.0	0.0	-0.2	-0.4	0.0	0.4	-0.4	0.6
ρ^5	0.0	0.0	0.0	0.0	0.0	0.0	0.0	-0.1	0.3	-0.2	0.4	-0.1	0.2
ρ^6	0.0	0.0	0.0	0.0	0.0	0.0	0.0	-0.2	0.6	-0.1	0.3	-0.1	-0.2
ρ^7	0.0	0.0	0.0	0.0	0.0	0.0	0.0	-0.3	0.4	0.0	0.1	-0.1	0.0
ρ^8	0.0	0.0	0.0	0.0	0.0	0.0	0.0	-0.7	0.0	0.7	-0.1	0.1	-0.1
h_1	-0.6	0.3	0.5	-0.5	0.0	-0.1	0.3	0.0	0.0	0.0	0.0	0.0	0.0
h_2	0.3	0.5	-0.5	-0.6	0.2	-0.2	0.1	0.0	0.0	0.0	0.0	0.0	0.0
h_3	0.0	0.0	-0.1	-0.3	0.0	1.0	-0.1	0.0	0.0	0.0	0.0	0.0	0.0
h_4	0.0	0.0	0.0	0.0	0.0	0.0	0.0	-0.6	-0.3	-0.7	0.0	0.3	-0.2
h_5	0.0	0.0	0.0	0.0	0.0	0.0	0.0	0.2	-0.3	0.2	0.7	0.2	-0.5
h_6	0.0	0.0	0.0	0.0	0.0	0.0	0.0	-0.1	-0.2	-0.1	-0.2	-0.8	-0.5
h_7	0.0	0.0	0.0	0.0	0.0	0.0	0.0	0.0	-0.1	0.0	0.2	-0.3	-0.1
Damping Factor	1.0	1.0	1.0	0.7	0.4	0.0	0.0	0.0	0.0	0.0	0.0	0.0	0.0
Resolved combination	$\frac{\rho_2 h_2}{h_1}$	$\frac{h_1 h_2}{\rho_1}$	$\frac{\rho_1 h_1}{h_2}$	$\frac{\rho_2 \rho_3}{\rho_1 h_1 h_2 h_3}$	ρ_3								

Effective parameters : 4.123

Layer No.	Resistivity	Thickness
1	0.2	46.41
2	296.23	30.7
3	0.28	469.8
4	5.92	355.83
5	9.65	524.69
6	12.52	794.45
7	13.78	1319.85
8	13.65	0
# Calibration factor:	9.7017	
# Error:	0.913	



Layer resistivities - 68 percent confidence interval (damped)				
1	RO(I)	BOUND(1)	BOUND(2)	IMPORTANCE
1	0.2041	0.1894	0.2199	0.9088
2	296.2303	284.7075	308.2196	0.2371
3	0.278	0.2487	0.3108	0.5359
4	5.9198	5.913	5.9266	0.0061
5	9.6521	9.6443	9.66	0.004
6	12.516	12.5078	12.5242	0.0029
7	13.7842	13.7773	13.7911	0.002
8	13.6472	13.6428	13.6516	0.0013
Layer depths (to base) - 68 percent confidence interval (damped)				
1	Z(I)	BOUND(1)	BOUND(2)	IMPORTANCE
1	46.4113	42.8533	50.2647	0.8956
2	77.1077	70.0324	84.8978	0.8519
3	546.903	526.8027	567.7701	0.2002
4	902.7326	901.9727	903.4932	0.0047
5	1427.4255	1426.7803	1428.0712	0.0021
6	2221.8748	2221.5923	2222.1575	0.0005
7	3541.7212	3541.6799	3541.7625	0.0001

Figure E. 32 Resolved combination and importance analyzed using Eigenparameter for Marquardt inversion of Rx2 E-field (Ex), inline transmitter configuration (7th May 2015). Starting model generated using cumulative transverse resistance.

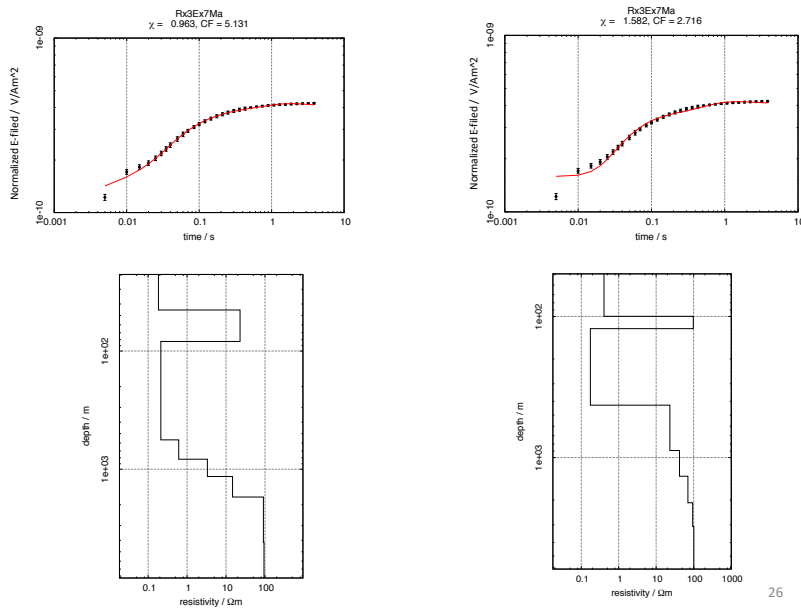
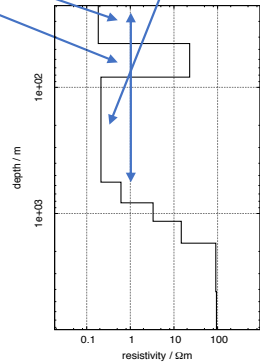


Figure E. 33 Marquardt inversion of Rx3 E-field (Ex) inline transmitter configuration, data measured on 7th May 2015. The starting models generated using cumulative conductance (left) and transverse resistance (right).

Transform Original par.	P1	P2	P3	P4	P5	P6	P7	P8	P9	P10	P11	P12	P13
ρ_1	0.0	-0.8	0.0	-0.1	0.0	-0.4	0.3	-0.1	0.0	0.0	0.0	0.0	0.0
ρ_2	0.3	0.2	0.0	0.1	0.0	0.3	0.9	-0.2	0.0	0.0	0.0	0.0	0.0
ρ_3	0.1	0.1	0.2	-0.6	-0.8	-0.1	0.0	-0.2	0.0	0.0	0.0	0.0	0.0
ρ_4	0.0	0.0	0.1	0.1	-0.1	-0.1	0.0	-0.1	-0.9	-0.4	0.3	0.0	0.0
ρ_5	0.0	0.0	0.0	0.0	0.0	0.0	0.0	-0.1	-0.1	0.1	0.0	-0.6	0.4
ρ_6	0.0	0.0	0.0	0.0	0.0	0.0	0.0	0.0	-0.1	0.2	-0.1	-0.8	-0.4
ρ_7	0.0	0.0	0.0	0.0	0.0	0.0	0.0	0.0	0.0	0.0	-0.2	0.0	0.5
ρ_8	0.0	0.0	0.0	0.0	0.0	0.0	0.0	0.0	0.0	0.0	0.0	0.0	0.3
h_1	-0.4	0.3	0.5	-0.4	0.4	-0.4	0.2	-0.1	0.0	0.0	0.0	0.0	0.0
h_2	0.7	0.3	-0.2	-0.1	0.2	-0.5	-0.1	0.0	0.0	0.0	0.0	0.0	0.0
h_3	0.0	-0.1	-0.4	-0.6	0.4	0.3	-0.1	-0.5	-0.1	0.0	0.0	0.0	0.0
h_4	0.0	-0.1	-0.2	-0.4	0.0	0.1	0.2	0.8	0.0	-0.3	0.1	-0.1	0.0
h_5	0.0	0.0	0.0	-0.1	0.0	0.0	0.1	0.2	-0.4	0.9	0.0	0.2	0.0
h_6	0.0	0.0	0.0	0.0	0.0	0.0	0.0	0.1	-0.3	-0.1	-0.9	0.1	-0.1
h_7	0.0	0.0	0.0	0.0	0.0	0.0	0.0	0.0	0.0	0.1	0.0	0.0	0.6
Damping Factor	1.0	1.0	1.0	1.0	0.7	0.0	0.0	0.0	0.0	0.0	0.0	0.0	0.0
Resolved combination	$\rho_2 h_2$	$\frac{h_1 h_2}{\rho_1}$	$\frac{h_1}{h_3}$	$\frac{1}{\rho_3 h_1 h_2 h_3}$	$\frac{h_1 h_3}{\rho_3}$								

Effective parameters: 4.7

Layer No.	Resistivity	Thickness
1	0.18	44.97
2	22.91	38.02
3	0.21	481.48
4	0.61	258.93
5	3.33	330.1
6	14.71	565.54
7	91.2	2448.28
8	94.36	0
# Calibration factor:	5.1315	
# Error:	0.963	



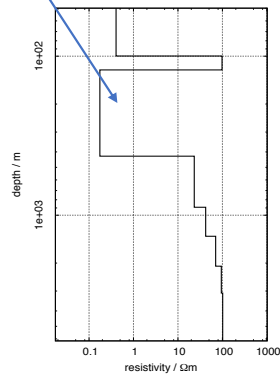
Layer resistivities - 68 percent confidence interval (damped)				
l	RO(l)	BOUND(1)	BOUND(2)	IMPORTANCE
1	0.18	0.18	0.19	0.84
2	22.91	22.69	23.13	0.37
3	0.21	0.19	0.24	0.77
4	0.61	0.60	0.62	0.18
5	3.33	3.32	3.34	0.04
6	14.71	14.69	14.73	0.01
7	91.20	91.16	91.23	0.00
8	94.36	94.35	94.37	0.00
Layer depths (to base) - 68 percent confidence interval (damped)				
l	Z(l)	BOUND(1)	BOUND(2)	IMPORTANCE
1	44.97	42.16	47.97	0.82
2	82.99	80.49	85.57	0.81
3	564.47	524.74	607.21	0.74
4	823.40	790.51	857.64	0.46
5	1153.50	1143.50	1163.58	0.10
6	1719.03	1714.79	1723.29	0.03
7	4167.31	4167.25	4167.37	0.00

Figure E. 34 Resolved combination and importance analyzed using Eigenparameter for Marquardt inversion of Rx3 E-field (Ex), inline transmitter configuration (7th May 2015). Starting model generated using cumulative conductance.

Transform Original par.	P1	P2	P3	P4	P5	P6	P7	P8	P9	P10	P11	P12	P13
ρ^1	0.1	-0.8	0.1	-0.2	0.4	-0.2	0.1	0.0	0.0	0.0	0.0	0.0	0.0
ρ^2	0.1	0.0	0.0	0.0	-0.1	0.2	1.0	0.0	0.0	0.0	0.0	0.0	0.0
ρ^3	0.0	0.1	-0.4	-0.4	0.6	0.6	-0.1	0.0	0.0	0.0	0.0	0.0	0.0
ρ^4	0.0	0.0	0.0	0.0	0.0	0.0	0.0	0.7	0.1	0.0	-0.4	-0.4	-0.4
ρ^5	0.0	0.0	0.0	0.0	0.0	0.0	0.0	0.3	0.2	-0.4	-0.3	0.0	0.7
ρ^6	0.0	0.0	0.0	0.0	0.0	0.0	0.0	0.1	0.0	-0.3	0.3	0.0	0.2
ρ^7	0.0	0.0	0.0	0.0	0.0	0.0	0.0	0.1	-0.1	-0.2	0.4	-0.2	0.0
ρ^8	0.0	0.0	0.0	0.0	0.0	0.0	0.0	0.0	0.2	-0.4	0.5	-0.3	-0.1
h_1	-0.7	0.1	-0.4	0.4	0.4	-0.3	0.2	0.0	0.0	0.0	0.0	0.0	0.0
h_2	0.7	0.3	-0.1	0.3	0.4	-0.4	0.0	0.0	0.0	0.0	0.0	0.0	0.0
h_3	0.0	-0.1	0.5	0.6	0.2	0.5	-0.1	0.0	0.0	0.0	0.0	0.0	0.0
h_4	0.0	0.0	0.0	0.0	0.0	0.0	0.0	-0.6	0.1	-0.5	-0.4	-0.3	-0.2
h_5	0.0	0.0	0.0	0.0	0.0	0.0	0.0	-0.2	0.7	0.4	0.0	-0.4	0.3
h_6	0.0	0.0	0.0	0.0	0.0	0.0	0.0	-0.1	-0.6	0.2	0.0	-0.7	0.3
h_7	0.0	0.0	0.0	0.0	0.0	0.0	0.0	0.0	0.3	-0.1	0.2	-0.2	-0.2
Damping Factor	1.0	1.0	1.0	0.6	0.2	0.0	0.0	0.0	0.0	0.0	0.0	0.0	0.0
Resolved combination	$\frac{h_2}{h_1}$	$\frac{h_2}{\rho_1}$	$\frac{h_3}{\rho_2 h_1}$	$\frac{h_1 h_2 h_3}{\rho_3}$									

Effective parameters : 3.8

Layer_No.	Resistivity	Thickness
1	0.41	99.75
2	98.14	22.26
3	0.18	303.42
4	23.25	466
5	42.02	465.38
6	70.47	735.75
7	94.52	995.09
8	101.57	0
# Calibration factor:	2.7161	
# Error:	1.582	



Layer resistivities - 68 percent confidence interval (damped)				
I	RO(I)	BOUND(1)	BOUND(2)	IMPORTANCE
1	0.4059	0.3912	0.4212	0.867
2	98.1357	97.6304	98.6436	0.1304
3	0.1752	0.1661	0.1847	0.4578
4	23.2506	23.2389	23.2623	0.0047
5	42.0173	42.01	42.0245	0.0016
6	70.4737	70.4658	70.4816	0.001
7	94.5224	94.5158	94.529	0.0006
8	101.5712	101.5598	101.5827	0.0006
Layer depths (to base) - 68 percent confidence interval (damped)				
I	Z(I)	BOUND(1)	BOUND(2)	IMPORTANCE
1	99.7471	94.5435	105.2371	0.7928
2	122.0037	116.8974	127.3331	0.7967
3	425.4279	394.9148	458.2985	0.6394
4	891.4321	891.1436	891.7207	0.0031
5	1356.8142	1356.5846	1357.0439	0.0017
6	2092.5625	2092.4233	2092.7017	0.0006
7	3087.6489	3087.5974	3087.7004	0.0001

Figure E. 35 Resolved combination and importance analyzed using Eigenparameter for Marquardt inversion of Rx3 E-field (Ex), inline transmitter configuration (7th May 2015). Starting model generated using cumulative transverse resistance.

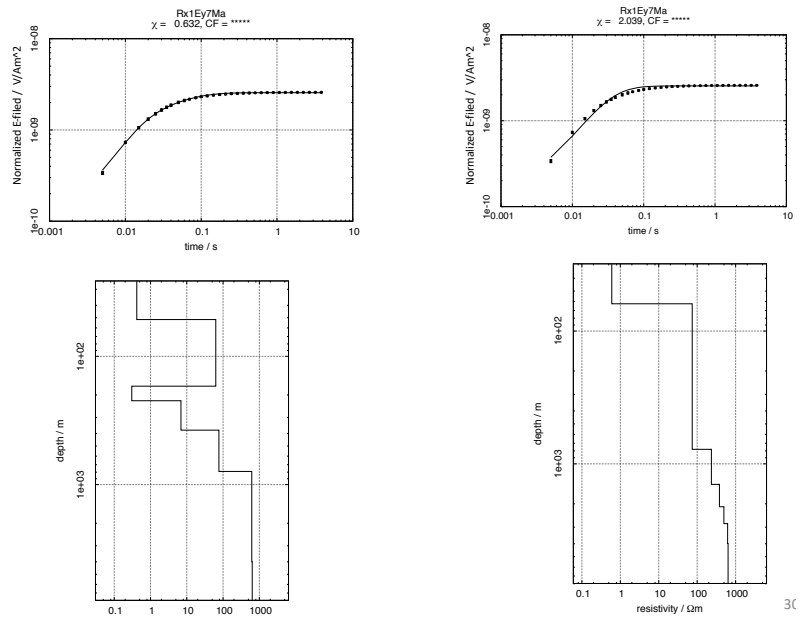
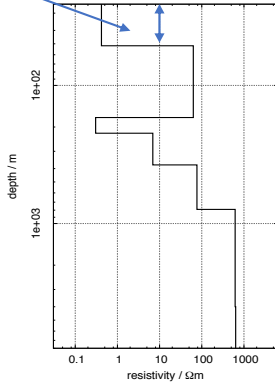


Figure E. 36 Marquardt inversion of Rx1 E-field (Ey) inline transmitter configuration, data measured on 7th May 2015. The starting models generated using cumulative conductance (left) and transverse resistance (right).

Transform Original par.	par.	P1	P2	P3	P4	P5	P6	P7	P8	P9	P10	P11	P12	P13
ρ_1		0.5	-0.4	0.4	-0.1	0.6	0.0	0.0	0.0	0.0	0.0	0.0	0.0	0.0
ρ_2		0.1	-0.1	0.1	-0.1	-0.2	0.9	0.3	0.0	0.0	0.0	0.0	0.0	0.0
ρ_3		0.0	0.1	0.2	0.0	0.1	0.3	-0.8	0.4	0.0	0.0	0.0	0.0	0.0
ρ_4		0.0	0.0	0.0	0.0	0.0	0.0	0.1	0.2	0.9	0.4	0.1	-0.1	0.0
ρ_5		0.0	0.0	0.0	0.0	0.0	0.0	0.0	0.2	0.2	-0.7	0.6	0.3	-0.1
ρ_6		0.0	0.0	0.0	0.0	0.0	0.0	0.0	0.0	0.1	-0.5	-0.1	-0.8	0.1
ρ_7		0.0	0.0	0.0	0.0	0.0	0.0	0.0	0.0	0.0	-0.1	0.0	0.0	0.5
h_1		-0.6	0.2	-0.1	-0.4	0.7	0.2	0.1	0.0	0.0	0.0	0.0	0.0	0.0
h_2		0.1	0.6	0.2	0.7	0.2	0.1	0.2	-0.1	0.0	0.0	0.0	0.0	0.0
h_3		0.0	-0.4	-0.7	0.4	0.2	0.2	-0.1	0.1	0.0	0.0	0.0	0.0	0.0
h_4		0.0	0.0	0.0	0.0	0.0	0.1	-0.4	-0.9	0.2	0.0	0.2	0.0	0.0
h_5		0.0	0.0	0.0	0.0	0.0	0.0	0.0	-0.1	0.4	-0.4	-0.7	0.4	0.1
h_6		0.0	0.0	0.0	0.0	0.0	0.0	0.0	0.0	0.1	0.2	0.2	0.8	0.0
Damping Factor		1.0	1.0	1.0	0.9	0.4	0.0	0.0	0.0	0.0	0.0	0.0	0.0	0.0
Resolved combination		$\frac{\rho_1}{h_1}$	$\frac{h_2}{\rho_1 h_3}$	$\frac{\rho_1}{h_3}$	$\frac{h_2 h_3}{h_1}$	$\rho_1 h_1$								

Effective parameters is 4.2

Layer No.	Resistivity	Thickness
1	0.42	51.66
2	63.09	119.21
3	0.30	50.94
4	6.90	154.38
5	76.76	413.37
6	619.38	3203.00
7	638.02	0.00
# Calibration factor:	15.9903	
# Error:	0.632	



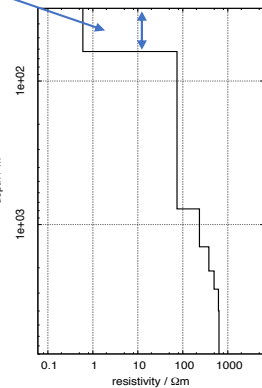
Layer resistivities - 68 percent confidence interval (damped)				
l	RO(l)	BOUND(1)	BOUND(2)	IMPORTANCE
1	0.418	0.3974	0.4396	0.8327
2	63.092	61.86	64.35	0.20
3	0.3037	0.30	0.31	0.21
4	6.9029	6.89	6.91	0.02
5	76.7599	76.75	76.77	0.00
6	619.3792	619.37	619.38	0.00
7	638.0192	638.02	638.02	0.00
Layer depths (to base) - 68 percent confidence interval (damped)				
l	Z(l)	BOUND(1)	BOUND(2)	IMPORTANCE
1	51.6624	48.7014	54.8034	0.7458
2	170.8765	159.88	182.63	0.89
3	221.8213	208.97	235.47	0.92
4	376.1994	375.30	377.10	0.03
5	789.568	789.52	789.62	0.00
6	3992.5649	3992.56	3992.57	0.00

Figure E. 37 Resolved combination and importance analyzed using Eigenparameter for Marquardt inversion of Rx1 E-field (Ey), inline transmitter configuration (7th May 2015). Starting model generated using cumulative conductance.

Transform Original par.	par.	P1	P2	P3	P4	P5	P6	P7	P8	P9	P10	P11	P12	P13
ρ_1		0.6	-0.5	0.6	-0.1	0.0	0.0	0.0	0.0	0.0	0.0	0.0	0.0	0.0
ρ_2		0.0	0.0	0.1	1.0	-0.1	0.0	0.0	0.0	0.0	0.0	0.0	0.0	0.0
ρ_3		0.0	0.0	0.0	0.0	0.3	0.6	-0.3	0.4	-0.3	0.3	-0.1	0.1	0.1
ρ_4		0.0	0.0	0.0	0.0	0.0	0.5	-0.1	-0.1	0.3	0.0	0.2	0.0	-0.7
ρ_5		0.0	0.0	0.0	0.0	0.0	0.3	0.7	-0.2	-0.5	-0.2	0.1	0.0	-0.1
ρ_6		0.0	0.0	0.0	0.0	0.0	0.1	-0.2	0.1	0.0	-0.5	0.6	-0.4	0.3
ρ_7		0.0	0.0	0.0	0.0	0.0	0.3	-0.2	-0.3	-0.1	-0.3	-0.5	-0.2	0.3
h_1		-0.6	0.3	0.8	-0.1	0.0	0.0	0.0	0.0	0.0	0.0	0.0	0.0	0.0
h_2		0.0	0.0	0.0	-0.1	-1.0	0.2	-0.1	0.1	-0.1	0.1	0.0	0.0	0.0
h_3		0.0	0.0	0.0	0.0	0.0	0.0	0.3	0.7	0.1	-0.4	-0.1	0.3	0.0
h_4		0.0	0.0	0.0	0.0	0.0	0.3	0.4	0.0	0.7	0.2	-0.2	-0.4	0.3
h_5		0.0	0.0	0.0	0.0	0.0	0.2	-0.1	-0.4	0.3	-0.3	0.0	0.7	0.2
h_6		0.0	0.0	0.0	0.0	0.0	-0.1	-0.1	0.0	0.0	-0.5	-0.5	-0.3	-0.4
Damping Factor		1.0	1.0	0.7	0.0	0.0	0.0	0.0	0.0	0.0	0.0	0.0	0.0	0.0
Resolved combination		$\frac{\rho_1}{h_1}$	$\frac{h_1}{\rho_1}$	$\rho_1 h_1$										

Effective parameters 2.7

Layer No.	Resistivity	Thickness
1	0.6	62.35
2	74.32	715.12
3	234.1	650.3
4	378.99	676.89
5	495.93	712.97
6	619.27	1163
7	638.03	0
# Calibration factor:	11.9445	
# Error:	2.039	



Layer resistivities - 68 percent confidence interval (damped)				
l	RO(I)	BOUND(1)	BOUND(2)	IMPORTANCE
1	0.5988	0.5062	0.7083	0.8877
2	74.3166	71.8849	76.8304	0.0907
3	234.1045	233.8756	234.3336	0.0024
4	378.9861	378.927	379.0451	0.0004
5	495.9302	495.9106	495.9498	0.0001
6	619.2723	619.2684	619.2761	0
7	638.0328	638.0254	638.0403	0
Layer depths (to base) - 68 percent confidence interval (damped)				
l	Z(I)	BOUND(1)	BOUND(2)	IMPORTANCE
1	62.3493	50.0868	77.6141	0.7997
2	777.4664	774.5347	780.4092	0.0095
3	1427.7661	1427.3712	1428.1611	0.0007
4	2104.6606	2104.2778	2105.0435	0.0004
5	2817.6323	2817.3232	2817.9414	0.0003
6	3980.6296	3980.53	3980.7292	0.0001

Figure E. 38 Resolved combination and importance analyzed using Eigenparameter for Marquardt inversion of Rx1 E-field (Ey), inline transmitter configuration (7th May 2015). Starting model generated using cumulative transverse resistance.

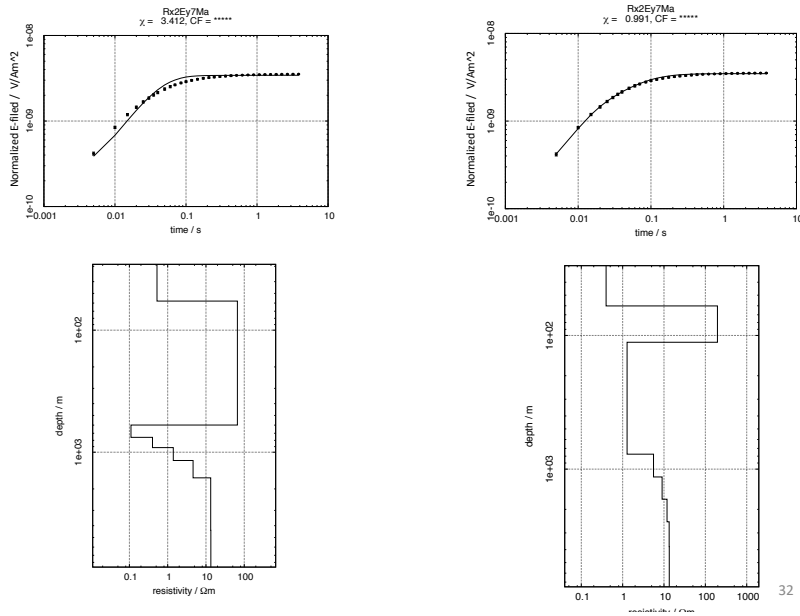
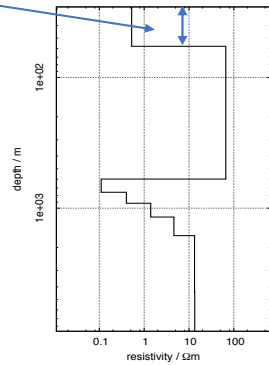


Figure E. 39 Marquardt inversion of Rx2 E-field (Ey) inline transmitter configuration, data measured on 7th May 2015. The starting models generated using cumulative conductance (left) and transverse resistance (right).

Transform Original par.	par.	P1	P2	P3	P4	P5	P6	P7	P8	P9	P10	P11	P12	P13	P14	P15
ρ_1		0.6	-0.5	0.6	-0.1	0.1	0.0	0.0	0.0	0.0	0.0	0.0	0.0	0.0	0.0	0.0
ρ_2		0.1	0.0	0.0	1.0	0.1	0.0	-0.1	0.0	0.0	0.0	0.0	0.0	0.0	0.0	0.0
ρ_3		0.0	0.0	0.0	0.1	-0.2	-0.1	0.9	-0.3	0.0	0.0	0.0	0.0	0.0	0.0	0.0
ρ_4		0.0	0.0	0.0	0.0	0.0	0.0	-0.1	-0.1	-0.2	-0.4	0.6	-0.5	0.0	0.2	0.0
ρ_5		0.0	0.0	0.0	0.0	0.0	0.0	0.0	-0.1	0.1	-0.2	0.6	0.8	0.2	0.2	0.0
ρ_6		0.0	0.0	0.0	0.0	0.0	0.0	0.0	0.0	0.1	-0.1	0.2	0.1	-0.8	-0.2	-0.5
ρ_7		0.0	0.0	0.0	0.0	0.0	0.0	0.0	0.0	0.1	-0.1	-0.1	0.2	-0.3	-0.3	0.4
ρ_8		0.0	0.0	0.0	0.0	0.0	0.0	0.0	0.0	-0.1	0.1	0.0	0.5	-0.7	-0.5	0.0
h_1		-0.6	0.3	0.8	0.0	-0.1	0.1	0.0	0.0	0.0	0.0	0.0	0.0	0.0	0.0	0.0
h_2		0.0	0.2	0.0	0.0	0.7	-0.6	0.1	0.0	0.0	0.0	0.0	0.0	0.0	0.0	0.0
h_3		0.0	0.0	0.0	0.0	0.6	0.8	0.2	-0.2	0.0	0.0	0.0	0.0	0.0	0.0	0.0
h_4		0.0	0.0	0.0	0.0	0.1	0.1	0.4	0.9	0.2	-0.1	0.2	-0.1	0.0	0.1	0.0
h_5		0.0	0.0	0.0	0.0	0.0	0.0	0.1	0.2	-0.9	0.1	0.0	0.2	-0.1	-0.1	0.0
h_6		0.0	0.0	0.0	0.0	0.0	0.0	0.0	0.0	-0.1	-0.9	-0.4	0.1	0.0	0.1	0.0
h_7		0.0	0.0	0.0	0.0	0.0	0.0	0.0	0.0	0.0	-0.1	0.2	-0.1	-0.1	-0.6	0.6
Damping Factor		1.0	1.0	0.1	0.0	0.0	0.0	0.0	0.0	0.0	0.0	0.0	0.0	0.0	0.0	0.0
Resolved combination	$\frac{\rho_1}{h_1}$	$\frac{h_1}{\rho_1}$														

Effective parameters: 2.1

Layer No.	Resistivity	Thickness
1	0.53	57.75
2	66.23	541.16
3	0.11	156.78
4	0.4	161.74
5	1.4	251.88
6	4.6	452.95
7	13.3	2750
8	13.4	0
# Calibration factor:	32.1593	
# Error:	3.412	



Layer resistivities - 68 percent confidence interval (damped)				
I	RO(I)	BOUND(1)	BOUND(2)	IMPORTANCE
1	0.5253	0.4897	0.5635	0.7837
2	66.2278	65.8668	66.5908	0.0672
3	0.1099	0.1097	0.11	0.008
4	0.4008	0.4008	0.4008	0
5	1.401	1.401	1.401	0
6	4.6012	4.6012	4.6012	0
7	13.3015	13.3015	13.3015	0
8	13.4	13.4	13.4	0
Layer depths (to base) - 68 percent confidence interval (damped)				
I	Z(I)	BOUND(1)	BOUND(2)	IMPORTANCE
1	57.7476	54.5617	61.1195	0.6233
2	598.9062	584.8071	613.3453	0.2085
3	755.6873	755.5042	755.8704	0.0004
4	917.4304	917.4188	917.442	0.0001
5	1169.3087	1169.3031	1169.3143	0
6	1622.2557	1622.2495	1622.262	0
7	4372.2603	4372.2578	4372.2627	0

Figure E. 40 Resolved combination and importance analyzed using Eigenparameter for Marquardt inversion of Rx2 E-field (Ey), inline transmitter configuration (7th May 2015). Starting model generated using cumulative conductance.

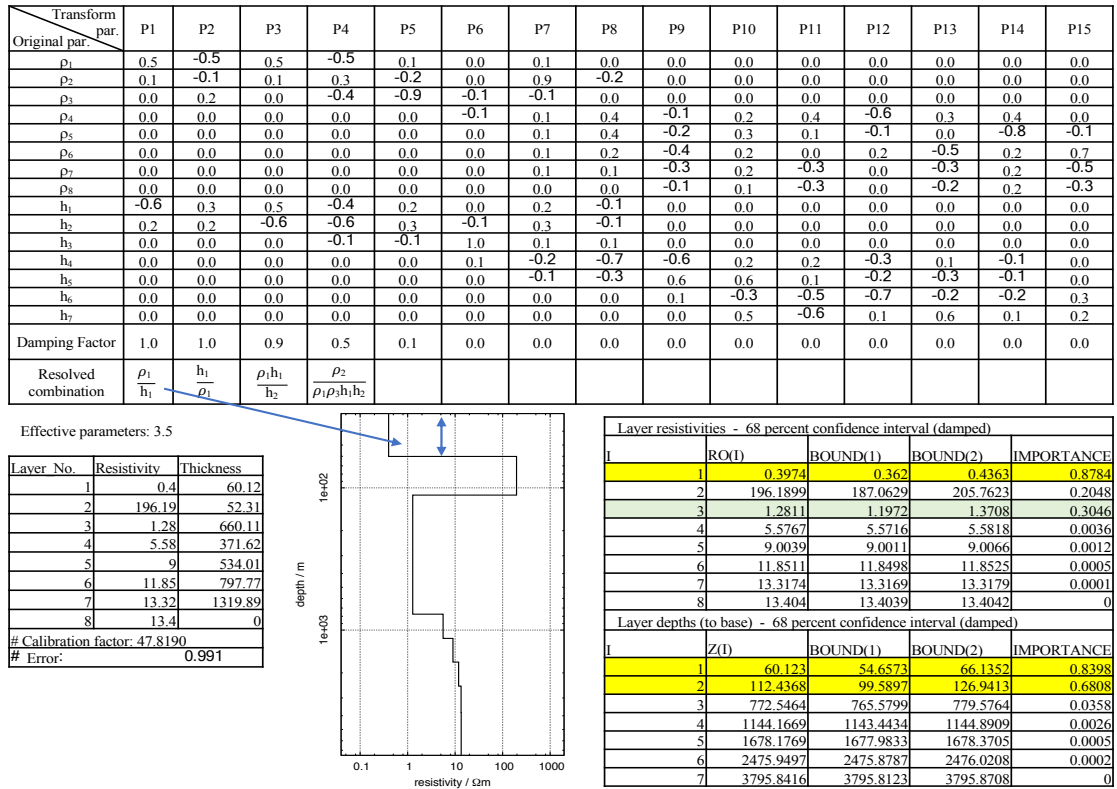


Figure E. 41 Resolved combination and importance analyzed using Eigenparameter for Marquardt inversion of Rx2 E-field (Ey), inline transmitter configuration (7th May 2015). Starting model generated using cumulative transverse resistance.

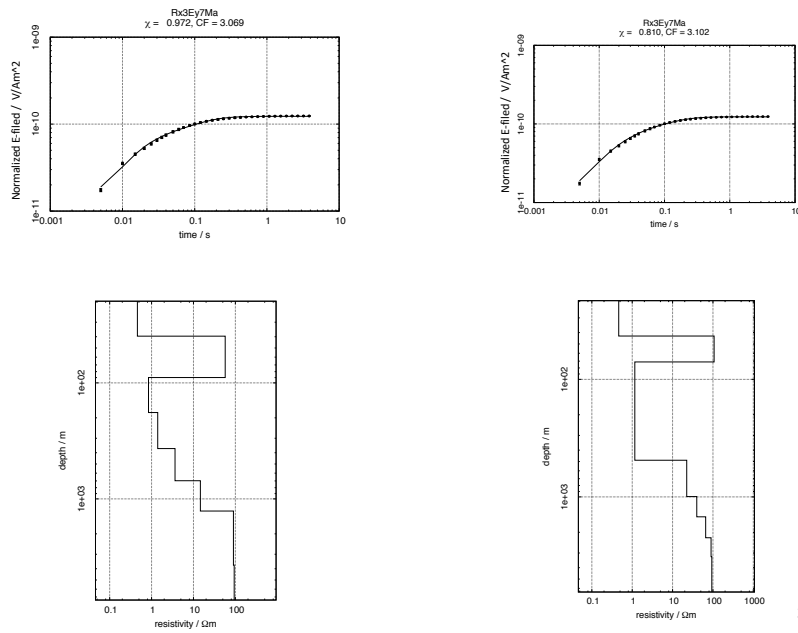
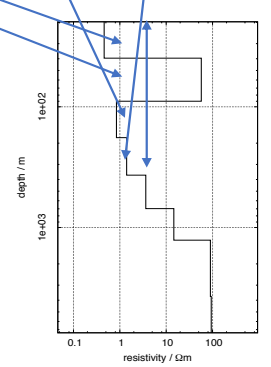


Figure E. 42 Marquardt inversion of Rx3 E-field (Ey) inline transmitter configuration, data measured on 7th May 2015. The starting models generated using cumulative conductance (left) and transverse resistance (right).

Transform par.	P1	P2	P3	P4	P5	P6	P7	P8	P9	P10	P11	P12	P13	P14	P15
Original par.															
ρ_1	0.2	-0.7	0.4	-0.4	0.1	-0.2	0.1	-0.1	0.1	-0.2	0.2	-0.2	0.1	0.0	0.0
ρ_2	0.3	-0.1	-0.2	0.4	-0.3	0.4	-0.1	0.0	0.2	-0.3	0.3	-0.4	0.2	0.0	0.0
ρ_3	0.0	0.2	0.0	-0.7	-0.1	0.3	-0.5	0.3	-0.1	0.0	0.0	-0.1	0.0	0.0	0.0
ρ_4	0.0	0.1	0.1	-0.2	-0.5	-0.2	0.5	0.2	-0.6	0.0	0.1	-0.2	0.1	0.0	0.0
ρ_5	0.0	0.1	0.1	0.0	-0.2	-0.2	-0.3	-0.2	0.1	0.5	-0.5	-0.6	0.1	0.0	0.1
ρ_6	0.0	0.0	0.0	0.0	0.0	0.0	-0.1	-0.1	-0.1	-0.2	0.0	-0.3	-0.5	0.7	0.1
ρ_7	0.0	0.0	0.0	0.0	0.0	0.0	0.0	0.0	0.0	-0.1	0.0	-0.2	-0.7	-0.4	0.0
ρ_8	0.0	0.0	0.0	0.0	0.0	0.0	0.0	0.0	0.0	0.0	0.1	-0.2	-0.1	-0.6	-0.1
h_1	-0.5	0.5	0.1	-0.1	0.3	-0.1	0.1	-0.2	0.2	-0.3	0.3	-0.4	0.2	0.0	0.0
h_2	0.5	0.2	-0.6	-0.3	0.2	-0.4	0.1	-0.1	0.1	0.0	0.0	0.0	0.0	0.0	0.0
h_3	0.0	-0.1	-0.1	0.3	0.4	-0.3	-0.3	0.5	-0.4	-0.1	0.1	-0.2	0.1	0.0	0.0
h_4	0.0	-0.1	-0.1	0.0	0.5	0.3	-0.3	-0.4	0.2	-0.1	-0.2	0.1	0.0	0.0	0.0
h_5	0.0	-0.1	-0.1	-0.1	0.1	0.2	0.4	0.7	0.4	0.0	-0.3	-0.2	0.0	0.1	0.1
h_6	0.0	0.0	0.0	0.0	0.0	0.0	0.1	0.1	0.2	0.7	0.6	-0.1	-0.1	0.2	-0.1
h_7	0.0	0.0	0.0	0.0	0.0	0.0	0.0	0.0	0.0	0.0	0.1	0.1	0.0	-0.1	1.0
Damping Factor	1.0	1.0	1.0	0.8	0.4	0.0	0.0	0.0	0.0	0.0	0.0	0.0	0.0	0.0	0.0
Resolved combination	$\frac{\rho_2 h_2}{h_1}$	$\frac{h_1}{\rho_1}$	$\frac{\rho_1}{h_2}$	$\frac{\rho_2 h_3}{\rho_1 \rho_3 h_2}$	$\frac{h_2 h_3 h_4}{\rho_2 \rho_4}$										

Effective parameters 4.2

Layer No.	Resistivity	Thickness
1	0.46	39.54
2	57.18	50.35
3	0.84	90.24
4	1.4	188.28
5	3.63	328.72
6	14.61	575.34
7	89.83	2449.09
8	93.6	0
# Calibration factor:	3.0694	
# Error:	0.972	



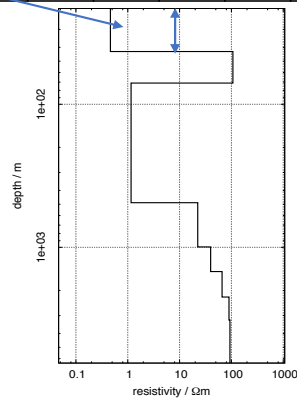
Layer resistivities - 68 percent confidence interval (damped)				
I	RO(I)	BOUND(1)	BOUND(2)	IMPORTANCE
1	0.46	0.43	0.49	0.86
2	57.18	53.12	61.56	0.50
3	0.84	0.76	0.94	0.59
4	1.40	1.30	1.51	0.32
5	3.63	3.55	3.71	0.11
6	14.61	14.56	14.67	0.03
7	89.83	89.78	89.87	0.00
8	93.60	93.59	93.60	0.00
Layer depths (to base) - 68 percent confidence interval (damped)				
I	Z(I)	BOUND(1)	BOUND(2)	IMPORTANCE
1	39.54	37.86	41.29	0.69
2	89.89	84.29	95.86	0.87
3	180.13	167.60	193.60	0.34
4	368.41	346.23	392.01	0.29
5	697.13	680.68	713.98	0.14
6	1272.47	1266.60	1278.36	0.03
7	3721.56	3721.51	3721.60	0.00

Figure E. 43 Resolved combination and importance analyzed using Eigenparameter for Marquardt inversion of Rx3 E-field (Ey), inline transmitter configuration (7th May 2015). Starting model generated using cumulative conductance.

Transform Original par.	par.	P1	P2	P3	P4	P5	P6	P7	P8	P9	P10	P11	P12	P13	P14	P15
ρ_1		0.2	-0.6	0.5	-0.3	0.1	-0.3	0.3	0.0	0.0	0.0	0.0	0.0	0.0	0.0	0.0
ρ_2		0.2	0.0	-0.1	0.1	-0.2	0.5	0.8	0.0	0.0	0.0	0.0	0.0	0.0	0.0	0.0
ρ_3		0.1	0.4	0.1	-0.9	-0.3	0.2	0.0	0.0	0.0	0.0	0.0	0.0	0.0	0.0	0.0
ρ_4		0.0	0.0	0.0	0.0	0.0	0.0	0.0	-0.9	0.0	0.1	0.3	0.0	-0.1	0.0	0.0
ρ_5		0.0	0.0	0.0	0.0	0.0	0.0	0.0	-0.1	-0.2	0.3	-0.4	0.2	0.3	0.7	0.4
ρ_6		0.0	0.0	0.0	0.0	0.0	0.0	0.0	0.0	-0.1	0.2	-0.2	0.3	-0.8	0.1	-0.2
ρ_7		0.0	0.0	0.0	0.0	0.0	0.0	0.0	0.0	0.0	0.2	0.0	0.3	-0.1	-0.6	0.7
ρ_8		0.0	0.0	0.0	0.0	0.0	0.0	0.0	0.0	0.1	0.1	0.0	0.1	-0.1	0.0	0.0
h_1		-0.6	0.4	0.1	-0.1	0.4	-0.3	0.5	0.0	0.0	0.0	0.0	0.0	0.0	0.0	0.0
h_2		0.6	0.1	-0.6	-0.1	0.2	-0.5	0.1	0.0	0.0	0.0	0.0	0.0	0.0	0.0	0.0
h_3		0.0	-0.2	-0.2	-0.3	0.8	0.5	-0.1	0.0	0.0	0.0	0.0	0.0	0.0	0.0	0.0
h_4		0.0	0.0	0.0	0.0	0.0	0.0	0.0	0.3	0.2	0.4	0.8	0.1	-0.1	0.3	0.1
h_5		0.0	0.0	0.0	0.0	0.0	0.0	0.0	-0.1	0.9	-0.1	-0.2	0.1	0.0	0.1	0.0
h_6		0.0	0.0	0.0	0.0	0.0	0.0	0.0	0.0	-0.1	-0.5	0.2	0.8	0.2	0.1	-0.1
h_7		0.0	0.0	0.0	0.0	0.0	0.0	0.0	0.0	0.6	-0.1	0.3	0.4	-0.3	-0.5	0.0
Damping Factor		1.0	1.0	1.0	0.5	0.2	0.0	0.0	0.0	0.0	0.0	0.0	0.0	0.0	0.0	0.0
Resolved combination		$\frac{h_2}{h_1}$	$\frac{\rho_3 h_1}{\rho_1}$	$\frac{\rho_1}{h_2}$	$\frac{1}{\rho_1 \rho_3 h_3}$											

Effective parameters: 3.7

Layer No.	Resistivity	Thickness
1	0.46	42.82
2	106.82	28.28
3	1.16	416.79
4	22.43	505.57
5	39.73	483.46
6	66.14	748.21
7	89.89	996.77
8	93.68	0
# Calibration factor:	3.1022	
# Error:	0.810	



Layer resistivities - 68 percent confidence interval (damped)				
I	RO(I)	BOUND(1)	BOUND(2)	IMPORTANCE
1	0.4635	0.4431	0.4848	0.8437
2	106.8198	104.9168	108.7574	0.2661
3	1.1593	1.0671	1.2594	0.5795
4	22.4344	22.3993	22.4695	0.0139
5	39.729	39.7161	39.7418	0.0027
6	66.1367	66.1275	66.1459	0.001
7	89.8875	89.8831	89.8918	0.0003
8	93.6798	93.6774	93.6822	0.0001
Layer depths (to base) - 68 percent confidence interval (damped)				
I	Z(I)	BOUND(1)	BOUND(2)	IMPORTANCE
1	42.8231	41.979	43.6841	0.6964
2	71.1054	68.559	73.7464	0.8349
3	487.8906	465.8495	510.9744	0.3515
4	993.4589	992.6895	994.2289	0.0063
5	1476.9233	1476.5078	1477.339	0.0022
6	2225.1362	2225.0066	2225.2659	0.0004
7	3221.9062	3221.8875	3221.925	0

Figure E. 44 Resolved combination and importance analyzed using Eigenparameter for Marquardt inversion of Rx3 E-field (Ey), inline transmitter configuration (7th May 2015). Starting model generated using cumulative transverse resistance.

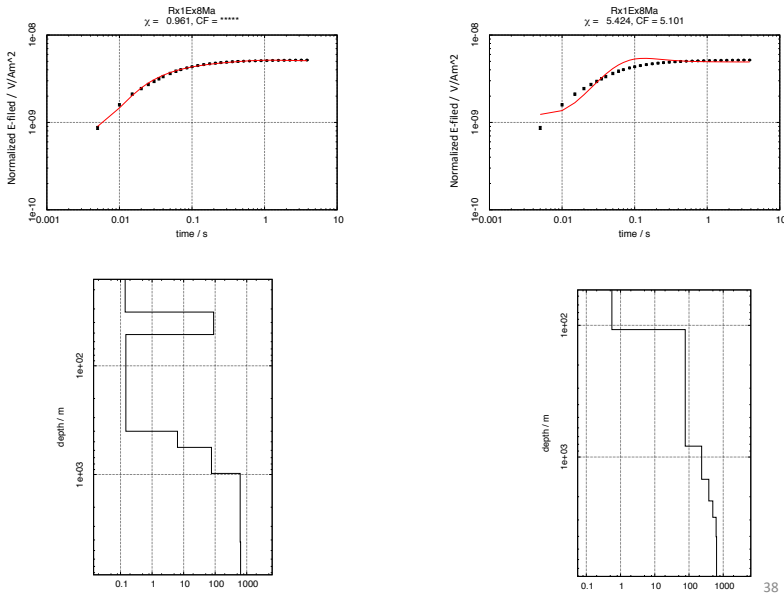
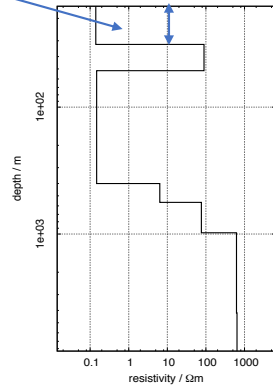


Figure E. 45 Marquardt inversion of Rx1 E-field (Ex) inline transmitter configuration, data measured on 8th May 2015. The starting models generated using cumulative conductance (left) and transverse resistance (right).

Transform Original par.	P1	P2	P3	P4	P5	P6	P7	P8	P9	P10	P11	P12	P13
ρ_1	0.2	-0.8	0.3	-0.3	0.2	-0.3	0.3	0.0	0.0	0.0	0.0	0.0	0.0
ρ_2	0.2	0.1	-0.1	0.3	-0.1	0.4	0.8	0.0	0.0	0.0	0.0	0.0	0.0
ρ_3	0.0	0.2	0.3	0.2	0.9	0.1	-0.1	0.0	0.0	0.0	0.0	0.0	0.0
ρ_4	0.0	0.0	0.0	0.0	0.0	0.0	0.0	0.2	-0.3	0.8	-0.4	-0.2	-0.1
ρ_5	0.0	0.0	0.0	0.0	0.0	0.0	0.0	0.1	-0.3	0.3	0.9	0.1	0.1
ρ_6	0.0	0.0	0.0	0.0	0.0	0.0	0.0	0.0	0.0	0.2	-0.3	0.7	0.2
ρ_7	0.0	0.0	0.0	0.0	0.0	0.0	0.0	0.0	0.1	0.0	0.1	0.7	-0.1
h_1	-0.6	0.3	0.3	-0.5	0.0	-0.2	0.4	0.0	0.0	0.0	0.0	0.0	0.0
h_2	0.6	0.4	-0.4	-0.4	0.1	-0.4	0.1	0.0	0.0	0.0	0.0	0.0	0.0
h_3	0.0	-0.1	-0.2	-0.6	0.2	0.7	-0.1	0.0	0.0	0.0	0.0	0.0	0.0
h_4	0.0	0.0	0.0	0.0	0.0	0.0	0.0	-1.0	0.1	0.3	0.0	0.0	0.0
h_5	0.0	0.0	0.0	0.0	0.0	0.0	0.0	-0.2	-0.9	-0.4	-0.2	0.1	0.0
h_6	0.0	0.0	0.0	0.0	0.0	0.0	0.0	0.0	0.0	0.0	0.0	-0.1	1.0
Damping Factor	1.0	1.0	1.0	0.6	0.4	0.0	0.0	0.0	0.0	0.0	0.0	0.0	0.0
Resolved combination	$\frac{h_2}{h_1}$	$\frac{h_1 h_2}{\rho_1}$	$\frac{\rho_1 \rho_3 h_1}{h_2}$	$\frac{\rho_2}{\rho_1 h_1 h_2 h_3}$	ρ_3								

Effective parameters: 4.0

Layer No.	Resistivity	Thickness
1	0.14	32.07
2	89.21	19.55
3	0.15	348.50
4	6.40	162.85
5	76.25	414.38
6	620.16	3202.96
7	639.00	0.00
# Calibration factor: 12.6378		
# Error: 0.961		



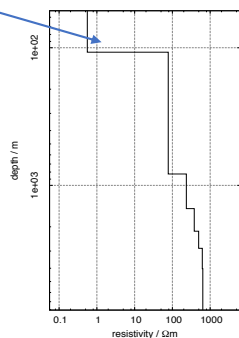
Layer resistivities - 68 percent confidence interval (damped)				
l	RO(l)	BOUND(1)	BOUND(2)	IMPORTANCE
1	0.1403	0.1345	0.1464	0.8627
2	89.2088	86.44	92.06	0.29
3	0.1475	0.14	0.16	0.52
4	6.3951	6.39	6.40	0.00
5	76.2458	76.24	76.26	0.00
6	620.1632	620.14	620.19	0.00
7	639.001	639.00	639.01	0.00
Layer depths (to base) - 68 percent confidence interval (damped)				
l	Z(l)	BOUND(1)	BOUND(2)	IMPORTANCE
1	32.0737	30.4223	33.8146	0.807
2	51.6214	49.21	54.15	0.84
3	400.118	373.16	429.02	0.47
4	562.9633	561.89	564.04	0.01
5	977.3474	977.18	977.52	0.00
6	4180.3047	4180.30	4180.31	0.00

Figure E. 46 Resolved combination and importance analyzed using Eigenparameter for Marquardt inversion of Rx1 E-field (Ex), inline transmitter configuration (8th May 2015). Starting model generated using cumulative conductance.

Transform Original par.	P1	P2	P3	P4	P5	P6	P7	P8	P9	P10	P11	P12	P13
ρ_1	0.6	-0.6	0.5	0.0	0.0	0.0	0.0	0.0	0.0	0.0	0.0	0.0	0.0
ρ_2	0.0	0.0	0.0	1.0	-0.2	0.0	0.1	0.0	0.0	0.0	0.0	0.0	0.0
ρ_3	0.0	0.0	0.0	0.0	0.3	-0.3	0.3	-0.2	0.0	-0.1	0.6	-0.6	0.2
ρ_4	0.0	0.0	0.0	0.0	0.1	-0.2	0.3	0.0	-0.2	-0.5	0.3	0.4	-0.5
ρ_5	0.0	0.0	0.0	0.0	0.0	-0.1	0.1	0.0	-0.1	-0.5	-0.3	0.2	0.7
ρ_6	0.0	0.0	0.0	0.0	0.0	-0.1	0.0	-0.1	0.0	-0.4	-0.1	0.2	-0.1
ρ_7	0.0	0.0	0.0	0.0	0.0	-0.8	-0.5	0.0	0.2	0.1	-0.1	0.0	0.0
h_1	-0.6	0.2	0.8	0.0	0.0	0.0	0.0	0.0	0.0	0.0	0.0	0.0	0.0
h_2	0.0	0.0	0.0	-0.2	-0.9	-0.2	0.2	0.0	0.0	0.1	-0.1	0.0	0.0
h_3	0.0	0.0	0.0	0.0	-0.2	0.3	-0.7	-0.1	-0.3	-0.4	0.4	-0.1	0.0
h_4	0.0	0.0	0.0	0.0	0.0	0.2	0.0	-0.6	0.8	-0.2	0.1	0.1	0.0
h_5	0.0	0.0	0.0	0.0	0.0	0.1	0.0	0.8	0.5	-0.3	0.1	-0.2	0.0
h_6	0.0	0.0	0.0	0.0	0.0	0.0	0.0	-0.2	-0.1	-0.3	-0.6	-0.6	-0.3
Damping Factor	1.0	1.0	1.0	0.0	0.0	0.0	0.0	0.0	0.0	0.0	0.0	0.0	0.0
Resolved combination	$\frac{\rho_1}{h_1}$	ρ_1	$\rho_1 h_1$										

Effective parameters: 3.0

Layer_No.	Resistivity	Thickness
1	0.56	107.69
2	77.65	718.63
3	234.17	649.33
4	379.64	676.4
5	496.64	712.75
6	620.15	1162.95
7	639.61	0
# Calibration factor: 5.1010		
# Error: 5.424		



Layer resistivities - 68 percent confidence interval (damped)				
I	RO(I)	BOUND(1)	BOUND(2)	IMPORTANCE
1	0.5577	0.4521	0.688	0.9985
2	77.6513	77.1208	78.1853	0.0302
3	234.1737	233.8413	234.5066	0.0046
4	379.6432	379.4439	379.8426	0.0017
5	496.6354	496.518	496.7529	0.0009
6	620.1537	620.0494	620.2581	0.0007
7	639.6071	639.4611	639.7531	0.0011
Layer depths (to base) - 68 percent confidence interval (damped)				
I	Z(I)	BOUND(1)	BOUND(2)	IMPORTANCE
1	107.6889	81.3703	142.52	0.9967
2	826.318	822.9388	829.711	0.0139
3	1475.6527	1474.2767	1477.0299	0.003
4	2152.0515	2151.4163	2152.687	0.001
5	2864.8062	2864.3738	2865.2385	0.0006
6	4027.7603	4027.6768	4027.8438	0.0001

Figure E. 47 Resolved combination and importance analyzed using Eigenparameter for Marquardt inversion of Rx1 E-field (Ex), inline transmitter configuration (8th May 2015). Starting model generated using cumulative transverse resistance.

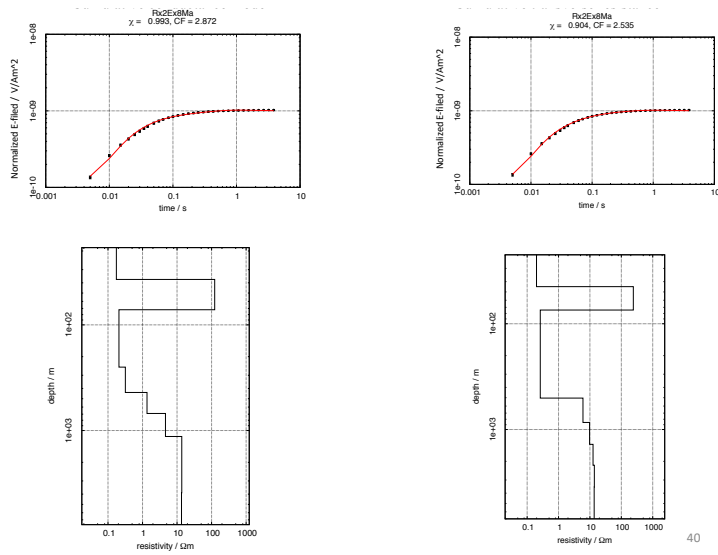
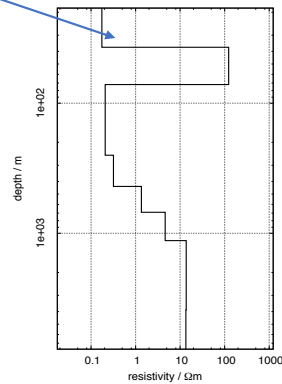


Figure E. 48 Marquardt inversion of Rx2 E-field (Ex) inline transmitter configuration, data measured on 8th May 2015. The starting models generated using cumulative conductance (left) and transverse resistance (right).

Transform Original par.	par.	P1	P2	P3	P4	P5	P6	P7	P8	P9	P10	P11	P12	P13	P14	P15
ρ_1		0.4	-0.7	0.3	-0.5	0.1	-0.2	0.0	-0.2	0.0	0.0	0.0	0.0	0.0	0.0	0.0
ρ_2		0.2	0.0	-0.1	0.4	0.0	0.3	0.2	-0.8	0.1	-0.1	0.0	0.0	0.0	0.0	0.0
ρ_3		0.0	0.2	0.2	-0.1	0.9	0.3	-0.1	0.0	0.0	0.0	0.0	0.0	0.0	0.0	0.0
ρ_4		0.0	0.0	0.1	0.2	0.2	-0.4	0.2	-0.1	-0.8	-0.2	0.3	0.0	-0.1	0.0	0.0
ρ_5		0.0	0.0	0.0	0.0	0.0	-0.1	-0.1	0.0	0.1	-0.1	0.1	-0.5	0.3	0.6	0.4
ρ_6		0.0	0.0	0.0	0.0	0.0	0.0	0.0	0.0	0.1	-0.2	0.1	-0.5	0.3	-0.1	-0.8
ρ_7		0.0	0.0	0.0	0.0	0.0	0.0	0.0	0.0	-0.1	-0.4	-0.6	-0.2	0.3	-0.5	0.3
ρ_8		0.0	0.0	0.0	0.0	0.0	0.0	0.0	0.0	-0.1	-0.3	-0.6	-0.1	-0.6	0.4	-0.2
h_1		-0.6	0.3	0.4	-0.4	-0.2	-0.1	0.1	-0.4	0.1	0.0	0.0	0.0	0.0	0.0	0.0
h_2		0.4	0.5	-0.5	-0.5	0.0	-0.3	0.0	-0.1	0.0	0.0	0.0	0.0	0.0	0.0	0.0
h_3		0.0	0.0	-0.1	-0.2	-0.2	0.4	-0.8	-0.2	-0.4	0.0	0.1	0.0	0.0	0.0	0.0
h_4		0.0	-0.1	-0.1	-0.3	-0.2	0.6	0.5	0.2	-0.2	-0.2	0.2	-0.1	-0.1	0.1	0.1
h_5		0.0	0.0	0.0	-0.1	0.0	0.1	0.2	-0.1	-0.4	0.6	-0.4	0.1	0.4	0.2	-0.2
h_6		0.0	0.0	0.0	0.0	0.0	0.0	0.0	0.0	0.0	0.5	0.0	-0.6	-0.4	-0.3	0.2
h_7		0.0	0.0	0.0	0.0	0.0	0.0	0.0	0.0	0.0	0.0	0.0	-0.1	-0.1	0.1	0.0
Damping Factor		1.0	1.0	1.0	0.7	0.6	0.1	0.0	0.0	0.0	0.0	0.0	0.0	0.0	0.0	0.0
Resolved combination		$\frac{\rho_2 h_2}{h_1}$	$\frac{h_1 h_2}{\rho_1}$	$\frac{\rho_3 h_1}{h_2}$	$\frac{\rho_2}{\rho_1 h_1 h_2 h_4}$	ρ_3										

Effective parameters: 3.0

Layer_No.	Resistivity	Thickness
1	0.17	37.16
2	123.22	34.78
3	0.21	179.34
4	0.32	185.3
5	1.35	252.8
6	4.62	448.86
7	13.69	2750.2
8	13.48	0
# Calibration factor:	2.8717	
# Error:	0.993	



Layer resistivities - 68 percent confidence interval (damped)				
I	RO(I)	BOUND(1)	BOUND(2)	IMPORTANCE
1	0.1747	0.1614	0.1892	0.9007
2	123.2204	115.8769	131.0293	0.3672
3	0.2075	0.1814	0.2375	0.6029
4	0.3185	0.3058	0.3317	0.1851
5	1.3508	1.3401	1.3616	0.0397
6	4.6234	4.6086	4.6382	0.0165
7	13.6863	13.6429	13.7298	0.0145
8	13.4795	13.4738	13.4852	0.0017
Layer depths (to base) - 68 percent confidence interval (damped)				
I	Z(I)	BOUND(1)	BOUND(2)	IMPORTANCE
1	37.159	34.3461	40.2022	0.8483
2	71.9378	65.5808	78.911	0.8839
3	251.2801	241.0173	261.9798	0.1854
4	436.5832	413.119	461.3801	0.2645
5	689.3824	679.9554	698.9402	0.071
6	1138.24	1132.2594	1144.2522	0.0262
7	3888.4436	3888.3662	3888.521	0.0001

Figure E. 49 Resolved combination and importance analyzed using Eigenparameter for Marquardt inversion of Rx2 E-field (Ex), inline transmitter configuration (8th May 2015). Starting model generated using cumulative conductance.

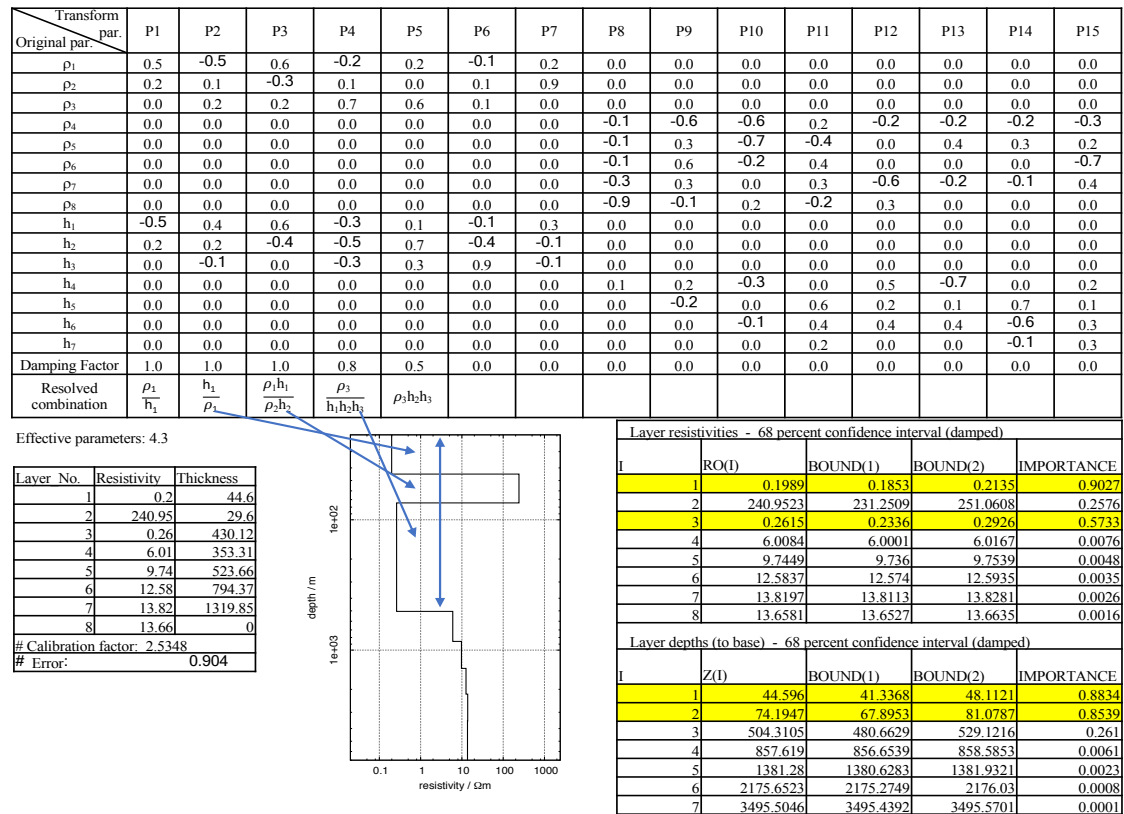


Figure E. 50 Resolved combination and importance analyzed using Eigenparameter for Marquardt inversion of Rx2 E-field (Ex), inline transmitter configuration (8th May 2015). Starting model generated using cumulative transverse resistance.

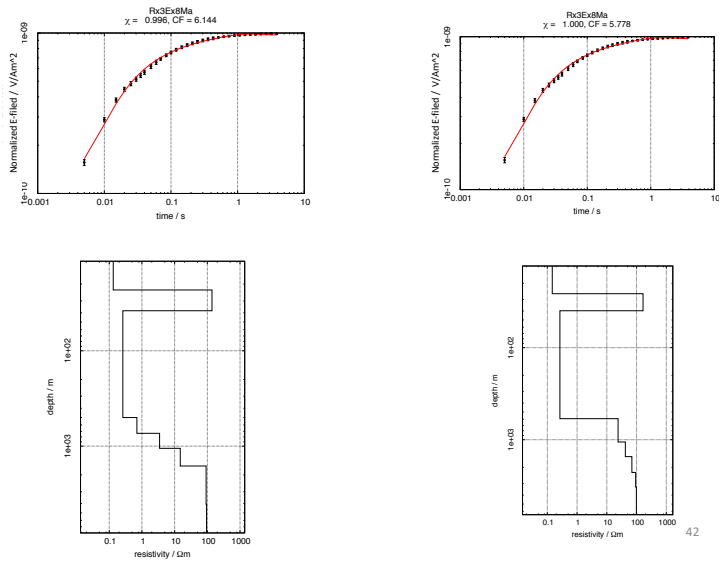
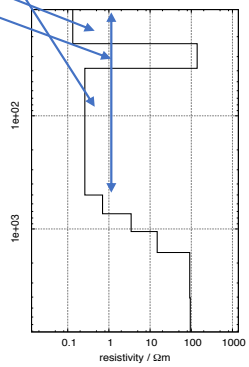


Figure E. 51 Marquardt inversion of Rx3 E-field (Ex) inline transmitter configuration, data measured on 8th May 2015. The starting models generated using cumulative conductance (left) and transverse resistance (right).

Transform Original par.	P1	P2	P3	P4	P5	P6	P7	P8	P9	P10	P11	P12	P13	P14	P15
ρ_1	0.1	-0.8	0.3	-0.2	0.1	-0.3	0.3	-0.3	0.0	0.0	0.0	0.0	0.0	0.0	0.0
ρ_2	0.3	0.1	0.0	0.1	-0.2	0.6	0.5	-0.5	0.0	0.0	0.0	0.0	0.0	0.0	0.0
ρ_3	0.1	0.3	0.3	-0.8	-0.4	-0.1	-0.1	0.0	0.0	0.0	0.0	0.0	0.0	0.0	0.0
ρ_4	0.0	0.0	0.1	0.1	-0.1	-0.1	0.0	-0.1	-0.6	0.7	-0.2	0.1	0.1	0.0	0.0
ρ_5	0.0	0.0	0.0	0.0	0.0	0.0	-0.1	-0.1	-0.1	0.1	-0.2	-0.5	-0.8	0.1	-0.3
ρ_6	0.0	0.0	0.0	0.0	0.0	0.0	0.0	0.0	0.1	0.0	0.0	-0.6	0.6	0.3	-0.4
ρ_7	0.0	0.0	0.0	0.0	0.0	0.0	0.0	0.0	0.1	-0.1	-0.2	-0.4	0.2	-0.2	0.5
ρ_8	0.0	0.0	0.0	0.0	0.0	0.0	0.0	0.0	0.1	-0.1	-0.4	0.0	-0.4	0.5	
h_1	-0.5	0.5	0.2	0.0	0.4	-0.2	0.4	-0.4	0.0	0.0	0.0	0.0	0.0	0.0	0.0
h_2	0.7	0.3	-0.4	-0.1	0.2	-0.5	0.1	-0.2	0.0	0.0	0.0	0.0	0.0	0.0	0.0
h_3	0.0	-0.1	-0.3	-0.4	0.6	0.4	-0.4	-0.3	-0.1	0.1	0.0	0.0	0.0	0.0	0.0
h_4	0.0	-0.1	-0.2	-0.3	0.3	0.1	0.6	0.6	0.1	0.2	-0.2	0.0	0.0	0.0	0.0
h_5	0.0	0.0	0.0	-0.1	0.0	0.0	0.2	0.2	-0.6	-0.2	0.7	-0.2	0.0	0.0	0.0
h_6	0.0	0.0	0.0	0.0	0.0	0.0	0.1	0.1	-0.5	-0.6	-0.6	0.1	0.0	0.1	0.0
h_7	0.0	0.0	0.0	0.0	0.0	0.0	0.0	0.0	0.0	0.0	-0.1	0.0	0.1	-0.8	-0.6
Damping Factor	1.0	1.0	1.0	0.7	0.2	0.0	0.0	0.0	0.0	0.0	0.0	0.0	0.1	-0.8	-0.6
Resolved combination	$\frac{\rho_2 h_2}{h_3}$	$\frac{h_1 h_2 \rho_3}{\rho_1}$	$\frac{\rho_4 \rho_3}{h_2 h_3}$	$\frac{1}{\rho_3 h_3 h_4}$											

Effective parameters: 4.0

Layer No.	Resistivity	Thickness
1	0.13	23.05
2	138.91	15.01
3	0.26	463.37
4	0.7	232.05
5	3.46	320.38
6	14.87	561.29
7	91.53	2448.07
8	94.53	0
# Calibration factor:	6.1445	
# Error:	0.996	



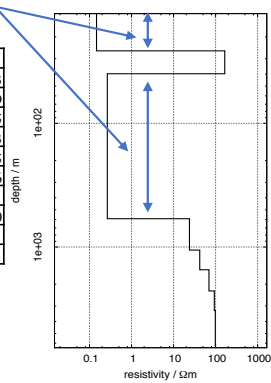
Layer resistivities - 68 percent confidence interval (damped)				
i	RO(I)	BOUND(1)	BOUND(2)	IMPORTANCE
1	0.13	0.13	0.14	0.83
2	138.91	136.68	141.18	0.29
3	0.26	0.24	0.29	0.72
4	0.70	0.69	0.71	0.11
5	3.46	3.45	3.48	0.03
6	14.87	14.85	14.89	0.01
7	91.53	91.49	91.58	0.00
8	94.5282	94.514	94.5425	0.001
Layer depths (to base) - 68 percent confidence interval (damped)				
i	Z(I)	BOUND(1)	BOUND(2)	IMPORTANCE
1	23.05	22.43	23.68	0.72
2	38.06	36.90	39.25	0.83
3	501.42	473.52	530.96	0.40
4	733.47	704.99	763.11	0.28
5	1053.85	1043.44	1064.36	0.07
6	1615.14	1610.29	1620.01	0.02
7	4063.2078	4063.1738	4063.2417	0.0001

Figure E. 52 Resolved combination and importance analyzed using Eigenparameter for Marquardt inversion of Rx3 E-field (Ex), inline transmitter configuration (8th May 2015). Starting model generated using cumulative conductance.

Transform Original par.	par.	P1	P2	P3	P4	P5	P6	P7	P8	P9	P10	P11	P12	P13	P14	P15
ρ_1		0.1	-0.7	0.3	-0.2	0.0	-0.4	0.4	0.0	0.0	0.0	0.0	0.0	0.0	0.0	0.0
ρ_2		0.2	0.1	0.0	0.1	-0.1	0.6	0.7	0.0	0.0	0.0	0.0	0.0	0.0	0.0	0.0
ρ_3		0.0	0.3	0.3	-0.6	-0.6	-0.1	0.0	0.0	0.0	0.0	0.0	0.0	0.0	0.0	0.0
ρ_4		0.0	0.0	0.0	0.0	0.0	0.0	0.0	0.6	0.1	0.6	-0.2	0.2	-0.2	0.2	0.1
ρ_5		0.0	0.0	0.0	0.0	0.0	0.0	0.0	0.2	0.1	0.2	0.4	0.2	0.4	-0.7	-0.1
ρ_6		0.0	0.0	0.0	0.0	0.0	0.0	0.0	0.0	0.1	0.3	0.4	-0.4	0.2	0.4	-0.6
ρ_7		0.0	0.0	0.0	0.0	0.0	0.0	0.0	-0.1	0.0	0.1	0.0	0.0	0.8	0.3	0.4
ρ_8		0.0	0.0	0.0	0.0	0.0	0.0	0.0	0.0	0.0	0.1	0.3	0.1	0.0	0.2	0.6
h_1		-0.6	0.4	0.1	-0.1	0.4	-0.3	0.5	0.0	0.0	0.0	0.0	0.0	0.0	0.0	0.0
h_2		0.7	0.3	-0.4	-0.1	0.1	-0.5	0.2	0.0	0.0	0.0	0.0	0.0	0.0	0.0	0.0
h_3		0.0	-0.2	-0.4	-0.7	0.4	0.3	-0.1	0.0	0.0	0.0	0.0	0.0	0.0	0.0	0.0
h_4		0.0	0.0	0.0	0.0	0.0	0.0	0.0	-0.7	0.5	0.5	-0.2	0.1	-0.1	-0.1	0.0
h_5		0.0	0.0	0.0	0.0	0.0	0.0	0.0	-0.3	-0.8	0.4	0.1	0.2	0.0	0.0	-0.1
h_6		0.0	0.0	0.0	0.0	0.0	0.0	0.0	-0.1	0.2	-0.2	0.6	0.6	-0.2	0.3	-0.1
h_7		0.0	0.0	0.0	0.0	0.0	0.0	0.0	0.0	0.0	0.1	0.4	-0.6	-0.3	-0.1	0.4
Damping Factor		1.0	1.0	1.0	0.7	0.3	0.0	0.0	0.0	0.0	0.0	0.0	0.0	0.0	0.0	0.0
Resolved combination		$\frac{h_2}{h_1}$	$\frac{h_1 h_2 \rho_3}{\rho_1}$	$\frac{\rho_1 \rho_3}{h_2 h_3}$	$\frac{1}{\rho_3 h_3}$	$\frac{h_1 h_3}{\rho_3}$										

Effective parameters: 4.0

Layer No.	Resistivity	Thickness
1	0.15	25.93
2	165.18	13.79
3	0.27	551.05
4	23.88	468.63
5	41.97	468.5
6	69.55	739.16
7	93.08	995.61
8	98.47	0
# Calibration factor:	5.7782	
# Error:	1.000	



Layer resistivities - 68 percent confidence interval (damped)				
I	RO(I)	BOUND(1)	BOUND(2)	IMPORTANCE
1	0.147	0.1417	0.1523	0.8351
2	165.1752	163.22	167.1539	0.2521
3	0.2653	0.2449	0.2874	0.6373
4	23.8816	23.8659	23.8973	0.0055
5	41.9726	41.9614	41.9838	0.0021
6	69.5485	69.5361	69.5608	0.0014
7	93.0791	93.0692	93.0891	0.0008
8	98.4677	98.4521	98.4833	0.0011
Layer depths (to base) - 68 percent confidence interval (damped)				
I	Z(I)	BOUND(1)	BOUND(2)	IMPORTANCE
1	25.9285	25.1578	26.7229	0.7241
2	39.7226	38.6614	40.813	0.831
3	590.7711	543.8289	641.7653	0.6575
4	1059.3972	1058.8447	1059.95	0.0042
5	1527.8975	1527.5123	1528.2827	0.0023
6	2267.0552	2266.8188	2267.2917	0.0007
7	3262.668	3262.6143	3262.7217	0.0001

Figure E. 53 Resolved combination and importance analyzed using Eigenparameter for Marquardt inversion of Rx3 E-field (Ex), inline transmitter configuration (8th May 2015). Starting model generated using cumulative transverse resistance.

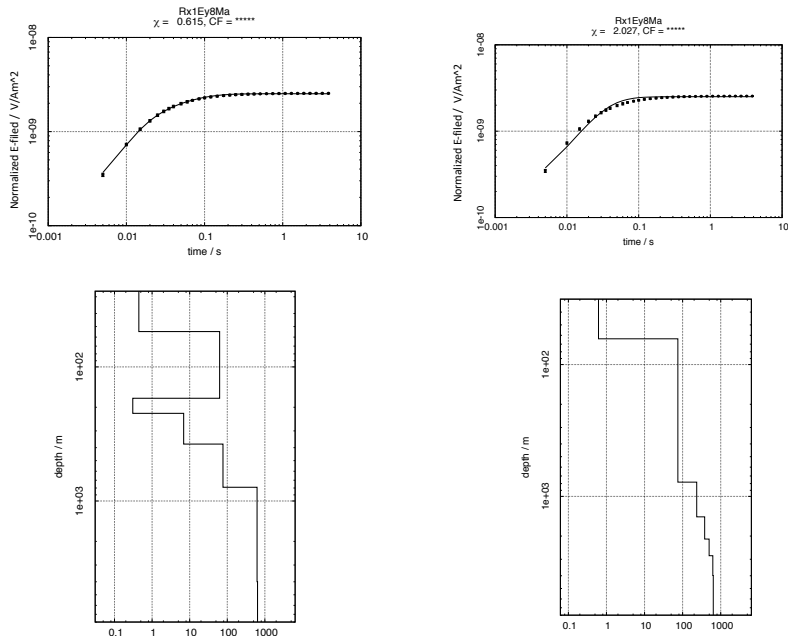


Figure E. 54 Marquardt inversion of Rx1 E-field (Ey) inline transmitter configuration, data measured on 8th May 2015. The starting models generated using cumulative conductance (left) and transverse resistance (right).

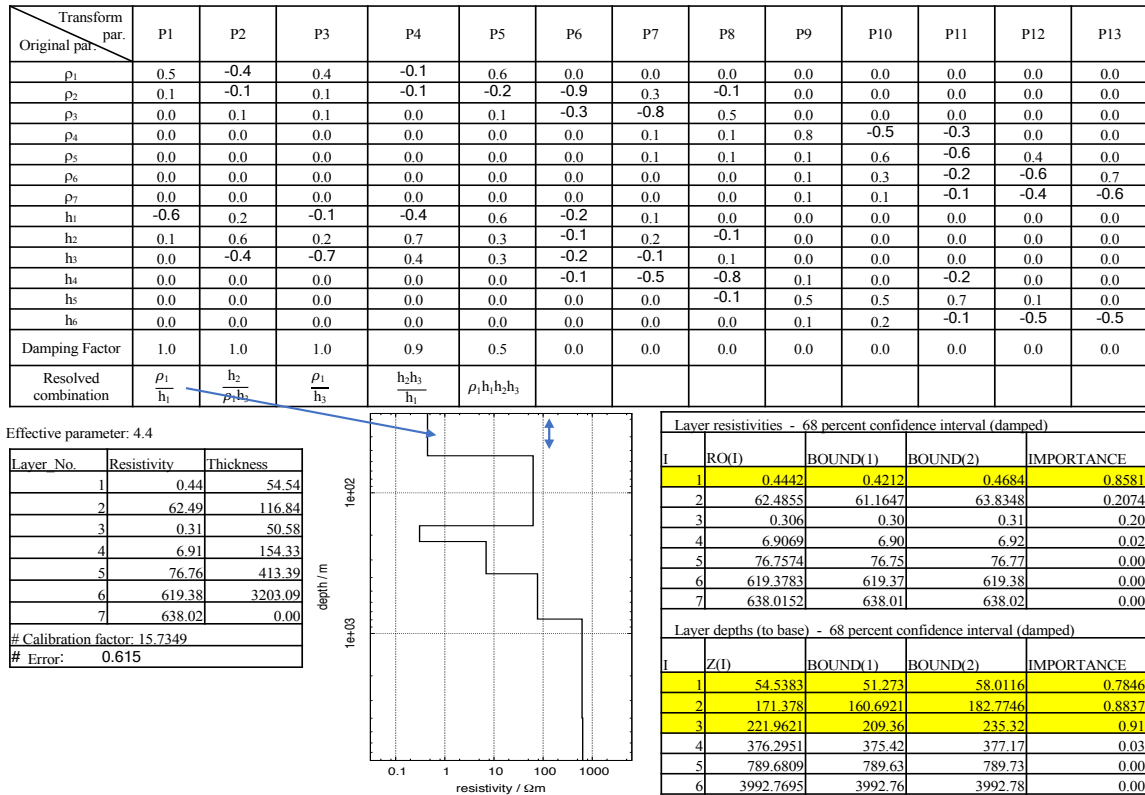


Figure E. 55 Resolved combination and importance analyzed using Eigenparameter for Marquardt inversion of Rx1 E-field (Ey), inline transmitter configuration (8th May 2015). Starting model generated using cumulative conductance.

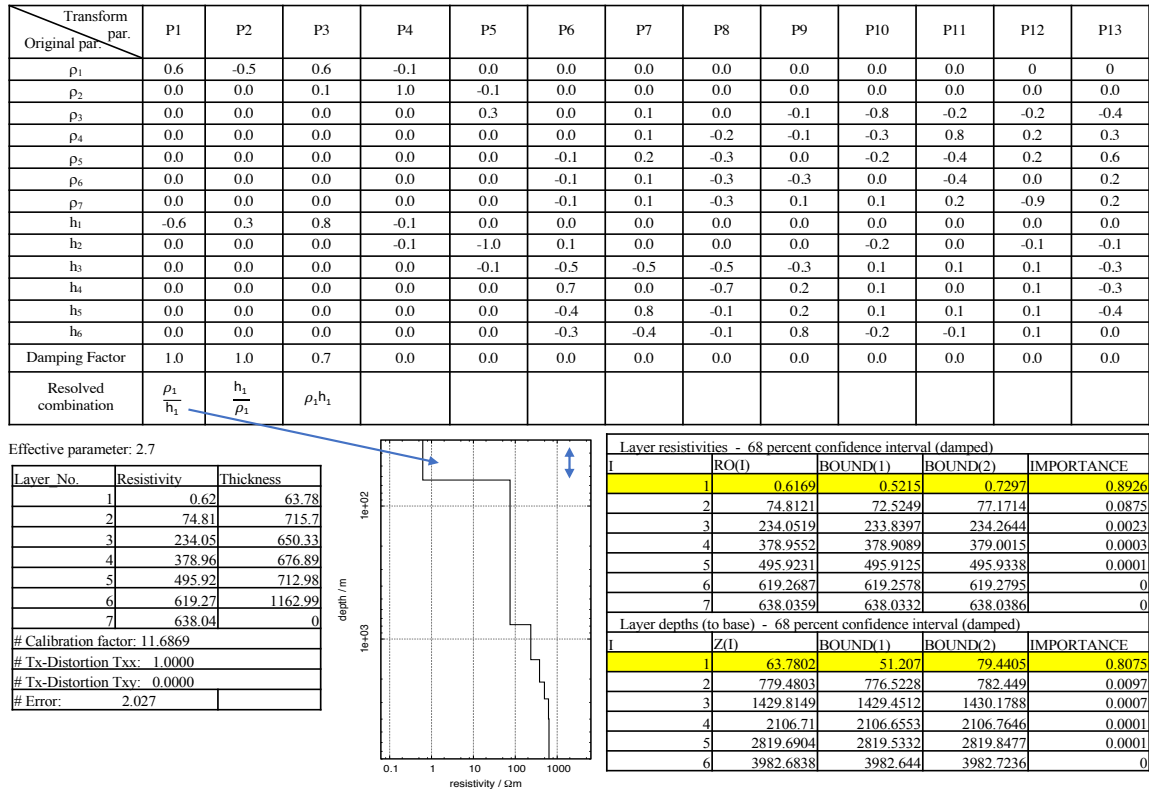


Figure E. 56 Resolved combination and importance analyzed using Eigenparameter for Marquardt inversion of Rx1 E-field (Ey), inline transmitter configuration (8th May 2015). Starting model generated using cumulative transverse resistance.

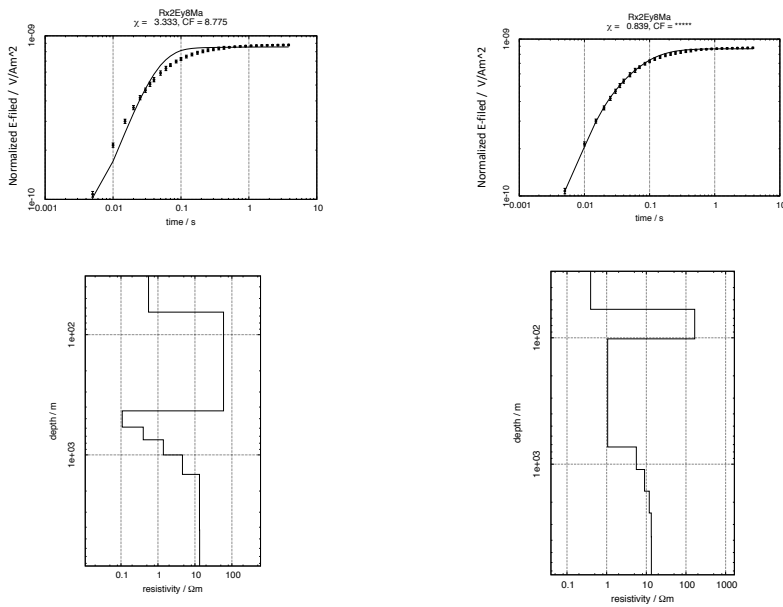
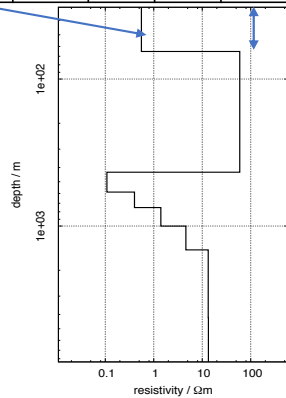


Figure E. 57 Marquardt inversion of Rx2 E-field (Ey) inline transmitter configuration, data measured on 8th May 2015. The starting models generated using cumulative conductance (left) and transverse resistance (right).

Transform Original par.	par.	P1	P2	P3	P4	P5	P6	P7	P8	P9	P10	P11	P12	P13	P14	P15
ρ_1		0.6	-0.5	0.6	-0.1	0.2	-0.1	0.0	0.0	0.0	0.0	0.0	0.0	0.0	0.0	0.0
ρ_2		0.1	0.0	-0.1	0.9	0.4	0.0	-0.1	0.0	0.0	0.0	0.0	0.0	0.0	0.0	0.0
ρ_3		0.0	0.0	0.0	0.2	-0.1	-0.2	0.9	-0.3	0.0	0.0	0.0	0.0	0.0	0.0	0.0
ρ_4		0.0	0.0	0.0	0.0	0.0	-0.1	-0.1	-0.1	-0.4	-0.1	0.6	-0.7	0.0	-0.1	0.0
ρ_5		0.0	0.0	0.0	0.0	0.0	0.0	0.0	-0.1	0.2	-0.2	-0.5	-0.4	-0.7	-0.1	-0.1
ρ_6		0.0	0.0	0.0	0.0	0.0	0.0	0.0	0.0	0.1	-0.2	-0.5	-0.3	0.4	-0.1	0.1
ρ_7		0.0	0.0	0.0	0.0	0.0	0.0	0.0	0.0	0.0	-0.1	-0.2	-0.3	0.5	0.5	-0.2
ρ_8		0.0	0.0	0.0	0.0	0.0	0.0	0.0	0.0	0.0	-0.1	-0.1	-0.1	0.1	-0.2	0.9
h_1		-0.6	0.3	0.8	0.1	0.0	0.0	0.0	0.0	0.0	0.0	0.0	0.0	0.0	0.0	0.0
h_2		0.0	0.4	0.0	-0.4	0.8	-0.3	0.1	0.0	0.0	0.0	0.0	0.0	0.0	0.0	0.0
h_3		0.0	0.0	0.0	-0.1	0.3	0.9	0.2	-0.2	0.0	0.0	0.0	0.0	0.0	0.0	0.0
h_4		0.0	0.0	0.0	0.0	0.0	0.1	0.3	0.9	0.2	-0.1	0.1	-0.2	-0.1	0.0	0.0
h_5		0.0	0.0	0.0	0.0	0.0	0.0	0.1	0.2	-0.8	0.3	-0.4	0.0	-0.1	0.0	0.0
h_6		0.0	0.0	0.0	0.0	0.0	0.0	0.0	0.0	-0.3	-0.9	0.0	0.3	0.0	0.1	0.0
h_7		0.0	0.0	0.0	0.0	0.0	0.0	0.0	0.0	0.0	-0.1	0.0	0.3	-0.8	-0.4	0.0
Damping Factor		1.0	1.0	0.2	0.0	0.0	0.0	0.0	0.0	0.0	0.0	0.0	0.0	0.0	0.0	0.0
Resolved combination		$\frac{\rho_1}{h_1}$	$\frac{h_1 h_2}{\rho_1}$													

Effective parameter: 2.2

Layer No.	Resistivity	Thickness
1	0.56	64.96
2	59.51	365.47
3	0.11	156.98
4	0.4	161.8
5	1.4	251.91
6	4.6	452.96
7	13.3	2750
8	13.4	0
# Calibration factor	8.7745	
# Error:	3.333	



Layer resistivities - 68 percent confidence interval (damped)				
I	RO(I)	BOUND(1)	BOUND(2)	IMPORTANCE
1	0.5559	0.5111	0.6047	0.7837
2	59.5089	58.988	60.0344	0.0793
3	0.108	0.1076	0.1084	0.0193
4	0.4006	0.4006	0.4007	0.0001
5	1.4007	1.4007	1.4008	0
6	4.6009	4.6009	4.6009	0
7	13.301	13.301	13.301	0
8	13.4	13.4	13.4	0
Layer depths (to base) - 68 percent confidence interval (damped)				
I	Z(I)	BOUND(1)	BOUND(2)	IMPORTANCE
1	64.9573	59.5874	70.8112	0.6291
2	430.4282	414.2611	447.2262	0.3556
3	587.41	586.9988	587.8216	0.0018
4	749.2084	749.1417	749.275	0.0004
5	1001.1172	1001.0751	1001.1593	0.0002
6	1454.0743	1454.0554	1454.0933	0
7	4204.0747	4204.0728	4204.0767	0

Figure E. 58 Resolved combination and importance analyzed using Eigenparameter for Marquardt inversion of Rx2 E-field (E_y), inline transmitter configuration (8th May 2015). Starting model generated using cumulative conductance.

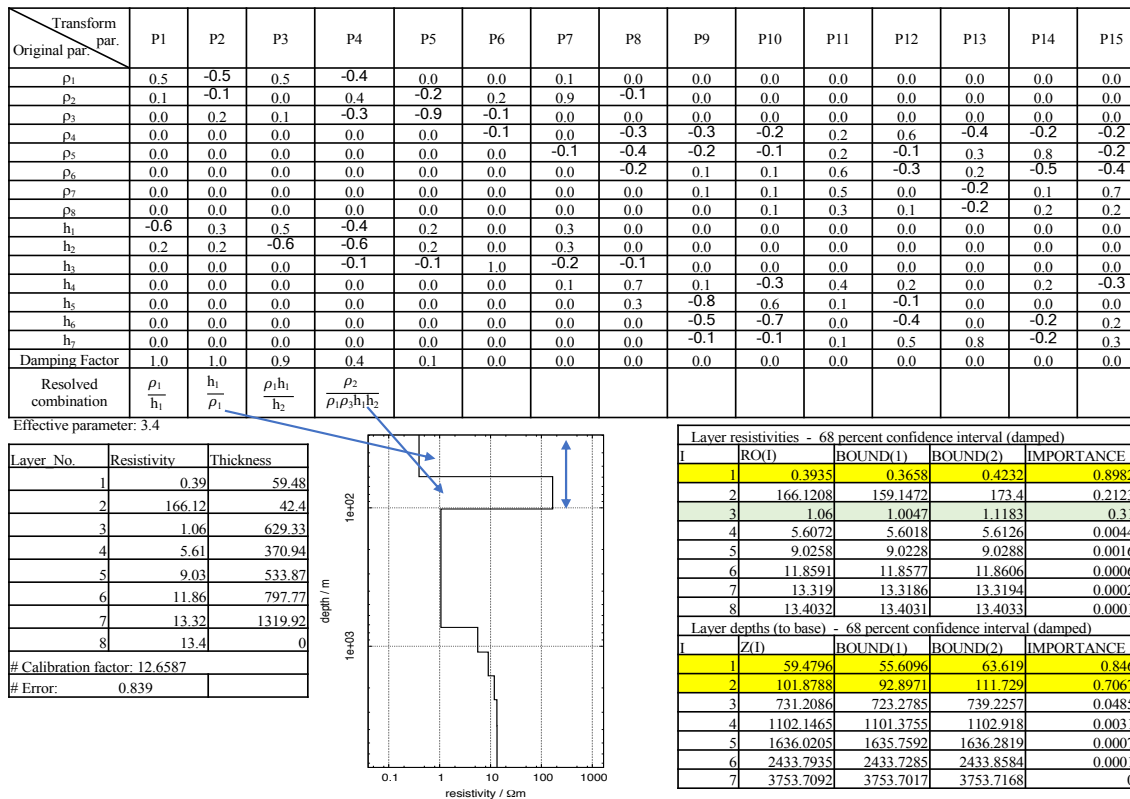


Figure E. 59 Resolved combination and importance analyzed using Eigenparameter for Marquardt inversion of Rx2 E-field (Ey), inline transmitter configuration (8th May 2015). Starting model generated using cumulative transverse resistance.

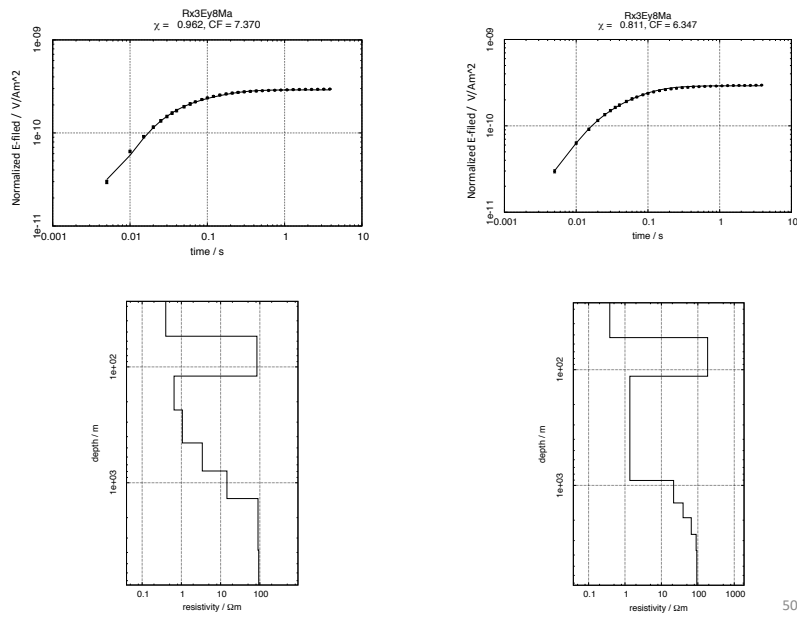


Figure E. 60 Marquardt inversion of Rx3 E-field (Ey) inline transmitter configuration, data measured on 8th May 2015. The starting models generated using cumulative conductance (left) and transverse resistance (right).

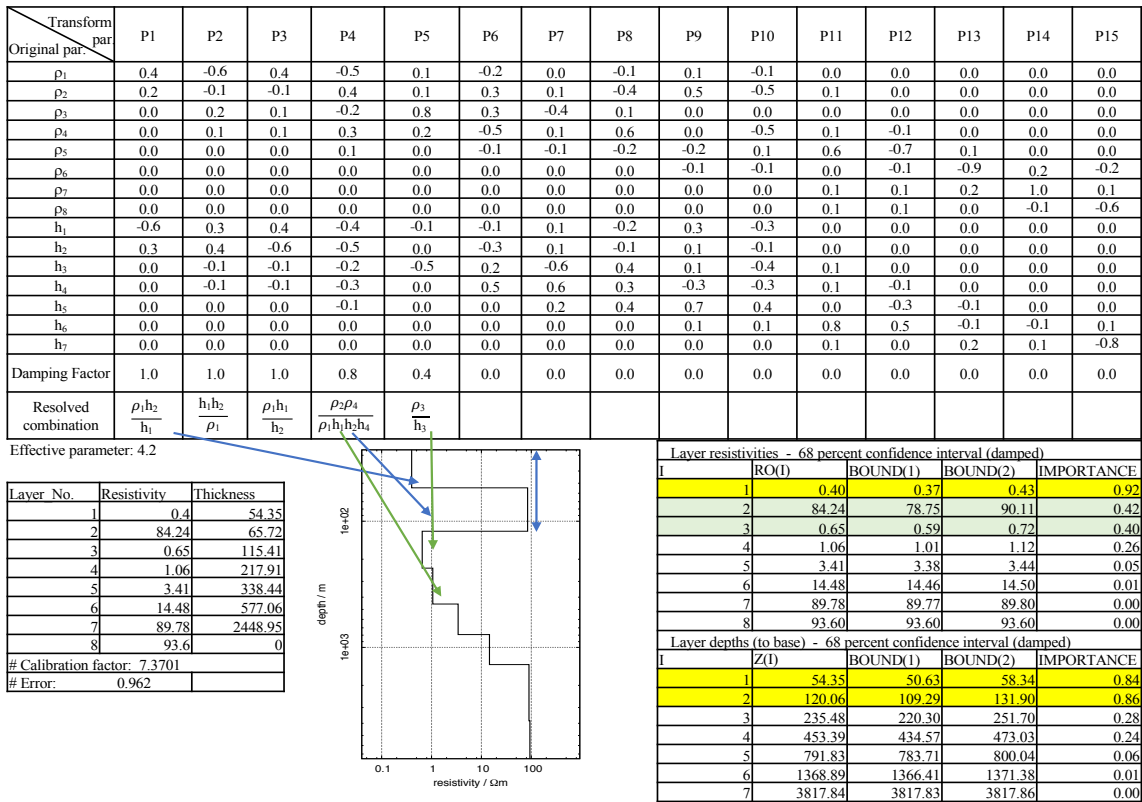


Figure E. 61 Resolved combination and importance analyzed using Eigenparameter for Marquardt inversion of Rx3 E-field (Ey), inline transmitter configuration (8th May 2015). Starting model generated using cumulative conductance.

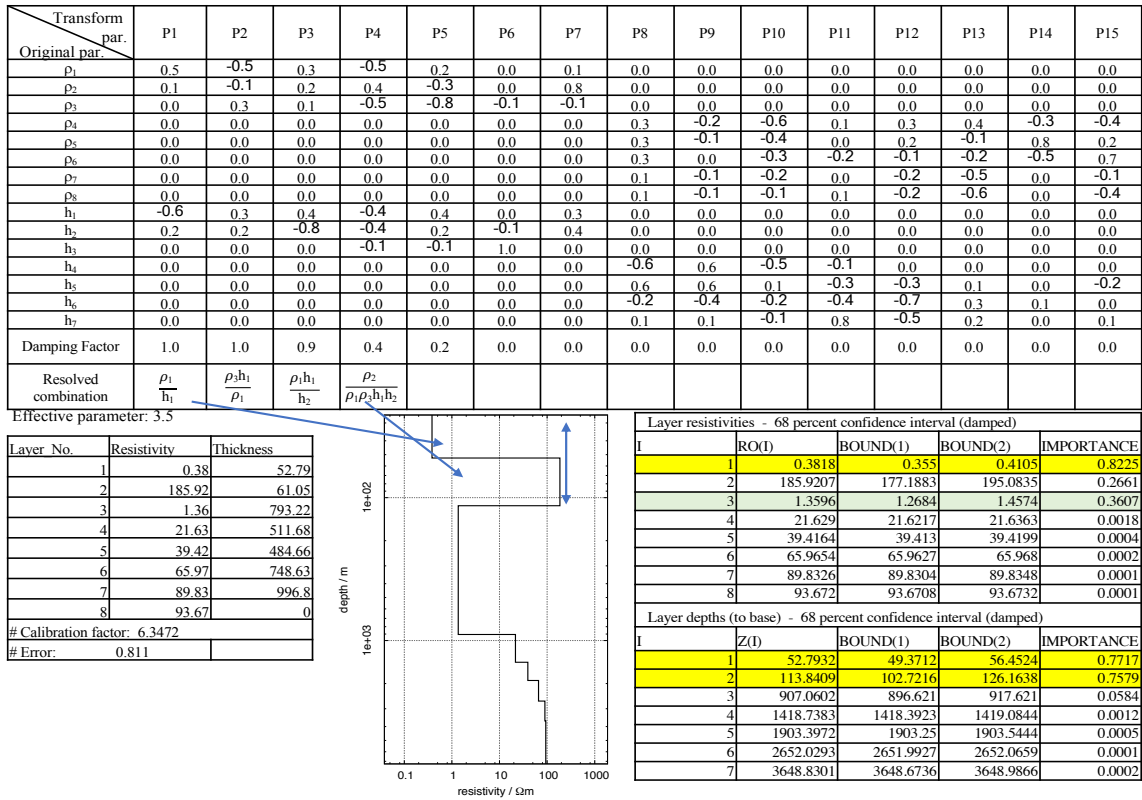
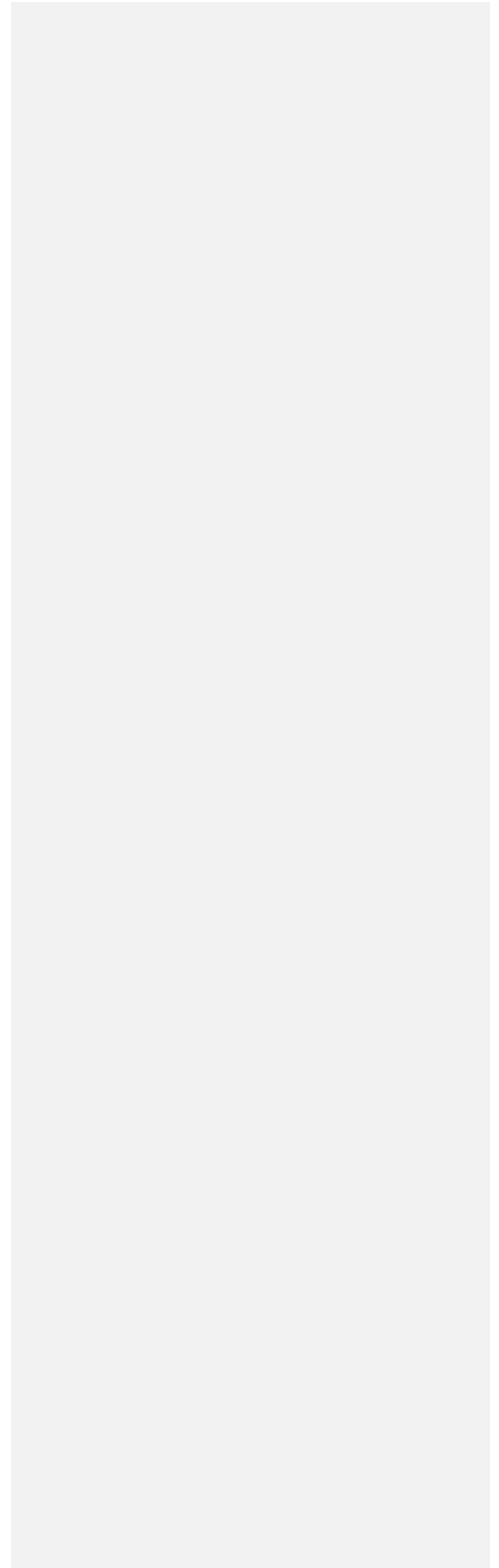


Figure E. 62 Resolved combination and importance analyzed using Eigenparameter for Marquardt inversion of Rx3 E-field (Ey), inline transmitter configuration (8th May 2015). Starting model generated using cumulative transverse resistance.

APPENDIX F
Time-Lapse and Feasibility Study



F.1 Time-lapse processing

In addition to understanding the processing of noisy data, a description of time-lapse processing is included as it requires more accurate detailed processing. The same processing steps as applied to the Hockley data, which have more noise as. The result is displayed in percentage differences from different days of measurements with the purpose of obtaining the resistivity changes, for example, due to the reservoir production or water flooding. Based on this concept, the relative differences of the processed data are calculated. In this research, only the magnetic field data (Figure F.1) are used due to its sensitivity to the noise as recorded in Hockley data. Hence, the time-lapse results are expected to clearly display the resistivity changes. The following formula presents the relative difference calculation related to the time-lapse measurements:

$$\% \text{ differences} = \left| \frac{U(t)_{day 2} - U(t)_{day 1}}{U(t)_{day 1}} \right| 100\% \quad (\text{F.1})$$

where $U(t)$ is the measured magnetic field (mV).

The processing results as well as the high quality of the data with less noise, that will lead the reliable interpretation in this research. The interpretation refers to several previous studies such as Colombo et al. (2010), Strack and Aziz (2012), and Yan et al. (2017).

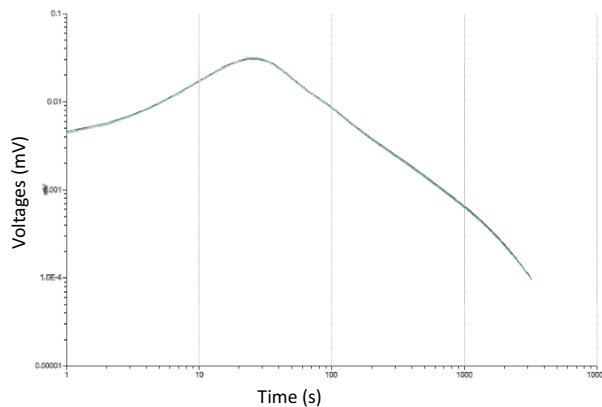


Figure F. 1 The smooth data after data processing displayed from two different days. The differences of two different signal will be further calculated to show the voltages change.

The result from time-lapse confirm the smooth signal after the processing steps. This means that the recorded signal contains the lower interference of the noise. The processed signals from two different days are shown in the Figure 4.16 below. Those smooth results lead to calculate the difference of two measurements accurately.

The differences (Figure F.2) show differences after 50 ms. As the water moves from the injection well spreading surrounding the area of survey, the second receiver located one thousand meters from the injection show the differences about 2 %. There are other data sets, but for the purpose of this thesis, the noisiest data are used as example. The other go up in anomaly to several tens or percent. A comparative consideration would be beyond this thesis.

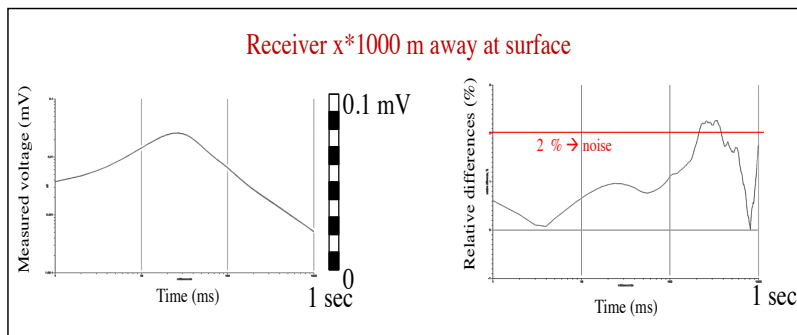


Figure F. 2 The smooth signals from two different day measurements produced after data processing (right). Data recorded from the real oil field monitoring showing the differences voltage after two days (left).

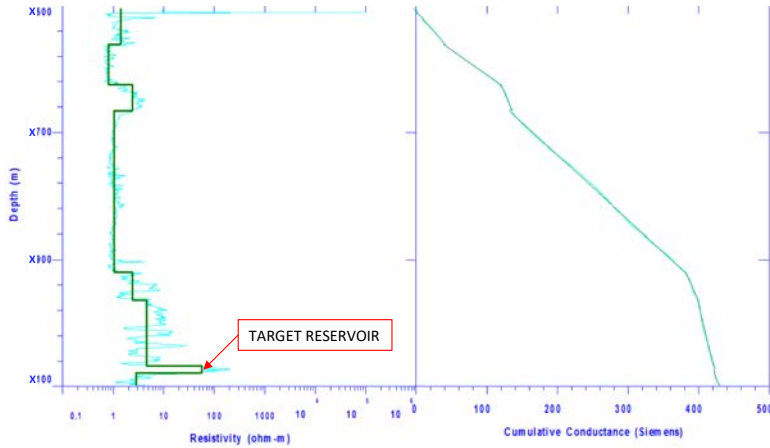
F.2 Feasibility study

When applying LOTEM to real oil field applications, the translation from well log to a model usable for modeling is essential. In this scaling we use various scaling method (Keller & Frischknecht, 1966; Strack, 1992). They are based on physics of horizontal versus vertical current flow. When we invert we use the same techniques in the reverse sense. Here, the techniques starting from the most detailed measurement basis, the well log, are shown. Using Archie's equation, the oil and water saturation are calculated. This is related to the porosity and resistivity and the cumulative conductance analysis to calculate the average of resistivity from the well log. The oil and water saturation (S_w) in the target zone are estimated using Archie's equation as follow:

Deleted: 1967

$$S_w = \sqrt[n]{\frac{R_0}{R_t}} \tag{F.2}$$

where n, called saturation exponent, is very closed to 2, Ro is read from the deep induction curve in a clean non-shale formation fully saturated with water, and Rt is the formation true resistivity is the reading from the induction curve in the interested zone where the resistivity average is calculated using cumulative conductance analysis.



DATASET: Area-2-Well-Y				
LAYER	RESISTIVITY	THICKNESS	DEPTH	SW
1	1.4	x561	x561	68%
2	0.8	63	x625	90%
3	2.4	39	x664	52%
4	1	254	x920	80%
5	2.4	44	x964	52%
6	4.5	104	x067	38%
7	56.6	11	x079	11%
8	2.4	21	x100	52%

$R_t \approx \text{LLD}$
 $R_o (S_w \approx 100\%) = 0.37$
 $n=2$
 $S_w = \sqrt[n]{\frac{R_0}{R_t}}$

Figure F. 3 Bore hole analysis using cumulative conductance to produce resistivity layers (The real depth is hidden for confidential information). As this is real data, the thousand-meter mark is anonymized.

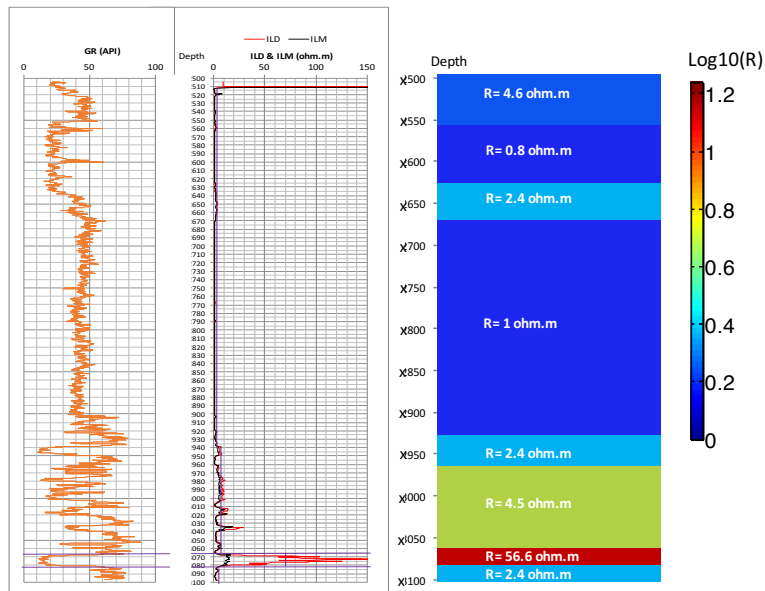


Figure F.4 An example of generated resistivity layered model from borehole data from real oil field (India). The well log data (left) analyzed using cumulative conductance to produce the horizontal resistivity layer visualized in the homogeneous cross section (right).

Forward calculation is performed using LOTEM suite by inputting the model (resistivities and thicknesses or depth) produced from the cumulative conductance analysis (Figure F.4). The equivalent for transverse resistance was not used because most of the section is conductive. The required parameters are offset, transmitter length current and the electrode space for E-field and the area of the loop for H-field. The result for the E-field with varying single layer resistivity is shown in Figure F.5, and % differences of varying layer resistivity of E-Field shown in Figure F.6. The signal from the H-field show the low response as expected (Figure F.7)

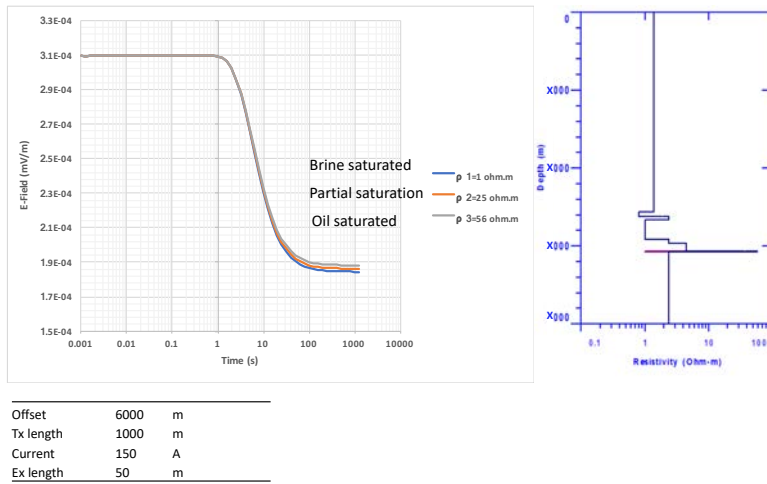


Figure F. 5 Forward model result (synthetic model) of E-field with varying single layer resistivity.

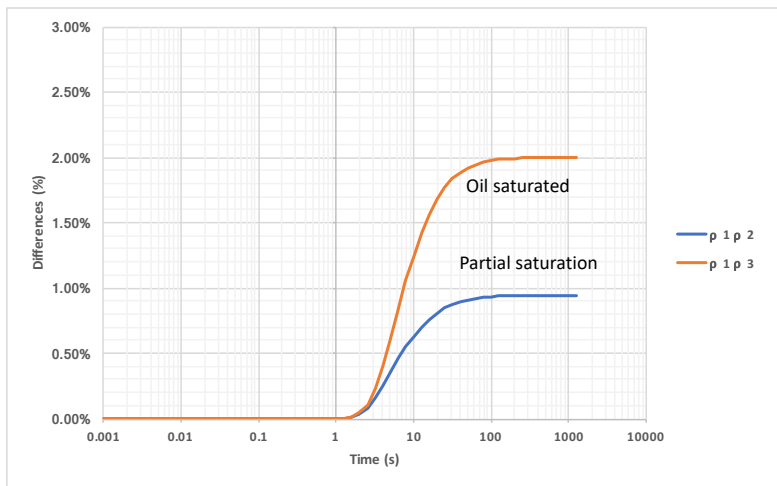


Figure F. 6 Percentage differences of varying reservoir saturation (layer resistivity of E-field model). The signals are strong, but the percentage variation is at the lower end.

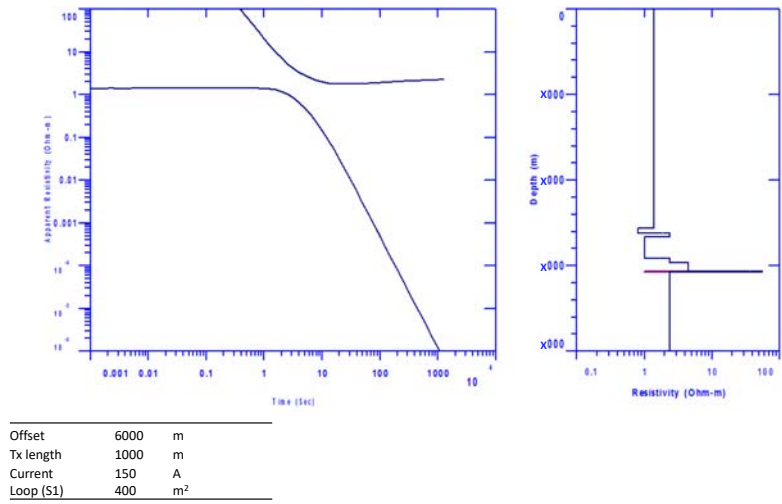


Figure F. 7 The early and late time apparent resistivity of H-field showing the low response as expected as only the electric field in this configuration see the resistive reservoir (similar to the example in Strack, 1992).

RESEARCH PUBLICATION

- Paembonan, A. Y., Arjwech, R., Davydycheva, S., & Strack, K. M. (2017). A Processing of very noisy LOTEM data from Hockley Salt Dome, Houston, Texas, EGU General Assembly Conference Abstracts, 2017 | conference-paper
- Paembonan, A. Y., Arjwech, R., Davydycheva, S. Smirnov, M. & Strack, K. M. (2017). An application of LOTEM around salt dome near Houston, Texas, AIP Conference Proceedings 2017, DOI: 10.1063/1.4990893.

CURRICULUM VITAE

Name : Andri Yadi Paembonan
Address : 57/44 Mittraphap Rd., Muang District, Khon Kaen, Thailand,
40000Tel. 099-893-5079
Email : andriyadi@kkumail.com
Date of Birth : January 23, 1989
Age : 28 years old
Nationality : Indonesia
Religion : Christian Protestant
Interest : Computer programming, Reading

Education

2015-2018 Studying Master's degree in Department of Geotechnology,
Faculty of Technology Khon Kaen University. (GPA 3.81)
Thesis topic is "An Application of Long-Offset Transient
Electromagnetic (LOTEM) around a Salt Dome near Houston,
Texas"
2007-2011 Bachelor of Science (Physics), Faculty of Mathematics and
Natural Sciences
State University of Makassar, Indonesia (GPA 3.34)

Work Experience/Internship

2016 - 2018 Training program with KMS Technologies (CSEM), Data
processing and software development.
2016 Special Projects in Geotechnology (2D Electrical Resistivity
Imaging for Saline Groundwater on Khon Kaen University
Campus)
2014 - 2015 Bridging Program International, Mulawarman University
2013 - 2015 Staff of International Office, Mulawarman University

- 2011 - 2012 Laboratory Assistant of Earth Physics Laboratory, Department of Physics, State University of Makassar
- 2009 Internship in PT. Antam Tbk. Unit Bisnis Pertambangan Nikel
- 2008 Computer Training of Physics Department, Makassar State University

Skills

- Computer: Seismic refraction and reflection processing, Resistivity processing software (1D and 2D), Controlled Sources Electromagnetic (CSEM) (KMSPRO Software-uncommercial software, EMUPLUS-Inversion software), Voxler 3D Windows and Microsoft office (Word, Excel, Power Point), Internet network and installation, Multimedia and product design (Photoshop, CorelDraw, and Movie editor).
- Language: Fair in written and spoken English

Scholarship

- 2018 Graduate Support Scholarship for Research Studying Abroad.
- 2017 Thesis Support Scholarship Application for Graduate Studies, Khon Kaen University Second Semester 2016.
- 2015 – 2017 KKKU Scholarship for ASEAN and GMS Countries' Personnel, Academic Year 2015
- 2014 – 2015 Beasiswa Kaltim Cemerlang 2014

Publication

A Processing of very noisy LOTEM data from Hockley Salt Dome, Houston, Texas, EGU General Assembly Conference Abstracts, 2017 | conference-paper

An application of LOTEM around salt dome near Houston, Texas, AIP Conference Proceedings 2017, DOI: 10.1063/1.4990893

EID: 2-s2.0-85026548327

[http://www.scopus.com/inward/record.url?eid=2-s2.0-](http://www.scopus.com/inward/record.url?eid=2-s2.0-85026548327&partnerID=MN8TOARS)

[85026548327&partnerID=MN8TOARS](http://www.scopus.com/inward/record.url?eid=2-s2.0-85026548327&partnerID=MN8TOARS)